NORTHWESTERN UNIVERSITY

Production of Charmonium in 300 GeV/c Hadronic Interactions

A DISSERTATION

SUBMITTED TO THE GRADUATE SCHOOL
IN PARTIAL FULFILLMENT OF THE REQUIREMENTS

for the degree

DOCTOR OF PHILOSOPHY

Field of Physics

By

Thomas Joseph LeCompte

EVANSTON, ILLINOIS

June 1992

AHB9613

© Copyright by Thomas Joseph LeCompte 1992

All Rights Reserved

ABSTRACT

Production of Charmonium in 300 GeV/c Hadronic Interactions

Thomas J. LeCompte

Production cross-sections for the J/psi and psi prime have been measured in 300 GeV pion, proton and antiproton-nucleon collisions in Fermilab experiment 705. Kinematic distributions for the J/psi are extracted, and compared with QCD predictions using published structure functions. Some evidence for a new state decaying into a psi, a pi+ and a pi- is seen. Limits are placed on psi-prime production via a decay from an isotriplet four quark state.

Acknowledgements:

I would like to thank the following people:

First and formost, my advisor, Professor J. Rosen for introducing me to the interesting problems of charmonium production and hadronic molecules, his support and advice throughout my tenure at Northwestern, and especially his refusal to accept anything less than my best work.

The people with whom I shared an office: Yao Tan, Steve Delchamps, Tom Bohanon, Merrill Jenkins and George Zioulas, for their discussions, helpful suggestions, and especially their patience. I would especially like to thank Marzia Rosati for her help and advice at all hours.

Dr. L. Spiegel for his watchful eye and ready ear, keeping me on track throughout my stay at Fermilab.

The Fermilab Accelerator, Research and Computing Divisions for the use of their facilities and expertise, and the Physics Department for providing a pleasant and productive work environment.

I would especially like to thank all of my teachers, especially Mr. R.S. Szorc and Sr. Ellen Springer, without whom I could never have gotten this far.

Finally, I would like to thank and dedicate this thesis to my parents, Rosemary Rendek and the late Arnold LeCompte.

This research was sponsored under Department of Energy contracts DE-FG02-91ER40684 and DE-AC02-76ER0229.

Contents

Chapter 1: Introduction 1

A. The Standard Model 1

B. Charmonium 5

1. Discovery 5

2. Interpretation and Spectroscopy 5

C. Experimental Goals 10

Chapter 2: Beam and Detector 26

A. The Tevatron 26

B. Beam Line 26

C. Experiment Target 31

D. Upstream Tracking 33

E. Analysis Magnet 42

F. Downstream Tracking 43

G. Charged Particle Hodoscope 44

H. Calorimeter 46

1. Main Array 46

2. Active Converter 50

3. Gas Tube Hodoscope 51

4. Lead-Gas Calorimeter 53

I. Muon Hodoscope 56

Chapter 3: Experimental Running 60

A. Run Eras 59

B. Beam Normalization 62
C. Triggers 79
D. Counter Efficiencies 84
E. Chamber Efficiencies 87
Chapter 4: Event Reconstruction 94
A. Basic Algorithm 94
1. Beam Tracks 94
2. Upstream Tracks 95
3. Vertex Position 97
4. Downstream Tracks 99
5. Matching and Momentum Calculation 99
B. Pass One 103
1. Filter Program 103
2. Dimuon Tracking 109
3. ACP 110
C. Pass Two 111
D. Post Pass Two 114
Chapter 5: J/ψ Production 115
A. Monte Carlo 115
B. J/ψ Feynman x distributions 132
C. J/ψ Transverse Momentum Distributions 143
C. Total Cross-Section: ψ(1*S*) 154
Chapter 6: States Heavier than 3.097 GeV/c^2 166
A. Monte Carlo 166

B. Dimuon spectrum and $\psi(2S)/\psi(1S)$ relative cross-section 170

C. $\psi 2\pi$ spectrum and $\psi(2S) \rightarrow \mu\mu$ branching fraction 177

D. $\psi_x(3837)$ signal and cross-section times Branching Fraction 197

E. $\psi'\pi$ spectrum 206

Chapter 7: Discussion of Results and Summary 222

A. J/ψ inclusive cross-sections 222

B. J/ψ differential cross-sections 227

C. $\psi(2S)$ inclusive cross-sections 235

D. Search for hadronic molecules 240

E. State at 3837 MeV 240

Chapter 1: Introduction

A. The Standard Model

The current understanding of matter is that the universe is composed of two classes of fundamental particles: fermions, which assemble in aggregates to form matter, and gauge bosons, which mediate the forces between these fermions.

The fermions that compose matter are divided into categories based on their interactions. Quarks are fundamental fermions that feel the strong force and leptons are fundamental fermions that do not.

Table 1.1
Fundamental Fermions

		Flavor	Charge
Quarks	First Generation	*d* (down)	-1/3
		u (up)	+2/3
	Second Generation	*s* (strange)	-1/3
		c (charm)	+2/3
	Third Generation	*b* (bottom)*	-1/3
		t (top)*	+2/3
Leptons	First Generation	*e*	-1
		ν_e	0
	Second Generation	μ	-1
		ν_μ	0
	Third Generation	τ	-1
		ν_τ	0

* Beauty and truth are alternative names for the *b* and *t* quarks; the *t* quark is not yet discovered.

Both quarks and leptons seem to come in generations. In each generation, there are two quarks, a charged lepton and a neutral lepton or neutrino. The origin of generations and masses is a problem that is not understood today.

Table 1.2
Fundamental Forces and Mediating Particles

	Number	Charge	Mass	Spin	Force
g (gluon)	8	0	0	1	strong
γ (photon)	1	0	0	1	electromagnetic
W	2	+1,-1	~ 80 GeV	1	weak
Z	1	0	~ 92 GeV	1	weak
H (Higgs)	?	one neutral	?	0	"Higgs"
G (graviton)	1	0	0	2?	gravitational

The electromagnetic force, as described by the theory of quantum electrodynamics (QED), is carried by the zero-mass (and therefore infinite range) photon, which couples to particles in proportion to their electric charge. QED predictions have been verified to a high degree of accuracy. For example, theory and observation of the electron's magnetic moment agree to one part in ten billion.[1]

Atoms are held together by the electromagnetic force; one photon exchange produces an α/r potential, which is strong enough to bind an electron to a nucleus, or a positron — the simplest atom is positronium, the bound state of an electron and a positron. In addition to the binding term in the potential, there are smaller terms treated as perturbations to this Hamiltonian. One such term is a spin-orbit (or $\mathbf{L}\cdot\mathbf{S}$) coupling, proportional to α^2 and another is a spin-spin term (the so-called hyperfine interaction) due to the interaction between the electron and nuclear magnetic moments.

The strong force is responsible for holding atomic nuclei together. The current theory of the strong force, quantum chromodynamics (QCD), describes a hadron as a composite object, being composed of quarks, which carry the quantum number of color, and gluons, the gauge bosons that mediate the color force. In this sense, hadrons are analogous to atoms in QED: fermions bound by the mutual attraction in a

one boson exchange potential. In this case, it is a gluon exchange rather than a photon exchange.

The force between two quarks of the same color is repulsive, just as charges repel in electromagnetism; similarly, the force between quarks of different color is attractive. States with net color are not seen, because the net force between their constituent particles is repulsive; only color singlet states are bound. There are two ways to create a color singlet: three quarks of different color (red, blue and green), or a quark and an antiquark of the same color (e.g. red and anti-red). Particles composed of three quarks are called baryons, and some examples are the proton (*uud*), neutron (*udd*), and Λ_c (*udc*). Particles composed of a quark and an antiquark are called mesons, and some examples are the K^+ ($u\bar{s}$), the ϕ ($s\bar{s}$), and the D^0 ($c\bar{u}$). For mesons, the Coulombic term in the potential is:

$$V(r) = -\frac{4\alpha_s}{3r}, \tag{1.1}$$

and for baryons it is half as large:

$$V(r) = -\frac{2\alpha_s}{3r}. \tag{1.2}$$

Unlike the photon, which is electrically neutral, gluons carry color. This leads to a gluon self-coupling, in the form of a three-gluon vertex and a four-gluon vertex. This self-coupling produces a long-distance confinement term, kr, in the potential, which causes quarks to be permanently confined in hadrons. In a continuum description, the lines of force form flux tubes from quark to quark, rather than radiate outward or inward in the case of electrostatic forces. Flux tubes are essentially one dimensional objects, so the force carried by the flux tube does not diminish with distance. Therefore the potential is proportional to the distance between the quarks. It takes an infinite amount of energy to move a quark from the other quarks (or

antiquark) in a hadron to infinity, or to carry the atomic analogy further, the QCD ionization potential is infinite. (There are no unbound states.)

QCD plays an additional important role in the structure of hadrons. Unlike atoms, where the virtual photon field carries almost none of the momentum, measurements of deep inelastic scattering of leptons on nuclei show that the gluons in hadrons carry a substantial fraction of the momentum — approximately half of the nucleon momentum. Also, the production of virtual quark-antiquark pairs (sea quarks) by these gluons is much more important dynamically than the analogous production of electron-positron pairs by virtual photons in atoms. This is because the QCD coupling strength α_s is much larger than the QED coupling strength α: ~1/5 as opposed to 1/137.

The weak force is the interaction responsible for nuclear β-decay. Eigenstates of the weak interaction are not eigenstates of flavor, so the weak interaction allows flavor- changing transitions between quarks and also between leptons. The weak coupling is actually the same as the electromagnetic coupling; the force appears both weaker and of shorter range because the gauge bosons that carry this force, the W and the Z are heavy —80 and 92 GeV. The Higgs boson emerges from the theory as a mechanism to insure local gauge invariance with massive mediators. No Higgs particle (the theory requires at least one, but there may be several) has been directly observed yet. Weak decays are not directly important in the experiment under discussion, except as a source of background: a dimuon trigger can be satisfied by muons from π or K decays.

No renormalizable quantum field theory of gravity has been developed for three dimensional space at this time. The tensor coupling of gravitation in General Relativity would imply a spin-2 carrier, but beyond this there is only speculation.

Since the gravitational force is not relevant to charmonium physics, it will not be discussed further.

B. Charmonium

1. Discovery

In November of 1974, two experiments simultaneously discovered an extremely narrow resonance at approximately 3.1 GeV. One experiment, at the Brookhaven National laboratory AGS, saw a sharp peak in the dielectron mass spectrum at 3.1 GeV in the reaction $p + \mathrm{Be} \rightarrow e^+ + e^- + \mathrm{X}$.[2] The other, at the Stanford Linear Accelerator Center SPEAR $e^+ e^-$ storage ring observed a narrow resonance at the same mass for the three reactions $e^+ + e^- \rightarrow e^+ + e^-$, $e^+ + e^- \rightarrow \mu^+ + \mu^-$, and $e^+ + e^- \rightarrow$ hadrons.[3]

The BNL group, under Samuel C.C. Ting, named this particle the J, and the SLAC group, under Burton Richter, named it the ψ. The official name of this particle is now the J/ψ; any references in this thesis to the ψ should be understood as referring to the J/ψ.

2. Interpretation and Spectroscopy

It has been clear almost from the discovery that this new particle is a bound state of a fourth quark and its antiquark. The fact that the J/ψ decayed primarily into hadrons and that it has the quantum numbers of the photon (because it is formed in electron-positron collisions and so must couple to a virtual photon) suggested that it was a vector meson. However, a hadron of that mass should have a decay width thousands of times larger if it were made up of light quarks — tens or hundreds of MeV, not the observed 68 ± 10 keV.[4] Even without a precise measurement of the width, because of its large branching fraction of ~15% into electromagnetic decays

(e^+e^- and $\mu^+\mu^-$) it is clear that the J/ψ is extraordinarily narrow. In comparison, the ω(783), which is also an isoscalar vector meson, has a branching fraction into e^+e^- of $7.09 \pm 0.19 \times 10^{-5}$.[5]

One mechanism for suppressing the decay into hadrons is the so-called Zweig rule or OZI rule, originally proposed by Okubo, Zweig and Iizuka[6], to explain why the decay $\phi(1020) \rightarrow 2K$ dominates over $\phi \rightarrow 3\pi$, even though the latter is energetically favored. They proposed that decays that involve the annihilation of all the valence quarks in the initial particle are suppressed relative to decays that preserve these quarks. (c.f. Figure 1.1) According to this argument, the J/ψ would otherwise decay into a pair of charmed mesons, but that channel is energetically forbidden, so that only the annihilation modes remain.

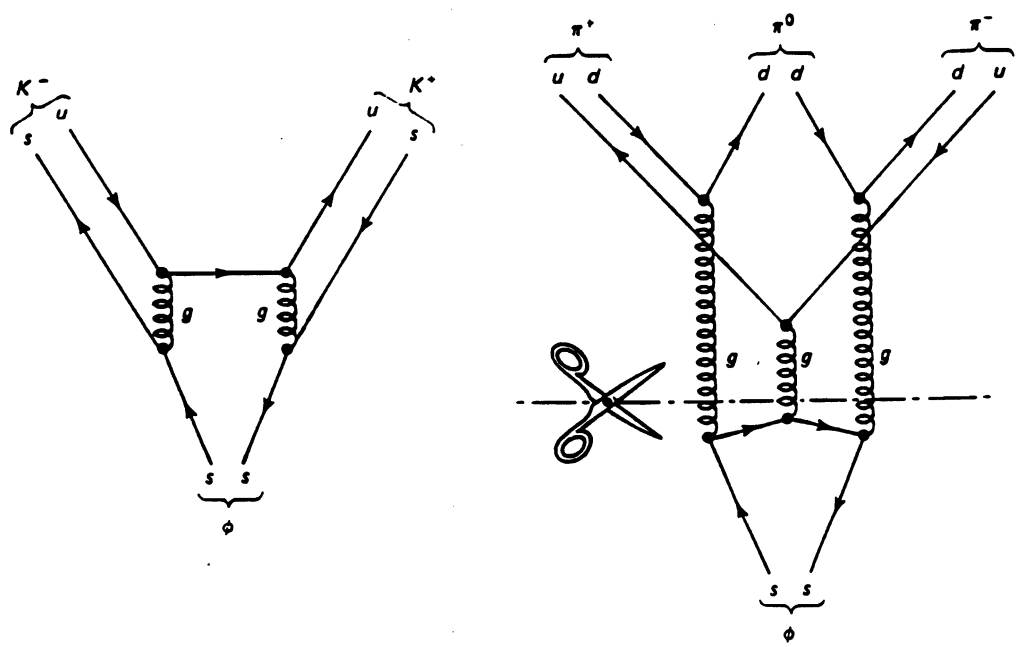

Figure 1.1 Feynman diagrams for OZI-suppressed decays (left) and OZI-allowed decays (right). If the diagram can be cut in two by slicing only gluon lines, the process is suppressed.[7]

There were theoretical reasons to suspect the existence of a fourth quark. One reason was the GIM mechanism of Glashow, Illiopoulos and Maiani[8], which postulated the existence of another charge +2/3 quark to explain the nonobservation of flavor-changing neutral currents, such as the decay $K_L \rightarrow \mu^+\mu^-$. Four quarks allow processes that proceed via intermediate *u*-quarks and processes that proceed via intermediate *c*-quarks to interfere destructively; flavor changing neutral currents are therefore strongly suppressed. A second theoretical motivation for the *c*-quark had to do with triangle anomalies.[9] Diagrams that have three gauge bosons connected via a fermion loop have divergent amplitudes unless the sum of the charges of all the fermions is zero. This requires three colors of quarks, and in addition that there be a charge +2/3 and a charge −1/3 quark in every generation. An orphan *s*-quark would not be allowed; the *c*-quark completed the second generation.

In analogy with positronium, a bound state between a quark and an antiquark is called quarkonium, and between a charmed quark and antiquark, charmonium. In this case, the attraction between the quark and antiquark is primarily due to the strong force, as opposed to the electromagnetic force.

The levels of charmonium are shown in Figure 1.2. This diagram includes states that have not been unambiguously discovered, but are predicted by the charmonium hypothesis: the η_c' (2^1S_0), the η_{c2} ($^1D_2$), and the ψ_2 and ψ_3 ($^3D_2$ and $^3D_3$). Also, the interpretation of the states $\psi(3686)$ and $\psi(3770)$ is complex. One would like to associate the lower state with 2^3S_1 and the higher state with $^3D_1$. (In a hydrogenic potential, the former would have $n = 2$, and the latter $n = 3$.) However, the $\psi(3770)$ can be produced in e^+e^- collisions; indeed that is the only way they have been observed. This is at odds with a pure $^3D_1$ interpretation, because of the small wavefunction overlap in the collision between two point-like particles. However,

since a $^3S_1$ and a $^3D_1$ both have the same spin and parity, it's possible that the states mix. (One example of this sort of mixing is the deuteron, which while predominantly $^3S_1$ has a small admixture of $^3D_1$ as evidenced by its non-zero electric quadrupole moment.) In this interpretation, the lighter $\psi(3686)$ is primarily 2^3S_1 with a small admixture of $^3D_1$ and the heavier $\psi(3770)$ primarily $^3D_1$ with a small admixture of $^3S_1$. This makes calculating the quark-antiquark potential from spectroscopy difficult, because the observed levels are not eigenstates of orbital angular momentum L. Furthermore, the proximity of the $\psi(3770)$ to open charm threshold, 3728 MeV, requires that coupled-channel effects be considered, which further complicate matters.[10]

The difference in mass between states of the same L but different S, such as the η_c and the J/ψ, or the h_c and the χ's is due to the QCD chromomagnetic hyperfine interaction. This is analogous to the magnetic hyperfine splitting in atomic spectra, but is much larger: MeV rather than μeV — a substantial fraction of the level spacing. This is because α_s is much larger than α.

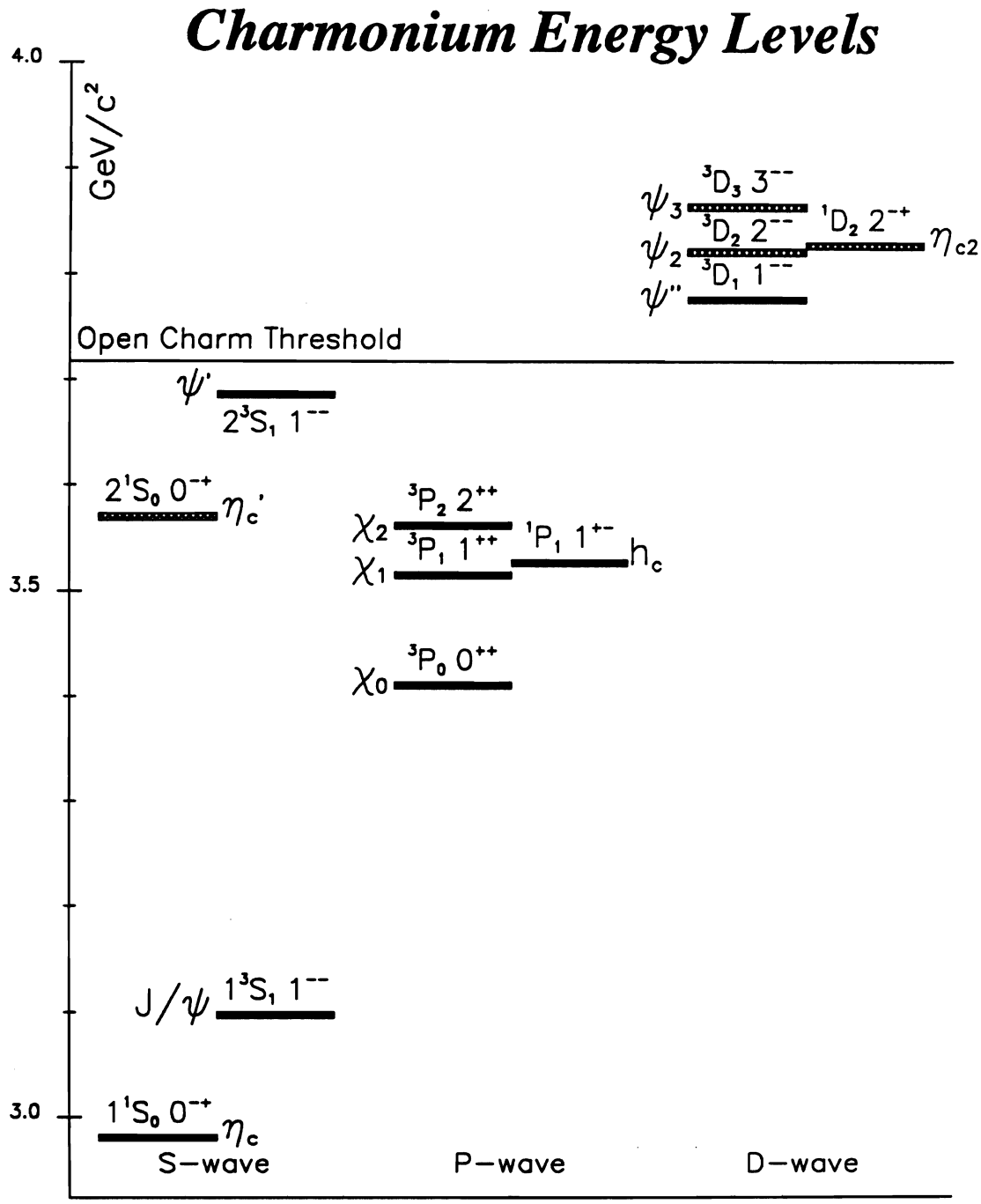

Figure 1.2 Charmonium Energy Levels. Undiscovered states are shown at masses predicted by theory.

C. Experimental Goals

Nearly all spectroscopic charmonium experiments have been at electron-positron colliders. Since production at these machines proceeds via a virtual photon, only those states that have the same quantum numbers as the photon can be directly produced. Some other states are accessible via decays of vector charmonium states, for example the χ mesons were discovered[11] via the decay $\psi' \rightarrow \chi\gamma$. However, there are some states, such as the h_c ($^1P_1$), which are difficult to populate by decays of vector charmonium states. Also, above open charm threshold, vector charmonium states decay predominantly into $D + \bar{D}$. This makes the branching fractions into radiative decays and decays via multiple pion emission small and experimentally inaccessible.

In hadronic production, this requirement of proceeding through a state with the same quantum numbers as the photon no longer exists. Quark-antiquark annihilation and gluon fusion provide a mechanism for producing states of various spins and parities. However, there is a price to pay: hadroproduction experiments have high backgrounds — typical cross-sections of interest are orders of magnitude smaller than the total cross-sections —and the events themselves are higher multiplicity because there are many particles in the final state that are not charmonium decay products. This necessitates a trigger that can quickly select candidate events. The dilepton decays of the J/ψ are the natural candidates for the basis of this trigger. However, this effectively limits hadroproduction experiments to observing charmonium states with a J/ψ in the final state of their decays.

Many early experiments were "closed geometry", or "beam dump" experiments. That is, they had a large absorber in front of their detector, so that only muons would penetrate the absorber and be measured in the spectrometer. The advantage of

this method is that high beam rates can be tolerated, because the spectrometer sees only the muons. The disadvantage is that any particles produced in association with the J/ψ, such as a gamma ray from χ decay, are stopped in the absorber and not observed. A further disadvantage is multiple scattering in the absorber: the muons' momenta are changed slightly as they pass through the absorber, and this degrades the spectrometer's resolution in mass, Feynman x, and transverse momentum.

E-705 is instead an example of an experiment using an open geometry spectrometer, to measure all the charged tracks, not just the muons. In addition, a calorimeter is used to measure photon energies. (The detector is described in detail in the following chapter.) The intent is to measure production of several charmonium states, in particular those that have a dimuon in the final state:

- $J/\psi \rightarrow \mu^+ + \mu^-$
- $\chi \rightarrow J/\psi + \gamma$, followed by $J/\psi \rightarrow \mu^+ + \mu^-$
- $\psi' \rightarrow J/\psi + \pi^+ + \pi^-$, followed by $J/\psi \rightarrow \mu^+ + \mu^-$
- $\psi' \rightarrow \mu^+ + \mu^-$

Additionally, the opportunity exists to search for other states that include a ψ in their decay products. This thesis discusses production of charmonium and searches for new particles in all-charged decay modes.

D. Charmonium Production Models

Four models for hadronic production have been proposed: a Drell-Yan mechanism[12], where a quark and antiquark annihilate to a virtual photon, which couples to a $c\bar{c}$ pair in the final state; $c\bar{c}$ excitation from the quark-antiquark sea; gluon fusion; and QCD quark-antiquark annihilation. Figure 1.3 shows Feynman diagrams for these

processes. Evidence from previous experiments eliminates the first two possibilities, favoring instead some combination of gluon fusion and quark-antiquark annihilation.

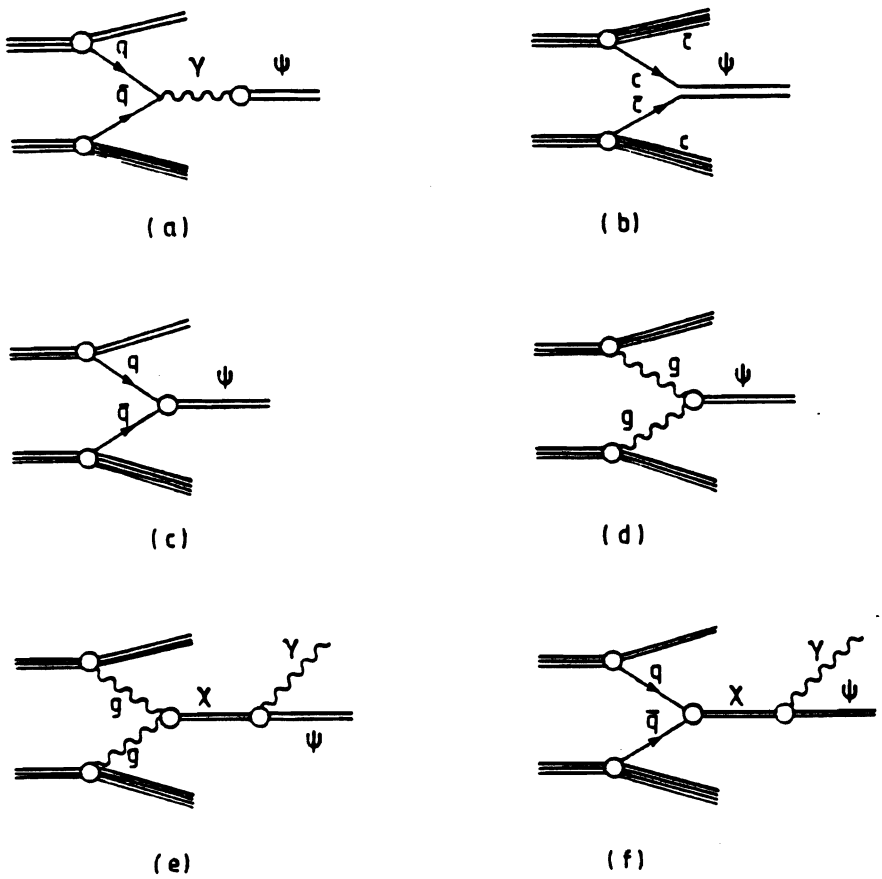

Figure 1.3 Feynman Diagrams for J/ψ hadroproduction: (a) electromagnetic production via virtual photons (Drell-Yan); (b) $c\bar{c} \rightarrow \psi$, utilizing charmed quarks from the hadron sea; (c) $q\bar{q} \rightarrow \psi$, suppressed by the OZI rule; (d) $gg \rightarrow \psi$, with a soft gluon radiated (not shown); (e) $gg \rightarrow \chi \rightarrow \psi\gamma$, via χ states which can couple directly to two gluons; (f) $q\bar{q} \rightarrow \chi \rightarrow \psi\gamma$.[13]

The Drell-Yan hypothesis makes some predictions with regard to charmonium production. First, in the case where valence quarks dominate, the production cross-section by π^-, which has the valence quark content ($d\bar{u}$) on an isoscalar target should be four times that of the π^+, ($u\bar{d}$) . This is because the coupling is

proportional to the square of the charge, or $\left(\frac{-2/3}{+1/3}\right)^2$. In addition, the production of charmonium by protons will be strongly suppressed relative to pions and especially antiprotons, because protons have no valence antiquarks. Production of J/ψ and ψ' will dominate, because these states have the same quantum numbers as the virtual photon produced in the annihilation. Other states, such as the χ_0, χ_1 and χ_2, will be produced only by decay of the ψ'. Finally, the angular distribution of the decay of the J/ψ or ψ' into two muons will be $1 + \cos^2(\theta)$, where θ is the angle of the positive muon, evaluated in the center of momentum frame, with respect to the direction of motion of the ψ. In contrast to these predictions, existing data show the cross-section to be nearly the same for pions of either sign, only slightly less for protons, χ production to be comparable to ψ production, and a flat or nearly flat angular distribution for the decay muons. This indicates that Drell-Yan production is a minor contribution.

Although neither our beam or target particles contained charmed valence quarks, it is possible that charmonium be produced via excitation of sea quark $c\bar{c}$ pairs. In this mechanism charmonium is produced via a combination of a c quark in one hadron and a $\bar{c}$ in the other into a charmonium bound state, a process that is OZI allowed. In addition, there must also be an unpaired charmed quark or antiquark in each hadron. This suggests that charmonium production must be accompanied by open charm production — there must be two charmed mesons in the final state. However, this has not been observed. For example, Fermilab experiment E-444 quotes an upper limit on the ratio of associated charm production to total J/ψ production as 1.6–3.5%.[14] The range is due to the uncertainty in production kinematics of the charmed particles. Despite this uncertainty, it is clear that this

mechanism also provides at most a minor contribution to the total charmonium cross-section. This can be understood by the unrealistically large demands on the center of mass energy needed to produce four charmed quarks or antiquarks.

Quark-antiquark annihilation via gluons is similar to Drell-Yan production, although the virtual photon is replaced by virtual gluons. Since all flavors of quarks carry the same magnitude of color charge, this model predicts that the production by π^- relative π^+ will be close to unity. Also, the production by protons will be much smaller than production by antiprotons, because the proton contains no valence anti-quarks.

Since gluons are also a fundamental constituent of hadrons, gluons can also fuse to form charmonium states. The gluon fusion mechanism predicts that the ratio of production by antiprotons relative to protons will be close to one, because their gluon distributions are identical. Similarly, the production by pions should be the same, independent of their charge. Although this mechanism does not make a quantitative prediction (without *a priori* knowledge of the gluon distributions in pions and protons) of the relative production by protons with respect to pions, it is the only one of the four that accommodates a substantial proton cross-section.

The theory of annihilation is simpler, but by no means simple. It is possible to calculate decay partial widths to leading order; a partial list is shown below:[15][16]

$$\Gamma(\eta \rightarrow gg) = \frac{8}{3}\frac{\alpha_s^2 \left|R_S(0)\right|^2}{(m_\eta)^2}, \tag{1.3}$$

$$\Gamma(\chi_0 \rightarrow gg) = \frac{96\,\alpha_s^2 \left|R'_P(0)\right|^2}{(m_{\chi 0})^4}, \tag{1.4}$$

$$\Gamma(\chi_2 \to gg) = \frac{128}{5} \frac{\alpha_s^2 \left|R'_P(0)\right|^2}{(m_{\chi 2})^4}, \tag{1.5}$$

$$\Gamma(\psi \to ggg) = \frac{40\,(\pi^2 - 9)\,\alpha_s^3 \left|R_S(0)\right|^2}{81\,\pi (m_\psi)^2}, \tag{1.6}$$

$$\Gamma(\psi \to \gamma^* \to q\bar{q}) = \frac{16}{3} \frac{\alpha^2\, e_q^2 \left|R_S(0)\right|^2}{(m_\psi)^2}. \tag{1.7}$$

Here R_S is the S-wave charmonium radial wavefunction, and R'_P is the first derivative of the P-wave charmonium radial wavefunction, and both are evaluated at the origin in these expressions for the widths. Equation 1.7 is a purely QED process; the ratio of $\Gamma(\psi \to ggg)/\Gamma(\psi \to \gamma^*)$ is relatively large. The total width for a given state is not the sum of the various partial widths, because of interference. For example, there is interference between the decay $\psi \to ggg \to q\bar{q}$ and the decay $\psi \to \gamma^* \to q\bar{q}$.

These expressions explain why the J/ψ is so long lived: it decays via a third order process (order α_s^3) while the other S-wave state, the η_c, decays via a second order process (order α_s^2). Besides this factor of α, the coefficient on the $^1S_0$ decay is approximately 20 times larger than the coefficient for the $^3S_1$. The strong decays of the J/ψ are so suppressed that electromagnetic decays, such as $\psi \to l^+l^-$, are competitive with them. Experimentally, $\Gamma(\eta_c)$ is approximately 200 times larger that Γ(J/ψ).

Starting from these decay widths, it is possible to create a simplistic production model. This model neglects any role of spectator quarks, any effects of hadronization and final state interactions, and any intrinsic transverse momentum of the interacting partons. Using time-reversal to relate the decay width to the subprocess cross-section, the subprocess cross-section for a charmonium state X of mass m and spin J produced by two gluon fusion is given by

$$\hat{\sigma}(gg \to \mathrm{X}) = \frac{2J+1}{8m^3}\Gamma(\mathrm{X} \to gg)\,\delta(1-\hat{s}/m^2) \quad , \tag{1.8}$$

where $\hat{s}$ is the square of center of mass energy of the interacting partons: in this case, the two gluons.

The J/ψ and ψ' cannot be produced by this mechanism, however. There is a theorem attributed to Yang[17] that states that a spin-odd particle cannot decay into a symmetric state of two identical spin-1 particles on their mass shells. It is therefore impossible for a color singlet ψ to decay into two gluons. Since the decay matrix element is zero, production by two gluon fusion is therefore also forbidden. Furthermore, two gluons form a C-even state, and the ψ is C-odd. The lowest order allowed processes are $gg \to \psi g$ and $q\bar{q} \to \psi$. In the first case, one can imagine a color octet $c\bar{c}$ pair (with C even) being produced, the color carried off by this "bleaching" gluon, and the $c\bar{c}$ pair emerging as a ψ. The subprocess cross-section for this is[18]

$$\hat{\sigma}(gg \to \psi g) = \frac{9}{8m^3(\pi^2-9)}\Gamma(\psi \to ggg)\, I\left[\frac{\hat{s}}{m^2}\right] \quad , \tag{1.9}$$

where m is the mass of the J/ψ or ψ', $\hat{s}$ is the two gluon invariant mass and

$$I(x) = \frac{2}{x^2}\left[\frac{x+1}{x-1} - \frac{2x\ln x}{(x-1)^2}\right] + \frac{2\,(x-1)}{x(x+1)^2} + \frac{4\ln x}{(x+1)^2}. \tag{1.10}$$

No delta function appears because the bleaching gluon can carry away momentum. $I(x)$ is a measure of the penalty paid for the final state gluon.

Similarly, for quark-antiquark annihilation to produce a state X of mass m and spin J, the subprocess cross-section is given by

$$\hat{\sigma}(q\bar{q} \to \mathrm{X}) = \frac{4\pi^2\,(2J+1)}{9m^3}\,\Gamma(\mathrm{X} \to q\bar{q})\;\delta(1 - \hat{s}/\mathrm{m}^2)\ . \tag{1.11}$$

These, however, all represent partonic subprocesses. That is, they measure what the cross-section would be for free quarks and gluons. Thus, each constituent carries only a fraction of the hadron's momentum. Furthermore, only the hadron momentum is directly measurable. To go from the subprocess cross-sections to the observable cross-sections, it is necessary to fold in the momentum density distributions of the constituent partons:

$$\sigma(AB \to X + \text{anything}) = \kappa \int_{\tau}^{1} dx\,\frac{\tau}{x} f_{a/A}(x,Q^2)\, f_{b/B}(\tau/x,Q^2)\;\hat{\sigma}\,(ab \to \mathrm{X}) \tag{1.12}$$

Here $f_{a/A}(x,Q^2)$ is the probability that parton a carries a fraction x of the momentum of hadron , and $f_{b/B}(x,Q^2)$ is the same thing for parton b in hadron B. Both of these are evaluated at momentum transfer Q^2, which is the scale at which the parton

distributions are evaluated. For this situation, $Q^2 \approx m^2$ where m is the mass of hadron X. These probability densities f_a and f_b are called structure functions. κ is an enhancement factor to include the effects of non-leading order QCD processes, and is approximately equal to two. This formula neglects any transverse momentum the partons may carry, and assumes that the other partons in the hadron are spectators; they do not affect this process in any way.

Using this formula, it would be possible to predict the distribution of $d\sigma/dx_F$, if we knew the parton distributions. Alternatively, we can turn this around and use the measured distributions in x_F of the J/ψ (and/or other charmonium particles) to measure these structure functions.

A commonly used parameterization of structure functions is:

$$x\ P(x) \sim x^b\,(1-x)^{\,a} \qquad , \qquad (1.13)$$

where the letter P represents the parton (sea quark, valence quark, or gluon). $P(x)$ is a probability density, so the fractional momentum is therefore given by $xP(x)$. Very crudely, $b \approx 1$ for valence quarks; $b \approx 0$ for sea quarks and gluons;$a \approx 3$ for valence quarks, $a \approx 5$ for gluons, and $a \approx 7$ for sea quarks.[19] The gluon structure function, is not as well known as the others, however. Drell-Yan and deep inelastic scattering measurements probe the quark's structure functions directly; the gluon structure functions can only be inferred by assuming that whatever momentum is not carried by the quarks must be carried by the gluons. Tung and Morfin[20], in a global fit of deep inelastic scattering data, find $a = 3.5 - 4.5$, and when they include Drell-Yan data, a softer gluon distribution is favored: $a = 6.5 - 7.5$. Using a next-to-leading order QCD fit incorporating direct photon data as well, Harriman et al.[21] fit $a = 4.4$ normalizing to EMC data and $a = 5.1$ normalizing to BCDMS data. Charm photoproduction, assuming a photon-gluon fusion model, provides a direct experimental

measure of the gluon structure function of the nucleon; Purohit[22] obtains $a = 7.1 \pm 2.2$ from E-516 data without a charmed quark mass constraint, and $a = 8.8 \pm 2.3$ with the constraint.

By substituting the equation 1.13 parameterization into equation 1.12, and differentiating with respect to x_F, we obtain:

$$\frac{d\sigma}{dx_F} \sim \frac{x_1^{a_1}(1-x_1)^{b_1} \quad x_2^{a_2}(1-x_2)^{b_2}}{x_1 + x_2}, \tag{1.14}$$

where $x_1 = ½\ (x^* + x_F)$, $x_2 = ½\ (x^* - x_F)$, and $x^* = \sqrt{x_F^2 + 4m^2/s}$.

Note that the product $x_1 x_2 = 4m^2/s$ or 4τ which is only a function of beam energy, not of any kinematic variable. So, if $a_1 = a_2$, the above equation reduces to

$$\frac{d\sigma}{dx_F} \sim \frac{(1-x_1)^{b_1} \quad (1-x_2)^{b_2}}{x_1 + x_2} . \tag{1.15}$$

For the J/ψ, two additional complications must be considered. First, not all J/ψs are produced directly; about 40% come from the radiative decay of χ mesons,[23] and about 8% from decays of the ψ'. Secondly, if they are produced by a process involving a bleaching gluon, such as $gg \rightarrow \psi g$, the gluon in the final state changes the differential distributions. The effect of indirect production is to increase b by one: for a structure function $(1 - x)^n$, the exponent in the $d\sigma/dx$ distribution is $n + 1$. The effect of the final state gluon is the same: for a structure function $(1 - x)^n$, the exponent in the $d\sigma/dx$ distribution is $n + 1$.[24] It does not matter if the final state

contains an additional spin-1 photon or spin-1 gluon; the effect on the differential distributions are the same.

E-672 has empirically observed that the mean transverse momentum grows linearly with the center of mass energy.[25] Since our experiment was performed at a fixed beam energy of 300 GeV, we can test this observation only by comparing with other experiments.

E. Hadronic Molecules

It has been known for years, long before there was a quark model, that there is an attractive force between hadrons, which allows the formation of bound states. Atomic nuclei are examples of these bound states.

Candidates for states of bound mesons also exist. The $f_0(975)$ is one example[26]; it can be interpreted as an isoscalar bound K and $\bar{K}$. Some indications favoring this interpretation are:

1. The $f_0(975)$ has spin-0 and even parity and charge conjugation. If it is made of light (u and d) quarks, it must be in a $^3P_0$ state. If so, there must also be a $^3P_1$ and a $^3P_2$. Unfortunately, the respective likely candidates (the next heaviest isoscalar 1^{++} and 2^{++} mesons) the $f_1(1285)$ and the $f_2(1270)$ are much heavier than the supposed $J = 0$ member of the multiplet.

2. Despite being below $K\bar{K}$ threshold, the branching fraction into $K + \bar{K}$ is extremely large: 22%. (This is because the line width is sufficiently broad that a substantial fraction is above threshold. The high mass tail of the resonance decays into kaons, and the remainder into pions.) This is particularly at odds with a u and d quark $^3P_0$ interpretation. Since the $^3S_1$ state of $s\bar{s}$ is the heavier $\phi(1020)$, a $^3P_0$ $f_0(975)$ must be the isoscalar mixture of $u\bar{u}$ and $d\bar{d}$. Why then should final states involving

strange quarks be preferred? If, however the $f_0(975)$ were a bound state of kaon and antikaon, the system breaking apart into $K\bar{K}$ is a likely decay mode. If instead, one wants to postulate a large admixture of $s\bar{s}$, the relatively light mass of the $f_0(975)$ becomes problematic — the P-wave $f_0(975)$ would be lighter than the S-wave $\phi(1020)$.

Another candidate is the isotriplet partner of the $f_0(975)$, the $a_0(980)$. As in the previous case, there is a large $K\bar{K}$ channel, and the $^3P_1$ and a $^3P_2$ states that one would like to include in the multiplet, the $a_1(1260)$ and the $a_2(1380)$, are again much heavier. A bound $K\bar{K}$ interpretation of the $f_0(975)$ strongly suggests that there be a nearly degenerate isotriplet partner, and the $a_0(980)$ seems to fit this role.

In the axial vector sector, there should be two isoscalar $^3P_1$ states. One would be the isoscalar mixture of $u\bar{u}$ and $d\bar{d}$, and the other $s\bar{s}$. However, *three* 1^{++} objects are seen: the $f_1(1285)$, the $f_1(1420)$ and the $f_1(1530)$. The $f_1(1420)$ is singled out as the likeliest candidate for a hadronic molecule, largely because of the absence of a $\phi\gamma$ mode makes it unlikely to have a large $s\bar{s}$ admixture in the wavefunction.[27] (However, Ishida et al. argue[28] that it is a hybrid state — $q\bar{q}g$ rather than $q\bar{q}$)

These hadronic molecules are not held together by one gluon exchange as hadrons are. A color singlet $q\bar{q}q\bar{q}$ molecule would have to have an antiquark of the complimentary color for each quark; these pairs will each form a color singlet. The picture we should have is not four quarks in a bag, but instead two mesons bound together, just as the deuteron is two baryons bound together. The degree of interpenetration of the mesons is something that will have to be determined by experiment. The attractive force between these color singlets must be due to the exchange of non-colored mediators, such as an effective two gluon exchange potential: single gluons, being colored, do not couple to color singlet objects. In this regard, four-quark

hadronic molecules will be similar to atomic nuclei: color singlets bound by a residual QCD force between color singlets, roughly an order of magnitude smaller than the binding force.

Unfortunately, in the light quark sector, interpretation of a resonance can be confusing. This suggests looking for hadronic molecule candidates containing heavier (charm, in our case) quarks.[29] For example, a ψK or a $\psi\rho$ resonance is extremely unlikely to originate from the decay of a quark-antiquark state. The detection of the ψ indicates a $c\bar{c}$ pair was already present in the state, but the presence of the K indicates the presence of a strange quark as well. Likewise, the presence of a ρ, an isotriplet particle, implies light quarks in the parent state, since neither the s nor c quarks carry isospin.

In discussing the possibility of hadronic molecules, Rosen[30] points out that the condition for square-well binding is:

$$\mu V R^2 \geq \frac{\pi^2}{8}\hbar^2 \tag{1.16}$$

for S-wave states, and

$$\mu V R^2 \geq \frac{\pi^2}{2}\hbar^2 \tag{1.17}$$

for P-wave states, where μ is the reduced mass, V the effective potential depth, and R the effective range. From the f_0, one determines that $VR^2 \geq 200$ MeV fm^2. Unless VR^2 is substantially larger that this (at least 350 MeV fm^2), the pion will be too light to bind to anything. We should therefore focus our attention on heavier particles.

The charm analogs of the $a_0(980)$ and $f_0(975)$, bound states of a D and $\bar{D}$, are excellent candidates, and should be searched for. If the QCD potential is flavor-blind, the binding force should be the same; the reduced mass is larger, though, so the binding is actually stronger for charm than for strange. As in the bound kaon case, there should also be two particles: one isospin zero, one isospin one, and both spin zero. However, these states should not have a large probability to make a transition to the J/ψ, so it is difficult to search for these molecules experimentally.

If the K and $\bar{K}$ form a bound state, why not the K and the heavier $\bar{K}^*$? Although candidates exist, this is a very confusing region of light quark spectroscopy. However, quasi-stable bound states of D and $\bar{D}^*$ should be also considered as possible candidates. This spin-1 system of states should have even parity, either isospin-1 or isospin-0, and either even or odd charge conjugation. Other interesting states from the point of view of this experiment are $(\psi\rho)$ and $(\eta_c\rho)$. These states are listed in table 1.3, with the names in accordance with the Particle Data Group convention for hadron naming.

Table 1.3
Some Possible Hadronic Molecules in the Hidden Charm Sector

State	J^{PC}	I^G	Some Allowed Decays
$a_0(3700?)$ $(D\bar{D})$	0^{++}	1^-	$\eta_c + (2N+1)\pi$ $J/\psi + \gamma$ (small branching fraction)
$f_0(3700?)$ $(D\bar{D})$	0^{++}	0^+	$2N\pi$, $J/\psi + \gamma$ (small branching fraction)
$\chi_1(3850?)$ $(D\bar{D}^*)$	1^{++}	0^+	$J/\psi + \gamma$, $\psi' + \gamma$, $J/\psi + 2\pi$ (P-wave)
$a_1(3850?)$ $(\psi\rho)$, $(D\bar{D}^*)$	1^{++}	1^-	$J/\psi + \rho$, $\eta_c + \omega + \pi$
$b_1(3850?)$ $(D\bar{D}^*)$	1^{+-}	0^-	$\eta_c + \omega$, $J/\psi + \eta$
$b_1(3850?)$ $(D\bar{D}^*)$	1^{+-}	1^+	$J/\psi + \pi$, $\psi' + \pi$, $\eta_c + \rho$

E-705, because of its dimuon trigger, is most sensitive to finding particles that decay with a J/ψ (or ψ') in the final state. This thesis will discuss a search for these particles in all-charged decay modes involving a J/ψ or ψ': $J/\psi + \pi$, $\psi' + \pi$, and $J/\psi + 2\pi$ (which includes $\rho^0 \rightarrow \pi^+ \pi^-$). There is an opportunity for three states in particular to be detected. Two of them are the a_1 states of $(D\bar{D}^*)$ and $(\psi\rho)$. The mass of the first state would be the mass of the D plus the mass of the $\bar{D}^*$ less the binding energy, or 3875 MeV less the binding energy. The mass of the second would be the mass of the J/ψ plus the mass of the ρ, again minus the binding energy: 3867 MeV less the binding energy. It is difficult to estimate the binding energy without knowing the exact form of the potential, but the binding energy is approximately 15 MeV for the f_0. Because the reduced mass of these systems is heavier, the binding is apt to be larger. The close masses of these two systems and the large width of the ρ suggests that it is possible for the $(D\bar{D}^*)$ to undergo an internal rearrangement into a $(\psi\rho)$; the ρ then decays into two pions, leaving the ψ behind.

Another interesting possibility is the b_1. Following the same procedure as above, it would weigh approximately 3750 MeV, less binding. If it were broad enough and had a high mass tail, some of these particles could rearrange themselves

into a ($\psi'\pi$), of mass 3686 MeV + 139 MeV or 3825 MeV. Because the pion is too light to bind, it would then escape the potential, leaving the ψ' behind. Such a state would appear as a threshold enhancement in the $\psi'\pi$ mass spectrum. This is experimentally advantageous: the peak from the ($\psi'\pi$) will be in a region of very low background, because the background will be peak at higher mass. This is similar to the situation of the $D^* \rightarrow D + \pi$.

Interpretation of an enhancement in a mass spectrum may not be completely unambiguous, however. For example, a peak in the $J/\psi + \gamma$ spectrum could indicate a four-quark χ_1, or it could indicate a $\chi_1(2P)$, the first radial excitation of the $\chi_1(3515)$, which, although above open charm threshold, cannot decay into open charm and conserve all quantum numbers. Similarly, a peak in the $J/\psi + \pi^+ + \pi^-$ spectrum could be a four-quark a_1, or it could be a D-wave ψ_2. The mass provides some guidance, but any additional information (e.g. spin or parity) would be extremely helpful in identification.

Chapter 2: Beam and Detector

A. The Tevatron

The ultimate source for the particles used in E-705 was the Fermilab Tevatron, a 1km radius superconducting proton synchrotron fed by a cascade of other accelerators. (c.f. Table 2.1)

Table 2.1
Fermilab Accelerator Characteristics

Accelerator	Type	Particle Accelerated	Energy
pre-Accelerator	Cockroft-Walton	H^-	750 keV
Linac	Linear	H^-	200 MeV
Booster	Synchrotron	protons	8 GeV
Main Ring	Synchrotron	protons	150 GeV
Tevatron	Synchrotron	protons	800 GeV

An average spill cycle consisted of 31 seconds to accelerate the protons to 800 GeV, and the extraction (spill) time was 23 seconds, although there was structure on smaller scales due to the extraction process and the RF nature of the beam. Typically, about 10^{13} protons were accelerated per cycle.

B. Beam Line

These protons were extracted by means of electrostatic septa, and sent towards three major experimental areas: meson, neutrino, and proton. Each of these beam lines had further separation to send protons to the individual experiments. This experiment was located in the Proton West (PW) beam line, and typically received $(0.5–2.5) \times 10^{12}$ primary protons per spill.

In the PW6 enclosure, the primary protons impinged on a one interaction length beryllium target, and produced a spray of particles. These secondary particles and/or their decay and conversion products were what was actually used in the experiment. By adjusting the momentum slits PW6MS1 and PW6MS2 we could produce a fairly monochromatic beam ($\Delta p/p < 5\%$) of 300 GeV/c and by setting the current direction of the dipole strings we could supply either positively or negatively charged particles to the experiment. The positive beam mode was a secondary beam of approximately 45% pions and 55% protons.

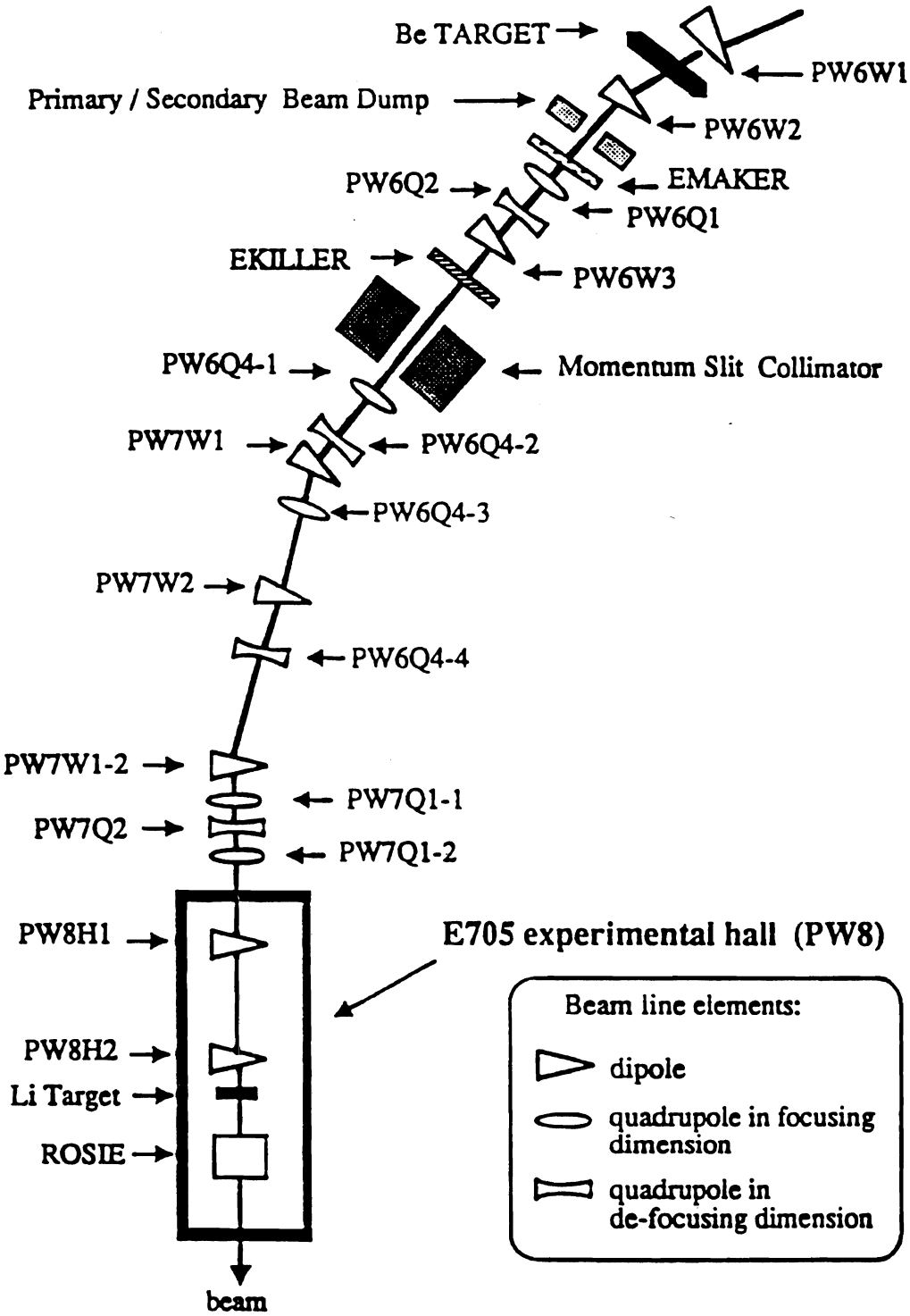

Figure 2.1 E-705 Secondary Beamline

There were three modes of negative beam running: charged, neutral and hybrid. In charged mode, the negatively charged secondary particles produced in the PW6 target were transported down the beam line to PW8. In neutral mode, the dipole PW6W2 acted to sweep away the charged particles, leaving a beam of neutral particles, predominantly photons, neutrons and lambdas. The decay of the $\bar{\Lambda}$ to $\bar{p} + \pi^+$ provides an enriched sample of antiprotons. Also, a piece of lead, the "EMAKER", could be placed in the neutral beam to cause photon conversions to electron-positron pairs, which could then be momentum selected, transported to PW8, and used for calibration. Finally, there was a hybrid mode, which used an intermediate current setting in the PW6W2 dipole, designed to be a compromise between the higher luminosity of the charged mode and the higher antiproton to pion ratio and lower kaon contamination of the neutral mode. Over the entire run, the average negative beam composition, as tagged by our Cerenkov counters, was approximately 98% pions and 2% antiprotons.

To monitor the beam, SWICs (Segmented Wire Ionization Chambers) and SEMs were placed at several distances along the beam line. A SWIC measures the beam position profile at selectable intervals, typically two seconds, and a SEM measures the total beam intensity. These were valuable in tuning the beam: adjusting the intensity, momentum spread and beam spot size and position. Both SWICs and SEMs give information on the beam on long time scales, not event-by-event.

Two threshold Cerenkov counters were installed at the far upstream end of PW8, to determine whether a given beam particle was a proton (antiproton in negative beam running) or pion. They were filled with a mixture of helium (80%) and nitrogen (20%) at 1.8 psi for 300 GeV running. In normal data taking, a 300 GeV pion would be above threshold, and would therefore produce light, detected by a phototube,

whereas a 300 GeV proton would be below threshold, and the counter would remain dark. Kaons, which were estimated to by approximately 11% of the true pion signal for positive beam and 6.4% for negative beam in charged mode, were above threshold, and therefore indistinguishable from pions in this scheme. In electron calibration mode, the pressure was adjusted so that electrons would be above threshold, and pions (there was always a small pion contamination to our electron beam at low momenta gradually increasing to a substantial proportion above 60 GeV) would not.

On an event-by-event basis, the beam position and direction was measured by three beam stations, each containing a scintillation hodoscope and a MWPC (multiwire proportional chamber). The scintillation hodoscopes, BY1, BY2 and BY3 were comprised of eight parallel scintillation counters (or "fingers") of varying widths pointing horizontally and placed vertically. The central fingers were narrowest, and the width increased with distance from the beam center. This tended to even out the distribution of hits, which would otherwise favor the central counters. The BY's were used to count beam particles, and this arrangement maximizes the probability of detecting a second beam particle. This is important, because except in the case when all particles were protons so the Cerenkov counters were unlit, multiparticle events have ambiguous beam particle identification. For example, if there are two beam particles and the Cerenkov detectors are lit, all that can be determined is that at least one particle is a pion.

The wire chambers, BC1, BC2 and BC3, were used to provide a finer measurement of the beam position relative to the nominal beam axis, and by measuring it at three different points along the beam path, the beam direction. This is very important in measuring the transverse momentum of particle produced, because the relevant

quantity is transverse momentum relative to the beam, as opposed to relative to the spectrometer.

All hadron beams, particularly secondary hadron beams, are accompanied by muon halo. There is always some beam that scrapes a piece of material or interacts with gas. A typical beam line contains SWICs, vacuum foils, air gaps between vacuum pipes, etc. and these are all potential sources of interaction. The most likely result of this interaction is one or more pions, which, if they are not themselves absorbed, decay to $\mu + \nu$. Since muons are so highly penetrating (c.f. section 2.I) they tend to travel downstream, all the way to the detectors, and can arrive displaced several meters from the beam pipe. Further, since one of our triggers involved muons, it was imperative that we have some way to detect and reject events associated with halo muons.

A wall of scintillation counters was built upstream of the spectrometer, to veto any event with a halo muon. Two hodoscopes were set up, one vertically (VX) and the other horizontally (VY). A central hole was designed in so that the beam particles could travel through without causing the veto to register.

Finally, a 20 x 10 x .1 centimeter scintillation counter, T1, was placed in the path of the beam after the last beam chamber and before the veto wall to serve as a timing reference for the spectrometer.

C. Experiment Target

The target used for the 1988 run of the experiment was a 33 cm long piece of natural lithium, which is mostly ^{7}Li. (c.f. Tables and 2.2 and 2.3) Lithium was chosen because of its favorable ratio of radiation length to interaction length, and its nearly equal number of protons and neutrons or, equivalently, of *u*-quarks and *d*-quarks. In

both of these respects deuterium is superior, and indeed in the first run an attempt was made to use a cryogenic liquid D_2 target. However, this target exploded twice during that run, causing damage to the spectrometer and loss of beam time, so it was decided to replace it with lithium.

A high ratio of radiation length to interaction length means that it is relatively unlikely that a photon produced in the primary interaction will convert to an electron-positron pair. Many such conversions would degrade both the χ physics (χ decays to $J/\psi + \gamma$) and the direct photon physics. It was decided that 20% of a radiation length was acceptable, and given that constraint, and the difficulties associated with deuterium, lithium provided more interaction lengths than elements of higher atomic number Z.

The target was located 533 centimeters upstream of the magnet center, which is at $z = -533$ cm in E-705 coordinates. These coordinates were defined so that the beam direction was positive z, skyward was positive y, and positive x was defined so that the coordinate system was orthogonal and right-handed. (approximately west) The origin was placed at the center of the analysis magnet.

The target was nearly cylindrical in shape. It was actually slightly conical, with an opening angle of approximately 1/4 of a degree. The ends were not cut perfectly perpendicular to the long axis; also, they are flat only to about 5 millimeters.

Table 2.2
Target Properties

Material	Lithium (c.f. Table 2.3)
Reference Length	32.9 cm
Minimum Diameter	9.89 cm
Maximum Diameter	10.02 cm
Mass	1347.5 g
Radiation Lengths	0.21
Interaction (absorption) Lengths (protons)	.238
antiprotons	.253
π^+	.175
π^-	.174

Table 2.3
Target Composition

Element	Weight percentage
Lithium (92.5% ^{7}Li, 7.5% ^{6}Li) [31]	99.97 %
Nitrogen	0.01%
Calcium	0.006 %
Sodium	0.004 %
Potassium	0.004 %

D. Upstream Tracking

Downstream of the target was a system of nine multi-wire proportional chambers, (c.f. Table 2.4) to determine the trajectories of particles as they traveled from the target to the magnet.

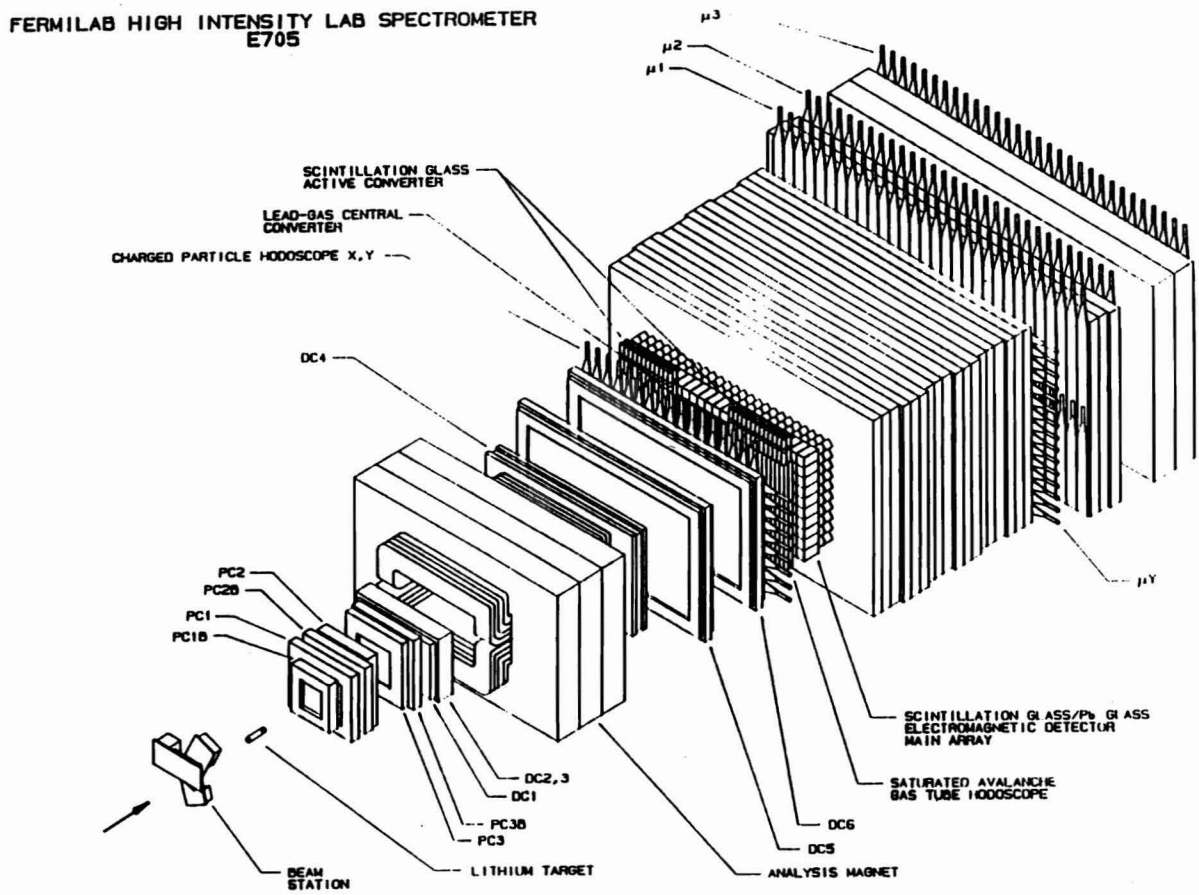

Figure 2.2 E-705 Spectrometer (3-d view)

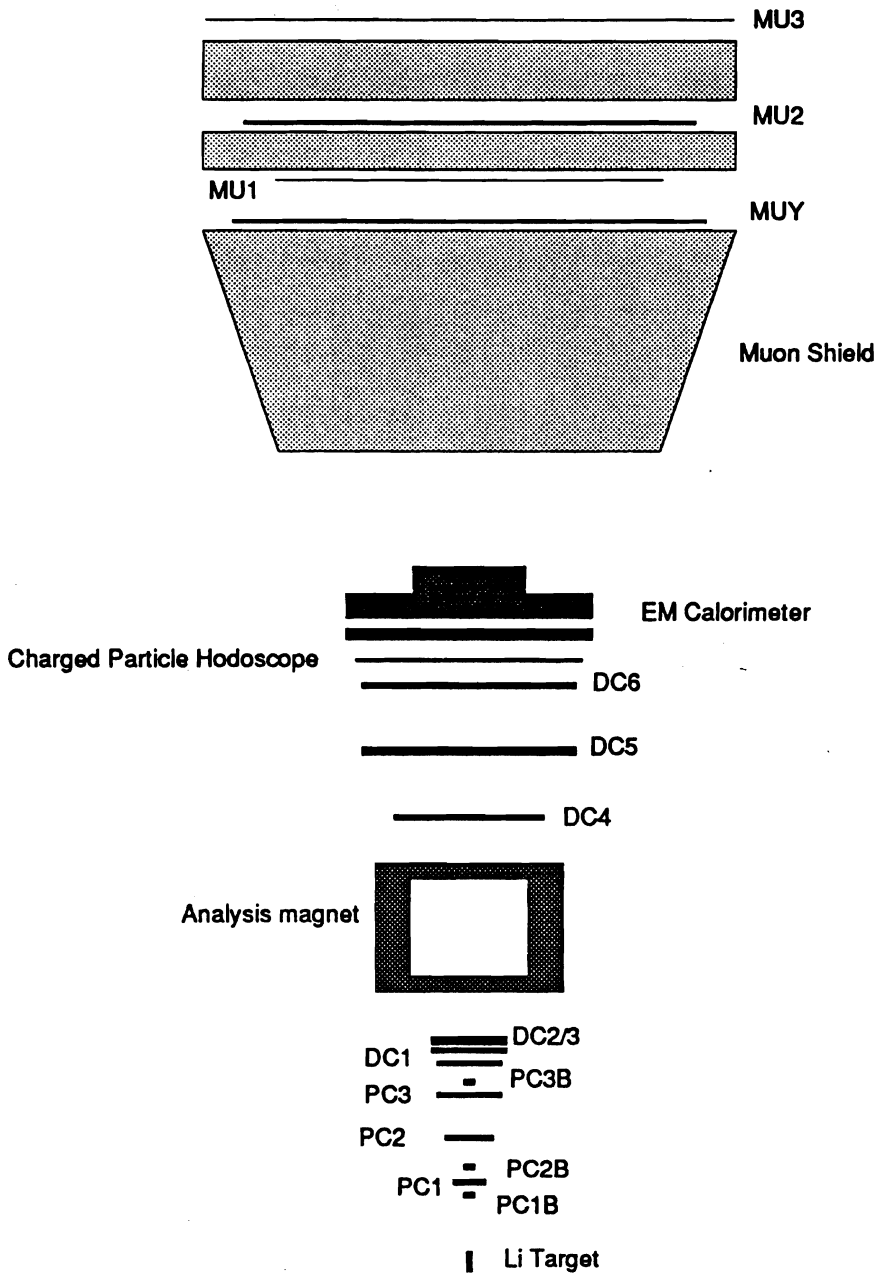

Figure 2.3 E-705 Spectrometer (plan view)

Table 2.4
Wire Chamber Specifications

Chamber	Views	Wires/View	Wire dia. (μ)	Spacing	tan(θ)	z-position
BC1	U,V,Y	128	12	0.10	1.73	-6722.3
BC2	U,V,Y	128	12	0.10	1.73	-4252.8
BC3	U,V,Y	128	12	0.10	1.73	-1022.0
PC1B	V,X,U	176	12	0.075	.533	-427.2
PC1	X',V,X,U	352	12	0.15	.3	-405.2
PC2B	V,X,U	176	12	0.075	.533	-379.9
PC2	U,X,V	480	20	0.15	.3	-333.7
PC3	V,X,U	512	20	0.20	.3	-265.6
PC3B	V,X,U	160	12	0.10	.533	-244.3
DC1	U,V	192	20	0.60	.3	-215.7
	X	176				
DC2	V,U	93	20	1.27	.3	-193.6
	X	92				
DC3	X,V	92	25	1.27	.3	-179.6
	U	93				
DC4	V,X	124	25	1.905	.3	174.8
	U,X'	123				
DC5	X',X	176	25	1.905	.3	276.7
	V,U	192				
DC6	X,X'	176	25	1.905	.3	381.4
	V,U	192				

All measurements are in centimeters, except wire diameter.
θ is the angle between u and v wires and vertical.

Multi-wire proportional chambers use gas ionization as a mechanism for determining the positions of charged particles. When a particle traverses the gas in a chamber, it leaves behind a trail of pairs of electrons and positive ions. Planes of sense wires at ground potential are sandwiched between planes of wires or pieces of foil at a large negative potential, and the ionization electrons drift towards the nearest sense wire in the plane. Near the wire, the electric field gets large ($E \sim 1/r$) and these

electrons themselves cause more ionization. This phenomenon is called gas multiplication, and is responsible if not for the possibility of using MWPC's, at least for the practicality. As the electrons rush towards the sense wire, positive ions travel away at a much slower pace, and induce a negative charge on the wire, which is detected as a voltage pulse through a capacitor. The chamber is called "proportional" because the number of electrons collected is proportional to the ionization caused by the charged particles. At extremely low sense wire voltages, the ions recombine before the they can be collected. As the voltage increases, the detector is called an ionization chamber, which gives a signal roughly independent of the ionization, and after that a proportional chamber. Above this voltage, the chamber enters a region of limited proportionality, leading ultimately to the Geiger-Müller region, where the voltage is so high that the gas breaks down and the sense wire discharges because of the ionization. In this mode, the signal is large and independent of the ionization produced by the primary particle. If the voltage is increased further, the chamber discharges, whether or not ionizing radiation is present. Gas mixtures used in the E-705 chambers are listed in the table on the following page:

Table 2.5
Gas Mixtures for Wire Chambers[32][33]

Chamber Type	Gas Used
Beam Chambers (BC's)	16.7% Isobutane 6% Methylal 0.3% Freon Balance Argon bubbled through ethanol at 5°C
Central Proportional (PCB's)	25% Isobutane 5% Methylal 0.8% Freon Balance Argon bubbled through ethanol at 5°C
Outer Proportional (PC's)	20-22% Isobutane 6% Methylal 0.5% Freon Balance Argon bubbled through ethanol at 5°C
Drift (DC's)	50% Argon 50% Ethane bubbled through ethanol at 5°C

The wires are arranged in X,U and V planes instead of X and Y to aid in the pattern recognition. In an alternate configuration of only X and Y planes a serious ambiguity arises when two or more particles are detected by a chamber. Two particles, at (x_1,y_1) and (x_2,y_2) will produce signals from the vertical wires at x_1 and x_2, and from the horizontal wires at y_1 and y_2. There are two ways to match x and y positions: the correct (x_1,y_1) and (x_2,y_2) and the incorrect (x_1,y_2) and (x_2,y_1), and no way to tell the difference. With three wires and two particles, however, there is only one way to consistently assign hits to tracks, so this "ghosting" problem doesn't occur. It is an elementary exercise in combinatorics to show that for n particles and two planes, that there are $n!$ possible matches of x and y coordinates, only one of which is correct. For

n particles and three planes, there are $(n!)^2$ possible matches of (x,u,v) triples, but there are also $(n!)^2$ constraints from (xu), (xv) and (uv) pairs, so the system provides for a unique assignment of (x,y) coordinates — in fact, it's over constrained by one degree of freedom. This analysis is rigorous only in the case where each plane is 100% efficient and never produces an extraneous hit. In a physical experiment, these ideal conditions never occur, and we must deal in probabilities of matches being correct.

One might suppose that the U and V planes should be placed at 60 degrees to the left and right of vertical, for a symmetric arrangement. However, E-705's planes are never tilted by more that 17 degrees. One reason is that it is difficult to construct a chamber with such large angles; the stereo plane wires get very long and difficult to place under tension. Another is that it is more important to get a precise measurement of the x-position than the y-position. The momentum magnitude determination (c.f. section 2.E) is from the measurement of the x-slope. An error in the y-slope would result in an error in p_y, but an error in the x-slope would result in an error in the magnitude of **p**, and therefore all four components of the momentum. The smaller stereo angle trades precision in y-measurement for precision in x-measurement.

Another possible configuration is X,Y and V planes, but this poses mechanical difficulties. In particular, large chambers have problems with the horizontal (Y) wires sagging.

Drift chambers are not intrinsically much different from proportional chambers. Although there are some construction differences, primarily field shaping wires to maintain as uniform a field as possible, the primary difference is in the electronics. Attached to the sense wire of a proportional counter is a discriminator and a latch, so a

PC wire tells if a hit is present or not. The resolution expected from a chamber with wire spacing d for a uniform distribution of hits is determined by

$$\sigma^2 = \int_0^d \left[x - \frac{d}{2}\right]^2 dx = \frac{d^2}{12} \tag{2.1}$$

so the resolution (as measured by the standard deviation) is

$$\sigma = \frac{d}{\sqrt{12}}. \tag{2.2}$$

However, that is not all the information that's available. The closer to the wire that the particle hits, the less time it takes the ions to drift to the wire, and the sooner the signal appears. By adding a TDC (time to digital converter) to the electronics, one can do better that the $d/\sqrt{12}$ resolution of a proportional chamber, except for an ambiguity as to which side of the wire the particle passed through; such a device is then called a drift chamber. In short, where a MWPC is a digital device, a DC is an analog device. Often, DC's will have fewer wires and a larger wire spacing than PC's; it's a more economical way to achieve the same resolution. In our case, the cells of the PC's and DC's were shaped differently: the PC's had long and narrow cells, and the DC's had square box cells.

Whether a chamber is operated in drift or proportional mode, only one hit per wire is may be recorded per event. (The E-705 drift chamber and TDC designs did not permit multi-hit recording.) In addition, the electrons have a finite drift time, of about 5 cm/μs. This means that after a particle passes through a chamber, it takes hundreds of nanoseconds before the particle's presence can be recorded, and the chamber again be ready for the next particle. Since we used a charged particle beam, it would be unwise to send the beam through the active area of the chamber. This

would insure that the wires nearest the beam would always be on — from beam particles, not particles from interactions. In order to avoid continually firing central wires due to the presence of the beam, most of the chambers had their central regions deadened by increasing the diameter of the wire, thus substantially reducing the gas gain. (c.f. Table 2.6) This was achieved by lowering the wires so that the region to be deadened was immersed in the meniscus of a copper solution. Copper was then electroplated onto the wires. The only chambers that did not have this deadening done to them were the PCB's — PC1B, PC2B and PC3B. These chambers had smaller wire spacings, which meant faster clear-out times, and were designed to cover the central region, where the other upstream chambers were deadened.

Table 2.6

Chamber Dead Regions

Chamber	Aperture Dimensions (cm)	Size of deadened region (cm)
PC1B	60 x 30	none
PC1	54 x 29	5.08 (radius)
PC2B	75 x 40	none
PC2	76 x40	5.08 (radius)
PC3	106 x 50	6.35 (radius)
PC3B	90 x 50	none
DC1	50 x 50	6.35 (radius)
DC2	50 x 50	6.35 (radius)
DC3	50 x 50	6.35 (radius)
DC4	200 x 100	30.48 x 15.24 (rectangular area)
DC5	335 x 167	30.48 x 15.24 (rectangular area)
DC6	335 x 167	30.48 x 15.24 (rectangular area)

Of course, the beam chambers are not deadened anywhere; they are supposed to detect the beam, and a dead region would defeat their purpose.

Not all of these chambers were used in the analysis, however. The beam intensity proved to be too much for the PCB's. For only a small fraction of the run were all three in place and operational; most of the time at least one was being

repaired. The radiation caused material (possibly the result of aluminum oxidation) to plate on the wires, severely decreasing their sensitivity.[34] Rather than dealing with the difficulty of tracking the ever changing status of the PCB's, this analysis ignores the PCB's altogether.

E. Analysis Magnet

To determine the momentum of a charged particle, we used the large aperture dipole magnet PW8AN2, sometimes referred to as "Rosie". The aperture measured 185.54 cm (in x) by 91.38 cm (y) by 152.40 cm (z) and the magnet was run at a current of 2100 A, and produced a field of about 12.5 kG in the vertical direction. A charged particle with momentum p in a uniform magnetic field B travels in a helical orbit with a radius determined by:

$$R = \frac{cp}{QeB} \tag{2.3}$$

In the limit of small deflection, the change in momentum, or the "p_T kick," is given by:

$$\Delta p_T = \frac{Qe}{c}\int \mathbf{B} \times \mathbf{dl} \tag{2.4}$$

For Rosie, $\int \mathbf{B} \times \mathbf{dl}$ is well approximated by $\int B_y dz - \int B_z dy$, and here even the second term is small compared to the first. For an operating current of 2100 A, the total p_T kick for a particle of unit charge is about 0.766 GeV/c, in the horizontal direction.

The ability to calculate the p_T kick depends of course, on the degree of knowledge of the magnetic field. Rather than relying on a calculation of the magnetic field from the coil and yoke properties, the field was actually measured by a device called a ziptrack. This is a device which has three perpendicular coils (or Hall-effect probes in later versions) that sit on a track. This track is positioned at a given x and y, and the

probe sent up and down the z-direction, measuring the field at 0.9725 inch intervals. For E-705, Rosie was ziptracked in October of 1985, following the first run.

To reduce the fringe field downstream, a mirror plate was mounted on the downstream side of Rosie, 146 centimeters from magnet center. The intent was to reduce the effect on the photomultiplier tubes in the calorimeter, so that the photoelectrons liberated would not bend in the magnetic field. A beneficial side effect of the mirror plate was an improvement in the downstream tracking. Gas ionization electrons bend less in the reduced fringe field, and the particles travel in straighter lines outside the magnet aperture because of the reduction in the downstream field integral.

F. Downstream Tracking

Downstream of Rosie were the drift chambers DC4, DC5 and DC6. (cf. Table 2.4) Unlike most of the upstream chambers (all but PC1), these had four wire planes: a u-plane, a v-plane and two x-planes. The second x-plane, referred to as "x-prime", "x'" or sometimes "p" had its wires offset by half a wire spacing. This is to help resolve the aforementioned left-right ambiguity of drift chambers. The drift time implies only distance from a wire, not the side of the wire through which the particle passed, so for each hit, there are two possible positions for the particle. By use of an offset x' plane, this ambiguity can be resolved in many cases.

Despite the two x-planes, the downstream system was somewhat weaker than the upstream system. There were fewer stereo planes (u and v) and fewer z-positions in which measurements are made. In fact, three chambers is the minimum needed to actually track more than one particle: since two points determine a line, a third point is needed to confirm whether a line segment defined by the other two points is due to a

track, or whether it is a mismatch of a point from one track and another point from a different one. However, since the proposal goal was to study the decay of χ's to $J/\psi + \gamma$ the tracking was designed with tracking pairs of muons in mind. Since the approximate position of the muons is already known from the muon hodoscope (described later) it was thought that the tracking could be confined to a small window on each chamber, and that three chambers would be more than sufficient to establish the trajectories of the muons.

G. Charged Particle Hodoscope

Following the downstream drift chambers were two planes of scintillation counters, 184 oriented vertically (CPX) in two rows of 92 each, and 48 oriented horizontally (CPY) in two columns of 24. (c.f. Table 2.7) A relatively unbiased interaction definition could be produced from this detector. To define an interaction, we required at least two lit CPX counters in coincidence with a beam particle. If no interaction occurred in the target, the beam particle would travel through the hole, without lighting any counters. To allow the beam to pass through, the central counters in both planes were shortened, leaving a 32 centimeter square hole for the beam.

The CPH counters (CPX and CPY together are referred to as CPH) were made of 1 centimeter thick NE110 plastic scintillator. Plastic scintillators were chosen over inorganic scintillators, such as NaI(Tl), for a number of reasons: they are faster, less expensive, and often less hygroscopic. Their major disadvantage, poor energy resolution, is unimportant for determining the presence or absence of a particle, especially a minimum ionizing particle.

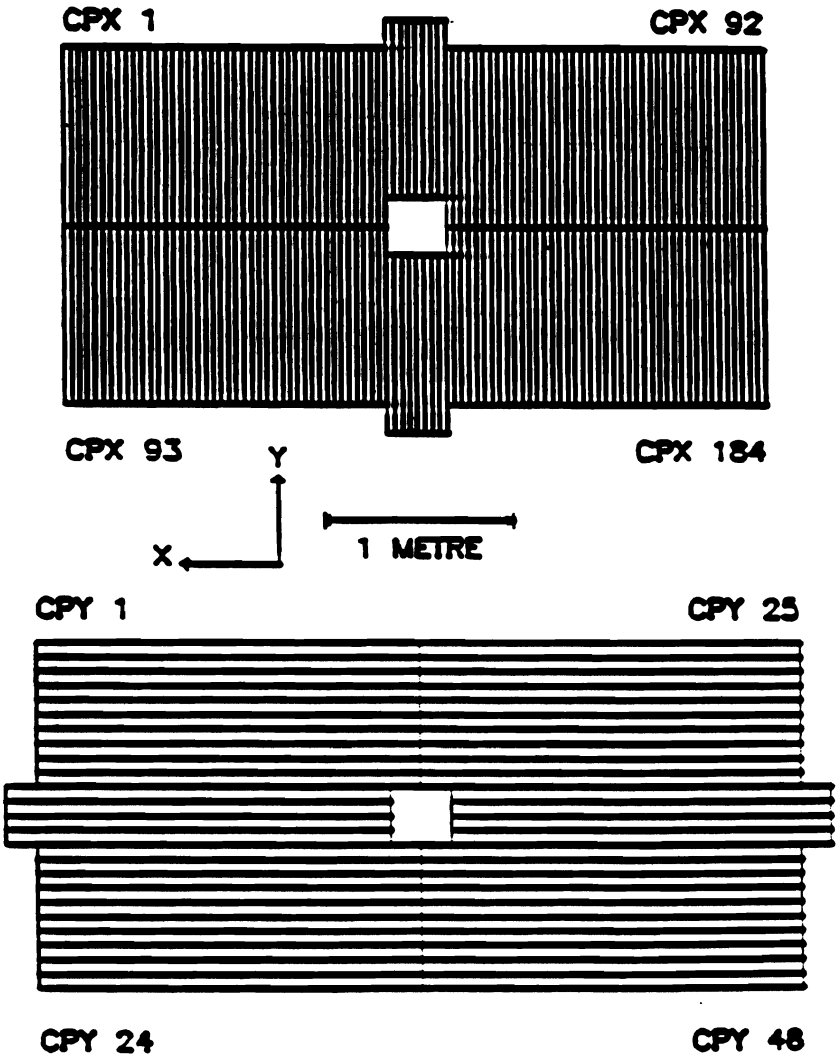

Figure 2.4 E-705 Charged Particle Hodoscope. Top is CPX; bottom is CPY.

Table 2.7

Properties of E-705 Scintillation Counters

Counter	Number of Counters	Dimensions	Hole Dimensions	Z-position
BY1	8	13.0 x *	none	-6751.2
BY2	8	13.0 x *	none	-4239.1
BY3	8	13.0 x *	none	-1008.3
VX	22	25.4 x 147.3	25.4 x 8.8	-636.4
VY	16	153.7 x 25.4	25.4 x 8.8	-655.8
CPX	184	3.8 x 99.7	33 x 33	423.2
CPY	96	99.2 x 7.5	32 x 32	417.2
MUY	60	186.7 x 13.0	40.6 x 40.6	1115.9
MU1	60	20.3 x 144.8	40.6 x 40.6	1181.5
MU2	62	22.9 x 157.5	40.6 x 40.6	1271.8
MU3	62	26.7 x 176.5	87.6 x 40.6	1436.3

All dimensions are in centimeters

* These counters had varying widths of 3.175, 1.429, 1.032 and .873 cm.

H. Calorimeter

1. Main Array

The largest part of the electromagnetic calorimeter was the main array, an array of glass blocks of two different sizes and compositions. Large blocks were 15 centimeters square in x and y, and small blocks were 7.5 centimeters square. The innermost blocks were small and composed of scintillating glass (SCG1-C); these were followed by large scintillating glass blocks; the outermost blocks were made of lead-glass (SF5). (c.f. Table 2.8)

Table 2.8

Properties of Glasses used in E-705

		SF-5 [35]	SCG1-C [36]
Composition (% by weight)	SiO_2	38	42.5
	PbO	55	0
	BaO	0	43.4
	K_2O	5	3.3
	Na_2O	1	0
	Li_2O	0	4.2
	MgO	0	3.3
	Al_2O_3	0	2.0
	Ce_2O_3	0	1.5
Radiation Length (cm)		2.54	4.35
Interaction Length (cm)		41.45	44.5
Block Length (cm)		41.45	89
		$18X_0$	$20.5X_0$
		$1.0\lambda_I$	$2.0\lambda_I$

There are advantages and disadvantages to both types of glass. SF-5 is much less expensive, and has a higher ratio of interaction length to radiation length, so hadrons on average deposit less energy in it. Because it is purely a Cerenkov radiator, it's very fast: typically only limited by the time resolution of the photomultiplier tube. However, when exposed to radiation over time, it darkens, attenuating the light produced in the glass. SCG1-C is radiation-hardened, so it can withstand the higher exposures of the central regions of the detector. Because it scintillates as well as acts as a Cerenkov radiator the light output is greater. This corresponds to in better energy resolution in principle, since the resolution is determined by the ability to count the photoelectrons produced in the photomultiplier. With more light $\sqrt{N}/N$ (where N is the number of photoelectrons) is smaller, so $\sigma(E)/E$ is as well. However, scintillators are slower, and many have long-lived components that produce an almost DC light level that must be corrected for, or eliminated (with the use of filters, for example).

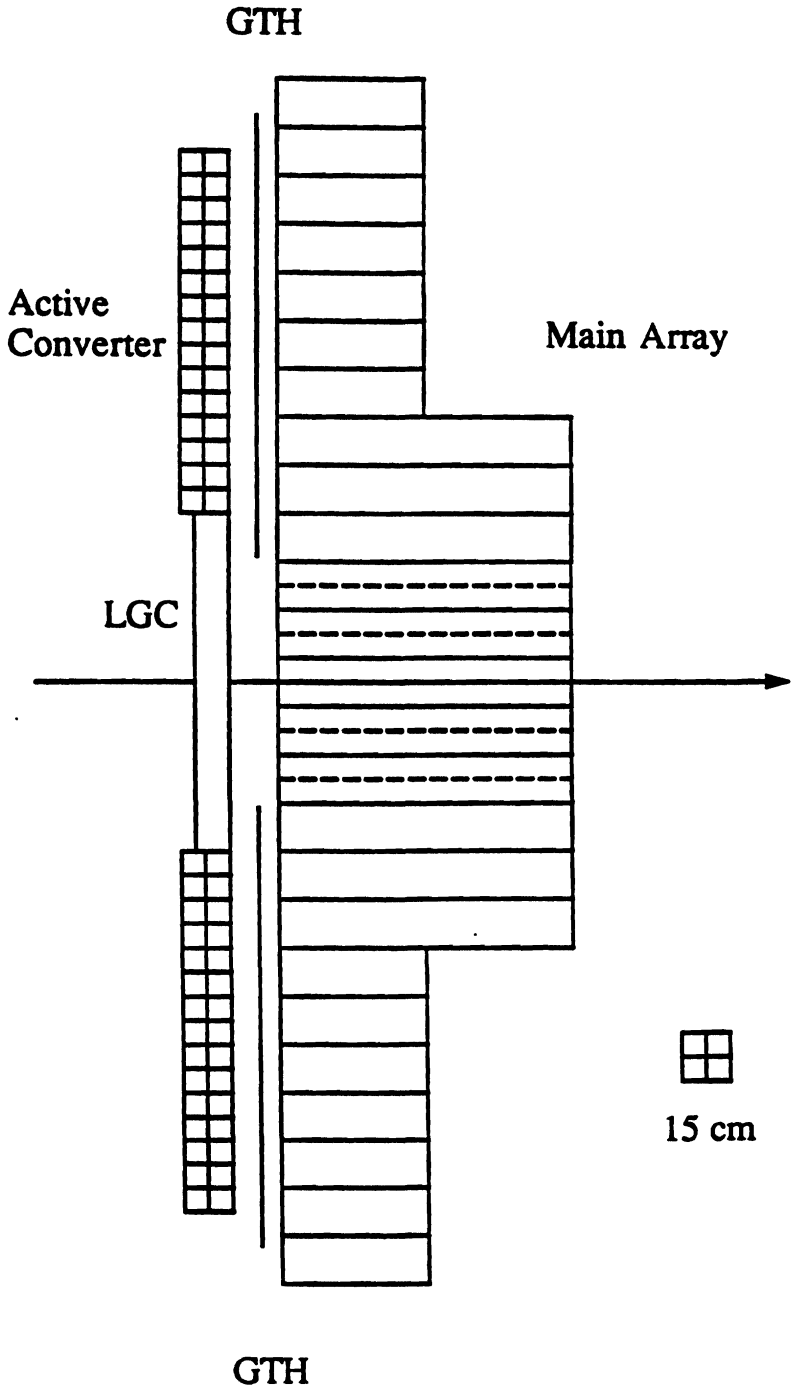

Figure 2.5 E-705 Electromagnetic Calorimeter. (Top View)

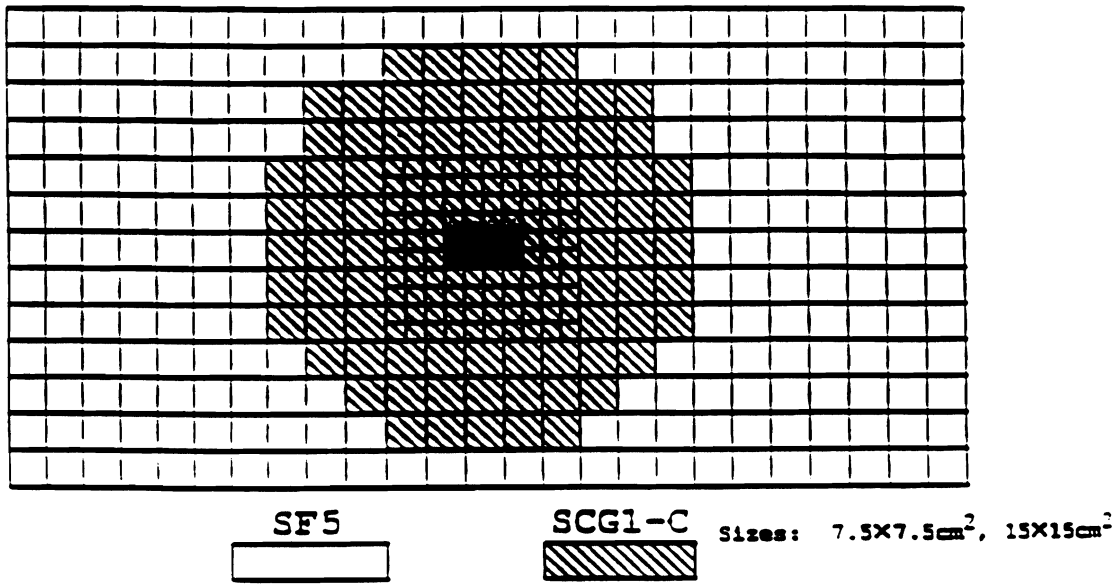

Figure 2.6 E-705 Main Array

To measure the scintillation or Cerenkov light, a photomultiplier tube (5" EMI 9791KB for the large blocks and 3" RCA 6342A for the small blocks) was mounted at the rear of each glass block. Each block was wrapped in aluminized Mylar and black vinyl tape to keep the glass light in, and, more importantly, to keep external light out. These phototubes were individually powered by LeCroy 1440 power supplies, through custom bases.

The calorimeter was periodically calibrated with either electron or positron beams. Typical calibration momenta (or energies) were 2, 6, 10, 30, 60 and 100 GeV/c. Between calibrations, a LED pulser system based on Hewlett-Packard HLMP-3950 diodes was used to monitor gain changes in the phototubes. This system used a set of filters of varying (but known) transmissions mounted on a wheel to automatically send a certain amount of light into each glass block, so the gains and

pedestals could be determined. To monitor the light output of the LEDs, Litronix BPX 66 diodes were used. For most of the run, gains and pedestals were measured between the spills; however, for a brief part of the run, in-spill data were also taken. There are slight changes in the gains and somewhat larger changes in the pedestals during the spill, and these are corrected in the period with in-spill data. For other periods, the correction was based on an extrapolation of in-spill data. However, since the analysis of this thesis uses the calorimeter only for electron-positron identification, this subtle effect will not be considered further.

2. Active Converter

One very useful piece of information is how the shower develops in time, or equivalently, in longitudinal distance. In particular, electrons and photons shower early (within the first few radiation lengths) whereas hadrons that shower interact more or less uniformly throughout the detector. This is because the calorimeter is thick in terms of radiation lengths, but relatively thin in terms of interaction lengths. By measuring the energy that is deposited in the first few radiation lengths, one gets some information on the z-profile of the shower, and therefore has some information by which to distinguish photons and electrons from hadrons.

In the outer regions of the calorimeter, SCG1-C glass blocks were hung vertically to measure the energy deposited in the first 3.45 radiation lengths of the calorimeter. These blocks were 7.5 centimeters square in x and z, two blocks high (195 centimeters) and two blocks deep, with an RCA 6342A phototube attached at the outside end to generate the signal. The electronics were identical to those used for the main array.

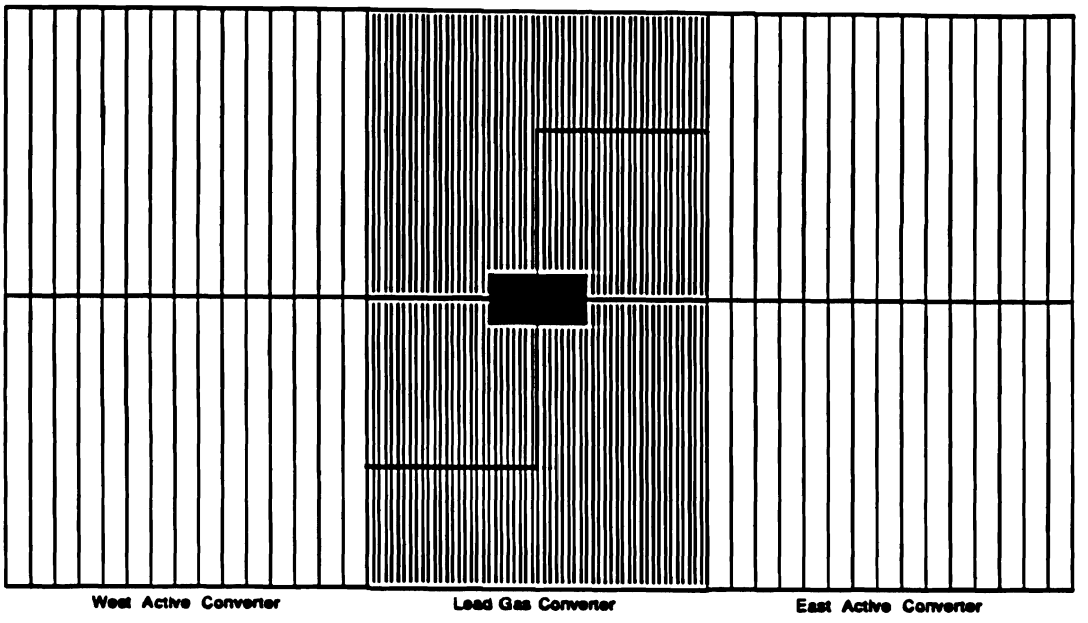

Figure 2.7 E-705 Active Converter and Lead-Gas Calorimeter: Front View.

3. Gas Tube Hodoscope

The active converter gives a coarse position measurement in only one view. (σ = block width/$\sqrt{12}$ or 4.3 cm) To measure the centroids of showers to better accuracy, a gas tube hodoscope was deployed behind the active converter column. It was built out of two planes of vertical conducting polystyrene tubes of 8.6 mm width. Centered in each tube was a wire at positive high voltage, so that electrons produced in the gas ionization would drift towards this wire and induce a voltage from the resulting positive ion drift, similar to what happens in a multi-wire proportional chamber. The gas used was 50% argon — 50% ethane, bubbled through isopropanol at 273K, and the tubes were operated in saturated avalanche mode, with the wire voltage at +2100V. The tubes were sandwiched between three sheets of 1/16" copper-clad G-10, and the two layers adjacent to the tube planes were etched into horizontal strips

.86 centimeters wide. The charge $-Q$ on the wires induced a charge of roughly $+Q/4$ on each strip, and this charge was used to provide measurement of the y-position of each shower. This is necessary not only to determine the position of the shower, but also the fraction of energy deposited in the hodoscope. In principle, since two measurements of the same statistical process (a shower) are made, the correlation between x and y energies of the same shower is greater than it would be between the x measurement of one shower of a given energy and the y measurement of a different shower of the same energy. This tends to aid the pattern recognition process — the assignment of x and y profiles to a common shower.

After the approximately four radiation lengths of shower development, a typical shower deposited charge into five to seven tubes. Because typical electromagnetic shower shapes are much broader than the width of a gas tube, the position of a shower can be fit to the shape of the tube energy distributions, and this way do better than $\frac{\text{size of tube} = .86\text{ cm}}{\sqrt{12}}$ or 0.25 centimeters that the single element resolution of using just the peak tube would imply. This requires that the integrated charge deposited in each tube be recorded, not just latched, as if it were a wire chamber. LeCroy 2280 analog-to-digital converters (ADC's) were used for this.

The front and back wires were ganged together, so that a single measurement of the integrated charge deposited in the x-view of a tube was made. In a similar manner, the front and back strips were also ganged together for the y-view charge measurement. Also, in the outermost region of the GTH, adjacent pairs of x-tubes were also ganged together. In the wings, the shower energies are typically lower than in the center, so the shower radius is correspondingly larger. In addition, because the angle θ is larger, a larger $\Delta\theta$ can be tolerated.

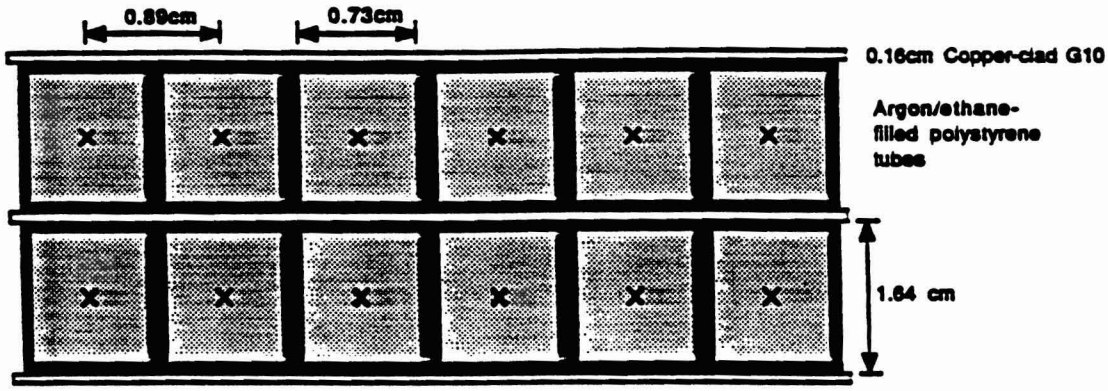

Figure 2.8 E-705 Gas Tube Hodoscope Section: Top View. The "x's" represent wires perpendicular to the page.

4. Lead-Gas Calorimeter

The active converter/GTH combination works best with a few showers in relative isolation. In the more active central region, however, pattern recognition would be extremely difficult, so a thin (four radiation lengths) lead-gas sampling calorimeter (LGC) was used as a pre-converter instead.

In general, energy resolution of gas sampling calorimetry is significantly worse than glass calorimetry. This is because what is actually measured is the energy deposited in the gas, which is only a small percentage of the energy deposited in the converter material. (Lead, in our experiment.) The usual problems with small sample size translate into poor resolution. However, position resolution can be substantially

better, because the spatial resolution is limited by the sense wire and stripe spacing, which in E-705 were much smaller than the block size. As mentioned earlier, position resolution becomes more important in the central region. In the case of the LGC, a thin pre-converter allowed the position to be measured with sampling accuracy, and the only portion of the energy that was measured with the poorer resolution was that deposited in the pre-converter, typically about 10% of the total. It was considered worth sacrificing energy resolution on a small portion of the shower to improve position resolution and therefore pattern recognition, at least in the more active central region. Furthermore, the mean photon and electron energies in the LGC region are higher than in the GTH region, and this partially offsets the decreased absolute energy resolution.

The LGC measured 105 x 195 centimeters in area, and 12 centimeters, or 4.2 radiation lengths in depth.[37] It had a central hole of 15 x 30 centimeters for beam particles to pass through, matching the size of the hole in the Main Array. This was sufficient to cover the calorimeter from top to bottom, in front of all the small SCG-1C blocks, and the next outer layer of large blocks. It had a 1.27 centimeter layer of iron and a .81 centimeter layer of lead to act as inactive, starting radiators, followed by eight sampling layers. Each layer consisted of 0.12 centimeters of lead, a 1.0 centimeter aluminum extrusion proportional tube followed by a .05 centimeter sheet of resistive PVC, and .16 centimeters of copper-clad G-10 etched with horizontal strips in a manner similar to that of the GTH. Also like the GTH, the LGC used a 50% argon — 50% ethane mixture, bubbled through isopropanol at 273K, as its operating gas.

After a shower initiated — typically in the starting layer of iron and the lead, the shower electrons and positrons ionized the gas as they passed through it, just as

they would in a MWPC or the GTH. The sense wires picked up charge from the ionization, and a smaller charge was induced on the strips. Wires from eight longitudinally arranged tubes, like the two wires in the GTH were ganged together to a single output. Having eight samples instead of two, however, decreases the detector's sensitivity to fluctuations. The strips were also ganged together in longitudinal groups of eight. The outputs were amplified at the LGC by individual custom amplifiers, by a factor of approximately 5 for the wires and 25 for the strips. From there, the signals went to the LeCroy 2280 ADCs. These ADCs were usually read out in a sparsified mode, where only the channels whose pedestal-subtracted value was above a certain threshold were written to tape. Pedestals were subtracted automatically, and several times a week the pedestals were measured to keep the subtraction table up to date.

Because of the greater proportion of high-Z elements, particularly lead, the LGC is much less responsive to hadrons than the Active Converter/GTH combination is. This partially offsets the greater relative hadron response of the SCG-1C glass over the SF-5.

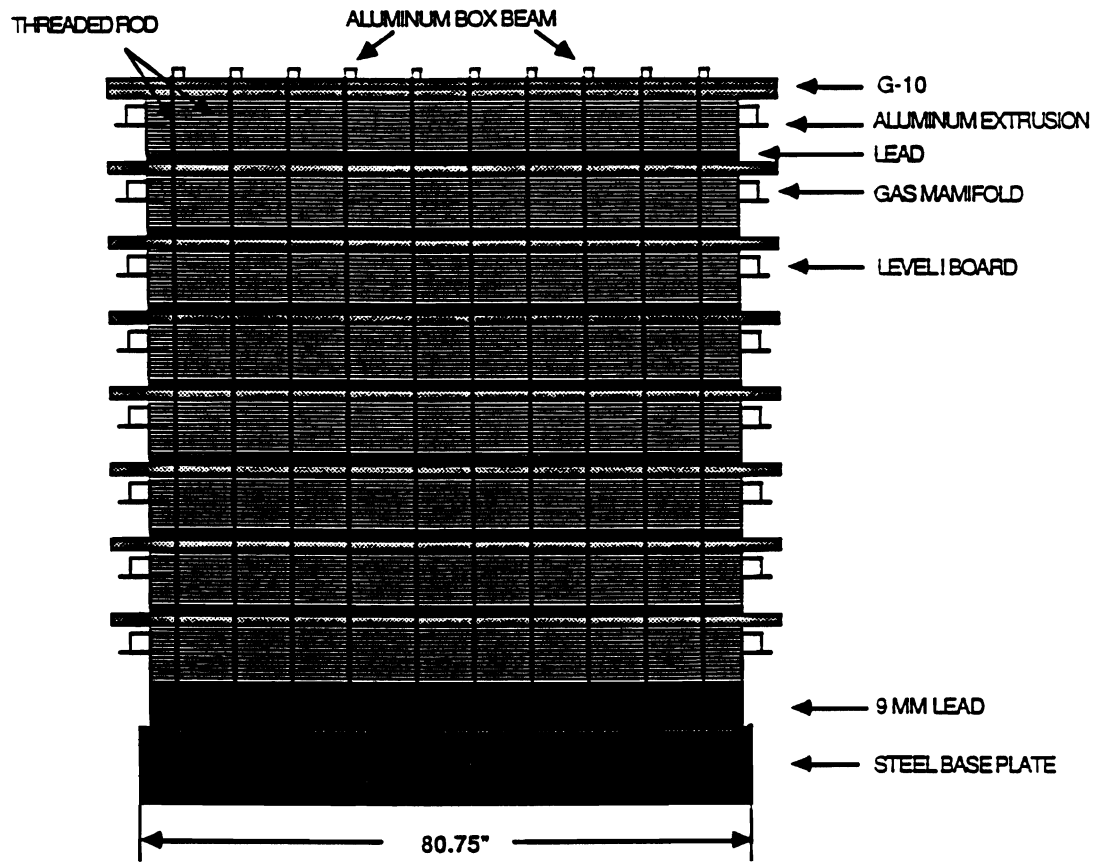

Figure 2.9 E-705 Lead Gas Calorimeter Assembly: Top View.

I. Muon Hodoscope

To identify which tracks were from muons, a set of four planes of 1 centimeter thick NE114 scintillation counters, 184 in x and 96 in y, was placed behind a series of walls of absorbing material. Directly behind the calorimeter was 40 centimeters of copper in front of 310 centimeters of iron. Behind this first shield were the MUY and

MU1 counters. Behind these two planes of counters was the second shield, a 60 centimeter iron wall, in front of the MU2 plane. The third and final shield was a 91 centimeter concrete wall, behind which were the MU3 counters. Hadrons will interact strongly with the material in the muon shields, and will therefore be greatly attenuated, whereas muons will interact only electromagnetically, and lose much less energy per centimeter, ionization being the dominant mechanism. The rate of energy lost due to ionization by a particle of unit charge passing through a medium of atomic number Z, is given by the Bethe-Block formula[38]:

$$-\frac{dE}{dx} = 4\pi N_A r_e^2 c^2 \frac{Z}{A\beta^2}\left[\ln\left(\frac{2mc^2\gamma^2\beta^2}{I}\right) - \beta^2 - \frac{\delta}{2}\right] \tag{2.5}$$

A minimum ionizing particle has a dE/dx of 1.46 MeVcm^2/g in iron, corresponding to 11.6 MeV/cm or 3.6 GeV for the front muon shield. However, this energy loss is higher due to the logarithmic relativistic rise, given by the term in brackets, by a factor of about 1.5 for a 50 GeV muon, increasing to a factor of approximately two for a 300 GeV muon. So, an 50 GeV muon would lose on average 5.4 GeV traversing the front muon shield, and an additional 1.0 GeV traversing the second.

On the other hand, since the nuclear interaction length of iron is 131.9 g/cm^2 and it's density 7.87 g/cm^3,[39] the front shield is 18.5 interaction lengths thick. Only $e^{-18.5}$ or 9.6×10^{-9} of the hadrons will pass through the iron without interacting. The eighteen interaction lengths is enough to contain nearly all of the energy of nearly all of the hadronic showers. In the infrequent cases where it is not, the energy is deposited in the second or third muon walls.

The geometry of the counters was designed to make a fast (TTL speed) muon trigger simple to implement in hardware. Each of the top and bottom rows of MU1 had thirty counters, and each row of MU2 and MU3 had thirty-one, offset by a half-counter spacing. A muon passing through a given MU1 counter will pass through one of the two MU2 and the two MU3 counters, even when the magnet deflection and multiple scattering is taken into account. Such a situation defines a "triple coincidence." Because there

is a top and bottom set of x-counters, even without looking at the MUY counters, the quadrant in which the muon passed can be established quickly. This allows a fast dimuon trigger to have some information about position as well as energy, and therefore opening angle and mass. By demanding two different quadrants, the trigger possessed a natural bias towards large opening angle, and therefore high mass.

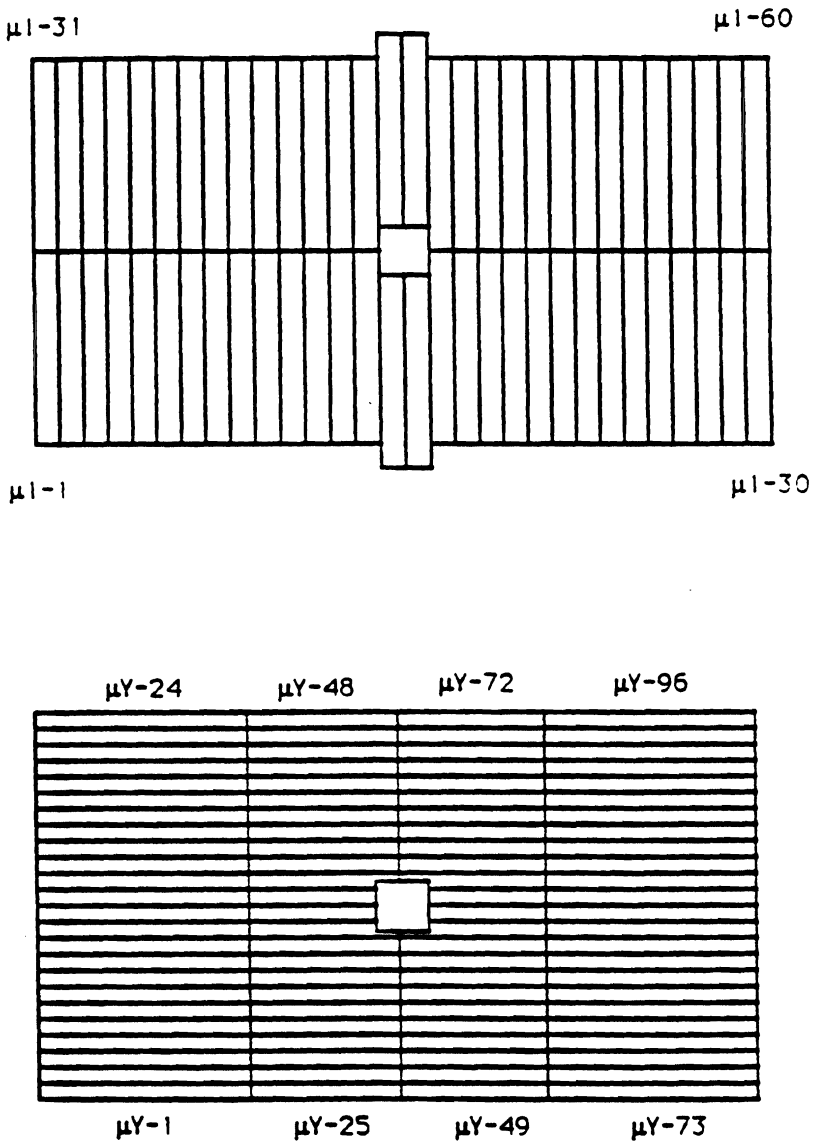

Figure 2.10 E-705 Muon Hodoscope. Top: MU1 Counter Plane. Bottom: MUY Counter Plane.

Chapter 3. Experimental Running

A. Run Eras

Throughout the run, the beam and detector conditions, such as intensity and magnet and beam polarity were varied. The entire run can be divided into five eras, named for the month the era started and the beam polarity: August Negative, September Negative, November Positive, January Negative and January Positive. Between these eras were brief periods of electron calibration, tests and special runs. (c.f. Table 3.1 on the following page) The average intensity of the beam (interactions per second) during data taking runs was about 400 kHz in the August Negative era, and increased to an average of 700 kHz for the January Positive era. However, for some periods in January, the interaction rate was over 1 MHz.

Table 3.1

E-705 Run Eras

Period	Beam sign	Rosie sign*	Tape Range	# Skipped	Good Tapes	Era
8/8 – 8/27	Negative	Forward	689–1209	16	505	AUGN
8/28 –8/31	Calibration		1210–1266			
8/31 – 9/1	μ tests		1267–1289			
9/1 – 9/5	Negative	Forward	1290–1366	3	74	SEPN
9/5 – 10/24	Negative	Reverse	1367–3153	18	1769	SEPN
10/24 – 10/25	Calibration		3154–3171			
10/25 – 10/27	Other Tests		3172–3202			
11/3 – 11/6	Positive	Forward	3203–3354	7	145	NOVP
11/7 – 11/8	Calibration		3355–3407			
11/9 – 11/14	Positive	Forward	3408–3597	8	182	NOVP
11/14 – 11/16	Other Tests		3598–3663			
11/16 – 12/14	Positive	Forward	3664–5118	40	1415	NOVP
12/23	Calibration		5119–5130			
12/23 – 12/24	Other Tests		5131–5141			
1/2 – 1/13	Negative	Reverse	5142–6018	16	861	JANN
1/13	μ tests		6019–6030			
1/16 – 1/17	Calibration		6031–6068			
1/17 – 2/1	Positive	Forward	6069–7350	52	1230	JANP
2/1 – 2/14	Tests	Varies	7350–7539			

* Rosie forward is B_y pointing towards +y, reverse is B_y towards –y.

The # skipped column refers to tapes that were taken with the magnet off (for chamber alignment), the target out (for measuring the muon halo rate), special trigger processor tests, and tapes that were subsequently found to be unreadable.

Periodically, to monitor the alignment of chambers, a tape was recorded with Rosie off. Track segments were found in the front (upstream) and rear (downstream) chambers, and the tracks that matched at the magnet were subsequently used. For each plane of each chamber, the residual distance between the found hit and the projected position of the track as determined by the other chambers was calculated. The standard deviation of the residual distance provides a measurement of the chamber

resolution, and the mean of the distribution is the difference between the true and nominal chamber position — the distance that the chamber position has to be moved in software to match the physical position. This was done twenty-eight times during the run. The results, averaged over X,U and V planes, are in table 3.2.

Table 3.2
Average Chamber Resolutions

Chamber	Resolution (microns)	$d/\sqrt{12}$ (microns)
PC1	662	450
PC2	666	450
PC3	742	590
DC1	418	1730
DC2	389	3670
DC3	369	3670
DC4	665	5500
DC5	481	5500
DC6	656	5500

B. Beam Normalization

To measure a cross-section of a particular reaction, three things must be determined: the number of final states of interest observed, the fraction of created states which are accepted in the detector, produce a trigger, and are reconstructed offline, and the number of beam particles incident on the target. This section explains what was done to calculate the last quantity.

After every spill, a special end of spill (EOS) record was written to tape. Unlike individual events, these records contained the output of the experiment's scalers for an entire spill cycle. Some of the quantities scaled were the number of protons in the beam, the number of pions in the beam, the number of muon triple coincidences for each of the sixty tripe coincidence definitions, and the number of interactions.

Table 3.3 lists the number of EOS records, by era, used in this analysis. This does not include calibration or special tests, only periods of actual data taking.

Table 3.3
Number of End of Spill Records by Era

AUGN	SEPN	NOVP	JANN	JANP
7098	28385	23341	11260	14452

In all this analysis, we make the requirement that the EOS record is not duplicated, and that eras are not crossed — we don't count November beam in September, even though there are, for example, some tapes from November in the nominal September file.

A beam particle was defined in the following way: The output pulses from the BY fingers were discriminated, set to a width of 10 ns, and both ORed and summed together to form six pulses, BY1, BY2 and BY3 as well as ΣBY1, ΣBY2 and ΣBY3. The BY signals were sent to a four-input AND gate, set in coincidence with the T1 signal. This four-fold coincidence insured a beam particle to be following a trajectory through all three beam stations. This signal (B) was vetoable by the presence of a halo particle (often a muon) defined to be a signal from each of the two veto planes, in coincidence. The halo rate was approximately 2.8 MHz in the January Positive era, 2.0 MHz in the January Negative eras, and proportionately lower in the earlier eras. An additional veto was based on the apparent presence of more than two beam particles. The ΣBY counters were sent to discriminators, and the thresholds of these discriminators were set to greater than two particles. The three discriminator outputs were ORed together to form a high beam particle multiplicity veto: if any beam station reported more than two particles, the event was vetoed. Early in the run,

before tape 2952, the multiple beam particle was tighter; any event with more than one beam particle was vetoed. This resulted in an unacceptable loss of events, and the restriction was loosened. This veto was called BG. The final beam signal, BV, was B in coincidence with the absence of BG.

After the presence of a valid beam particle had been established, the identity of this particle was determined by logic using information from the Cerenkov counters. Early in the run, before tape 2879, the pion definition was that both Cerenkov counters, C1 and C2, be on. Since the Cerenkov efficiencies were approximately 92% for C1 and 90% for C2, this definition resulted in a loss of 17% of the pion sample. To rectify this, a new pion definition was established, requiring either Cerenkov to be set in coincidence with beam, i.e. $BV \cdot (C1 + C2)$. Protons were defined by $(BV \cdot \overline{C1}) \cdot (BV \cdot \overline{C2})$ which corresponds to a valid beam particle with neither Cerenkov lit. The PION and PBAR scalers counted these signals. Despite the name, the PBAR scaler counted protons in the positive data as well. After the change in the pion definition, the number of beam particles passing the original pion definition was counted by the OLDPI scaler.

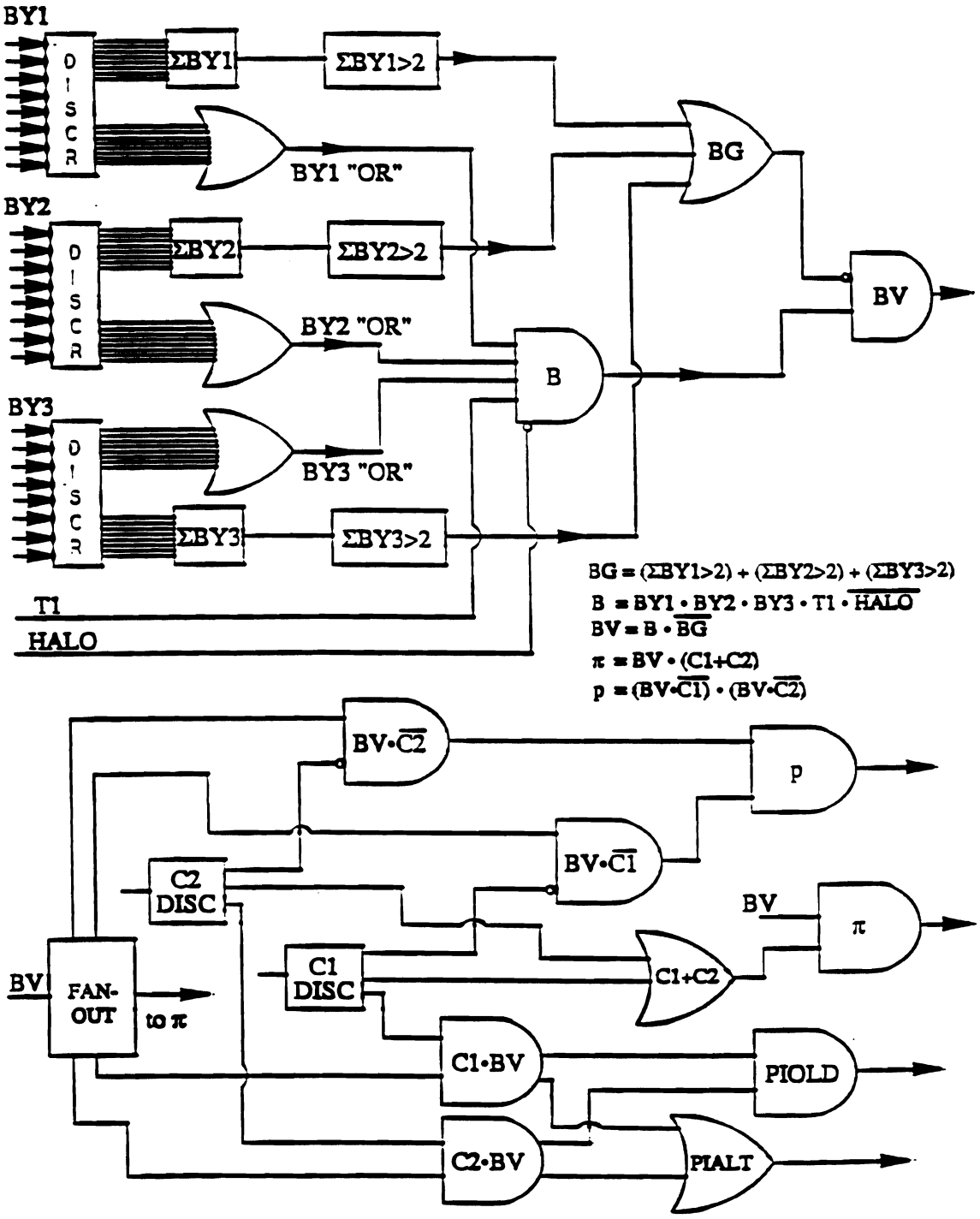

Figure 3.1 Beam Logic.

It turned out that counting the beam was not as simple as summing up the PION and PBAR scalers. The scaler outputs showed indications of sagging — a non-linear behavior with beam intensity. Although the scaler counting rates did increase with beam, they increased slower than linearly. Figures 3.1 show the PION and PBAR scalers versus MTC20, for the January Positive era. MTC20 is a muon triple coincidence scaler, corresponding to the triple coincidence indexed by MUX1 counter number twenty. Because the muon flux is much less than the beam flux and divided among sixty counters, the muon triple scalers counted at rates much lower than the beam scalers, so they should be less susceptible to any sort of rate dependent effect.

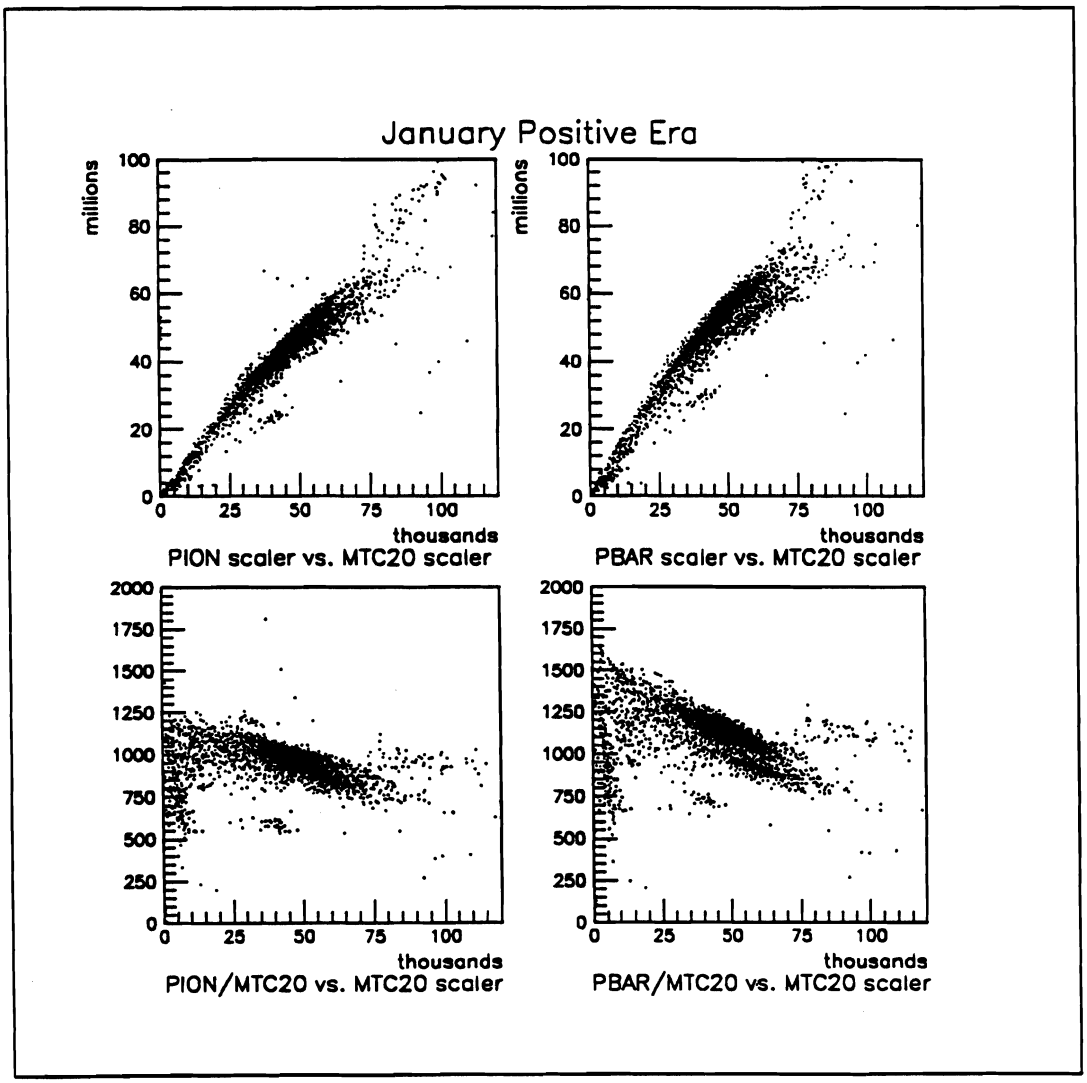

Figure 3.2 Indication of non-linearities in beam scalers. Upper Left: PION scaler vs. MTC20 scaler. Upper Right: PBAR scaler vs. MTC20 scaler. Lower Left: PION/MTC20 vs. MTC20. Lower Left: PBAR/MTC20 vs. MTC20.

The next step was to try to figure out what caused this observed sagging. One piece of data that is easily obtained is the intensity at which sagging began. Plots of PION/MTC20 and PBAR/MTC20 were therefore made. (c.f. Figure 3.1) Without any sagging, these plots should be flat; instead, they show a negative slope at even the

very lowest intensities. It's very unlikely that the fast electronics would have difficulty at these low intensities, so another hypothesis was formed: multiple bucket occupancy is causing this effect.

If two beam particles were to enter the spectrometer at the same time (within the 10 ns beam gate) either the PION or PBAR latch would be set, and only a single beam particle would be counted. As the intensity increases, the probability that this double bucket occupancy will occur per bucket increases linearly. This is in agreement with the observed scaler behavior.

More directly, plotting PION vs. the logical sum of the BY fingers instead of the arithmetic sum shows a linear response. (c.f. Figure 3.2) So, the correction factor that we need is approximately the ratio of the scaled arithmetic sum to the scaled logical OR of the BY fingers — approximately because it is possible for there to be two particles in the same bucket and the same finger. For eight counters with a uniform distribution the correction is 9/8; for two counters it is 3/2. For a non-uniform distribution, such as ours (c.f. figure 3.3) it is given by:

$$\frac{\sum_{i=1}^{8} BY_i^2 + \sum_{i=1}^{8} BY_i}{\sum_{i=1}^{8} BY_i} \tag{3.1}$$

which equals 1.250 or approximately 5/4 in our case. Effectively, we have four BY fingers as far as counting two beam particles in the same bucket.

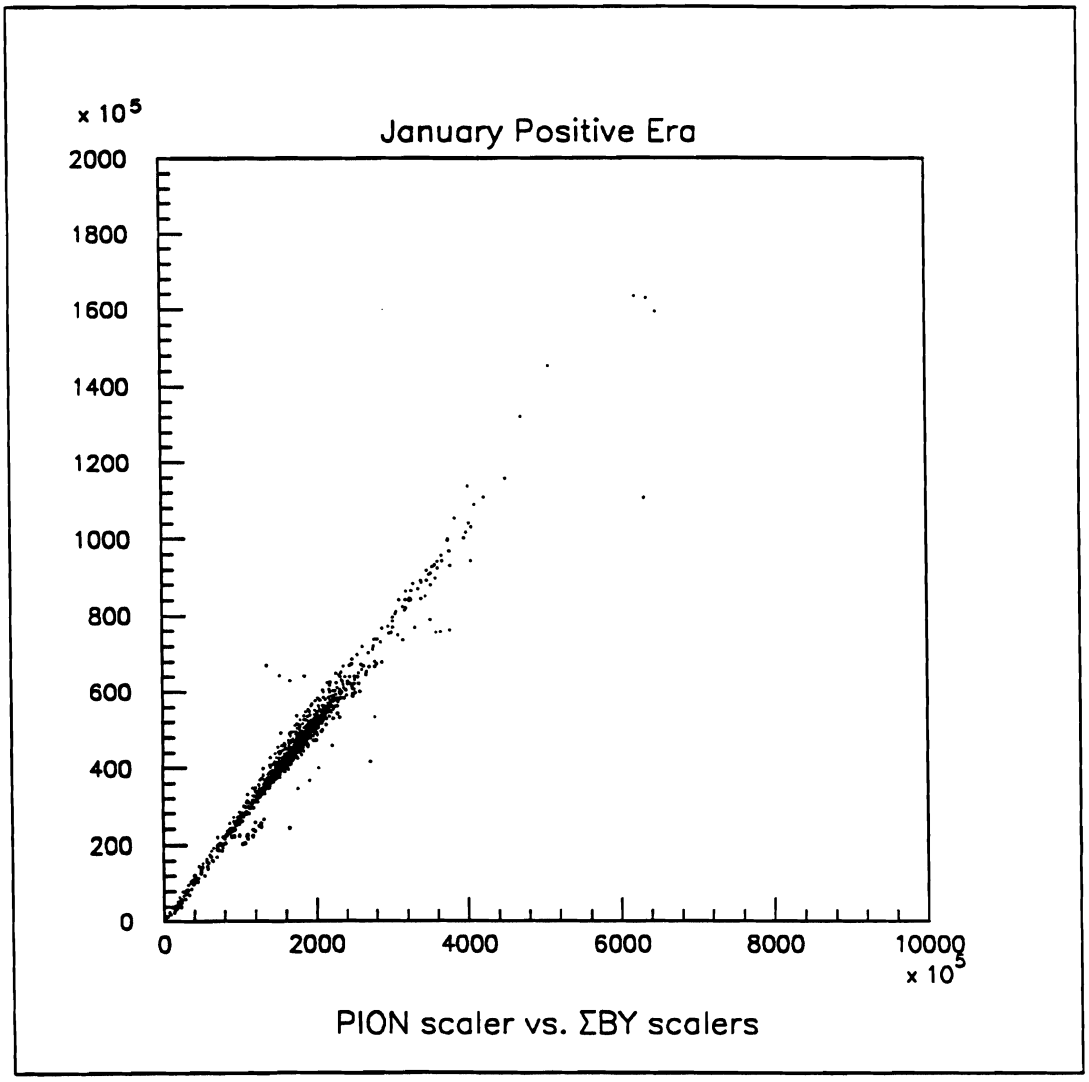

Figure 3.3 PION scaler vs. the arithmetic sum of the BY fingers.

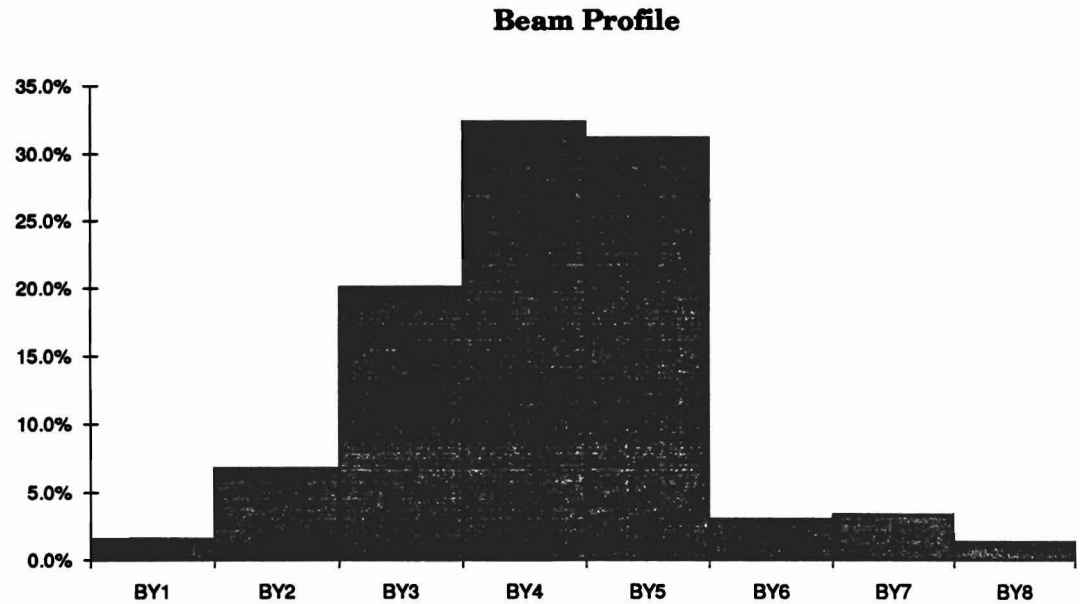

Figure 3.4: Beam Profile

Therefore, our final beam sagging correction term is:

$$F(x) = \mathrm{A}\left(1 - \frac{5}{4}\left(1 - \frac{\mathrm{DIFF2}}{\mathrm{SMBY2}}\right)\right) \qquad (3.1)$$

where DIFF2 is the corrected sum of BY2 scalers (or BY1 or BY3 scalers for the periods where they were scaled instead) and SMBY2 is the scaled logical OR. A is a factor to insure that for zero beam intensity the correction reduces to one: that is, that there is no sagging correction at zero intensity. Intensity was determined by the readings of the secondary emission monitors: whichever of PW5SEM and PW6SEM was scaled at the time of the correction.

The other correction that has to be made is for the live time. When a trigger occurs, there is a gate inhibit signal sent to the trigger electronics, preventing a second trigger from occurring before the first one is processed. Dead time is the time during

this gate inhibit. A scaler, LBEAM, counted beam particles only when there was no gate inhibit. So, the number of pions actually able to produce a trigger is given by:

$$\sum_{\text{spills}} \left[\left(\frac{\text{LBEAM}}{\text{PION+PBAR}} \right) F(x)\ \text{PION} \right] \tag{3.2}$$

and the number of protons by:

$$\sum_{\text{spills}} \left[\left(\frac{\text{LBEAM}}{\text{PION+PBAR}} \right) F(x)\ \text{PBAR} \right] \tag{3.3}$$

Live time was nearly 100% in the lowest intensity running, dropped 60% or lower at extremely high intensity — beam fluxes in excess of 5 MHz — and was typically about 80%.

This correction was applied to the positive beam data, as well as the negative pions. However, it is difficult to apply to the antiprotons. Again, the problems stem from multiple bucket occupancy. If there are two particles in a single RF bucket, the only time that the PBAR latch is set is if they are both antiprotons. If at least one is a pion, the Cerenkov counters will light, and PION will be set instead. Since there are roughly fifty pions per antiproton, it's very likely that if there is another particle in a bucket with an antiproton, it will be a pion. This means that the PBAR latch sags even faster than PION — so fast, in fact, that at the very highest intensities, the PBAR scaler is anticorrelated with the intensity.

Instead of trying to correct a counter that sags so much, the actual antiproton count is determined in an entirely different manner. The assumption is made that the ratio of antiprotons to pions is independent of the intensity of the beam. This ratio is then used to calculate the corrected antiproton count from the corrected pion count.

This gives a much smaller uncertainty than the alternative method of correcting by subtracting the corrected PION scaler from the corrected PIPB (pion plus antiproton) scaler. To determine the uncertainty associated with this method, the number of protons in the positive beam was calculated by the ratio method, and compared to the corrected direct count. In all cases, the two methods agreed within 10%.

It's important to establish the uncertainty in the beam normalization. One route would be to estimate the error at each stage of the process, and to propagate these through to calculate the overall uncertainty. Another would be to find a quantity in the data that includes the beam and that should be the same for all spills. The width of its distribution is a measure of the uncertainty in beam normalization. The quantity chosen was the ratio of the number of interactions to the number of corrected beam particles. Both methods were tried.

To propagate uncertainties through the correction algorithm, the uncertainty of the scalers must be somehow determined. The quantities PION, PBAR and PIPB were all scaled. PIPB is a scaler set to read the logical OR of PION and PBAR. Since they are mutually exclusive, this is the same as the sum. We plotted the ratio of $\frac{\text{PIPB}}{\text{PION} + \text{PBAR}}$ and found that it had a mean of 0.9868 and a standard deviation of 0.0583. (c.f. Figure 3.6) If the scalers were perfect, the mean should be one, and the standard deviation zero. Adding the standard deviation and the relative deviation from the known mean together in quadrature, that is, treating the deviation from the expected mean as a systematic uncertainty, we obtain a total uncertainty of 5.97%. Partitioning this equally (again, in quadrature) among the three scalers involved implies that each scaler has an uncertainty of 3.45%. Without sagging correction , there are also three independent scalers necessary to count the beam: PION, PBAR and LBEAM. Three scalers with a 3.45% uncertainty give a total uncertainty of 5.97%. The correction

term involves one scaler in the numerator and effectively four from the eight BY counters in the denominator. This yields an uncertainty of 8.45% from these scalers. However, there is also a 10% uncertainty in the overall correction normalization; adding it in quadrature results in a 13.1% uncertainty on the correction. The sagging correction is typically about 20% of the total beam, and so adds another 2.6% uncertainty.

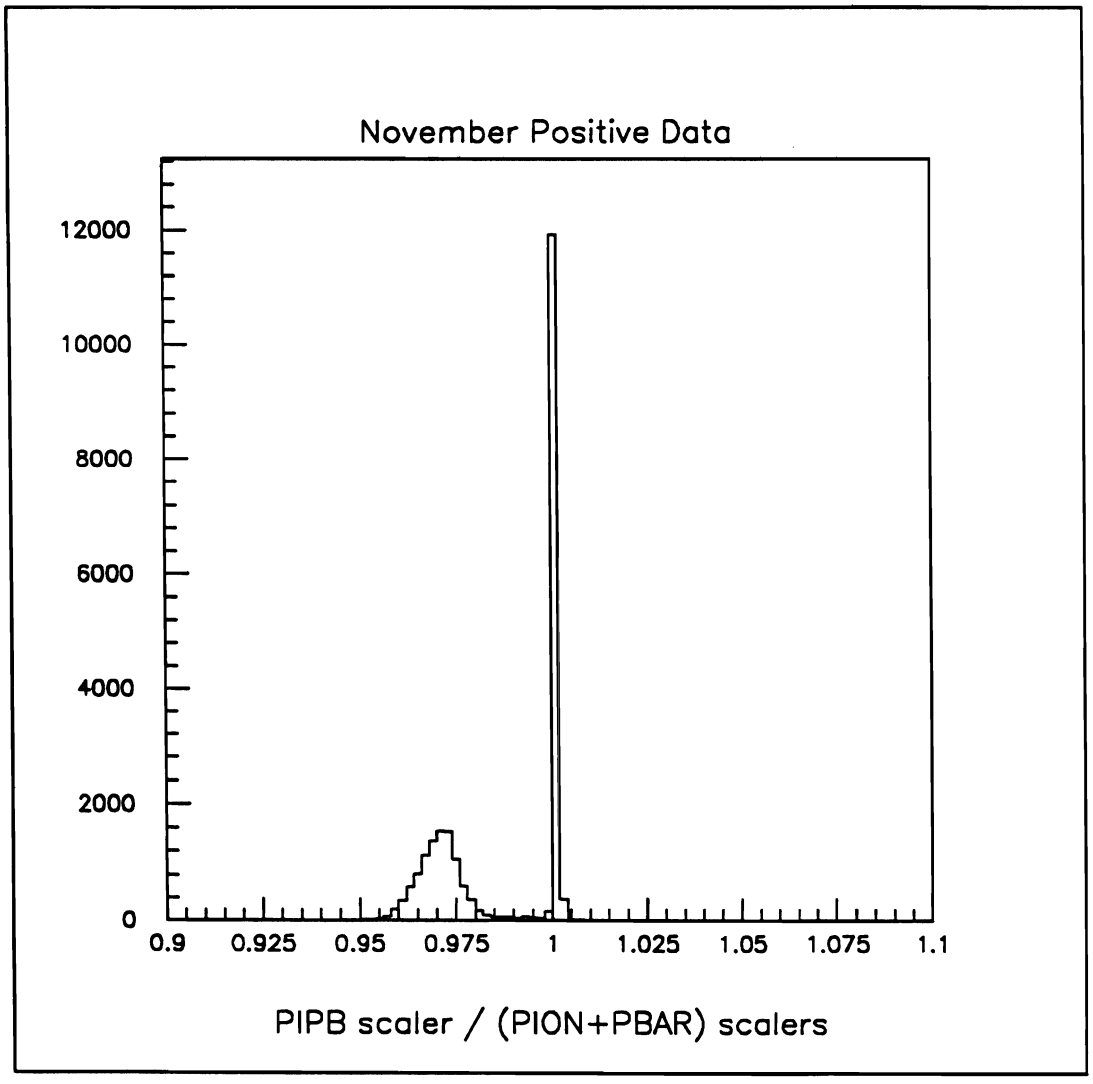

Figure 3.5: PIPB / (PION + PBAR) histogram. For an ideal set of scalers, this should be a delta function at one.

Although the interaction scaler is presumably sagging like PION or PBAR, since the interaction rate is only about 20% of the beam rate, the sagging is relatively small. Only in the rare case when there are two beam particles in the bucket and both interact with the target does this effect become important. The width of the distribution of the number of interactions divided by the corrected sum of the BY counters is approx-

imately 9%. (See Figure 3.6 on the following page) This is in agreement with the direct propagation of errors.

More importantly, this second method can be used to see if any beam is missing the target in the negative data. The total cross-section for the four beam types is known, as is the mix of pion and proton, so the total interaction probability for beam of each era is calculable. This cannot be used for an accurate absolute normalization because there are processes to which the interaction trigger cannot respond . (e.g. $\pi^- + p \rightarrow n + N\pi^0$) Trying to correct for this requires understanding in great detail all of these difficult to see processes as well as an equally detailed understanding of the interaction trigger's efficiency in responding to each of the individual processes that make up the total cross-section. The ratios, however, of the interaction probabilities should be relatively insensitive to these complications.

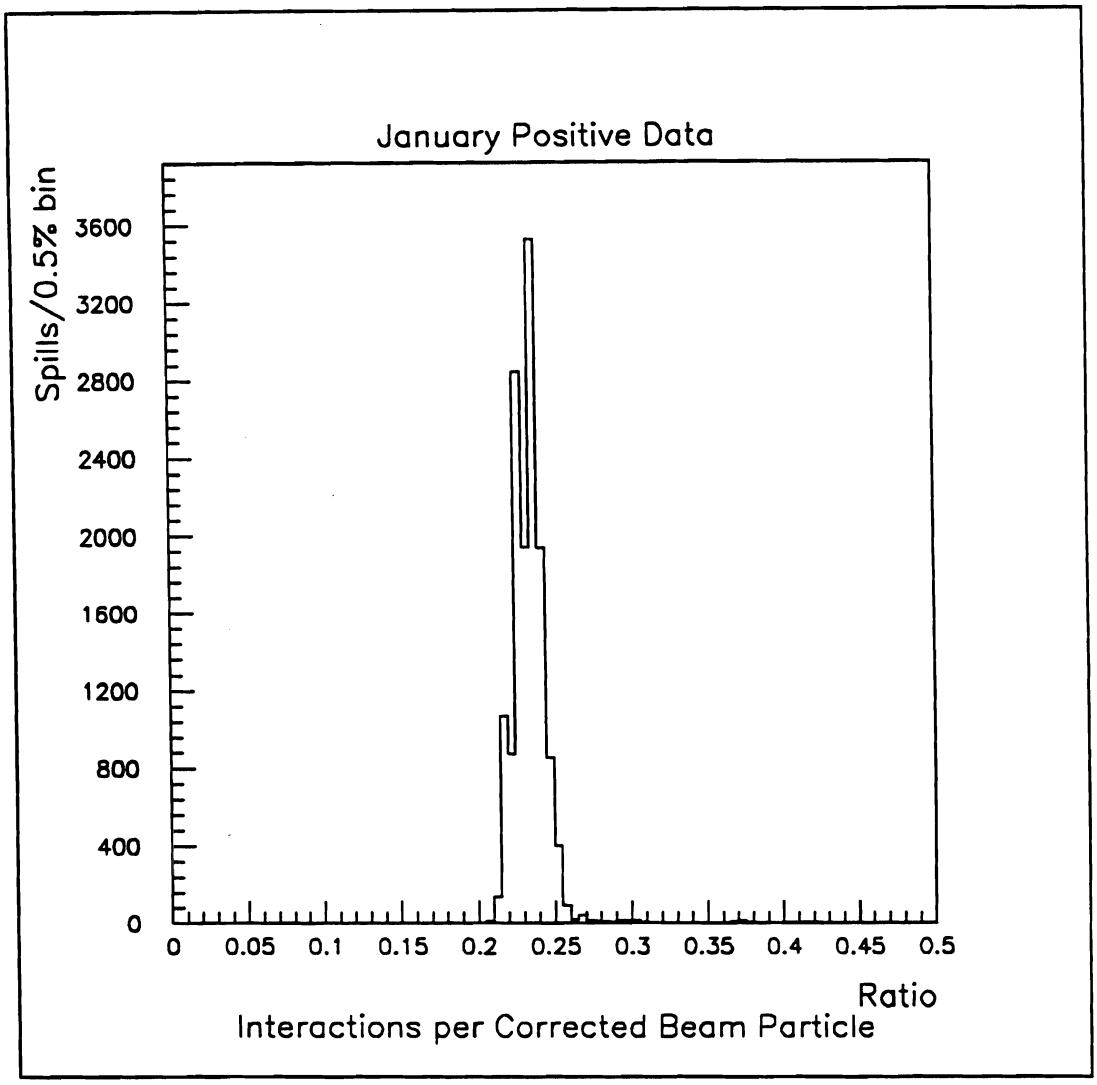

Figure 3.6: Interactions per corrected sum of BY counters.

The negative data beam profile is larger and less symmetric than the positive; it is possible that some beam is missing the target. To measure this, we look at the number of interactions per unit beam, corrected for sagging and different particle mix, and compare positive and negative beam. Doing this, we obtain a fraction of negative beam missing the target of $-2 \pm 2\%$. So, fortunately, all of the beam is incident on the

target; we do not have to correct for this. Table 3.4 contains the beam count after all these corrections have been made.

Table 3.4
Corrected and Uncorrected Beam Count

Era	Beam Particle	Uncorrected (10^9)	Corrected (10^9)
August Negative (AUGN)	π^-	468.8	286 ± 17
	antiproton	9.1	5.55 ± 0.39
September Negative (SEPN)	π^-	1581.1	1304 ± 79
	antiproton	23.9	19.8 ± 1.4
November Positive (NOVP)	π^+	672.4	562 ± 34
	proton	864.1	725 ± 51
January Negative (JANN)	π^-	768.2	641 ± 71
	antiproton	25.1	70.5 ± 2.3
January Positive (JANP)	π^+	595.8	485 ± 51
	proton	692.0	563 ± 45

This is a global measurement of the beam flux. Also needed is a determination of the beam particle on an event-by-event basis. The Cerenkov counter signals and the PION and PBAR latches were recorded for every event, and the beam type determined according to the rules in table 3.5.

Table 3.5
Offline Beam Particle Identification

C1	C2	PION	PBAR	Conclusion
Lit	Lit	Set	Not Set	pion
Lit	Lit	Not Set	Not Set	pion
Lit	Unlit	Set	Not Set	pion
Unlit	Lit	Set	Not Set	pion
Unlit	Unlit	Not Set	Set	proton
Unlit	Unlit	Not Set	Not Set	proton
Lit	Unlit	Not Set	Set	proton
Unlit	Lit	Not Set	Set	proton
All Other Cases				ambiguous

These rules can be summarized as follows:

• If both PION and PBAR are set, the event is ambiguous.

• If either PION and PBAR is set (but not both), the event is ambiguous only if both Cerenkov counters contradict the PION/PBAR latches. Otherwise, the pion and pbar latch data are taken to be correct.

• If neither PION nor PBAR is set, the event is ambiguous unless both Cerenkov counters agree. If they are both lit, the beam particle is called a pion; if neither are lit it is called a proton.

Effectively, this allows for three counters to overrule one in most cases.

To determine the efficiency of the offline beam tagging, the set of minimum bias events (CFSTROBE triggers) was studied. If the tagging were perfect, the ratio R of proton-induced interactions to pion-induced interactions would be given by the following expression:

$$R = \left(\frac{\#\text{ protons}}{\#\text{ pions}}\right)\left(\frac{1-e^{z/\lambda_i(\mathrm{p})}}{1-e^{z/\lambda_i(\pi)}}\right) \tag{3.4}$$

where z is the physical target length and λ_i is the absorption length of lithium for the appropriate beam particle. However, the tagging is not perfect; that there are events in the ambiguous category proves that. For N interactions, $N/(R+1)$ of them should be pion-induced and $NR/(R+1)$ of them proton-induced; by dividing the actual number of interactions tagged by this, we calculate the tagging efficiency. Note that a hyper-efficiency is possible — for example, sometimes neither Cerenkov fires for a pion. This would inflate the number of observed protons relative to the number of actual protons. The table on the following page shows the offline tagging efficiencies.

Table 3.6
Offline Beam Particle Tagging Efficiencies

Era	Beam Particle	Efficiency
August Negative	π^-	99.0 ± 1.2 %
(AUGN)	antiproton	58.8 ± 5.5 %
September Negative	π^-	100.8 ± 0.8 %
(SEPN)	antiproton	41.5 ± 3.2 %
November Positive	π^+	100.4 ± 2.0 %
(NOVP)	proton	90.8 ± 1.4 %
January Negative	π^-	97.8 ± 0.8 %
(JANN)	antiproton	67.4 ± 2.8 %
January Positive	π^+	99.0 ± 1.2 %
(JANP)	proton	90.0 ± 0.9 %

C. Triggers

Typically, several million interactions occurred during each spill. Most of these did not contain the sort of physics event that we were interested in. Furthermore, writing out this many events per spill was beyond the capability of our data acquisition system and would make the off-line analysis significantly more difficult and time-consuming. Only those events which had a high probability of containing an interesting event triggered the data acquisition and caused the spectrometer data to be written to tape. Each event written to tape contained a 13-bit word representing the status of the trigger latches (c.f. table 3.7).

Table 3.7
Trigger Type Summary

Trigger Bit	Prescale factor	Label	Description
1	normally off	PT1	Cluster finder level 1 (p_T >1.7 GeV/c)
2	128	PT2	Cluster finder level 2 (p_T >2.5 GeV/c)
3	8	PT3	Cluster finder level 3 (p_T >3.5 GeV/c)
4	1	PT4	Cluster finder level 4 (p_T >4.5 GeV/c)
5	1	Di-mu	Dimuon
6	normally off	INT	Interaction
7	normally off	test	Test pulser
8	1	LED	LED pulser
9	normally off	XEN	Xenon lamp flasher
10	2^{19}	STRB	Cluster finder strobe
11	1	di-photon	Two cluster trigger
12	normally off	CAL	Pulser for counters and chambers
13	varied	Two-V	Multiplicity jump

These triggers fall into four general categories: photon, interaction, dimuon, and miscellaneous.

Photon triggers were generated by the cluster finder. This hardware trigger looked for energy clusters in the main array, and calculated the transverse momentum (actually, transverse energy, but for photons $p_T = E_T$) of each cluster. It did this in three stages: first, it found a non-perimeter main array block with more energy than any adjacent block, and above a minimum threshold of about 4 GeV. This block and a hard wired cluster of six to nine nearby blocks formed a *cluster*. Next, the energies of all the blocks in the cluster were added, and multiplied (using resistor weighting) by the sine of the angle from the target between the center of the main array and the center of the block, to convert energy to transverse energy. Finally, this transverse energy was compared to one of four thresholds, and the result placed in coincidence with the interaction trigger. In addition to the four single photon triggers, there was a

diphoton trigger, which was defined by two clusters in opposite quadrants that passed, the lowest p_T threshold, PT1. The events recorded because of photon triggers are used in this analysis to measure the muon and counter and charged particle hodoscope efficiencies.

Two triggers which appear to do much the same thing are the interaction and the cluster finder strobe triggers. The interaction trigger was based on the charged particle hodoscope. The analog outputs of the individual CPX counters were summed, and the result was sent to a discriminator set to a threshold corresponding roughly to two hits. The output of this was placed in coincidence with BV to form the interaction trigger, which was counted by the INTER scaler. The interaction trigger was sent to the cluster finder, and was returned by it as CFSTROBE. The difference between INTER and CFSTROBE was that the latter was only set while the cluster finder was live, that is, able to process an event. Scaling both quantities allowed us a measure of the cluster finder live time, which was the ratio of CFSTROBE to INTER. Finally, CFSTROBE was then heavily prescaled, and a small number of these triggers written to tape to provide a minimum bias data sample.

The dimuon triggers were established in two steps. First was the fast dimuon trigger. This was simply two (or more) muon triple coincidences from different quadrants in coincidence with an interaction. (The interaction requirement reduces triggers caused by halo muons.) After this, an on-line trigger processor[40] was invoked to make a fast but somewhat crude measurement of the dimuon mass. Figure 3.7 shows the trigger processor's mass estimate for a sample of Monte Carlo J/ψ's. If the estimate mass was above 2.4 GeV, the event was recorded to tape. The mass was calculated by the following procedure: Starting from the muon counter hits, roads were projected from the muon counters to the magnet, and in these roads the X-planes of DC4, DC5

and DC6 were searched for hits. Track segments were searched for, using only the coordinates of the wire positions; drift times were not used. If a track candidate was found, an estimate was made of its three-dimensional position by looking at the MUY counters. If a MUY counter in the same quadrant as a triple coincidence was lit, the y-slope of the track was calculated as the ratio of the position of the outside edge of that counter to the distance of the muon counters from the target. If multiple MUY counters were lit, the one farthest from the beam hole was selected, because this would result in the largest opening angle, and therefore the largest mass. The mass would not be underestimated, and if the wrong counter was chosen, the event could later be rejected off-line. Three-fourths of the raw fast dimuon triggers were rejected by the trigger processor, but only a very small number (well under 10%) of the reconstructible J/ψ's were rejected.

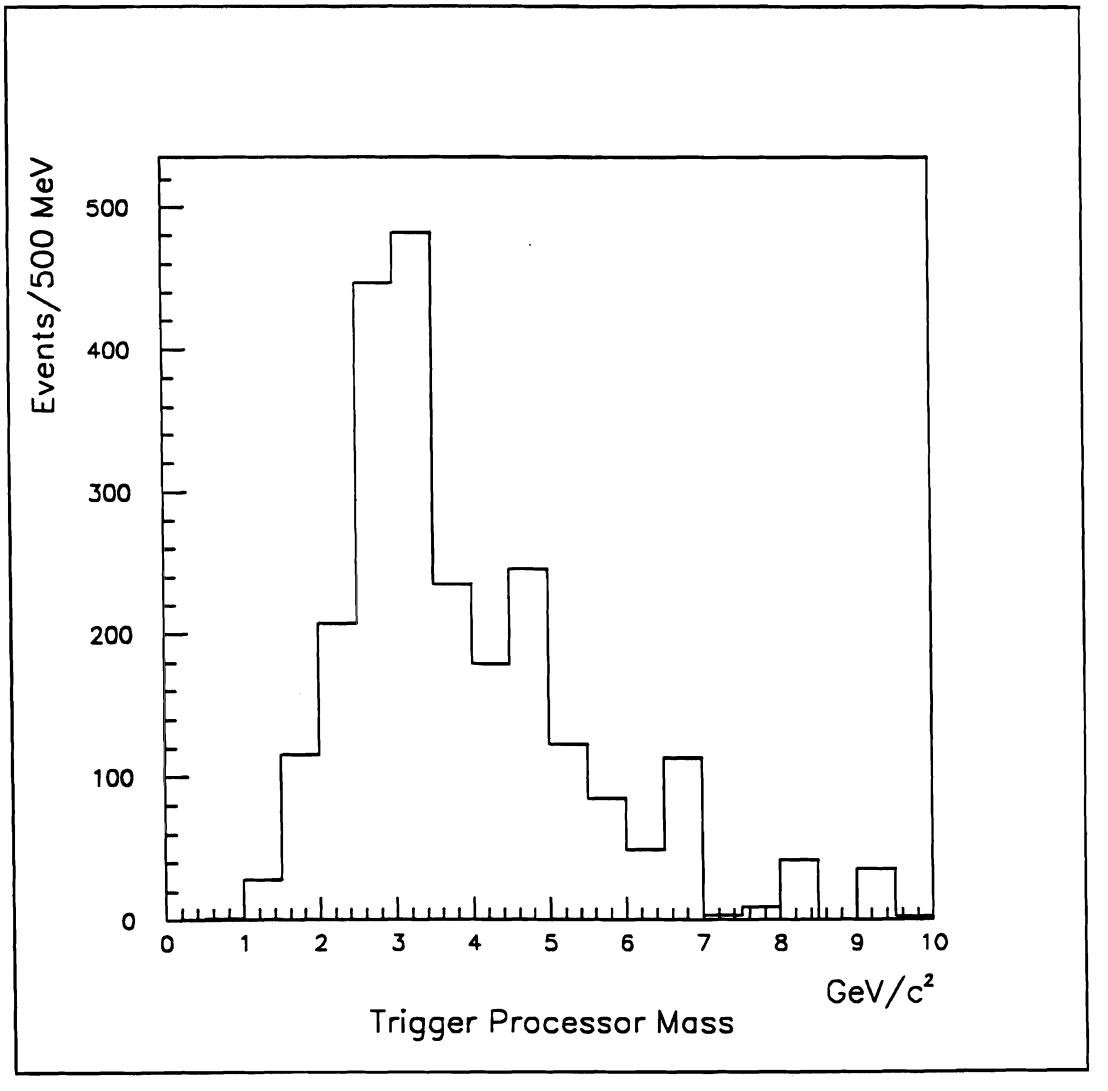

Figure 3.7 Trigger Processor Mass for Monte Carlo J/ψ's.

The LED and Xenon triggers were included for glass calibration, although the Xenon lamp system was never actually used. The LED system was based on a common light signal sent through a filter wheel, and then via fiber optics into the individual glass blocks, and the gains and pedestals were determined from the glass response. For most of the run, this was done in the non-spill portion of the spill cycle

where beam is being accelerated. For a brief portion of the January era, in-spill LED triggers were also written to tape. The Calibration trigger was used only for electron beam calibration. It was defined as the beam trigger plus at least one lit Cerenkov counter, after the pressure in the Cerenkov counter had been adjusted to make it sensitive to electrons.

Finally, the Two-V trigger, triggering on an X-plane multiplicity jump between chambers PC2 and PC3, was incorporated in an attempt to record events from the decays of particles containing *b*-quarks (via decays like $B^0 \rightarrow J/\psi + K_s$). These triggers were not used in this analysis.

More than one trigger bit may be set in the same event. For example, a PT1 trigger may have both the PT1 and Interaction bits set (but not always, since Interaction and PT1 are prescaled at different rates.)

D. Counter Efficiencies

To measure the muon counter efficiencies, we looked at muons in events with photon triggers. Photon triggers were used because the dimuon triggers already required a pair of muon triple coincidences; that sample was therefore strongly biased. Photon triggers were less plentiful than dimuon triggers, but more plentiful than any other trigger type. For this measurement, several million photon triggers (c.f. Table 3.8) were used which corresponded to approximately 8% of our entire data set.

Table 3.8
Number of Photon Triggers Used To Establish Chamber Efficiencies (thousands)

AUGN	SEPN	NOVP	JANN	JANP
1050	950	540	1880	360

First we found tracks that projected to a set of at least three lit counters in the muon hodoscope. If these tracks passed a set of quality cuts (c.f. Table 3.9), the fourth counter was checked; it was considered lit if it was lit, or if the track passed within 1 centimeters in x or 2 centimeters in y of an edge, and the next counter in that direction was lit. This was to take into account the possibility of multiple scattering in the muon wall causing the muon to hit an adjacent counter instead. The efficiency is the ratio of the number of times the fourth counter was lit divided by the number of times it was checked. (c.f. Table 3.10)

Table 3.9
Track Cuts for Counter Efficiency Measurements

Cut	Muon Hodoscope	CPH
Hits on downstream segment	> 8	> 8
Downstream χ^2	< 3	< 3
Segment Match at Magnet Δx	< 1.5 cm	< 1.5 cm
Segment Match at Magnet Δy	< 4.0 cm	< 4.0 cm
Δy-slope	< 20 mR	< 20 mR
Momentum	> 10 GeV/c	> 6 GeV /c (muons)
Charged Particle Hodoscope	none	lit counter in other view

Table 3.10
Muon Counter Efficiencies by Era and Plane

Era	MU1	MU2	MU3	MUY
August Negative	94.3 ± 0.3 %	98.4 ± 0.2 %	95.6 ± 0.4 %	94.7 ± 0.2 %
September Negative	93.2 ± 0.4 %	97.9 ± 0.2 %	95.0 ± 0.3 %	96.6 ± 0.2 %
November Positive	89.3 ± 0.6 %	96.7 ± 0.4 %	96.2 ± 0.4 %	91.1 ± 0.4 %
January Negative	88.9 ± 0.6 %	96.2 ± 0.5 %	96.7 ± 0.4 %	87.2 ± 0.5 %
January Positive	91.3 ± 0.7 %	95.7 ± 0.5 %	96.6 ± 0.5 %	90.6 ± 0.5 %

A similar procedure was performed for the CPH. In this case, because multiple scattering in the muon walls is not an issue, all charged tracks were used without an explicit momentum requirement, although muons still need at least 6 GeV to penetrate the muon steel. Again, tracks are found that pass certain criteria, and projected to the CPH. If the counter pointed at by the downstream segment is lit, or if the track projects near a boundary (1 centimeter for an x-counter and 2 centimeters for a y-counter) and the next counter is lit, the counter is said to be lit. The efficiency is then the ratio of lit counters to the total number of tracks. Because of the higher statistics available by considering non-muon tracks, counter-by-counter efficiencies can be determined (c.f. Figure 3.8). Much of the 12% inefficiency in CPX can be attributed to the gaps between counters due to the way that they were taped during assembly.

Table 3.11
Average CPH Counter Efficiencies by Era and Plane

Era	CPX	CPY
August Negative	88.91 ± 0.09 %	97.25 ± 0.05 %
September Negative	89.01 ± 0.07 %	97.67 ± 0.05 %
November Positive	88.93 ± 0.08 %	95.08 ± 0.06 %
January Negative	88.82 ± 0.11 %	94.19 ± 0.08 %
January Positive	88.25 ± 0.11 %	94.44 ± 0.08 %

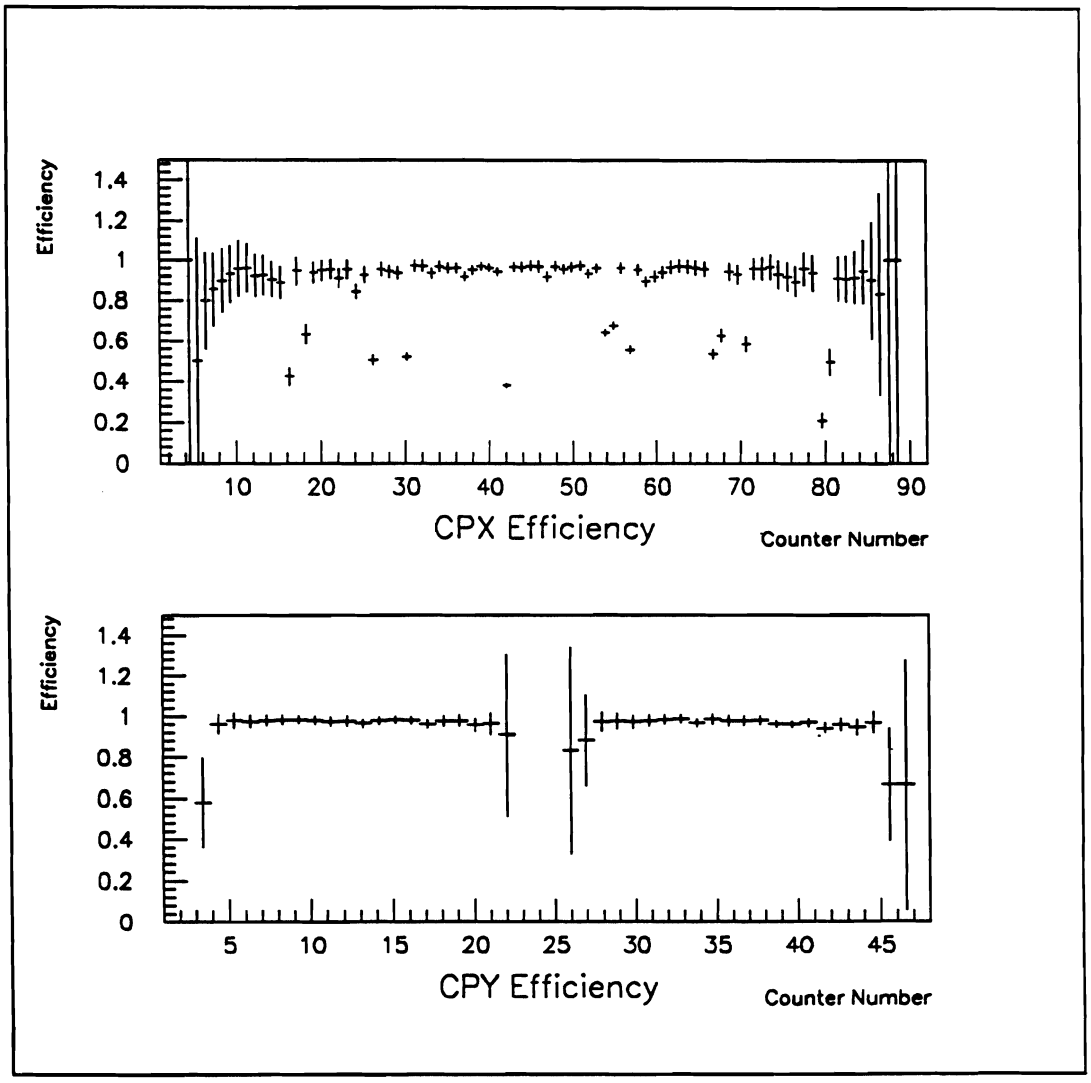

Figure 3.8 Charged Particle Hodoscope (CPH) efficiency profile. Upper: *x*-view. Lower: *y*-view.

E. Chamber Efficiencies

The efficiency of reconstructing a charged particle, or a particle decaying into two or more charged particles, such as the J/ψ, is a function of the chamber efficiencies. Having a chamber miss a hit causes two problems. First, the fewer the

measurements of a track, the greater the uncertainty on its position and slope, and consequently its momentum. Second, there is a combinatoric background due to mis-assignment of hits from both real tracks and out of time chamber hits. The fewer hits on a real track, the more difficult it is to distinguish from a coincidental alignment of hits.

The chamber efficiencies were determined by essentially the same computer program that aligned the chambers, operating on data taken with the magnet off. Tracks were found that were in the live regions of all the chambers, and passed a set of quality cuts (c.f. Table 3.12). The chamber efficiency for each plane is the ratio of the number of times the chamber found a hit on a given track divided by the number of tracks that passed through the live region of that chamber.

Table 3.12
Track Cuts for Chamber Efficiency Measurements

Item	Cut
Hits on downstream segment	> 8
Downstream χ^2	< 3
Segment Match at Magnet Δx	< 1.5 cm
Segment Match at Magnet Δy	< 4.0 cm
Δx-slope	< 10 mR
Δy-slope	< 20 mR
Charged Particle Hodoscope	X and Y counters lit

The chamber efficiencies were measured twenty-eight times during the run. Twenty "epochs" were defined: periods of a few hundred tapes nearest to a particular efficiency measurement. Eight efficiency measurements were not used — they were only a few tapes away from another measurement, so they provide very little new information.

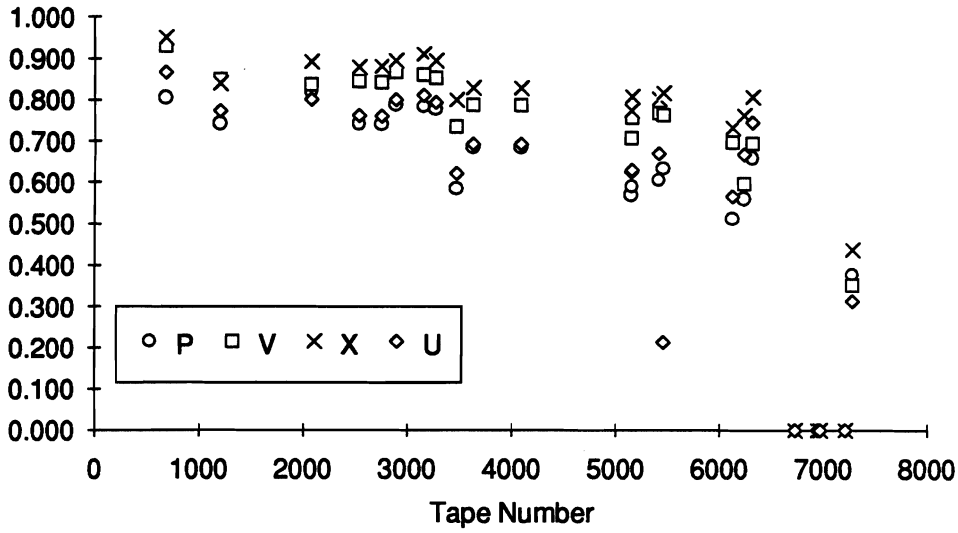

Figure 3.9: PC1 Efficiency By Plane

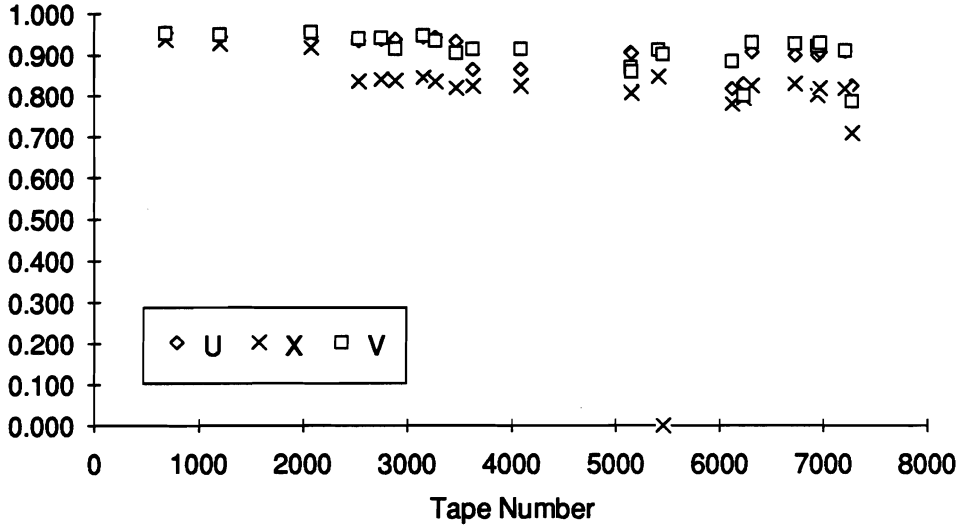

Figure 3.10: PC2 Efficiency By Plane

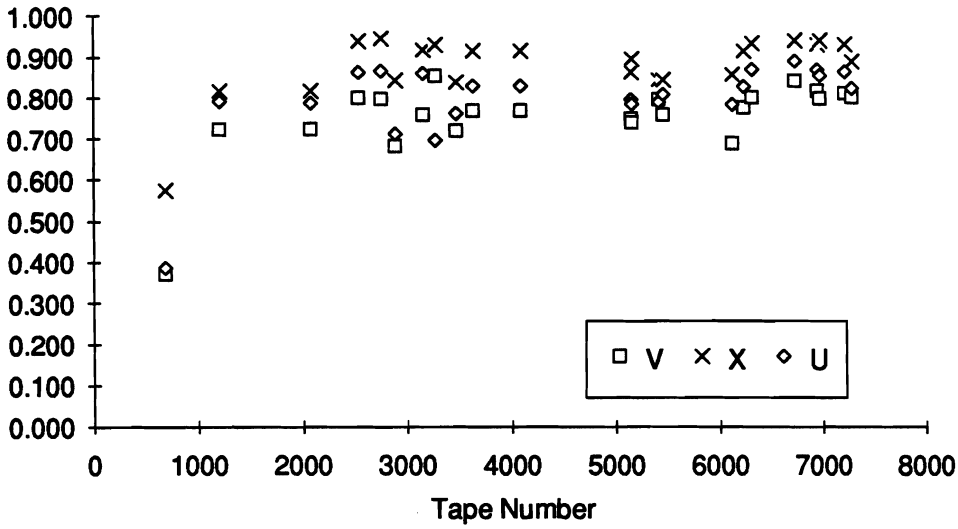

Figure 3.11: PC3 Efficiency By Plane

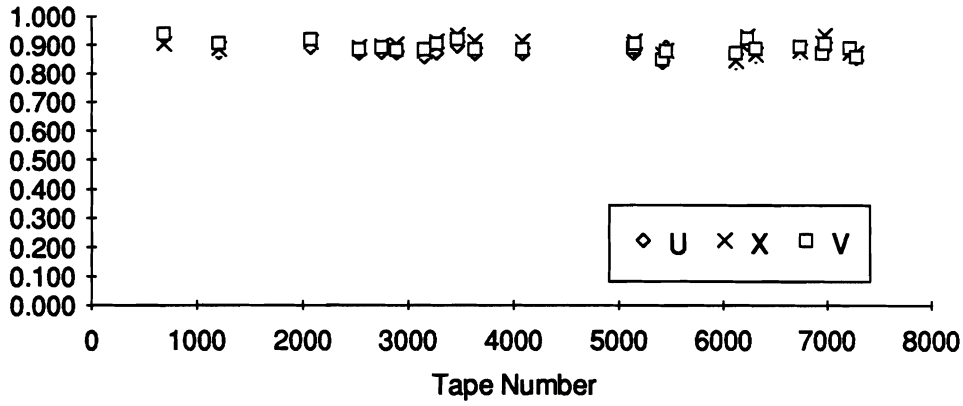

Figure 3.12: DC1 Efficiency By Plane

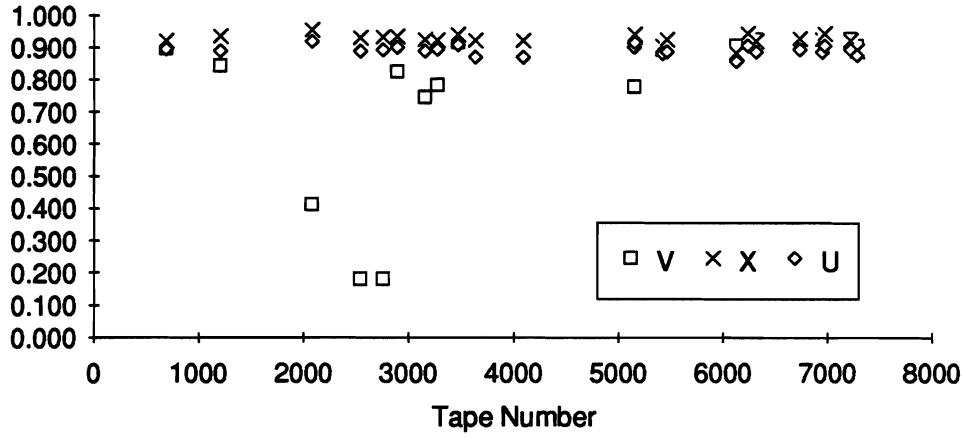

Figure 3.13: DC2 Efficiency By Plane

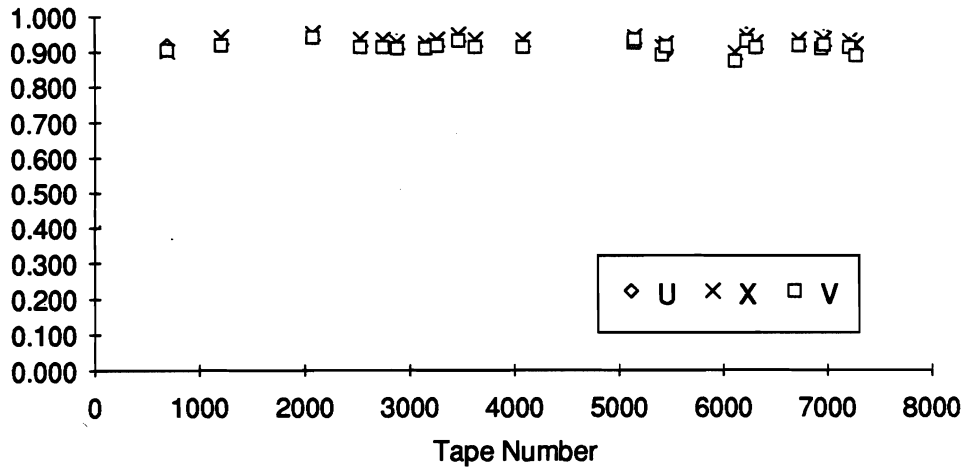

Figure 3.14: DC3 Efficiency By Plane

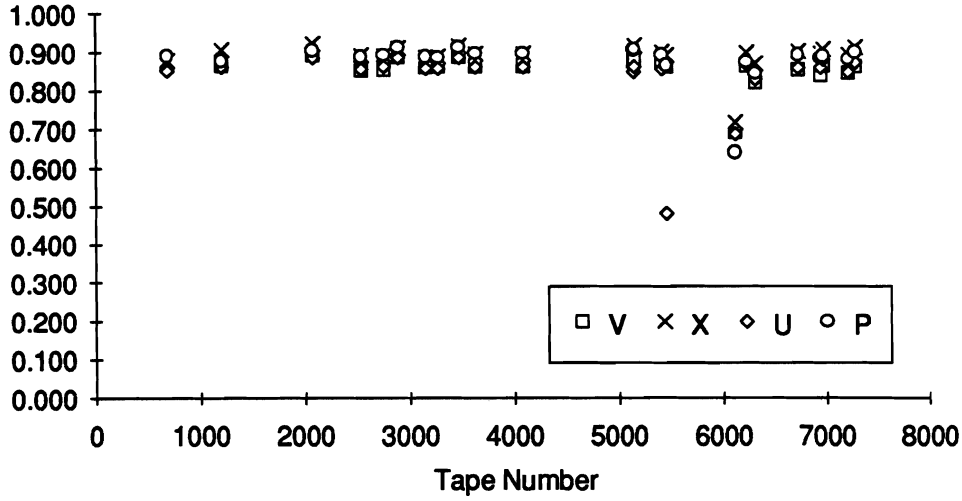

Figure 3.15: DC4 Efficiency By Plane

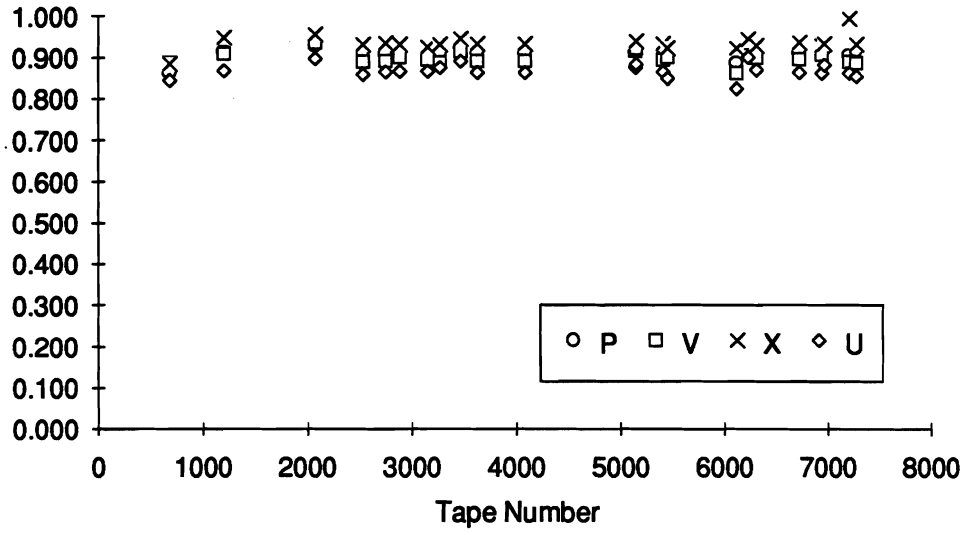

Figure 3.16: DC5 Efficiency By Plane

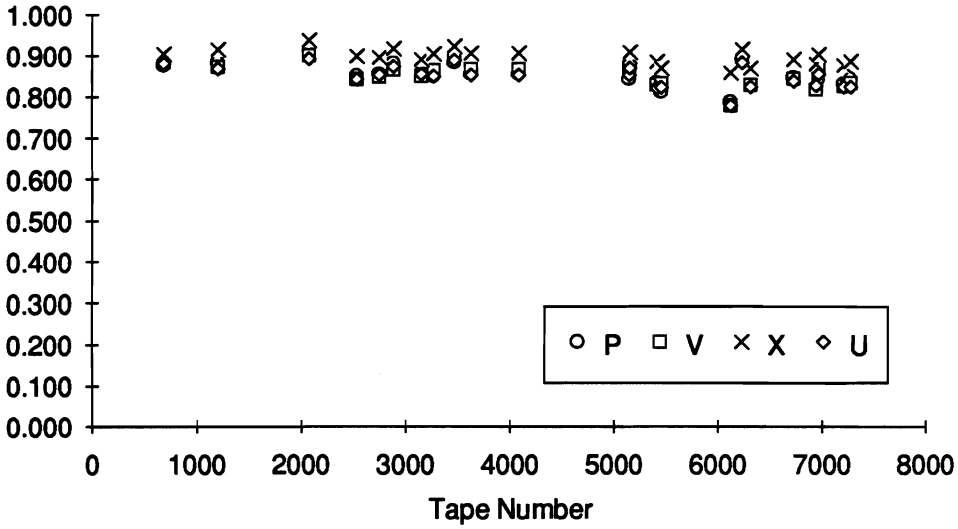

Figure 3.17: DC6 Efficiency By Plane

Chapter 4: Event Reconstruction

A. Basic Algorithm

1. Beam Tracks

The beam tracks were reconstructed from the hits they left in the three beam chambers: BC1, BC2 and BC3. First, the algorithm made points in space (x,y,z) by taking the (y,u,v) hits at the known z positions of the chambers, and then making (yu) and (yv) combinations that were consistent with a common x-position inside the chamber's active area. These triplet points from each chamber were then combined to make tracks. After the triplet points were used, the program looked at leftover doublet (yu), (yv) and (uv) combinations and tried to match these with triplet points that had not been matched in the earlier pass.

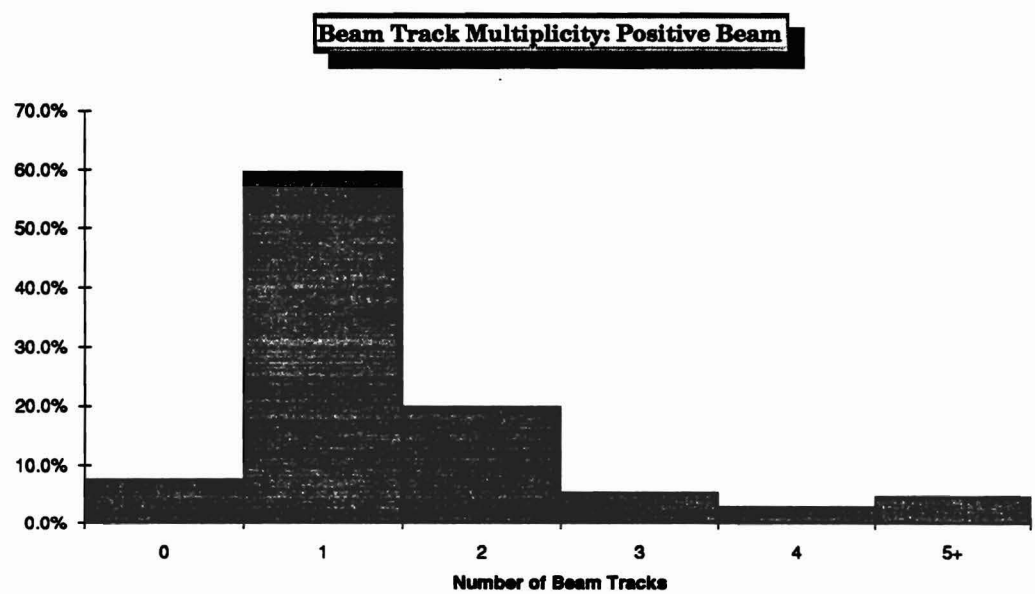

Figure 4.1 Number of beam tracks for positive beam J/ψs

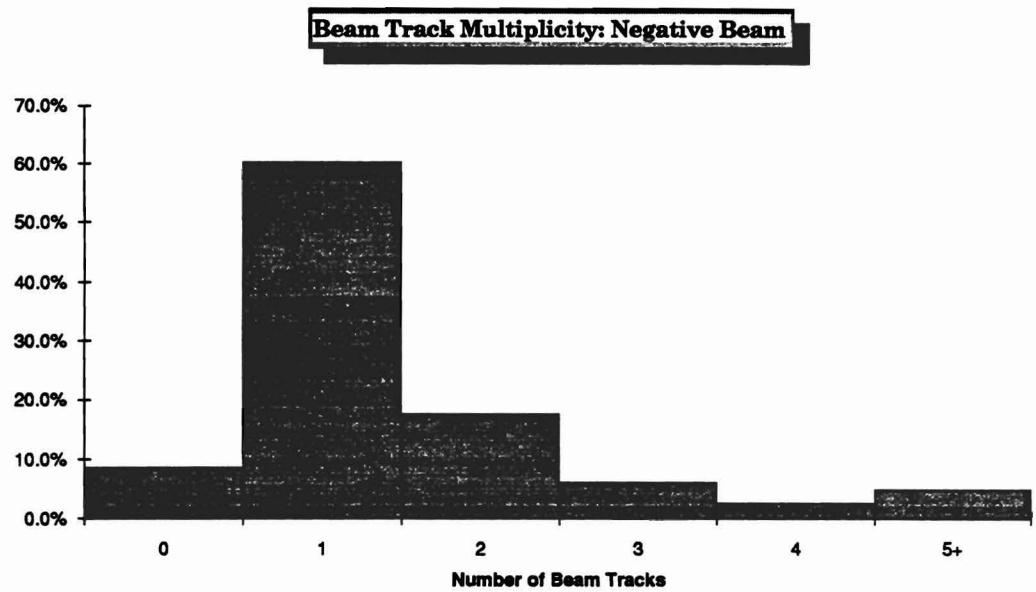

Figure 4.2 Number of beam tracks for negative beam J/ψs

Figures (4.1) and (4.2) show the beam multiplicity distributions for positively and negatively charged beams respectively. The case where no beam track was found is explained by inefficiencies in the beam chambers. More than one beam track results partially from the gate time for the chambers being approximately three RF buckets wide and partially from multiple bucket occupancy of the sort described in the previous chapter.

2. Upstream Tracks

Upstream of the magnet, all the stereo planes were at the same angle: 16.7° with respect to the vertical, positive for U-planes and negative for V-planes. This made it possible to form two dimensional tracks independently in all three views, after which the tracks could be combined to form three dimensional tracks.

In each view, a line was defined by two points from different chambers. The program looped over these seed planes, and formed lines from all possible two hit combinations. Lines that projected outside the magnet aperture and lines that did not point to within 3 centimeters of the target were then rejected. Once a line candidate was found, the other chambers were searched for additional hits in a ± 3 millimeter window. If fewer than four hits were found on the line, it was rejected; otherwise the track segment was fit to minimize the sum of the squares of the residuals divided by the resolution, and the track was kept if the χ^2 per degree of freedom was less than five. If the χ^2 per degree of freedom was greater than ten, the track was rejected. If the χ^2 per degree of freedom was between five and ten, the hit that contributed the most to the χ^2 was dropped from the track and the track refitted. This process was repeated until the χ^2 per degree of freedom was less than five, in which case the track was accepted, or fewer than four hits remained on the track, in which case the track was rejected. Once these track segment candidates were found, the program searched them for duplicate hits. If two tracks shared more than two wires, the track with the fewest hits was rejected. If they had the same number of hits, the track with the highest χ^2 was rejected. At this stage, a typical dimuon trigger had twenty upstream track segments per view.

Once two dimensional tracks had been found in all three views these tracks were combined to make three dimensional tracks. First, tracks in the U-view and V-view were paired to form a 3-d track. Lines that did not project to the magnet aperture and point to the target were rejected. Next, the program searched the *x*-view tracks for a matching track. A match was defined as an *x*-segment with a slope within 10 milliradians of that of the *uv*-line, and with a projection at magnet center to within 5 millimeters of the *uv*-segment. After all the possible matches were made, the pro-

gram took unmatched pairs in two views, formed a 3-d line, and searched for hits in the third view within ±3 millimeters of that 3-d track. If at least two hits were found, they were added to the 3-d track and the track segment was accepted.

Once the hits on a 3-d segment were found, the slopes and intercepts of the front track were fitted via a minimum χ^2 method. A χ^2 per degree of freedom larger than four caused the track to be rejected. If two tracks shared more than three wires, the track with the fewest hits was rejected. If they had the same number of hits, the track with the smallest χ^2 was accepted and the other rejected. Dimuon triggers averaged twelve upstream 3-d tracks.

3. Vertex Position

Once the upstream track segments had been found, the vertex could be calculated, via an algorithm that combined information from the beam tracking (excellent x and y measurement, no z measurement) and the upstream tracks (some z measurement, worse x and y measurement than the beam tracking).

If one beam track was found, the program took the beam x and y coordinates at the z coordinate of the target center to be the vertex x and y. It then stepped through in z, looking at the number of tracks that intersected a ring of radius 3 centimeters. The algorithm looked for the z of highest multiplicity, after which it took all of the tracks in the ring as well as the beam information and did a simultaneous fit (χ^2 minimization) to find the z-coordinate of the vertex, taking x and y coordinates from the extrapolation of the beam track. This method automatically weights the wide-angle tracks heavier, since their projection error at the target is smaller than tracks at smaller angles. (The projection error is inversely proportional to the angle.) The metric for this χ^2 minimization is given by equation (4.1). Here m_x and m_y are the x and y upstream slopes (p_x/p_z and p_y/p_z of each track), the vertex coordinate is given by

$(x_{vert}, y_{vert}, z_{vert})$ and the track projection resolutions in x and y are given by σ_x and σ_y, respectively. n is the number of upstream track segments used in the vertex calculation. In this case, x_{vert} and y_{vert} are fixed and are determined by the beam track.

$$\chi^2 = \sum_{i=1}^{n} \left[\left(\frac{m_x z_{vert} - x_{vert}}{\sigma_x} \right)^2 + \left(\frac{m_y z_{vert} - y_{vert}}{\sigma_y} \right)^2 \right] \tag{4.1}$$

If more than one beam track was found, the above algorithm was used one at a time with each beam track; the beam track that had the most tracks inside the ring was determined to be the one that caused the interaction, provided that it had at least two more tracks than any other candidate. If there were two or more tracks with the same number of tracks or one fewer track than the best candidate, the ring radius was reduced to 2 cm, and the beam track with the most tracks inside the ring was determined to be the correct one. If there was still a tie at this point, the beam track that gave the best χ^2 was judged to be the one that caused the interaction.

If no beam track was found, or if the wrong beam track was found — a beam track that doesn't match the vertex, as defined by there being fewer than two tracks in the ring — the algorithm used only the front track information. A χ^2 minimization using equation (4.1) was again performed, only allowing all three vertex coordinates to vary. After a vertex was found, track segments contributing more than 30 to the χ^2 were removed from consideration, and the vertex refitted. If the vertex was outside the target, or if fewer than two tracks remained to fit the vertex, the vertex was set to the center of the target.

The vertex position was not critically to reconstruction of the J/ψ decay because the momentum was determined from the upstream and downstream slopes only; the vertex never enters into the calculation. Even using the vertex as a constraint in the fitting produces only a modest improvement. Studies showed that most of this improvement was due to requiring the two muons to come from the **same** point — the exact location of this point was less important.

4. Downstream Tracks

In the rear chambers, the 2-d tracking was done in the x-view, in a manner similar to the front chambers. One hit in each chamber was required (making a minimum of three) and the χ^2 per degree of freedom cut was set to ten instead of five. At this level, the average number of rear tracks was 10 per dimuon trigger.

Once the x-projections were found, the program built space tracks out of them by combining them with y-projection information from two u and/or v hits. That is, a (xu) and/or a (xv) pair was converted to two (xy) pairs, and the y-slope was calculated from the two y-coordinates. The additional U and V planes were searched for hits, within a 3 millimeter window on each side around this 3-d line. Once these additional hits had been picked up, a 3-d fit was done on the track, and the track was accepted if there were at least 6 hits (including the 5 seed hits: 3 in x and 2 in u, v) and the χ^2 per degree of freedom was less than 8. Finally, the rear tracks were required to project to the target in y.

5. Matching and Momentum Calculation

For each downstream segment, the program looped over all upstream tracks to find the one that passed closest to it at the matching plane, $z = -4.8$ cm. This distance

was determined empirically to be where the front-rear matching residual was smallest. It is not $z = 0$, because of a field asymmetry in z. There was a mirror plate mounted on the downstream side of the magnet, but not the upstream side. Once the best matching upstream track segment was found, the program checked to see that it passed cuts on the difference in y-slope between the upstream and downstream tracks (the magnet did not significantly bend tracks in the y-plane, especially muons with $p >$ 60 GeV, and averaging 30 GeV, so this difference should be close to zero) and the x and y residuals at the match plane. The specific cuts at each pass are listed in tables (4.1) and (4.2).

In the case where a matching front track was not found, the subroutine TFAGAIN was called to attempt to find an upstream track out of the unused hits in the front chambers. This routine starts from the projection of the rear track at the matching plane, and forms a line to the vertex. It then looks within a cell width at all of the chambers, and tries to fit a 3-d front segment to the hits in this window, using the same requirements for front tracks that were picked up by the standard front tracking algorithm.

If no upstream segment is found, the track is said to be unmatched. A track can be unmatched for several reasons: the upstream segment is in the deadened region of the chambers; the upstream segment is in the live region, but the chambers were inefficient; the track was from a $\pi^{\pm}$ or $K^{\pm}$ that decayed to a $\mu^{\pm}$ in flight, ; finally, the rear segment could be spurious. In events with a J/ψ in them, the average number of downstream segments pointing to lit muon counters is greater than 4, which suggests that a substantial fraction of the downstream segments are not from real tracks. For unmatched tracks, a front pseudo-segment was defined by the line passing through the vertex and the rear segment's intercept with the plane $z = -4.8$ cm.

Once the upstream and downstream segments had been found or inferred, the momentum of a track could be calculated. Suppose there was a track of momentum $\boldsymbol{p}$ and components (p_x, p_y, p_z) upstream. The magnet imparts a kick of p_T in the x-direction, so downstream, the x-component is $p_x + p_T$. The magnet leaves p_y and the magnitude of $\boldsymbol{p}$ unchanged. This means that p_z is given by:

$$p_z = \sqrt{p^2 - p_y{}^2 - (p_x + p_T)^2} \tag{4.2}$$

or

$$p_z = \sqrt{p_x{}^2 + p_z{}^2 - (p_x + p_T)^2} \quad . \tag{4.3}$$

Because p_y is unaffected by the magnet, it is convenient to first consider only the xz-plane. Let p_{xz} be defined as $\sqrt{p^2 - p_y{}^2}$. In this plane, the angle the track makes with the z-direction is given by:

$$sin\theta = \frac{m_x}{\sqrt{1 + m_x{}^2}} \ , \tag{4.4}$$

where m_x is the measured slope in the x-direction. However, m_x is also equal to p_x/p_z. Substituting this in to the above equation we obtain:

$$sin\theta = \frac{p_x/p_z}{\sqrt{1 + (p_x/p_z)^2}} \tag{4.5}$$

or

$$sin\theta = \frac{p_x}{\sqrt{p_z{}^2 + p_x{}^2}} = \frac{p_x}{p_{xz}} \quad , \tag{4.6}$$

The difference in $sin\theta$ between the upstream and downstream segments is:

$$sin\theta_{\text{downstream}} - sin\theta_{\text{upstream}} = \frac{p_x + p_T}{p_{xz}} - \frac{p_x}{p_{xz}} , \tag{4.7}$$

which can be rewritten as:

$$p_{xz} = \frac{p_T}{sin\theta_{\text{downstream}} - sin\theta_{\text{upstream}}} . \tag{4.8}$$

Every term on the right hand side of this equation is known.

From p_{xz}, p_z can be determined, by the relation $p_z = p_{xz}cos\theta$. If $sin\theta$ is given by equation (4.9), $cos\theta$ can be calculated by the identity:

$$cos\theta = \sqrt{1 - sin^2\theta} , \tag{4.9}$$

which, when evaluated, yields:

$$cos\theta = \frac{1}{\sqrt{1 + m_x^2}} . \tag{4.10}$$

So, one can write an expression for calculating p_z in terms of measured angles (or equivalently slopes) and the magnet's p_T kick:

$$p_z = \frac{p_T}{sin\theta_{\text{downstream}} - sin\theta_{\text{upstream}}} \frac{1}{\sqrt{1 + m_x^2}} . \tag{4.11}$$

To get the other momentum components, the relations $p_x = m_x p_z$ and $p_y = m_y p_z$ can be used.

Note that the momentum calculation depends only on the measured slopes, and not on the tracks' relative positions at the matching plane. An attempt to do a global fit by "swimming" the track through the measured field and using a Runge-Kutta fit to **p** was attempted; the results were unsatisfactory. For example, the observed mass of the J/ψ was a strong function of its measured momentum. The exact reason for this failure is not known for certain, however it is possible that it stems from the analysis magnet's field being mapped only in a single quadrant, and symmetry used to extend this to the rest of the magnet. A later field map of the same magnet (although the magnet had been modified) for experiment E-771 has measurements of all four quadrants and shows some asymmetries in the field, and even the E-705 map shows some indications of this asymmetry. For instance, the B_x component at $x = 0$ is not 0. The two quadrant requirement in the fast dimuon trigger assures that at least part of at least one of the muon trajectories passes through an unmapped region. The box field or p_T kick approximation gave the best results, so it was the one used.

B. Pass One

The first pass analysis was always intended to be a starting point with relatively loose cuts. Speed of analysis was given a higher priority than completeness, as there was to be a second pass, which would spend more time on each event. Accordingly, only muons were tracked in this pass.

1. Filter Program

Because even the muon tracking was time-intensive, a filter was written to pre-analyze the dimuon triggers. In this respect, the filter program was the software ana-

logue to the hardware trigger processor. Indeed, the algorithm was similar, however, the filter program also incorporated the drift time information which was unavailable to the trigger processor. This allowed the filter to reject spurious tracks that would have been passed by the trigger processor, as well as to have somewhat better mass resolution, as shown in figure 4.3.

Like the trigger processor, the filter looked at downstream hits to determine the dimuon mass. The program started with the chambers DC4 and DC6, defining a hit as the average x of a hit in the X plane combined with its partner in the X' plane. If one plane was inefficient, the x hit was defined as the central wire position in whichever plane was efficient. A line was formed between these two points, and if a hit was found in DC5 within a window defined by the lines formed by the DC4 and DC6 cell edges, the 2-d track was accepted. At this stage, an average of 75 track candidates per event were found.

The filter then rejected tracks that did not pass geometric cuts: tracks that did not pass inside the magnet aperture were rejected, as were tracks that had an x-slope of greater than 300 milliradians, which was the maximum slope that a track could have and still intercept the muon wall. These cuts rejected approximately 17% of the track candidates. Remaining tracks were required to point within 39 cm of a lit MU1 counter. This window of 39 cm was determined by combining the track projection error of 3.8 cm with the effect of multiple scattering on a 6 GeV muon through the absorber in front of MU1, given by[41]:

$$\theta_0 = \frac{13.6\ \text{MeV}}{\beta c p}\sqrt{x/X_0}\,[1 + 0.2 \ln (x/X_0)] \qquad (4.12)$$

and

$$y = \frac{\theta_0}{\sqrt{3}} \tag{4.13}$$

where y is the 1σ displacement transverse to the original trajectory, βc is the velocity of the particle, p its momentum, and x/X_0 is the thickness of the absorber in measured in radiation lengths. For our absorber, y is approximately 13 centimeters, so the 39 centimeter cut corresponds to three standard deviations. 6 GeV was chosen because at this point, we have no momentum information, and 6 GeV is the energy that would be lost by a minimum ionizing particle penetrating the muon wall; muons with momentum less than 6 GeV would be absorbed and therefore could not cause a triple coincidence. Furthermore, since the multiple scattering varies inversely with the momentum, 6 GeV represents the maximum possible multiple scattering. The muon cut rejected 60% of the track candidates, leaving an average of 25 per event.

At this point, the TDC information from the drift chambers was used to increase the accuracy of the track position, and therefore ultimately the momentum. For each hit, two entries were made in the hit bank, corresponding to the particle being on the left side or the right side of the wire. Next, to resolve the left-right ambiguity, two hits from DC4 and DC6 were selected and used to define a line, which was then searched along a ± 6 mm window for additional hits in the remaining planes. These combinations were then fit, and tracks with a χ^2 per degree of freedom less than 10 were kept. Of these, the combination with the most hits was selected. If two combinations had the same number of hits, the one with the best χ^2 per degree of freedom was selected.

Once the rear segments had been found, upstream pseudo-tracks were created by the line determined by the vertex and the projection of the rear track at the center

of the magnet ($z = 0$). (The difference between the physical center and the field center is small because the filter program's cuts are quite loose.) The vertex position was estimated by one of two techniques: if there was one beam track, the x and y position of the vertex was the x and y projection of the beam track at the target center, and the z coordinate was taken as the z of the target center. If there were no beam tracks, or more than one beam track, the vertex was taken to be the center of the target.

At this point, the approximate momentum of the muon can be calculated, by the following formula:

$$p \approx p_{xz} = \frac{p_T \,\mathrm{kick}}{m_{x\mathrm{upstream}} - m_{x\mathrm{downstream}}} \quad . \tag{4.14}$$

Here the m's are the slopes of the segments in the x-z plane. This formula neglects the y-component of momentum, and so introduces an error of

$$\frac{\Delta p}{p} = 1 - \cos(\theta_y) \tag{4.15}$$

into the momentum measurement. However, the largest θ_y could be in our spectrometer was approximately 100 mR, corresponding to a maximum underestimation of 0.6%. Furthermore, since the average θ_y for muons from J/ψ decays was 33 mR, the typical underestimation from ignoring the y-component of momentum was 0.055%.

The uncertainty on $p_{x\text{-}z}$ is given by

$$\frac{\Delta p_{x\text{-}z}}{p^2} = \frac{\sqrt{\Delta m_{\text{front}}{}^2 - \Delta m_{\text{rear}}{}^2}}{p_T \,\text{kick}} \tag{4.16}$$

where again, the m's are the upstream and downstream slopes. The uncertainties on the downstream slope comes from the track fitting, and the uncertainty on the upstream slope is the quadrature sum of the track projection error with the vertex error from not calculating the z coordinate of the vertex. If the beam track information was used, the fractional momentum uncertainty was $0.0011p$ and if the beam track information was not used, it was $0.0066p$. Once the momentum of each muon had been calculated, muons with $p < 5.5$ GeV/c were rejected.

Next, the multiple scattering cut was re-evaluated, using the measured muon momentum, rather than 6 GeV/c. Since the error between the track position and the MU1 counter is dominated by multiple scattering, especially now that the TDC information is used and drift position is taken into account, the extrapolated track projection minus MU1 position cut was set to $3\sigma(p)$. $\sigma(p)$ was obtained via a Monte Carlo based on equation (4.12). At this stage, an average of 10 tracks remained.

At this point, the dimuon mass could be calculated. 65% of the events at this stage had at least one pair of opposite signed muons passing cuts, and the filter calculated the mass of all possible pair calculations, using the following formula:

$$m = \sqrt{2m_\mu{}^2 + 2E_+E_- - 2p_{xz+}p_{xz-}\cos(\theta_{\text{opening}})} \tag{4.17}$$

where the opening angle θ was calculated using the MUY counters that resulted in the largest opening angle, and hence the largest mass. If no counter was lit for a particular muon, the filter used the counter farthest from the beam axis. Figure 4.3 shows the filter mass resolution for Monte Carlo J/ψs and figure 4.4 shows the calculated mass distribution from the filter for actual dimuon triggers. The filter was twenty times faster than the full first pass program, and had an efficiency of 98.2%.[42]

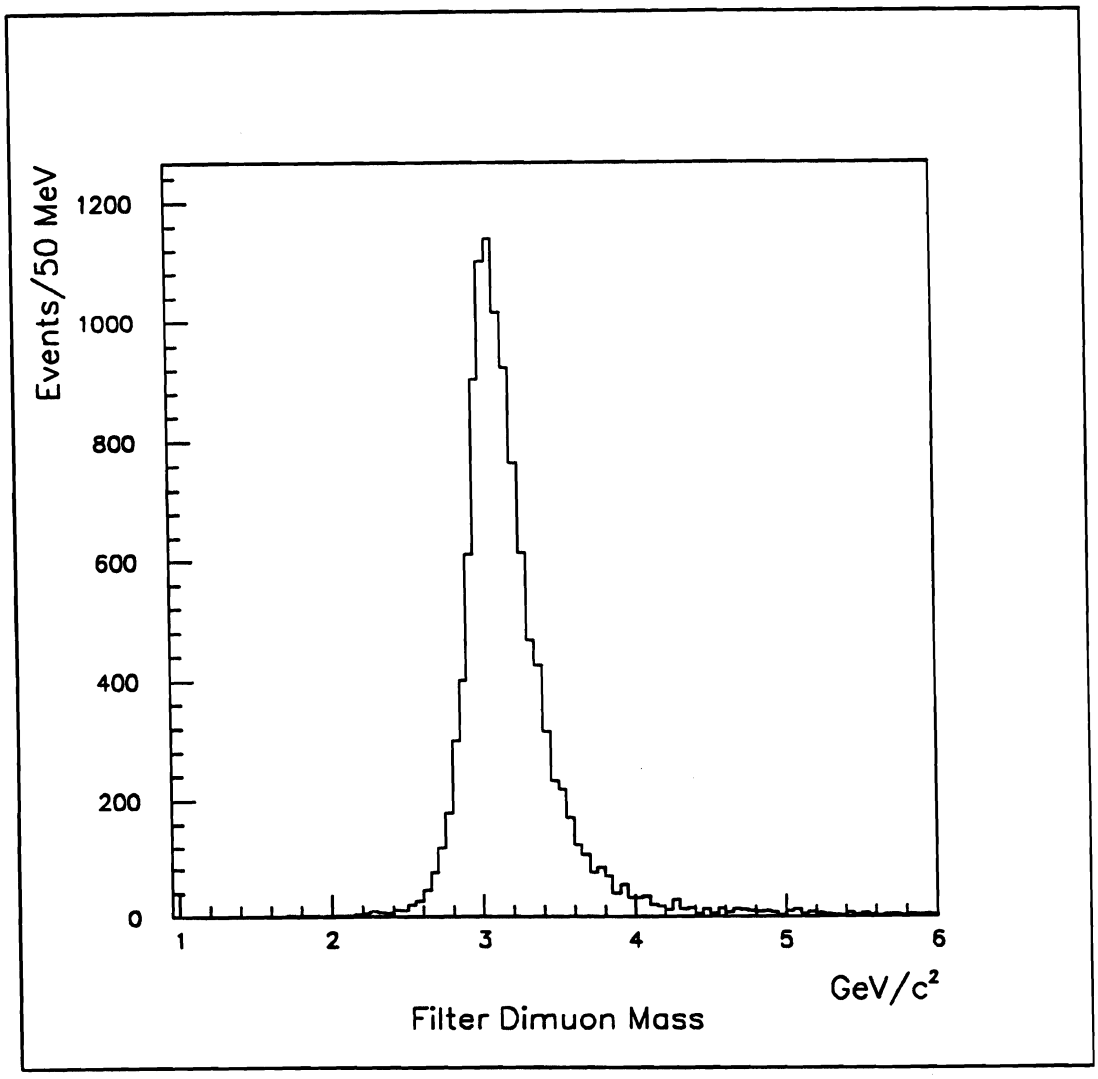

Figure 4.3 Filter reconstructed mass for Monte Carlo J/ψs

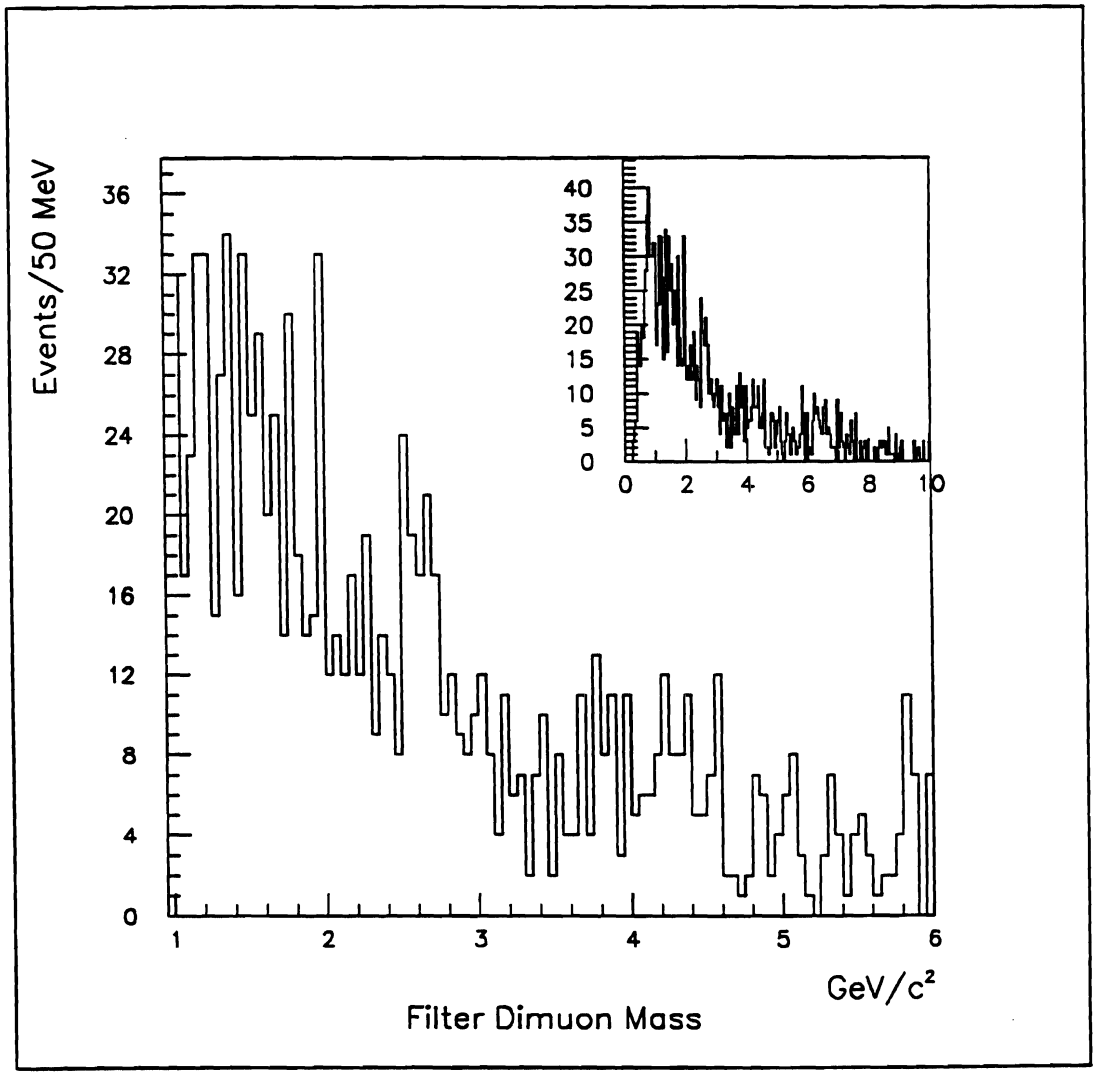

Figure 4.4 Filter reconstructed mass for data dimuon triggers

2. Dimuon Tracking

All events passing the filter had their muons tracked as described in Section A. The program required that the downstream segments point towards a lit muon triple coincidence; therefore only the muons in the event were tracked. The intent of this

was to keep the first pass as fast as possible, since the other particles could be tracked in the second pass.

The track cuts used in the first pass are listed in table 4.1. There are no CPX and CPY cuts on the muon tracks, which would further reduce background by eliminating out of time tracks and combinatoric background. These cuts improve the signal-to-noise ratio only marginally at the expense of approximately 20% of signal, probably because of the effectiveness of the muon counters: they already remove out of time tracks and combinatoric background, so adding an additional requirement to track acceptance doesn't help much..

The vertex was calculated, using a slightly different algorithm than described in Section A, but this vertex was never used in any analysis.

3. ACP

The first pass tracking on the dimuon triggers was done on the Fermilab Advanced Computer Project parallel processor farms.[43] The ACP-I systems each had typically fifty to a hundred Motorola 68020 microprocessors and 2 or 8 megabytes of memory per processor, all connected to a Digital Equipment Corporation MicroVAX, which handled the input/output and control functions. The MicroVAX would read an event from tape, and give it to any node that was free for analysis. After tracking, if the event passed cuts, the ACP node handed it back to the MicroVAX, which then wrote it to an output tape.

Table 4.1

First Pass Cuts

Item	Cut
Δy-slope(front-rear)	< 30 mR
Δx(front-rear) at magnet match plane	6 cm
Δy(front-rear) at magnet match plane	2 cm
Track-counter edge residuals: μ-Y	12.5 cm
μ-1	8.8 cm
μ-2	10.6 cm
μ-3	13.6 cm
Minimum Mass	2.5 GeV/c^2

C. Pass Two

The second pass was run on the Fermilab VAX cluster, using the Pass One output tapes as input, and writing out the dimuon data summary tapes as output. There were three primary objectives of this program:

- Tighter cuts on the muons
- Tracking of every particle in events passing the cuts
- Fitting of the J/ψ mass using vertex information.

These tighter cuts were intended to maximize the J/ψ signal-to-background ratio, but remove as few real J/ψ's as possible, and are listed in table (4.2) on the following page.

Table 4.2
Second Pass Cuts

Item	Cut (muons)	Cut (non-muons)
Δy-slope(front-rear)	< 15 mR	< 20 mR
Δx(front-rear) at magnet match plane	< 1 cm	< 1 cm
Δy(front-rear) at magnet match plane	< 4 cm	< 4 cm
Track-counter edge residuals: μ-Y	< 12.5 cm	—
μ-1	< 8.8 cm	—
μ-2	< 10.6 cm	—
μ-3	< 13.6 cm	—
Minimum Mass	2.6 GeV/c^2	—
Track-counter edge residuals: CPX	—	< 1 cm
Hits on rear track	> 6	> 6
Rear track $\chi 2$	< 8	< 8

First, the program unpacked the first pass tracking bank and then checked to see if there was a pair of muons that satisfied the tighter cuts. If so, it then calculated the vertex. Next, it recalculated the dimuon mass incorporating the vertex information. First, a set of refitted slopes was calculated,

$$m_x^{\text{refit}} = \frac{\dfrac{(x_{vertex} - x_0) z_{vertex}}{\sigma_{x_0}^2} + \dfrac{m_x}{\sigma_{m_x}^2}}{\dfrac{z_{vertex}^2}{\sigma_{x_0}^2} + \dfrac{1}{\sigma_{m_x}^2}} \tag{4.18}$$

$$m_y^{\text{refit}} = \frac{\dfrac{(y_{vertex} - y_0) z_{vertex}}{\sigma_{y_0}^2} + \dfrac{m_y}{\sigma_{m_y}^2}}{\dfrac{z_{vertex}^2}{\sigma_{y_0}^2} + \dfrac{1}{\sigma_{m_y}^2}} \tag{4.19}$$

and also the set of intercepts,

$$x_0^{\text{refit}} = x_{vertex} - m_x^{\text{refit}} z_{vertex} \tag{4.20}$$

$$y_0^{\text{refit}} = y_{vertex} - m_y^{\text{refit}} z_{vertex}. \tag{4.21}$$

The momenta and the mass were then calculated using equations (4.14) and (4.17). If the fit was successful, and the mass was between 2.88 and 3.24 GeV, the two muon momenta were rescaled so that their invariant mass would be the same as the J/ψ, 3.097 GeV. This rescaled mass and momentum could then be used in making mass combinations of particles with a ψ in the final state, such as $\chi \rightarrow \psi\gamma$ and $\psi' \rightarrow \psi\pi\pi$. Finally, if the fitted mass was greater than 2.6 GeV, the event was accepted, and tracked without requiring the tracks to project to a lit triple coincidence. This allowed particles other than muons, such as pions and electrons, to be tracked, so that topics like $\psi N\pi$ resonances and measuring calorimeter resolution by plotting the ratio E/p for electrons could be studied. For these tracks, the CPX requirement was included, to reject out of time hits and false combinations. At this point, the event as written has three tracking banks: one with only muons tracked, one with all tracks tracked, and a small one with the scaled J/ψ momentum.

D. Post Pass Two

After the second pass, there was a final momentum rescaling, to lock the centroid of the observed J/ψ mass peak at the accepted value of 3096.93 GeV.[44] Without this final correction, the J/ψ mass is observed to be 3088.3 ± 2.0 GeV, so the rescaling is less than 3 parts per thousand: within our ability to monitor the current through the analysis magnet. This method uses the well known J/ψ mass to set the momentum scale.

An attempt was made to replace the simple p_T kick by a p_T kick that varied according to the actual trajectory of the particle through the magnet aperture. The program stepped the track along the projection of the upstream segments in 5 cm increments, until the particle reached the half-field point, -4.8 cm. Then the program stepped along the downstream projection until the particle left the magnet. At each point, $B_y\Delta z$ - $B_z\Delta y$ was calculated from the field map, and summed at the end to determine the p_T kick. However, this method degraded the resolution by 6 ± 3%, so it was not used. The exact reason for this degradation is not known for certain, however it is possible that it stems from the analysis magnet's field being mapped only in a single quadrant, and symmetry used to extend this to the rest of the magnet. The E-771 field map of all four quadrants shows some asymmetries in the field. Because modifications were made to the magnet between E-705 and E-771, it is not clear how to extend this new information about the magnetic field back to E-705 data.

Chapter 5: J/ψ Production

A. Monte Carlo

The experimental determination of a production cross-section proceeds by the determination of the acceptance and efficiency of the spectrometer. Measurements of each individual detectors' efficiencies have to be combined with the geometry of the detector to obtain a reconstruction probability, both as a function of kinematic variables and overall. Rather than compute these functions algebraically, we used a Monte Carlo technique to calculate them numerically: a computer program generated simulations of J/ψs and used measured efficiencies and known chamber, counter and magnet geometries to calculate the spectrometer's response. Slightly fewer than one and one-half million Monte Carlo J/ψs were generated.

The Monte Carlo program ran in two steps: the first generated a J/ψ (or ψ') and propagated it through the spectrometer, and the second overlaid it on a data event, so that the effect of additional chamber and counter hits on the pattern recognition would be taken into account. The overlap program then tracked the event and wrote it out in the same format as the output of the second pass. The same program that analyzes data files can then be used to analyze files of Monte Carlo events.

The generation program first picked a random x_F and p_T, according to the input differential distributions. The initial input distributions were those obtained by NA3[45] and E-537[46]. Next, the acceptances are calculated, and these are used to calculate a new set of distributions based on the data. These distributions were then used as the input distributions, and the process iterated until the distributions converged. Convergence was defined by a change of less than one half a standard deviation in

kinematic parameters from one iteration to the next. The program generated a J/ψ with a random x_F and p_T from the above distributions, as well as a random ϕ from a flat distribution. This J/ψ was then decayed according to an input angular distribution, which was chosen to be flat in θ, the angle that the positive muon makes with the beam direction in the rest frame of the J/ψ (The *s*-channel helicity axis). The muon tracks were then propagated from the vertex through the spectrometer. The vertex was read from the same event that would later be overlaid on the J/ψ, so that the two muons would be coming from the same point as the other tracks in the event. At each chamber or CPH counter, a determination was made if the detector was efficient or not, using the efficiency measurements from the data. Only if the device was determined to be efficient was a hit recorded in the output file.

At this stage, the muon counters were treated as if they were 100% efficient; later the calculated efficiency would be multiplied by the overall muon counter efficiency ε_μ:

$$\varepsilon_\mu = \left[\varepsilon_{\mathrm{MUY}} \prod_{i=1}^{3} \varepsilon_{\mathrm{MU}i} \right]^2 \tag{5.1}$$

where the individual muon plane efficiencies are denoted by ε's and the square is because there are two muons per J/ψ decay. The reason for departing from a pure Monte Carlo approach in favor of this hybrid Monte Carlo-analytic technique is because the muon counter efficiencies were measured per plane, not per counter. The muon counter efficiency is therefore independent of anything upstream, so we can factor it out. The advantage to this method is that the convergence is faster, or alter-

natively, more accurate for the same number of generated events. Each era used the measurement of muon counter efficiencies taken in that era.

After the J/ψ had been reduced to a collection of hits, the Monte Carlo event was overlaid on a real data event by the second program. This data event was usually selected from dimuon triggers that did not have a J/ψ in them, but for special test runs other events were used: CFSTROBE triggers and even completely empty events, to determine if there was a strong dependence in the efficiency as a function of the underlying event. The entire set of muon counters in the data was reset; so that only the muon counters lit in the Monte Carlo were used. No attempt was made to remove the original muon hits from the wire chambers. If reconstructed, the tracks from the original muons would therefore be identified by the reconstruction algorithm as pions. If the J/ψ happened to share a lit muon counter with the overlaid event, that event was not used, and a counter was set and the normalization took this into account. This happened approximately 16% of the time.

Part of the overlap program was a software simulation of the hardware dimuon trigger processor. Only the events that generated a fast dimuon trigger and a trigger processor YES were processed by the remainder of the reconstruction program. This simulation was at the logic unit level: each module was represented by a software subroutine that emulated it.

The mass spectrum from the Monte Carlo (pion induced) is shown in Figure 5.1. A fit to the function

$$\frac{1}{1 + z^2 - 0.05236z^3 + 0.01475z^4} \tag{5.2}$$

where $z = (m - m_\psi)/\Gamma$, is superimposed. This functional form was chosen on an empirical basis, because it provided a good fit ($\chi^2/\nu = 1.501$ for 95 degrees of freedom) with only a few free parameters. The general function of the form $1/(1 + z^2 + \alpha z^3 + \beta z^4)$ does not always have a finite second moment, so the standard deviation is not always defined. However, a full width at half maximum Γ always exists, and for a Gaussian distribution $\Gamma = 2.36\sigma$. We therefore define an extended standard deviation σ to be $\Gamma/2.36$. Under this convention, the Monte Carlo indicates $\sigma = 44.1$ MeV for π induced J/ψ's.

For proton beam, the shape of the J/ψ is given by

$$\frac{1}{1 + z^2 - 0.049931z^3 + 0.01629z^4} \tag{5.3}$$

with $\sigma = 39.5$ MeV ($\chi^2/\nu = 1.186$ for 95 degrees of freedom) and is shown in figure 5.2.

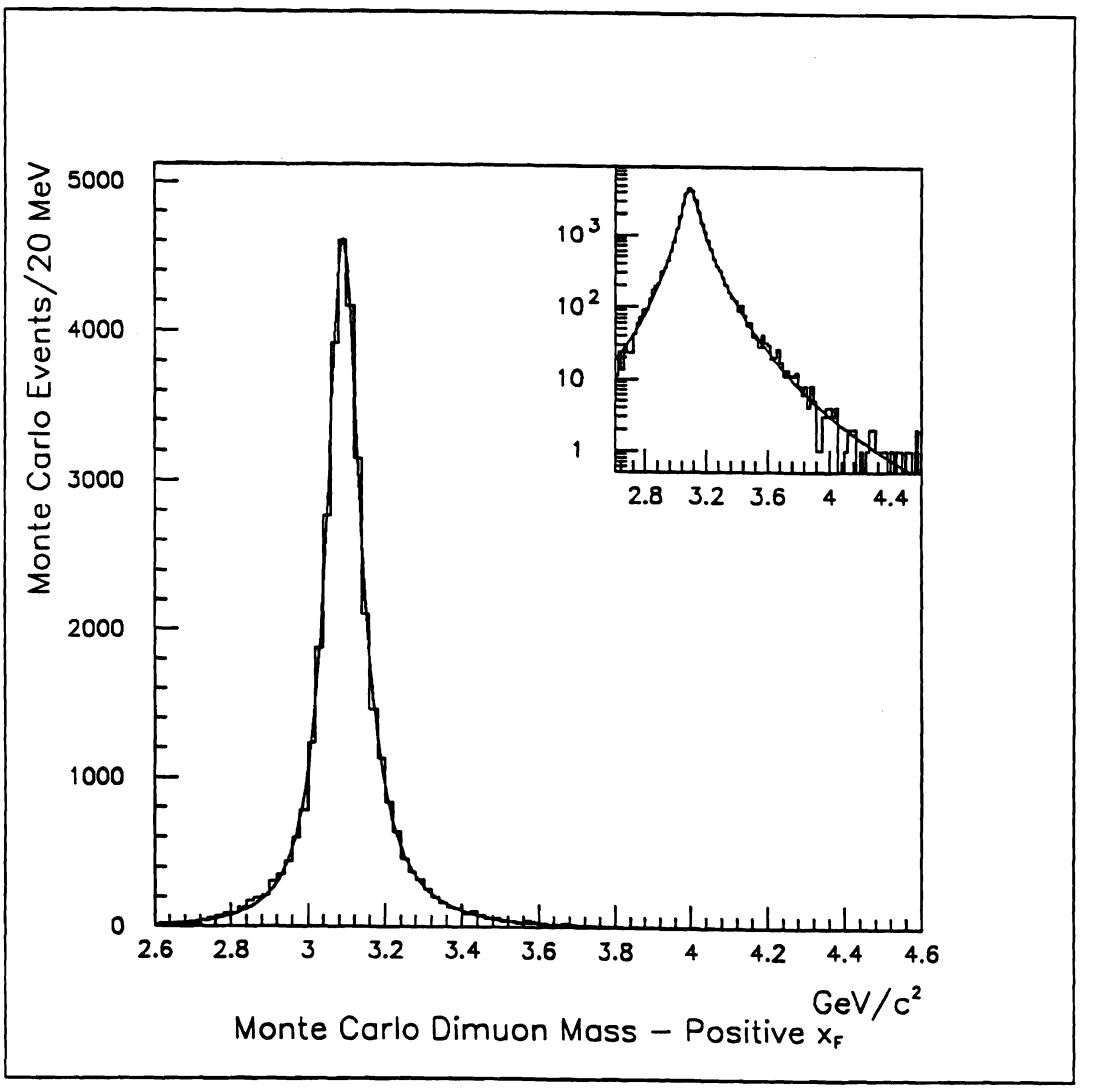

Figure 5.1 Monte Carlo J/ψ mass spectrum (pion beam)

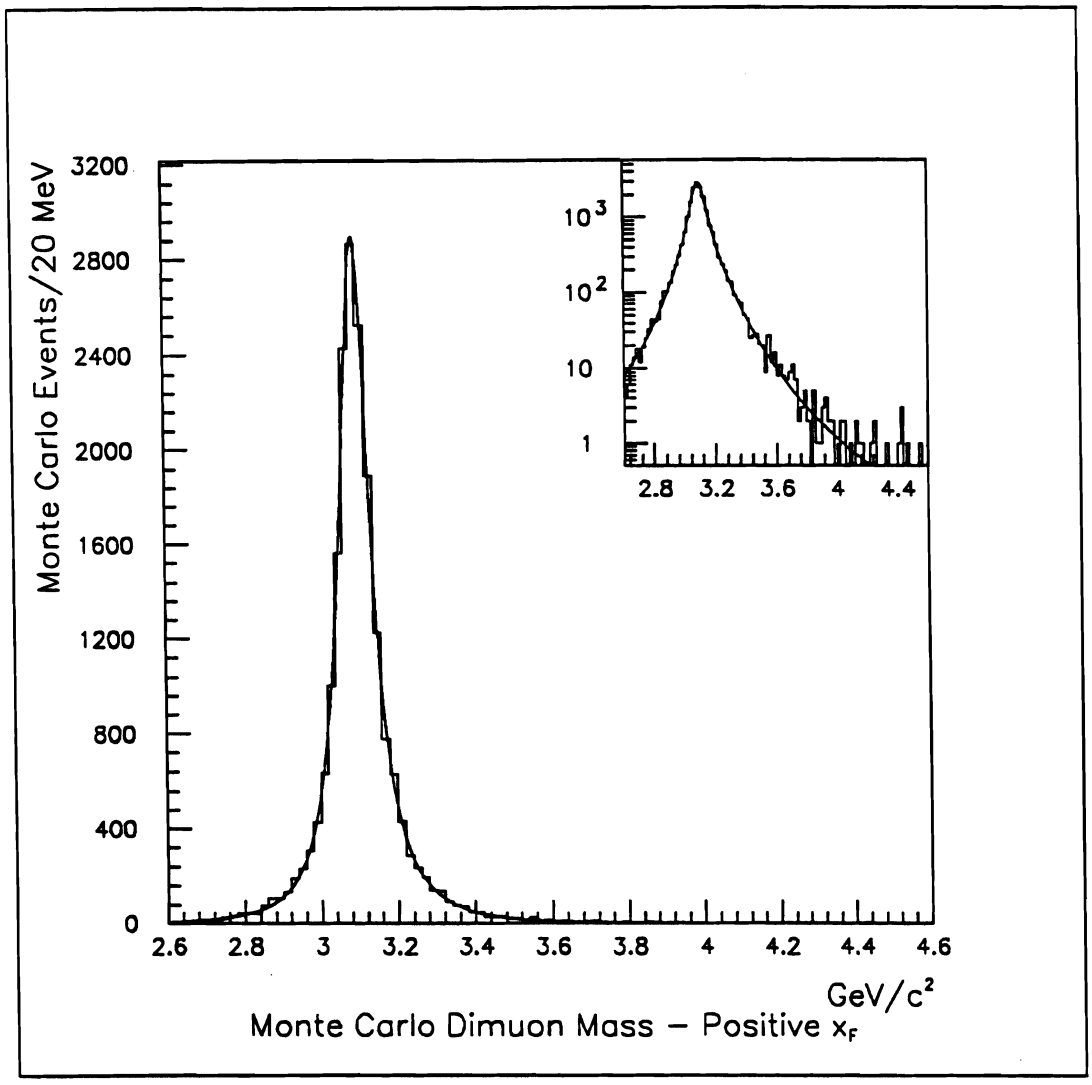

Figure 5.2 Monte Carlo J/ψ mass spectrum (proton beam)

For antiproton beam the shape is fit by

$$\frac{1}{1 + z^2 - 0.065529z^3 + 0.01833z^4} \tag{5.4}$$

with σ = 39.8 MeV (χ^2/ν = 1.046 for 95 degrees of freedom). Figure 5.3 shows the dimuon mass spectrum for J/ψs produced by antiprotons.

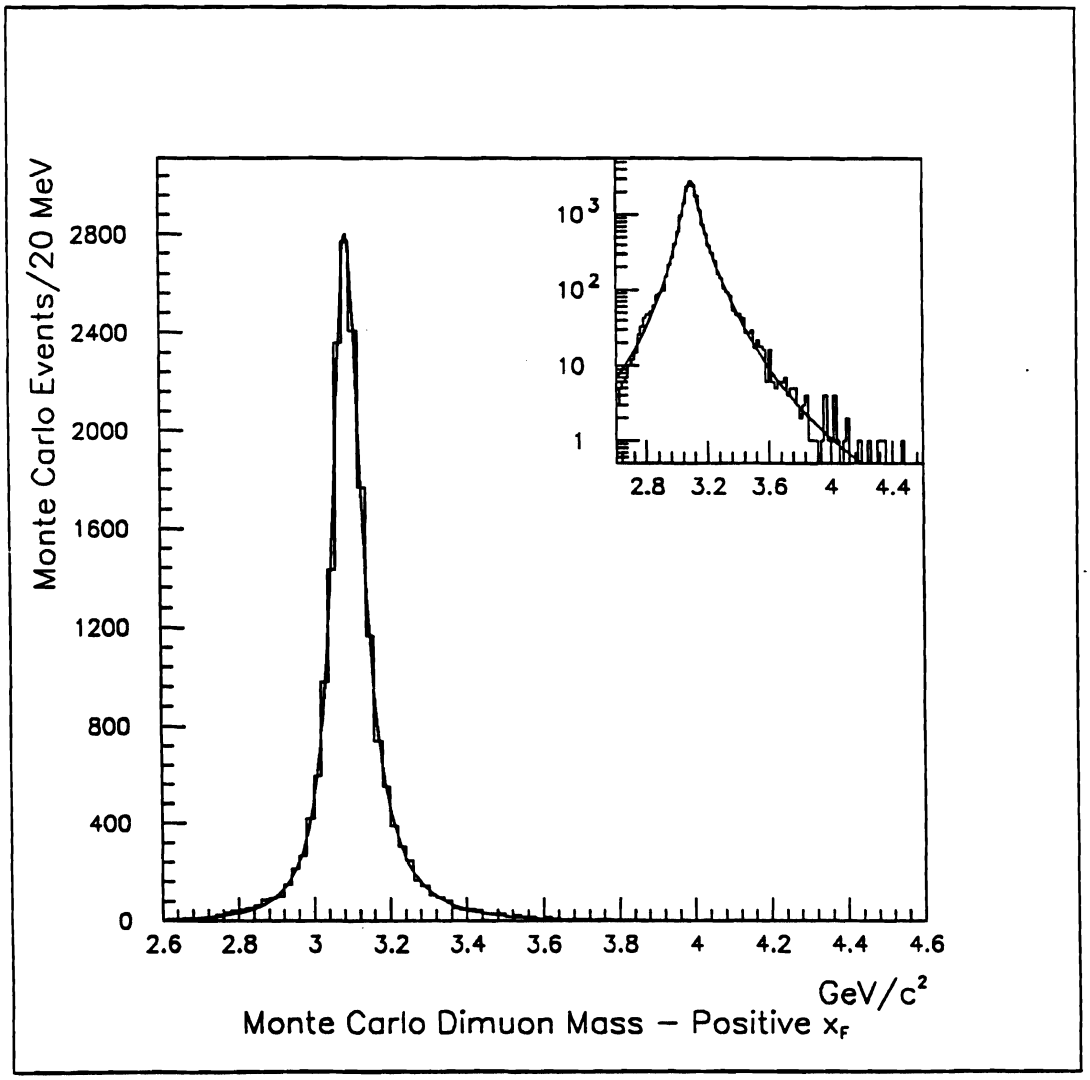

Figure 5.3 Monte Carlo J/ψ mass spectrum (antiproton beam)

The acceptance times efficiency as a function of Feynman x, $\varepsilon_A(x_F)$ was calculated as:

$$\varepsilon_A(x_F) = \frac{(d\sigma/dx_F)\ \text{reconstructed}}{(d\sigma/dx_F)\ \text{generated}} \quad . \tag{5.5}$$

This was fit to a function of the form

$$e^{-z^2/2 + \gamma z^3 + \delta z^4} \tag{5.6}$$

where

$$z = \frac{x_F - \alpha}{\beta}. \tag{5.7}$$

This is similar to a Gaussian distribution, although this distribution is slightly skewed towards large x and is somewhat leptokurtic. The skewness can be understood in terms of geometry: the low x limit of our detector is determined by the muon steel absorption and the p_T kick of the magnet sweeping soft muons out of the spectrometer; the large x limit is due to the deadened central regions in the chambers. This is a more gradual loss of acceptance; hence the acceptance distribution is skewed towards large x. Furthermore, track reconstruction is more difficult in the more densely populated central region of the chambers, so the efficiency also decreases gradually at large x. This also contributes to the skewness. Again, this function was chosen so that there would not be many parameters. These fit parameters are shown in table 5.1 on the following page:

Table 5.1

Feynman x Acceptance Fit Parameters

	pion beam	proton beam	antiproton beam
α	0.15423	0.14905	0.14749
β	0.11865	0.11950	0.12045
γ	0.11432	0.12045	0.15051
δ	-0.013056	–0.11412	– 0.020301
mean	0.196	0.202	0.204
standard deviation	0.132	0.145	0.140
skewness	0.57	0.78	0.60
kurtosis	3.35	3.85	3.19

For transverse momentum, the corresponding quantity $\varepsilon_A(p_T)$ was calculated as:

$$\varepsilon_A(p_T) = \frac{(d\sigma/dp_T)\ \text{reconstructed}}{(d\sigma/dp_T)\ \text{generated}}. \tag{5.8}$$

This was fit to a second degree polynomial

$$1 + \alpha\, p_T + \beta p_T^2, \tag{5.9}$$

and the fit parameters are shown in the following table.

Table 5.2

Transverse Momentum Acceptance Fit Parameters

	pion beam	proton beam	antiproton beam
α	– 0.232	– 0.304	– 0.355
β	0.117	0.123	0.083

This method of calculating acceptance automatically includes the x_F or p_T resolution error, which appears as either an additional inefficiency or hyperefficiency, depending

on the kinematic distribution. Hyperefficiencies tend to occur in regions of very low efficiency or acceptance, when a mismeasurement of an event that should be in a more populated bin moves it into a less populated bin. This is related to the well-known statistical phenomenon of regression to the mean.

Apart from this effect due to resolution, the differential acceptance times efficiency should be independent of beam type. That is, the acceptance is a function of each muon's momentum **p**, which is completely constrained by the kinematic variables x_F, p_T, ϕ, and θ for the J/ψ. Once these four variables are given, the acceptance and efficiencies are determined. So, once an entry in a bin of x_F and p_T is made (the ϕ and θ distributions being flat — for both beam types) it doesn't make any difference if the entry was from a proton-induced or pion-induced event. Furthermore, since the efficiency times acceptance is quite flat in transverse momentum, the effect of second order terms like $\partial^2\varepsilon_A/\partial x_F \partial p_T$ is small. An estimate of the systematic error of the efficiency times acceptance measurement can therefore be obtained by comparing the differential acceptances from proton beam and pion beam. Because of resolution effects this is an overly conservative measurement, however, this overestimation of the true systematic errors is concentrated in regions of low acceptance where there are very few events, and the statistical errors dominate.

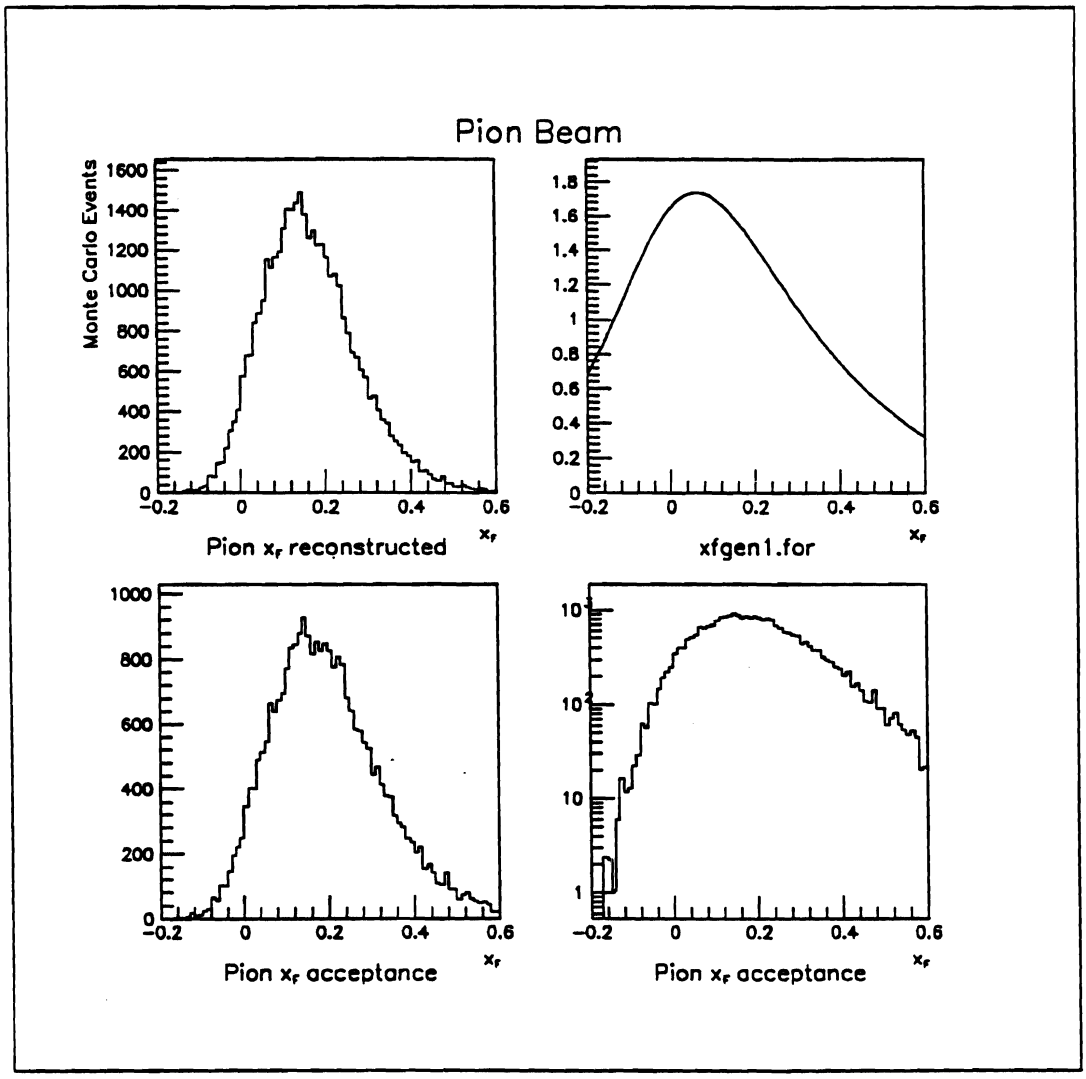

Figure 5.4 Monte Carlo Feynman x distribution (π beam). Upper left: Distribution of reconstructed J/ψ's. Upper right: Distribution of generated J/ψ's. Lower left: Acceptance (linear scale, arbitrary units). Lower right: Acceptance (logarithmic scale, arbitrary units).

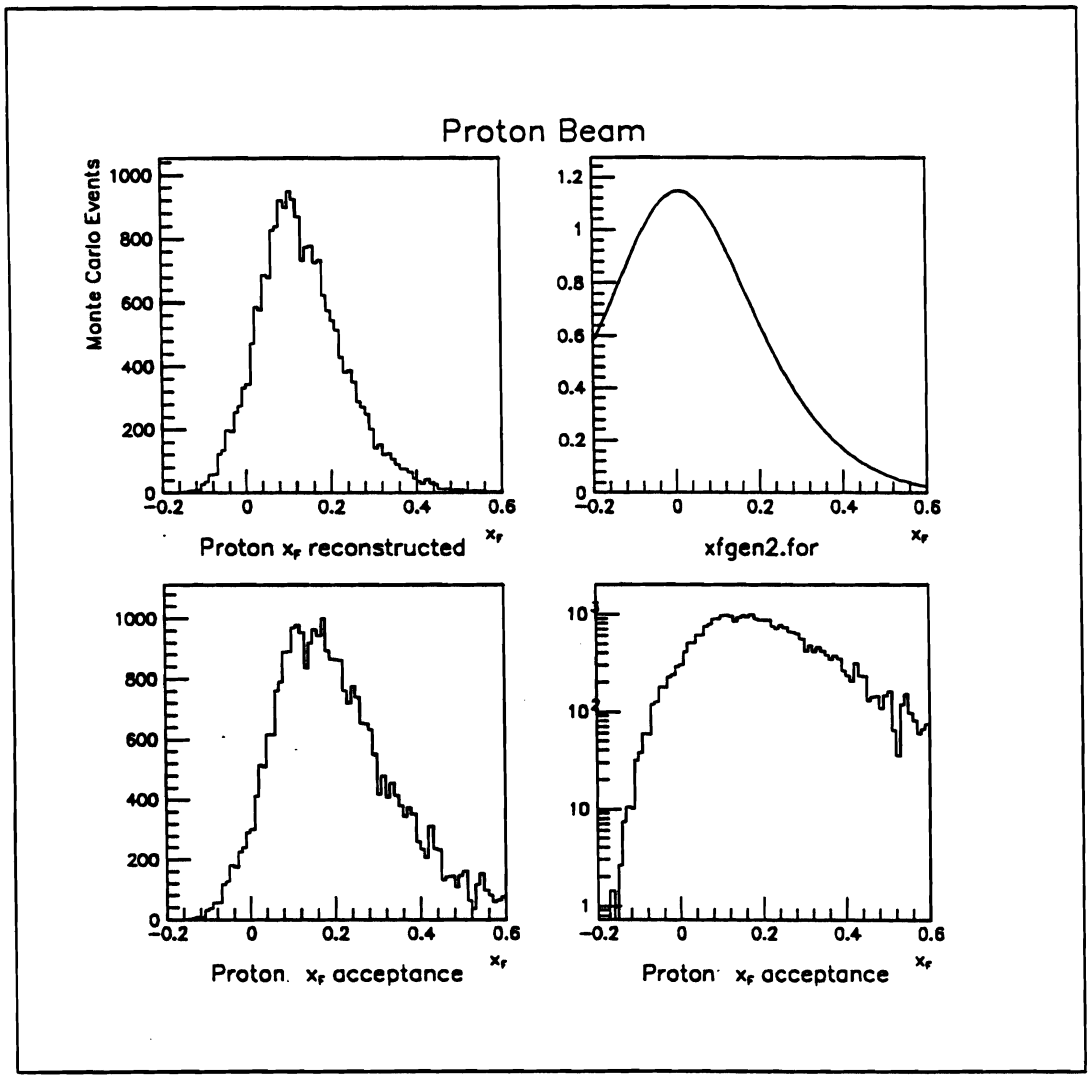

Figure 5.5 Monte Carlo Feynman x distribution (p beam). Upper left: Distribution of reconstructed J/ψ's. Upper right: Distribution of generated J/ψ's. Lower left: Acceptance (linear scale, arbitrary units). Lower right: Acceptance (logarithmic scale, arbitrary units).

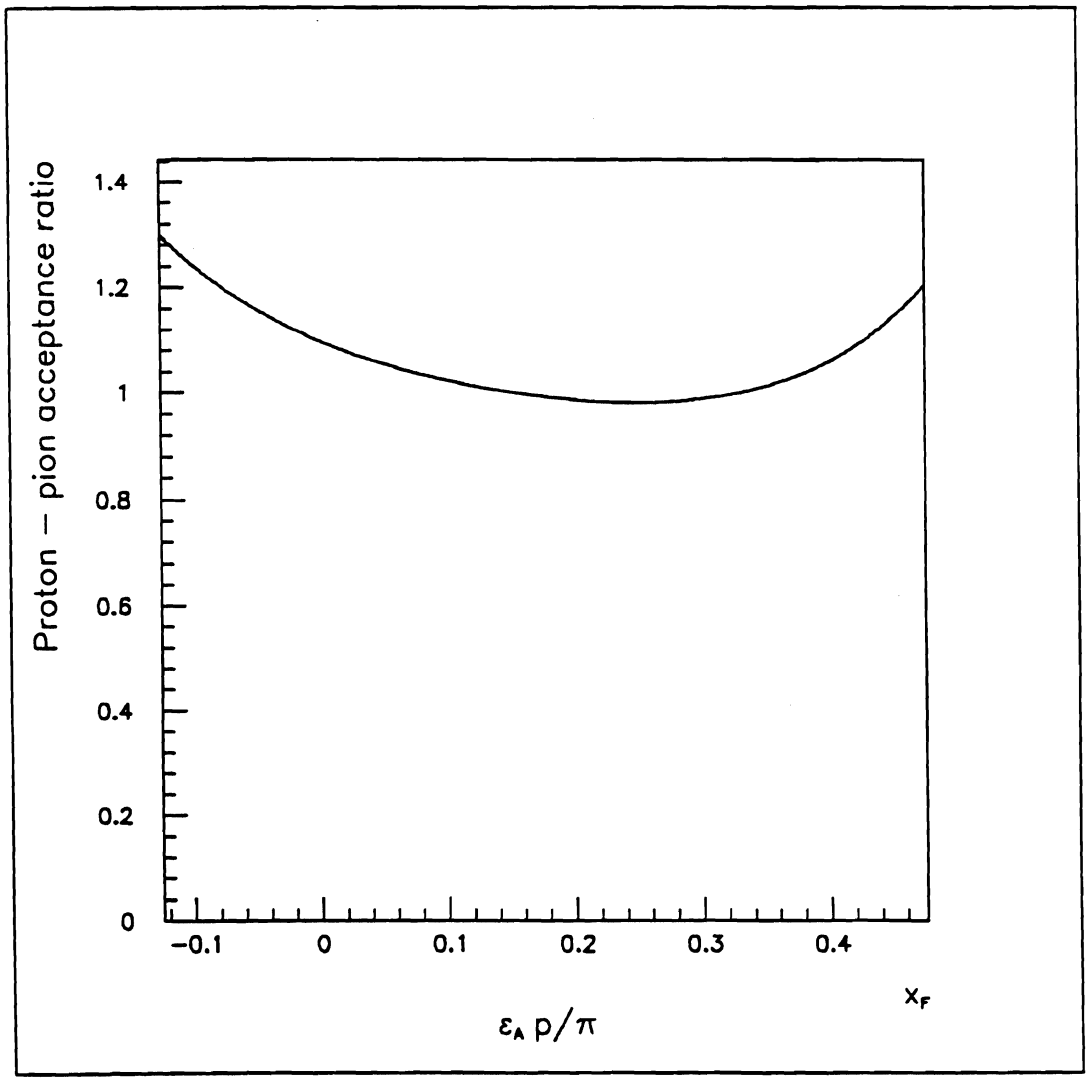

Figure 5.6 Acceptance vs. Feynman *x*: proton beam to π beam ratio (Monte Carlo).

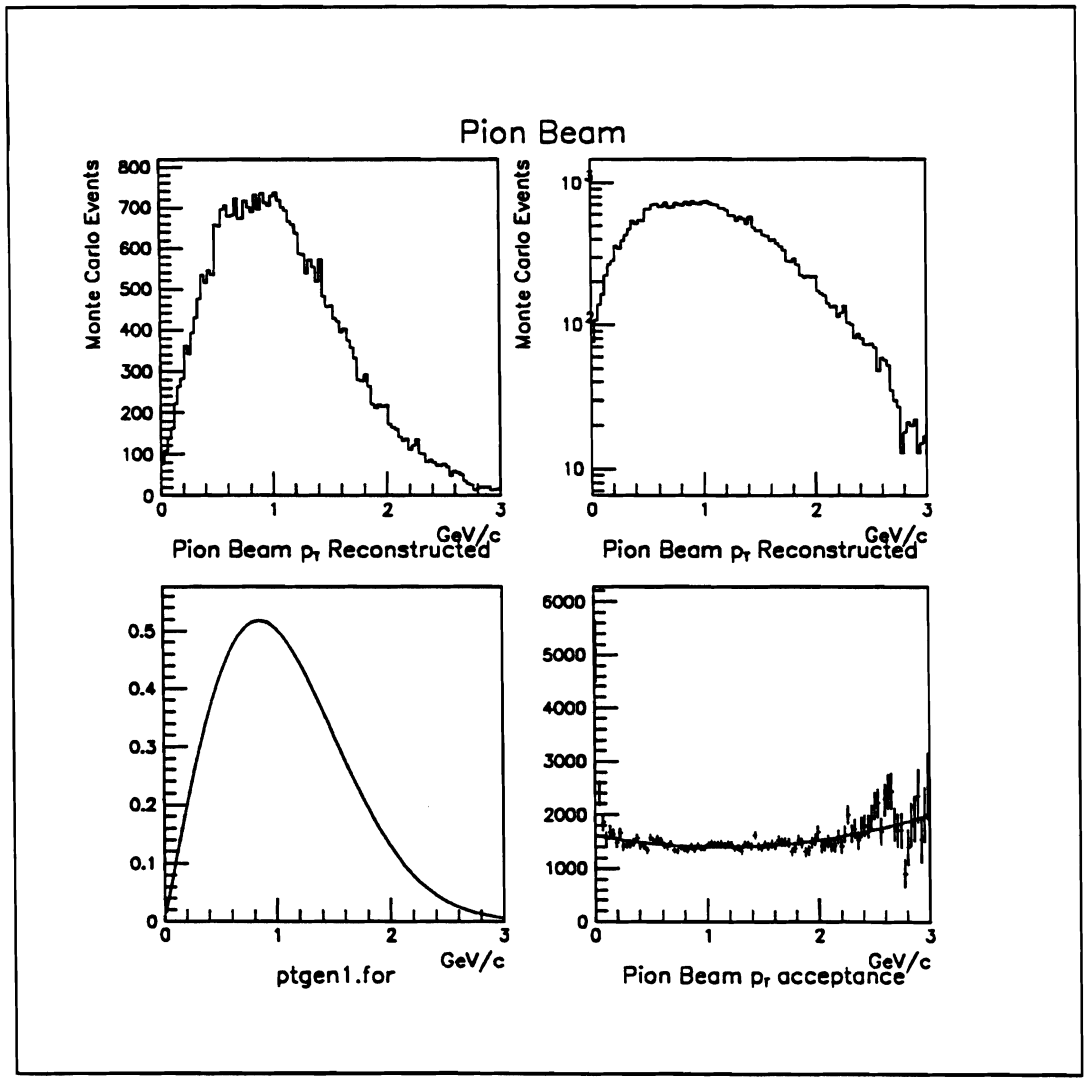

Figure 5.7 Monte Carlo transverse momentum distribution (π beam). Upper left: Distribution of reconstructed J/ψ's (linear scale). Upper right: Distribution of reconstructed J/ψ's (logarithmic scale). Lower left: Distribution of generated J/ψ's. Lower right: Relative acceptance (arbitrary units).

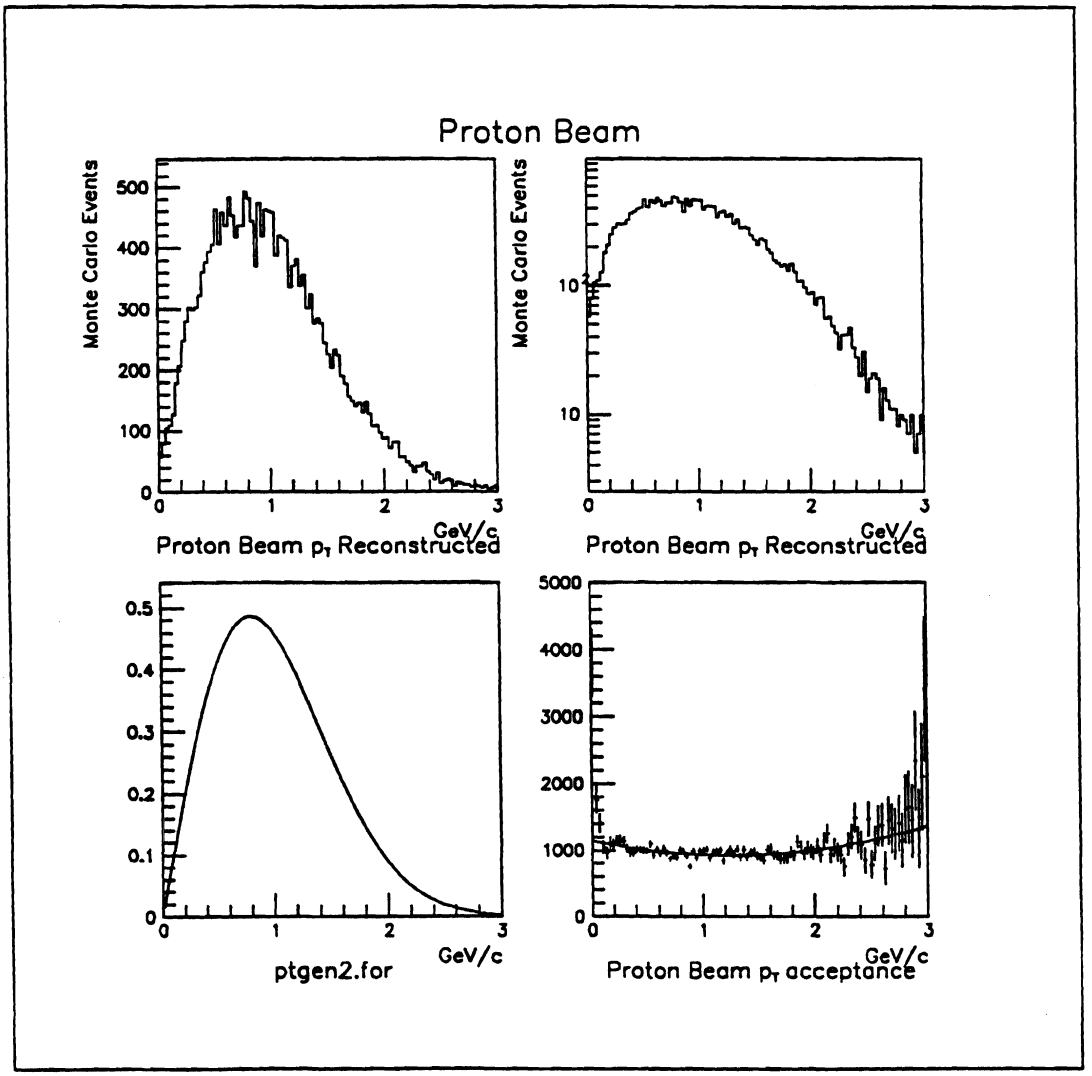

Figure 5.8 Monte Carlo transverse momentum distribution (*p* beam). Upper left: Distribution of reconstructed J/ψ's (linear scale). Upper right: Distribution of reconstructed J/ψ's (logarithmic scale). Lower left: Distribution of generated J/ψ's. Lower right: Relative acceptance (arbitrary units).

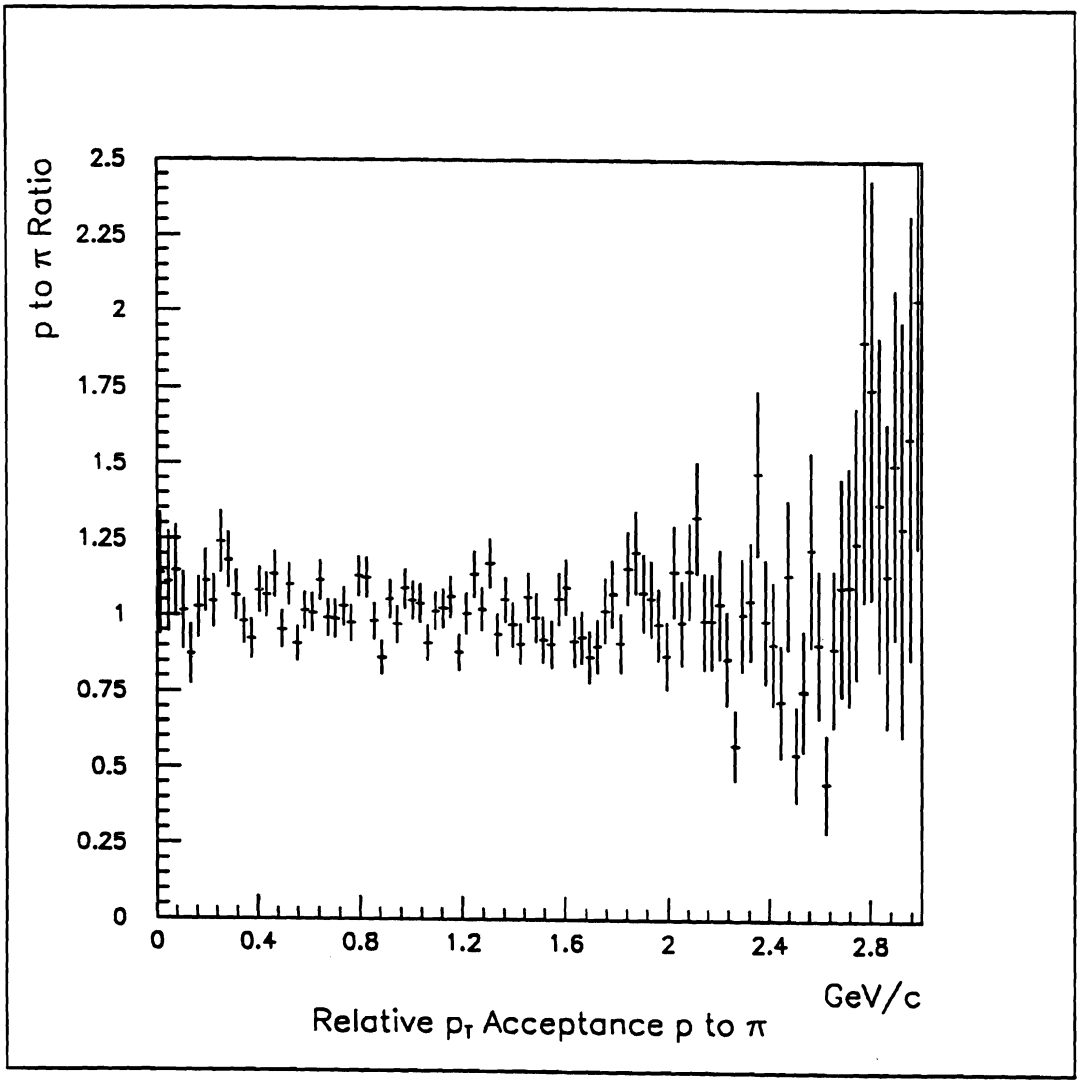

Figure 5.9 Acceptance vs. Transverse momentum: proton beam to π beam ratio (Monte Carlo).

Once the final differential distributions are determined, the total acceptance can be calculated. Events were generated with these differential distributions and overlaid on raw data events from twenty-three tapes. These tapes were chosen so that each chamber efficiency epoch would be represented, and also so that there would not be large gaps between tapes.

Table 5.3
J/ψ Acceptance times Reconstruction Efficiency — π beam ($x_F > 0$)

Era	Tape Number	Efficiency times Acceptance
AUGN	920	6.0 ± 0.2 %
	1209*	5.8 ± 0.2 %
SEPN	1209*	5.8 ± 0.2 %
	1381	6.6 ± 0.2 %
	2150	6.6 ± 0.2 %
	2465	7.0 ± 0.2 %
	2770	5.4 ± 0.2 %
NOVP	3220	4.3 ± 0.1 %
	3669	4.5 ± 0.1 %
	3700	4.5 ± 0.1 %
	4200	4.6 ± 0.2 %
	4534	4.7 ± 0.2 %
	4871	4.5 ± 0.1 %
JANN	5155	4.6 ± 0.2 %
	5420	4.4 ± 0.1 %
	5500	3.3 ± 0.1 %
	5751	3.5 ± 0.1 %
	6000	3.5 ± 0.1 %
JANP	6130	2.5 ± 0.1 %
	6260	5.0 ± 0.2 %
	6500	4.2 ± 0.2 %
	6750	4.8 ± 0.2 %
	7000	5.2 ± 0.2 %
	7115	4.7 ± 0.2 %

* Tape YA1209 is a late August tape. It's also included in September to increase the number of data points in that era. Differences reflect the differences in muon counter efficiencies in the two eras.

Table 5.4
J/ψ Acceptance times Reconstruction Efficiency — p beam ($x_F > 0$)

Era	Tape Number	Efficiency times Acceptance
AUGN	920	7.1 ± 0.2 %
	1209*	7.2 ± 0.2 %
SEPN	1209*	7.2 ± 0.2 %
	1381	8.1 ± 0.2 %
	2150	7.7 ± 0.2 %
	2465	8.2 ± 0.2 %
	2770	6.8 ± 0.2 %
NOVP	3220	5.5 ± 0.2 %
	3669	5.6 ± 0.2 %
	3700	5.0 ± 0.2 %
	4200	5.6 ± 0.2 %
	4534	5.9 ± 0.2 %
	4871	5.7 ± 0.2 %
JANN	5155	6.1 ± 0.2 %
	5420	5.3 ± 0.2 %
	5500	4.2 ± 0.2 %
	5751	4.2 ± 0.2 %
	6000	3.9 ± 0.1 %
JANP	6130	3.0 ± 0.2 %
	6260	6.2 ± 0.3 %
	6500	4.8 ± 0.2 %
	6750	5.3 ± 0.2 %
	7000	6.5 ± 0.3 %
	7115	6.3 ± 0.3 %

* Tape YA1209 is a late August tape. It's also included in September to increase the number of data points in that era. Differences reflect the differences in muon counter efficiencies in the two eras.

B. J/ψ Feynman x distributions

Before the total cross-section can be determined, the differential distributions must be calculated. As described above, the geometric acceptance is a function of the

kinematics of the produced ψ, and the reconstruction efficiency may also be. To obtain the differential distributions, the data was divided into bins of x_F, and the signal and background fitted to the Monte Carlo shape for the J/ψ and an exponential continuum for the background. The fit returned the number of J/ψ's and this number was corrected by dividing by the acceptance returned by the Monte Carlo. In cases where the statistics were too low for the fit to converge, the J/ψ's were counted by hand. The antiproton bins were different from the proton and pion bins because of the lower statistics; the binning was chosen to maximize the number of usable data points.

Table 5.5
Number of J/ψ's per bin of Feynman-x

x_F bin	π-	π+	proton	antiproton
– .125 - –.075	53 ± 10	16 ± 5	30 ± 7	
– .075 - –.025	280 ± 21	111 ± 12	150 ± 20	
– .025 - .025	710 ± 28	353 ± 22	502 ± 26	
.025 - .075	1362 ± 41	660 ± 30	888 ± 35	
.075 - .125	1897 ± 51	885 ± 35	1088 ± 45	
.125 - .175	1832 ± 51	986 ± 38	1044 ± 38	
.175 - .225	1611 ± 48	655 ± 42	740 ± 41	
.225 - .275	1187 ± 45	545 ± 37	439 ± 28	
.275 - .325	782 ± 39	352 ± 26	232 ± 29	
.325 - .375	476 ± 54	259 ± 80	103 ± 23	
.375 - .425	208 ± 40	106 ± 25	36 ± 12	
.425 - .475	68 ± 19	30 ± 30	10 ± 5	
– .1 - 0				10 ± 6
0 - .1				41 ± 12
.1 - .2				45 ± 11
.2 - .3				26 ± 8
.3 - .4				7 ± 5

Table 5.6

J/ψ's per bin of Feynman-x — Acceptance Corrected (Arbitrary Units)

x_F bin	π-	π+	proton	antiproton
– .125 - –.075	193 ± 41	128 ± 42	219 ± 45	
– .075 - –.025	238 ± 26	207 ± 27	255 ± 34	
– .025 - .025	219 ± 13	239 ± 18	310 ± 20	
.025 - .075	220 ± 10	233 ± 13	287 ± 14	
.075 - .125	216 ± 7	220 ± 9	247 ± 10	
.125 - .175	185 ± 5	217 ± 9	210 ± 8	
.175 - .225	173 ± 5	173 ± 10	159 ± 9	
.225 - .275	156 ± 6	155 ± 11	114 ± 7	
.275 - .325	137 ± 7	135 ± 10	81 ± 10	
.325 - .375	120 ± 14	143 ± 44	52 ± 12	
.375 - .425	80 ± 16	89 ± 21	28 ± 9	
.425 - .475	42 ± 12	40 ± 40	12 ± 5	
– .1 - 0				75 ± 45
0 - .1				66 ± 19
.1 - .2				46 ± 11
.2 - .3				34 ± 11
.3 - .4				18 ± 13

We have fit the differential distributions in Feynman-x to the following functional form:

$$\frac{d\sigma}{dx_F} \sim \frac{(1-x_1)^{n_1} \quad (1-x_2)^{n_2}}{x_1 + x_2}. \tag{5.10}$$

where $x_1 = ½\,(x^* + x_F)$, $x_2 = ½\,(x^* - x_F)$, and $x^* = \sqrt{x_F{}^2 + 4m^2/s}$. This is a structure function inspired parameterization. If the J/ψ's were created in the collisions of partons each with structure function $xF(x) = (1-x)^n$, and there were no complications such as production via χ decay or production with an associated gluon jet, the above equation could be used to determine structure functions exactly. Although with real data the interpretation of the parameters is more complicated, the parameterization

still fits the data quite well. Because of the physical significance of this fit shape, we can incorporate additional information. For the proton beam, there is a symmetry between the nucleon beam and the nucleons in the target, so n_2 is set equal to n_1. A similar situation exists for antiproton beam: the gluon distribution is the same (via the CPT theorem) for proton and antiproton, and the quark distribution in the proton is the same as the antiquark distribution in the antiproton (again, via the CPT theorem).

There is a strong correlation between n_1 and n_2. However, n_2 is not well measured — it corresponds to the parton distribution in the target nucleus, to which we are not very sensitive. To keep this uncertainty in n_2 from propagating into an uncertainty in n_1, for fitting the pion data we constrain n_2 to the same value as for proton beam. This is rigorously correct in the case where the same mechanism (e.g. gluon-gluon fusion) is responsible for ψ production from both protons and pions. Because the inclusive cross-sections are similar for pion and proton, it is reasonable to assume that a substantial fraction of J/ψs from pions do come from gluon fusion.

It is common for other experiments, particularly those at large x_F to use instead

$$\frac{d\sigma}{dx_F} \sim \left(1 - \left|x_F - x_0\right|\right)^c, \tag{5.11}$$

so we also fit to this form for comparison. The fits to this parameterization are also included in the table on the following page.

Table 5.7

Feynman x differential distribution fit parameters

Beam	n_1	n_2	x_0	c
π^-	1.81 ± 0.16	4.8 (fixed)	.030 ± .013	1.99 ± 0.15
π^+	1.90 ± 0.24	4.8 (fixed)	.062 ± .011	2.27 ± 0.27
$\pi^\pm$	1.81 ± 0.14	4.8 (fixed)	.034 ± .012	2.00 ± 0.14
proton	4.8 ± 0.3	$n_1 = n_2$	.026 ± .007	4.14 ± 0.16
antiproton	2.9 ± 2.1	$n_1 = n_2$	− .02 ± .10	3.2 ± 1.4

There is an overall systematic error arising from the momentum rescaling of 0.3% to force the J/ψ mass to the accepted value. This error, however, is much smaller than the statistical error: for example, for n_1 for π^- induced J/ψ's it is ±0.005. For this reason, it is excluded from the above table.

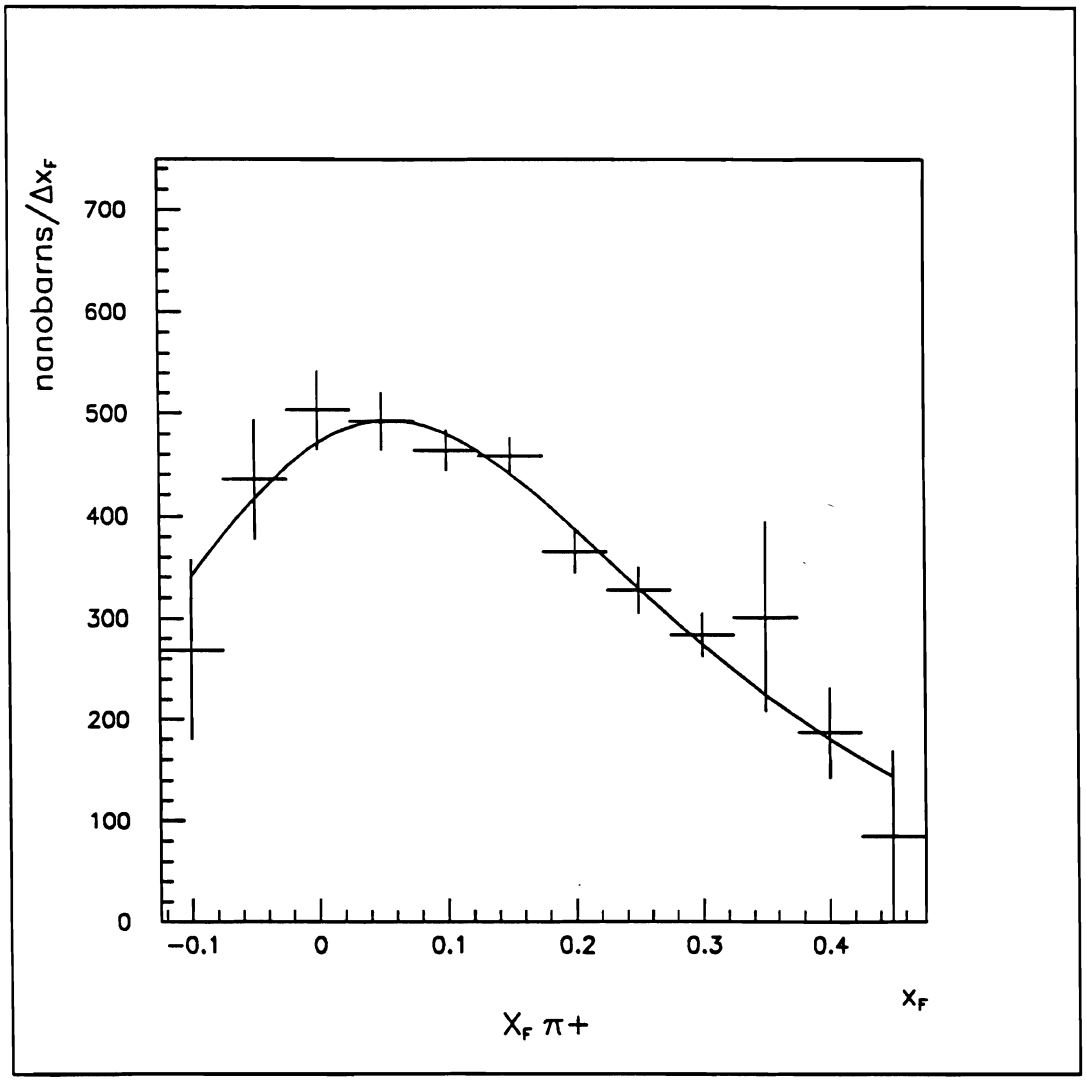

Figure 5.10 Acceptance corrected Feynman x distribution: π^+ beam.

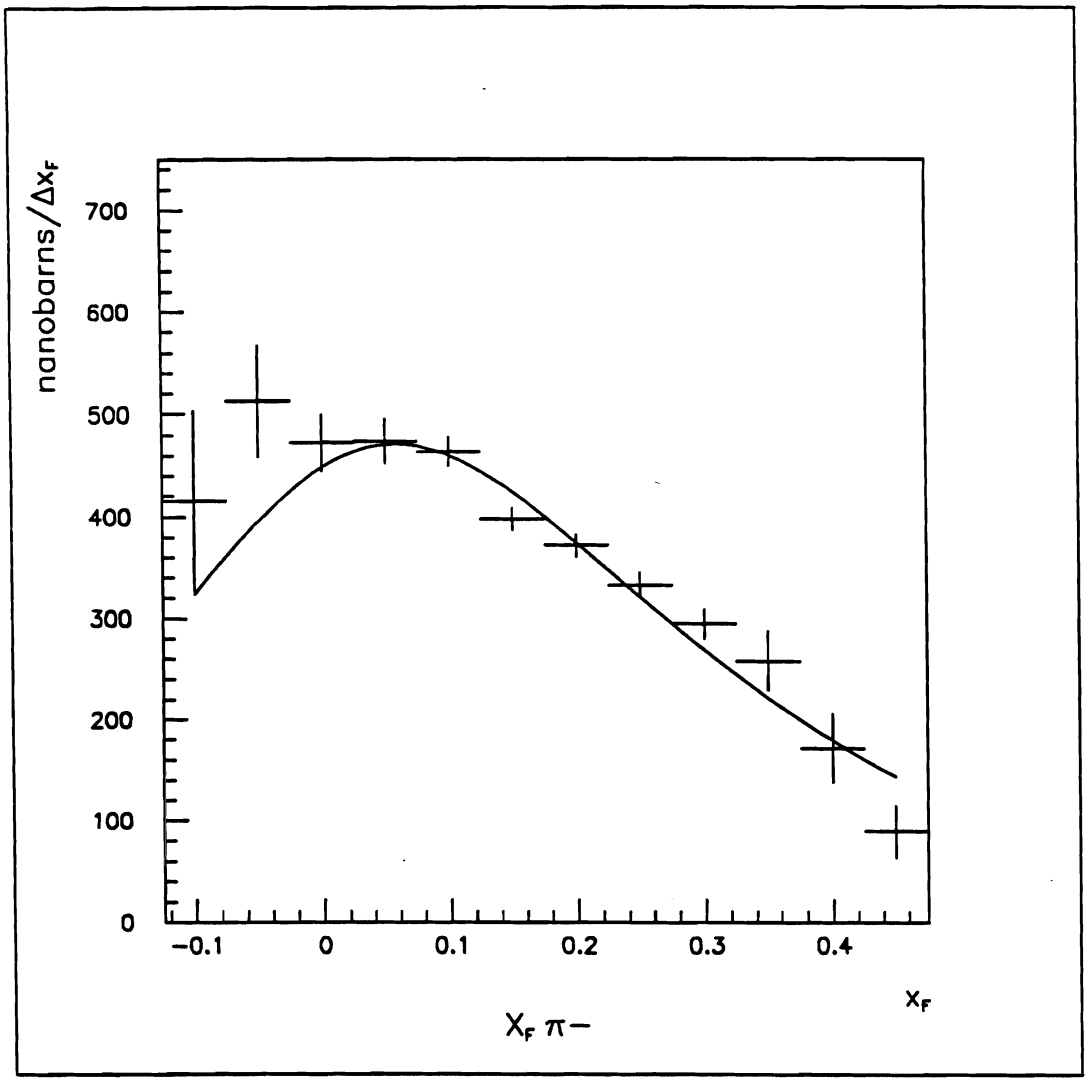

Figure 5.11 Acceptance corrected Feynman x distribution: π^- beam.

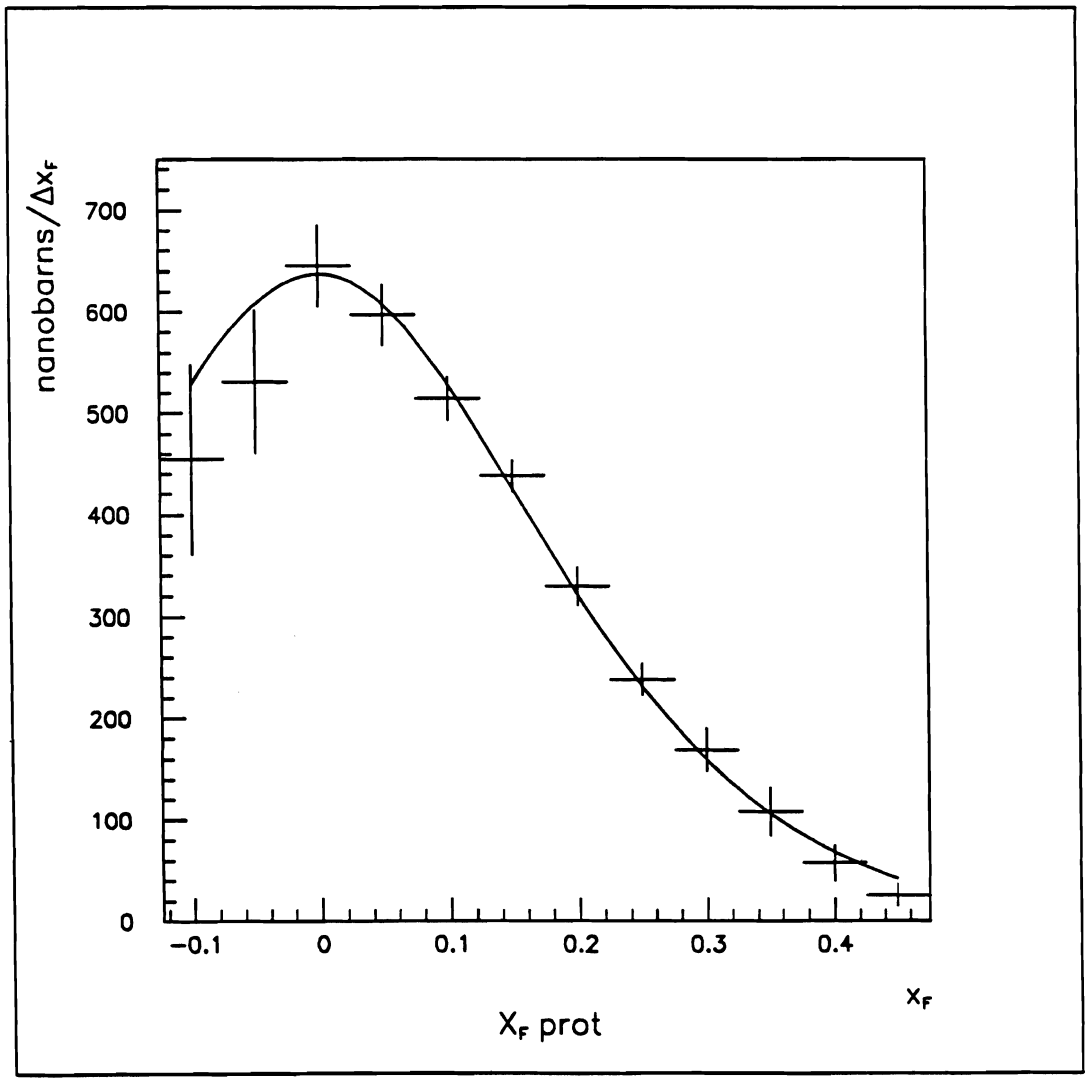

Figure 5.12 Acceptance corrected Feynman x distribution: proton beam.

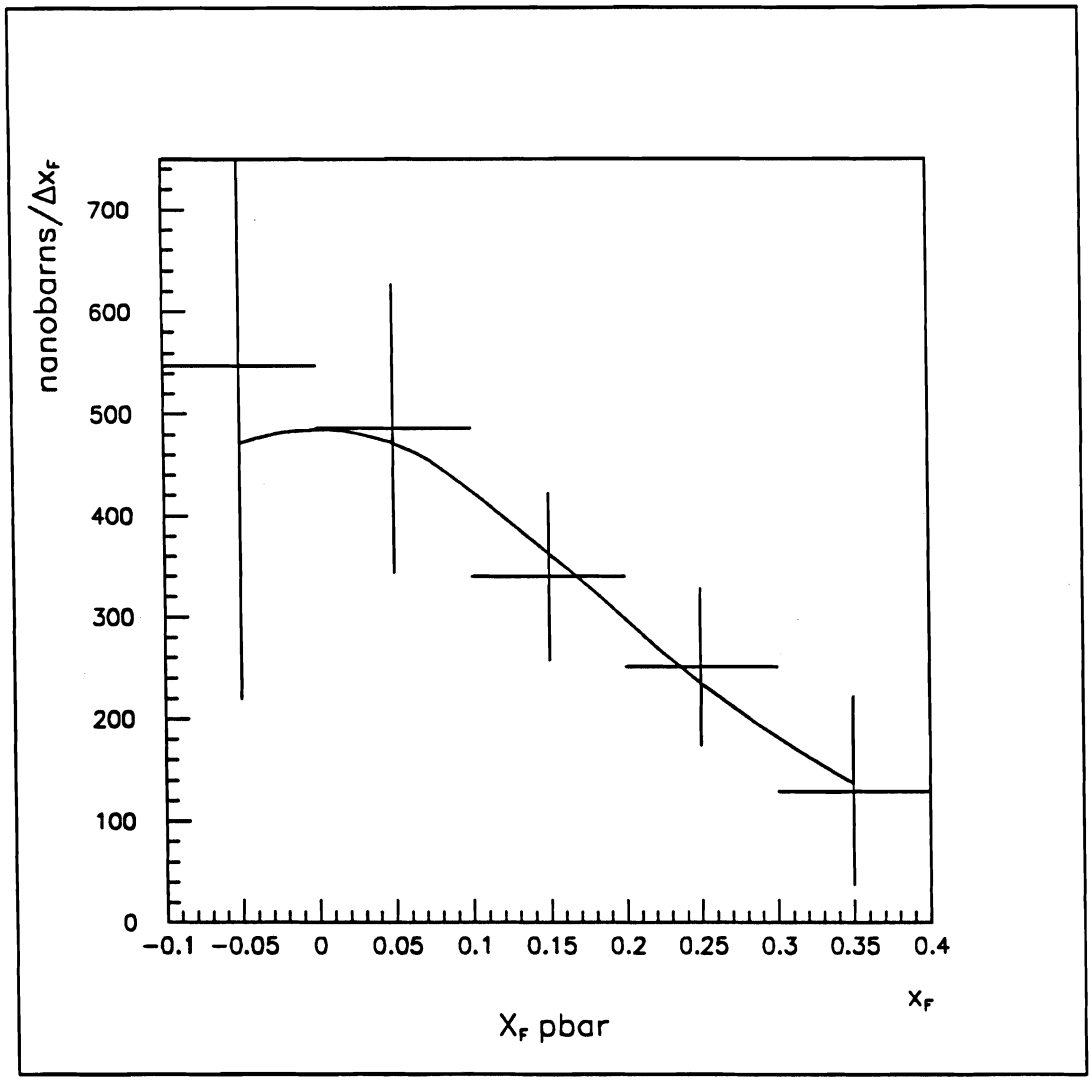

Figure 5.13 Acceptance corrected Feynman x distribution: antiproton beam.

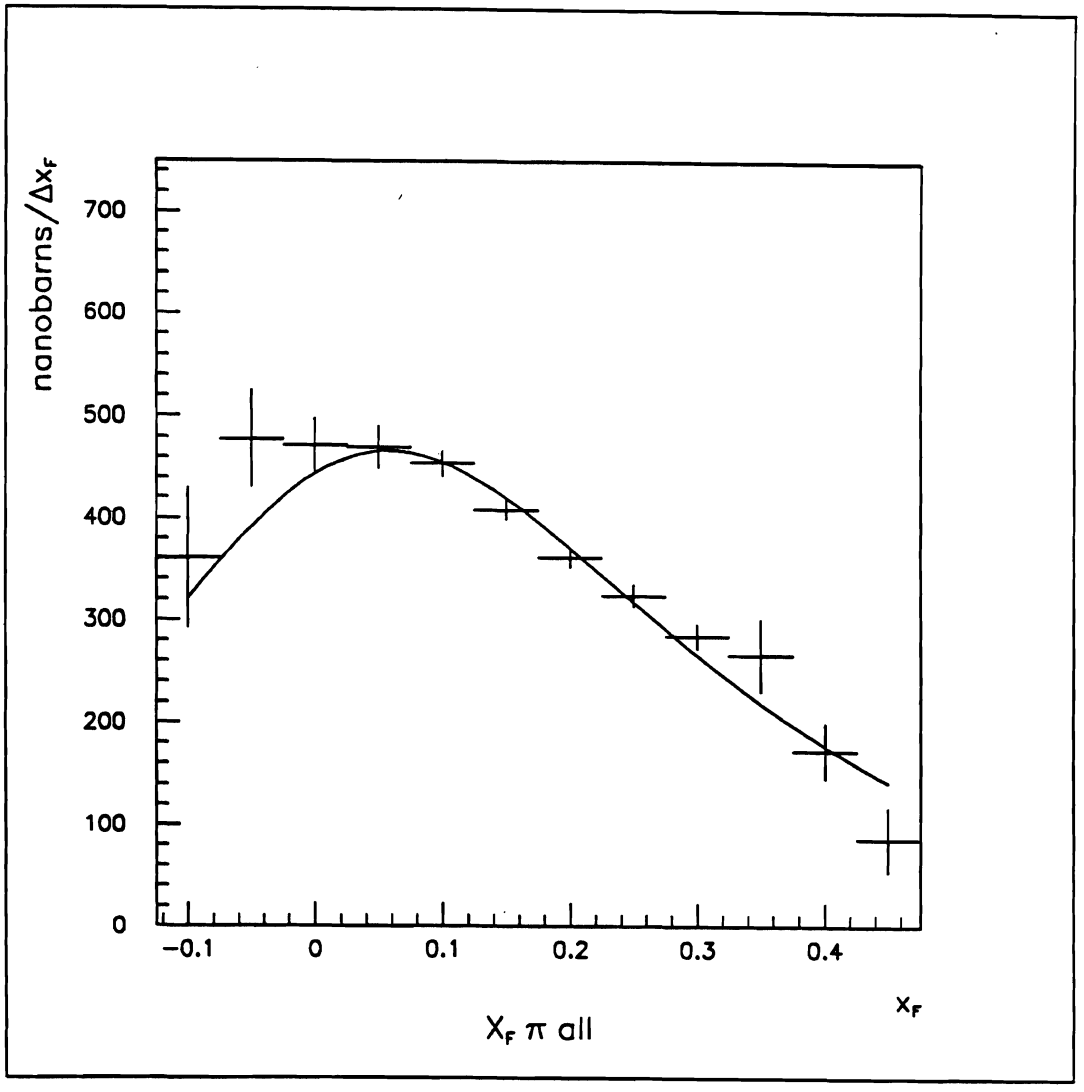

Figure 5.14 Acceptance corrected Feynman x distribution: $\pi^{\pm}$ beam.

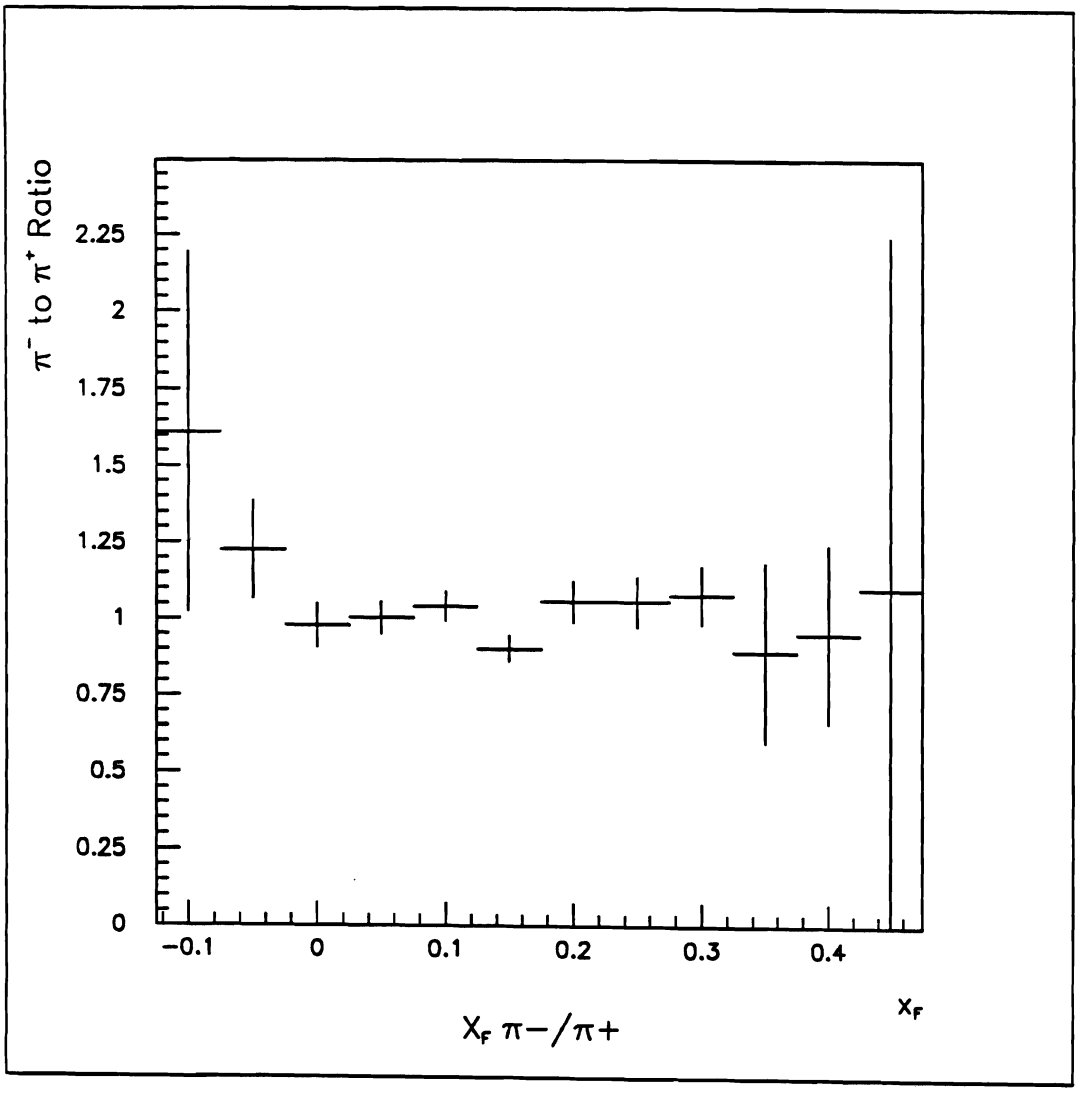

Figure 5.15 Acceptance corrected Feynman x distribution ratio: π^- beam to π^+ beam.

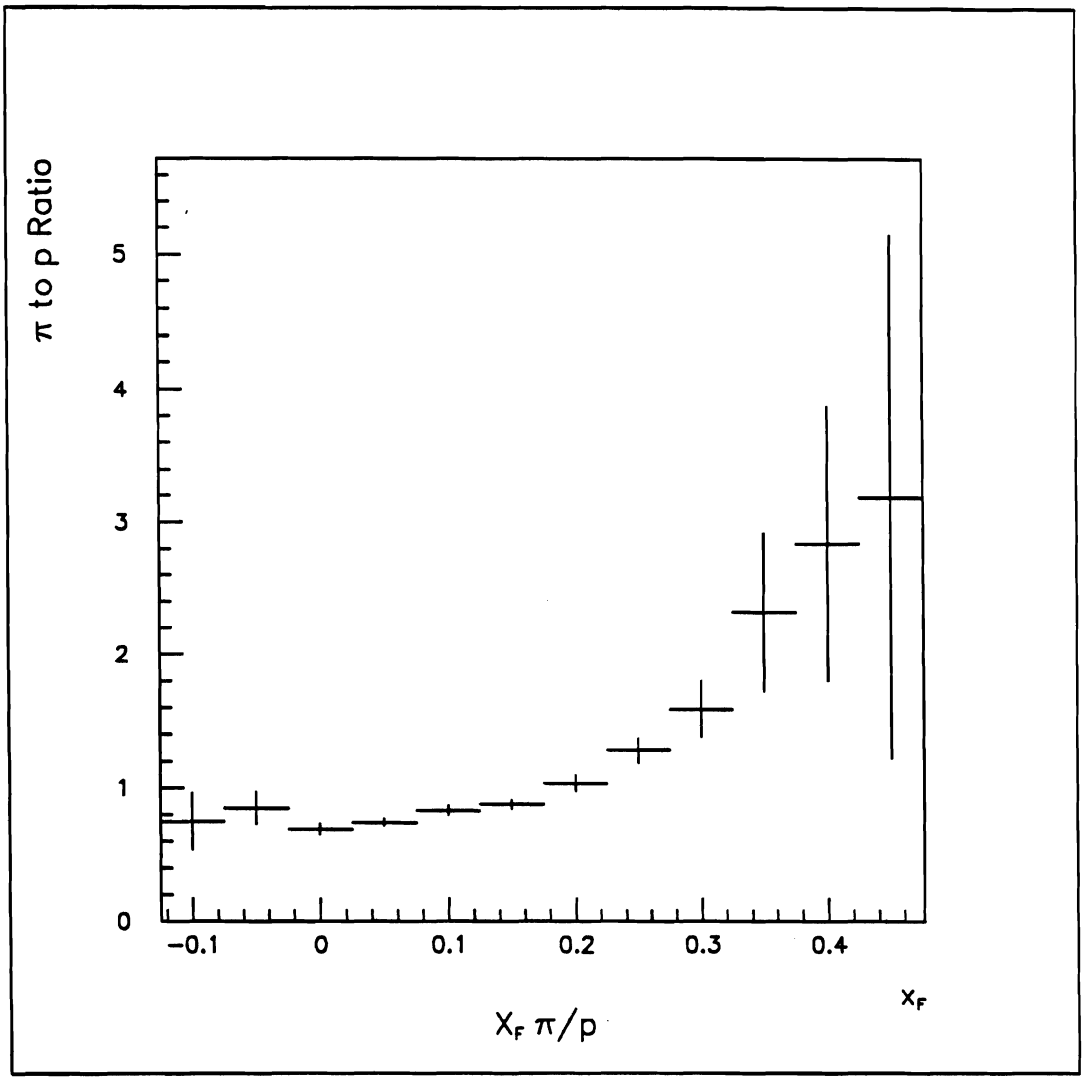

Figure 5.16 Acceptance corrected Feynman x distribution ratio: $\pi^{\pm}$ beam to proton.

C. J/ψ Transverse Momentum Distributions

Transverse momentum was measured relative to the beam direction, as measured by the beam chambers. If no beam particle was found due to beam chamber

inefficiencies, the event was not used in the p_T distribution analysis. Like the Feynman-x analysis, data were divided into bins of p_T and fitted to the known J/ψ shape and an exponential background. This has the advantage of not requiring an explicit background subtraction. If there were too few events for the fit to converge, entries above background were counted by hand. The results are shown in the following table:

Table 5.8

Number of J/ψ's per bin of transverse momentum

p_T bin (GeV)	π-	π+	proton	antiproton
0 - .25	546 ± 26	192 ± 19	248 ± 18	24 ± 13
.25 - .50	1180 ± 40	550 ± 29	612 ± 31	
.50 - .75	1497 ± 44	687 ± 32	748 ± 37	35 ± 9
.75 - 1.00	1448 ± 46	690 ± 34	736 ± 29	
1.00 - 1.25	1288 ± 44	622 ± 30	629 ± 31	23 ± 7
1.25 - 1.50	1011 ± 38	457 ± 28	470 ± 28	
1.50 - 1.75	783 ± 32	396 ± 25	316 ± 23	16 ± 5
1.75 - 2.00	532 ± 29	199 ± 20	233 ± 17	
2.00 - 2.25	375 ± 24	128 ± 15	134 ± 14	7 ± 5
2.25 - 2.50	189 ± 20	86 ± 14	62 ± 13	
2.50 - 2.75	114 ± 15	61 ± 10	23 ± 8	2 ± 3
2.75 - 3.00	76 ± 13	23 ± 10	8 ± 5	
3.00 - 3.25	34 ± 10	15 ± 10	5 ± 4	
3.25 - 3.50	17 ± 10	10 ± 10	4 ± 4	

Table 5.9

J/ψ's per bin of transverse momentum - acceptance corrected (arbitrary units)

p_T bin (GeV)	π-	π+	proton	antiproton
0 - .25	561 ± 27	197 ± 20	257 ± 19	25 ± 14
.25 - .50	1268 ± 43	591 ± 31	677 ± 34	
.50 - .75	1660 ± 49	762 ± 36	870 ± 43	39 ± 10
.75 - 1.00	1632 ± 52	778 ± 38	888 ± 35	
1.00 - 1.25	1451 ± 50	700 ± 34	772 ± 38	29 ± 8
1.25 - 1.50	1121 ± 42	507 ± 31	577 ± 34	
1.50 - 1.75	841 ± 34	425 ± 29	381 ± 28	17 ± 5
1.75 - 2.00	546 ± 30	204 ± 21	271 ± 20	
2.00 - 2.25	363 ± 23	121 ± 15	148 ± 15	7 ± 5
2.25 - 2.50	171 ± 18	78 ± 13	64 ± 13	
2.50 - 2.75	96 ± 13	51 ± 8	22 ± 8	2 ± 3
2.75 - 3.00	57 ± 10	18 ± 8	7 ± 4	
3.00 - 3.25	24 ± 7	11 ± 7	4 ± 3	
3.25 - 3.50	11 ± 6.5	6.5 ± 6.5	3 ± 3	

For transverse momentum, we fit to an Gaussian in p_T, which is the same as an exponential in p_T^2:

$$\frac{d\sigma}{dp_T^2} \sim e^{-p_T^2/p_0^2} \tag{5.12}$$

or alternatively:

$$\frac{d\sigma}{dp_T} \sim 2p_T\, e^{-p_T^2/p_0^2} \tag{5.13}$$

where p_0 is a scale factor with dimensions of momentum. The mean transverse momentum is $\frac{\sqrt{\pi}}{2}p_0$ and the mean square of the transverse momentum is p_0^2. The sys-

tematic term of 0.3% arises from the 0.3% momentum rescaling to force the J/ψ mass to be 3.097 GeV. This indicates a scale uncertainty in the momentum of 0.3%, and to be very conservative, this was included as a p_T scale uncertainty as well. As an additional check on systematic errors, the p_T distributions from even and odd numbered tapes was compared: they differ by 1.0%. Adding these two uncertainties linearly yields an estimate of systematic errors of 1.3%.

Table 5.10
Transverse momentum differential distribution fit parameters

Beam	$\langle p_T \rangle$ (GeV)	$\langle p_T^2 \rangle$ (GeV^2)
π^-	1.062 ± .008 ± .014	1.43 ± .02 ± .04
π^+	1.045 ± .012 ± .014	1.39 ± .03 ± .04
$\pi^\pm$	1.075 ± .003 ± .014	1.47 ± .01 ± .04
proton	0.993 ± .002 ± .013	1.255 ± .005 ± .033
antiproton	1.08 ± .11 ± .014	1.5 ± .3 ± .04

The figures on the following pages show the observed p_T distribution for J/ψ's produced in E-705, after correcting for acceptance.

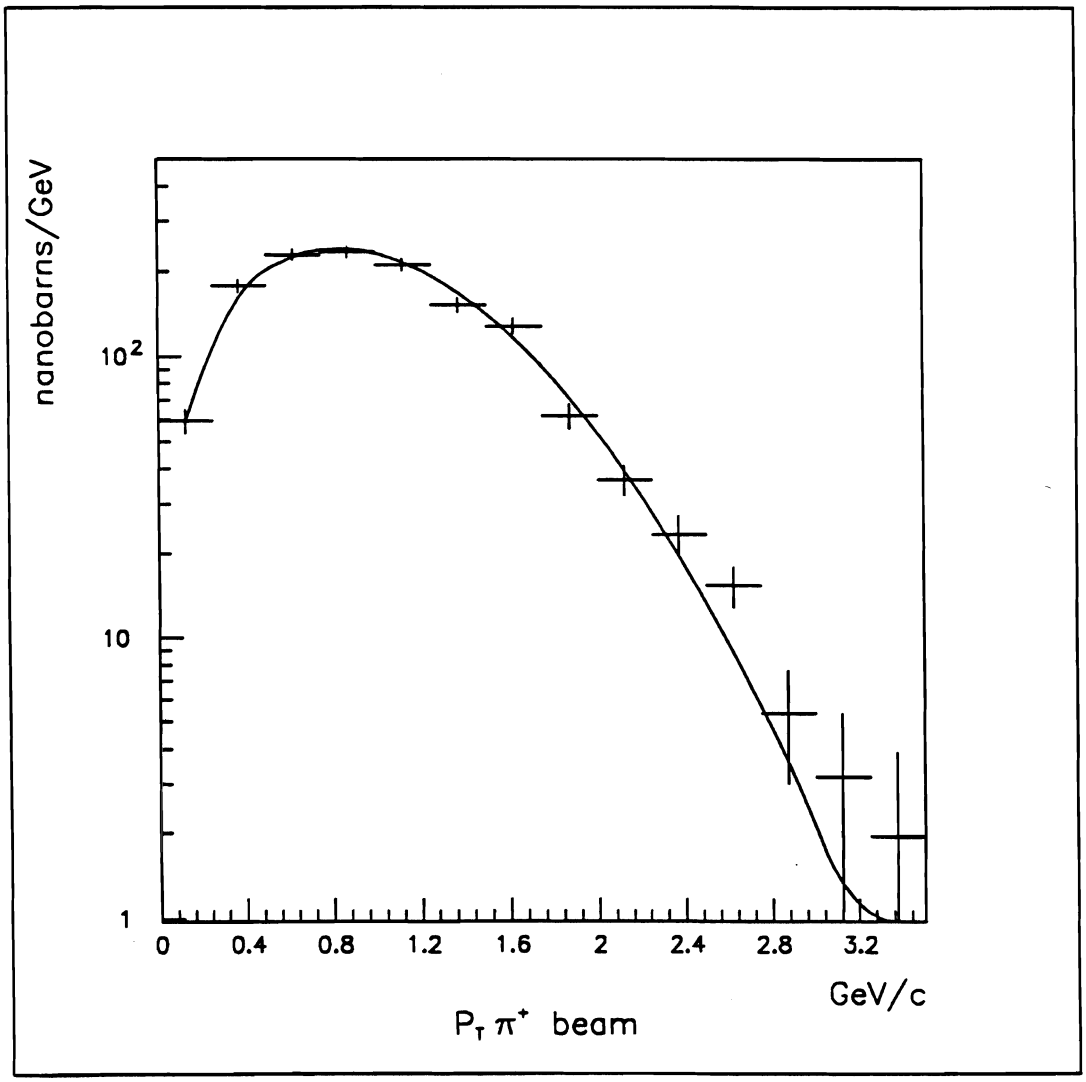

Figure 5.17 Acceptance corrected transverse momentum distribution: π^+ beam.

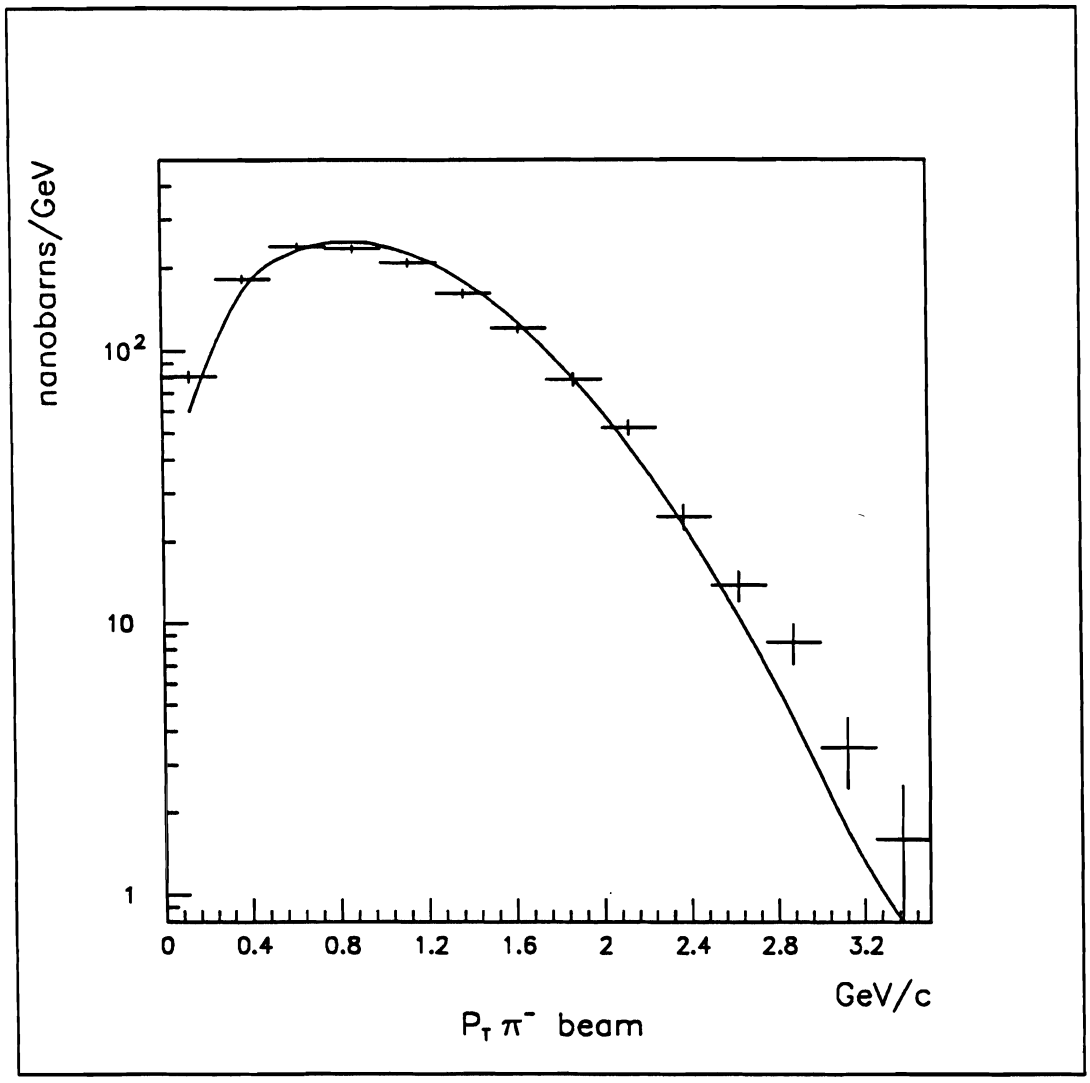

Figure 5.18 Acceptance corrected transverse momentum distribution: π^- beam.

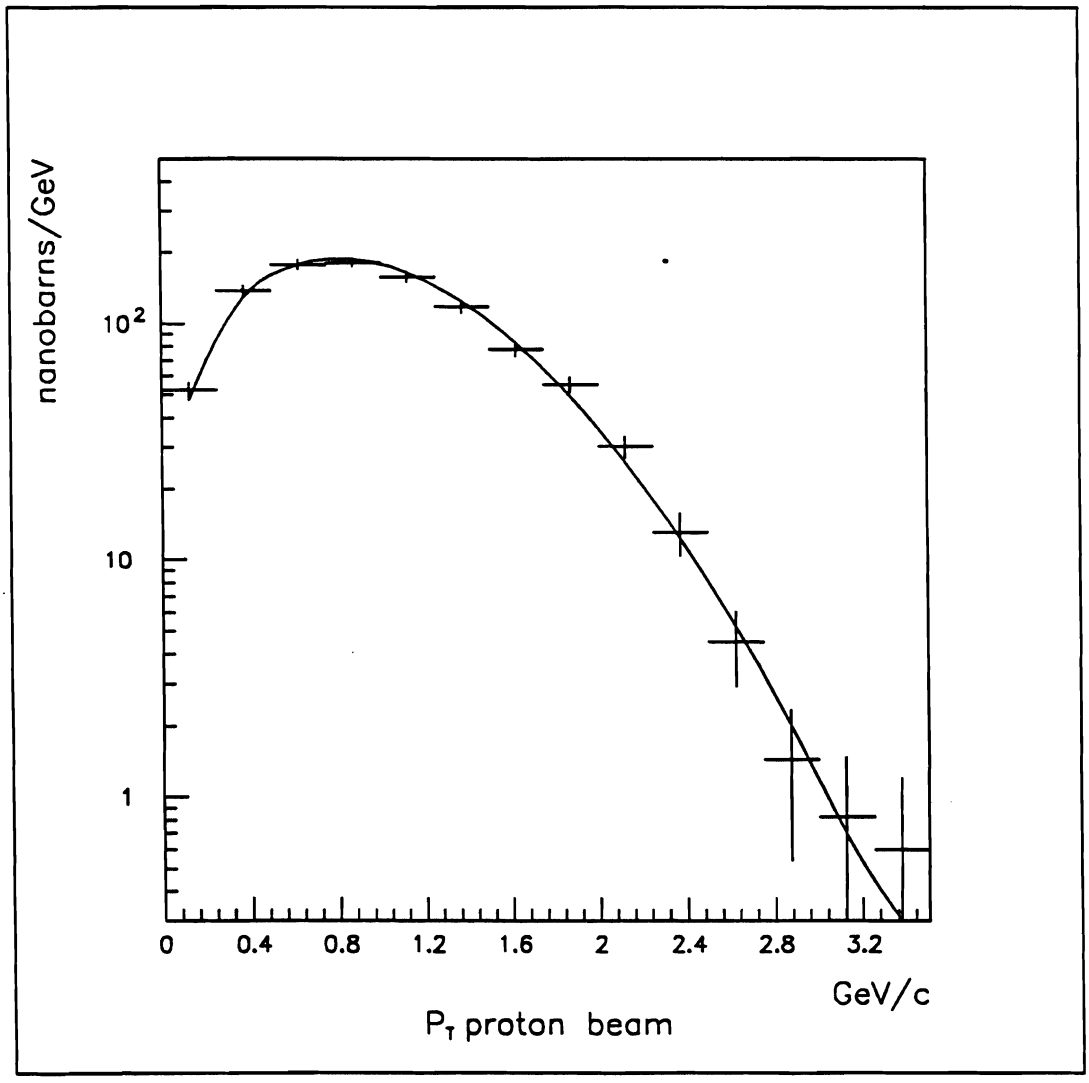

Figure 5.19 Acceptance corrected transverse momentum distribution: proton beam.

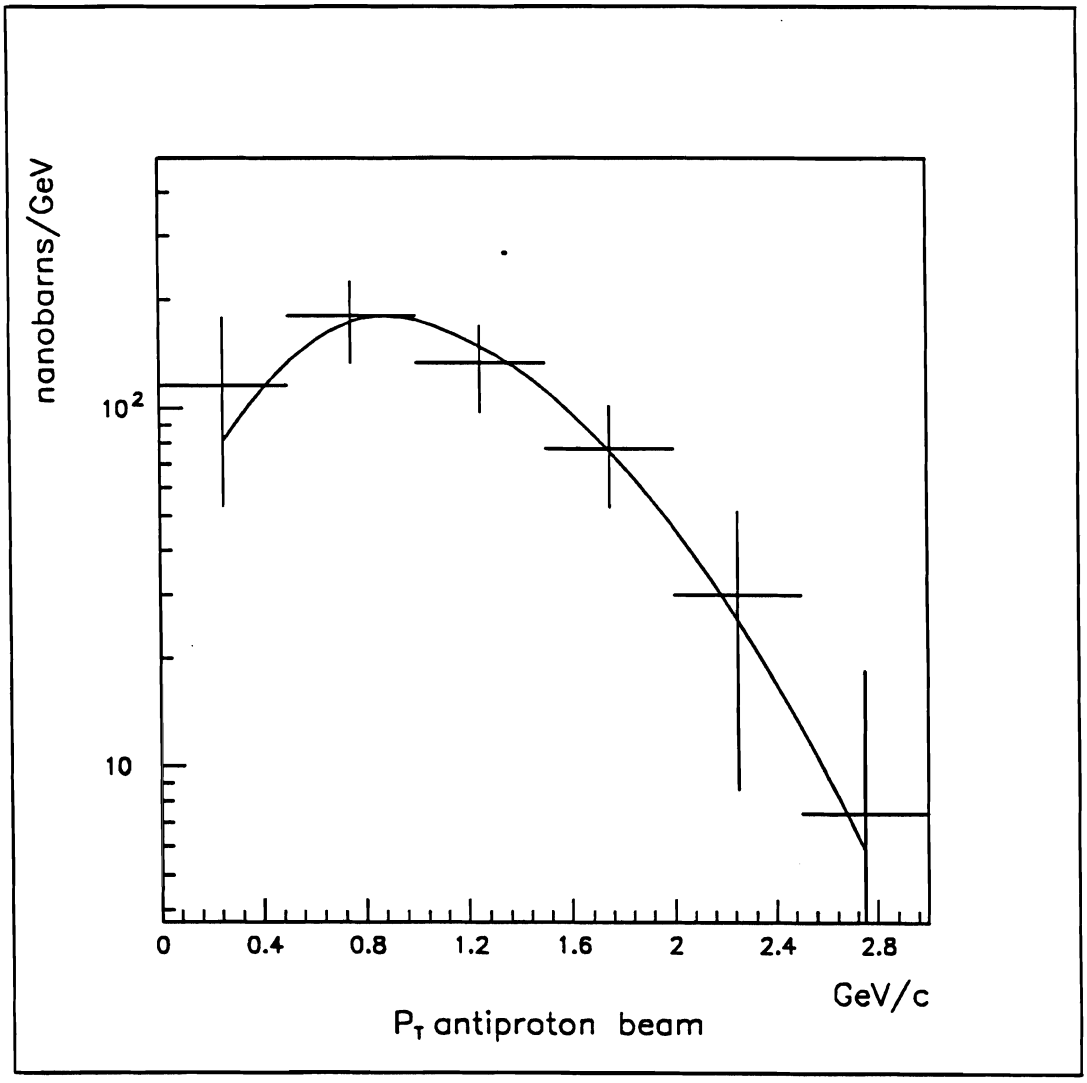

Figure 5.20 Acceptance corrected transverse momentum distribution: antiproton beam.

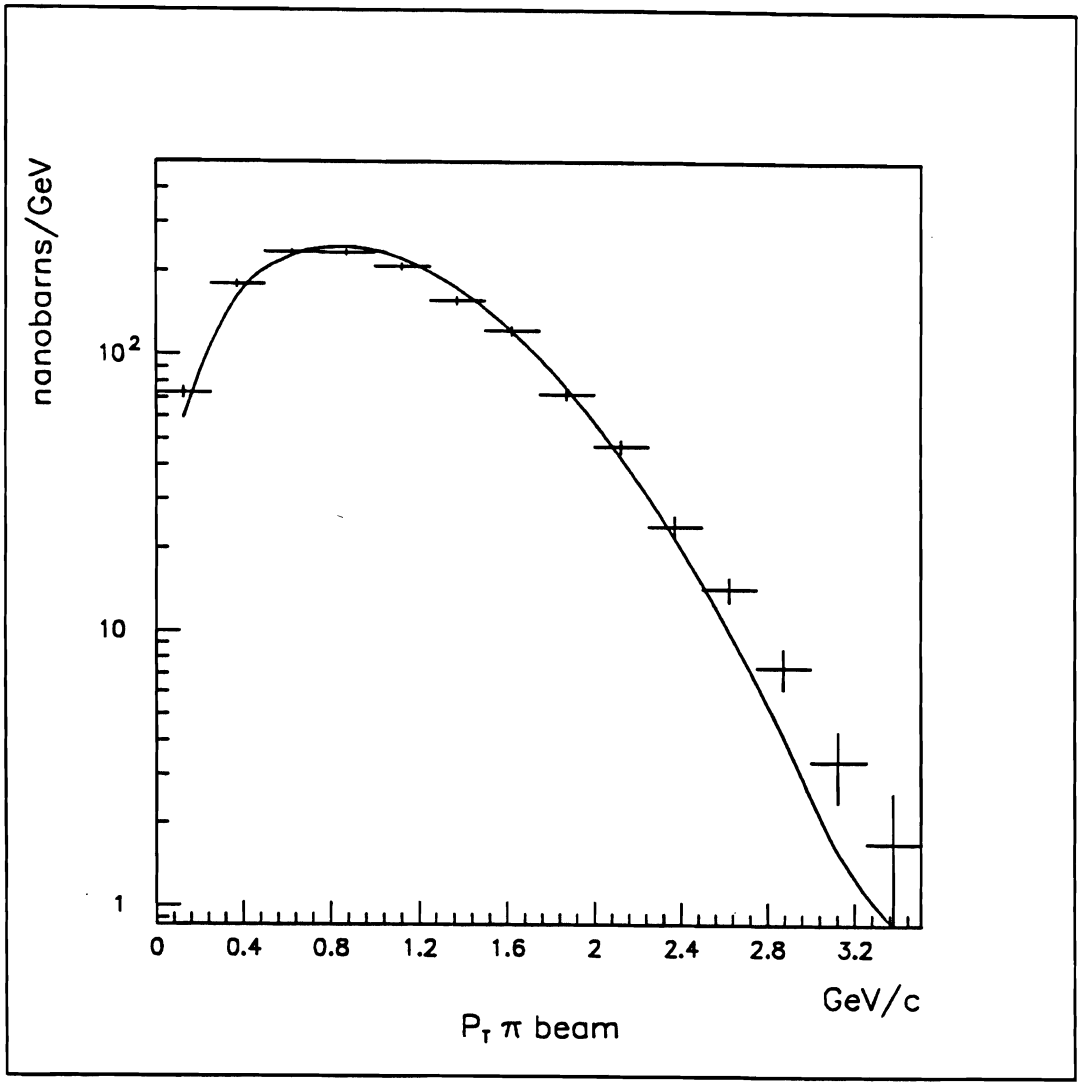

Figure 5.21 Acceptance corrected transverse momentum distribution: $\pi^{\pm}$ beam.

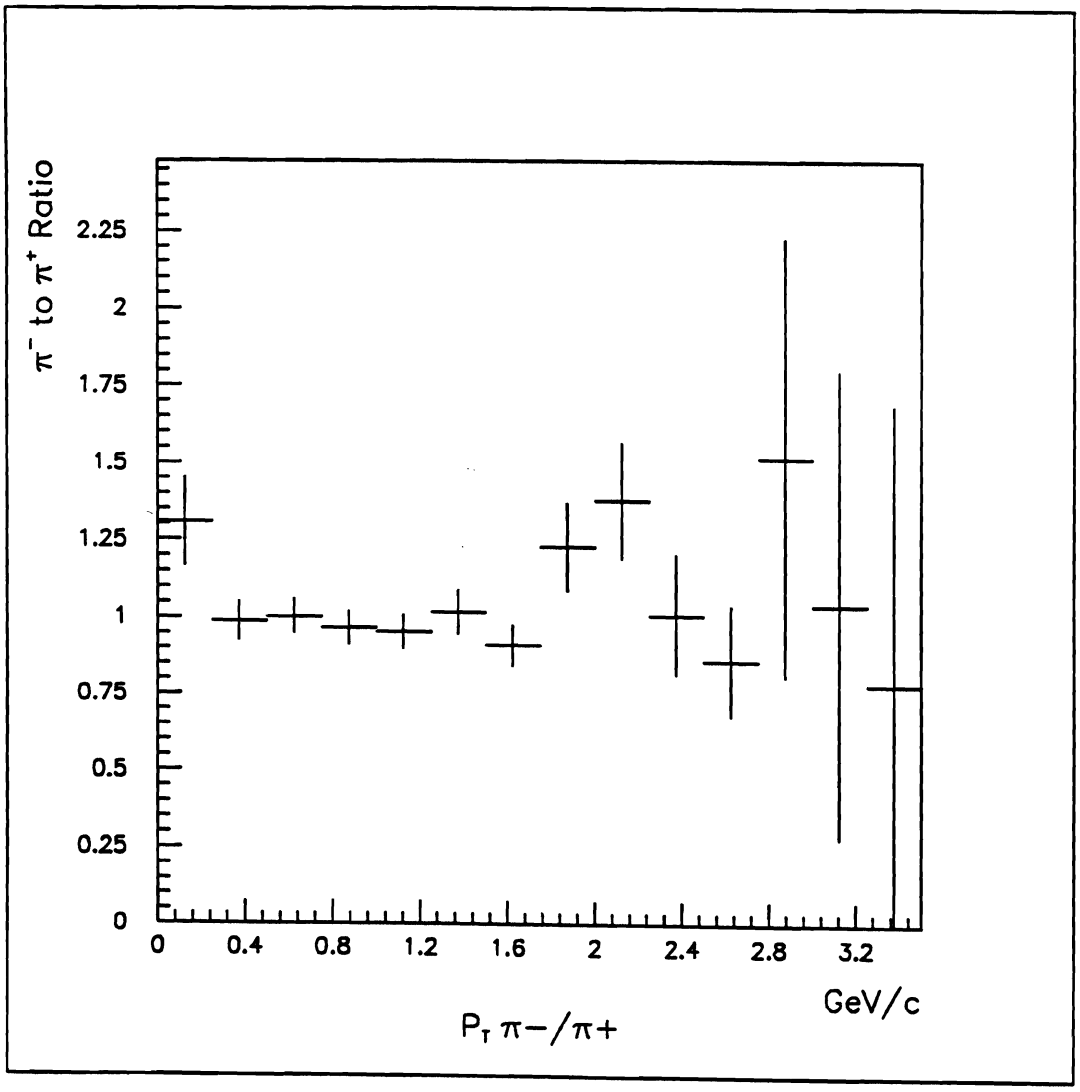

Figure 5.22 Acceptance corrected transverse momentum distribution ratio: π^- beam to π^+ beam.

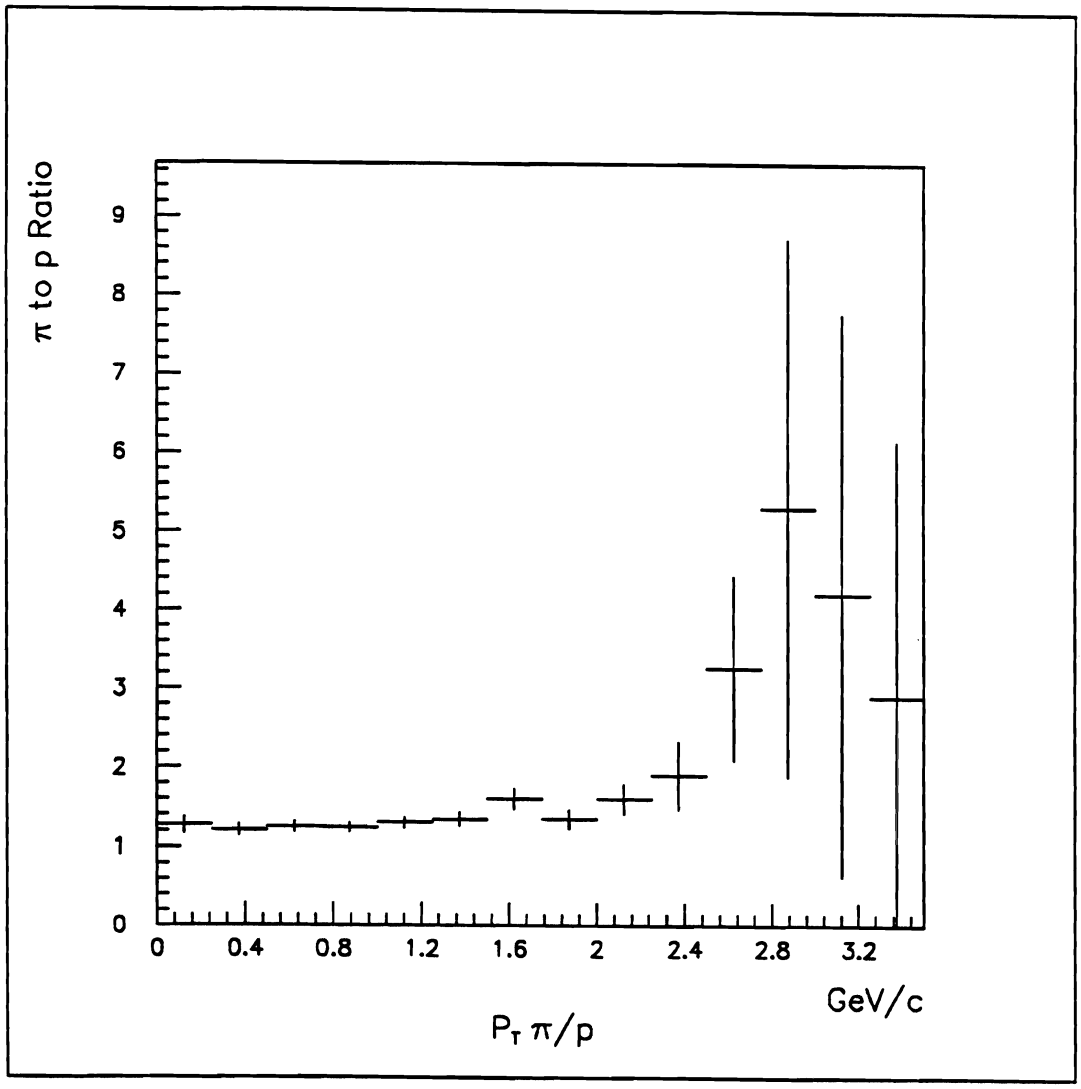

Figure 5.23 Acceptance corrected transverse momentum distribution ratio: $\pi^{\pm}$ beam to proton.

C. Total Cross-Section: ψ(1S)

We reconstructed a total of 20,300 J/ψs passing all cuts (c.f. figure 5.24). The following figures and table show the dimuon mass spectra and the number of J/ψs fitted for all the data and each beam type.

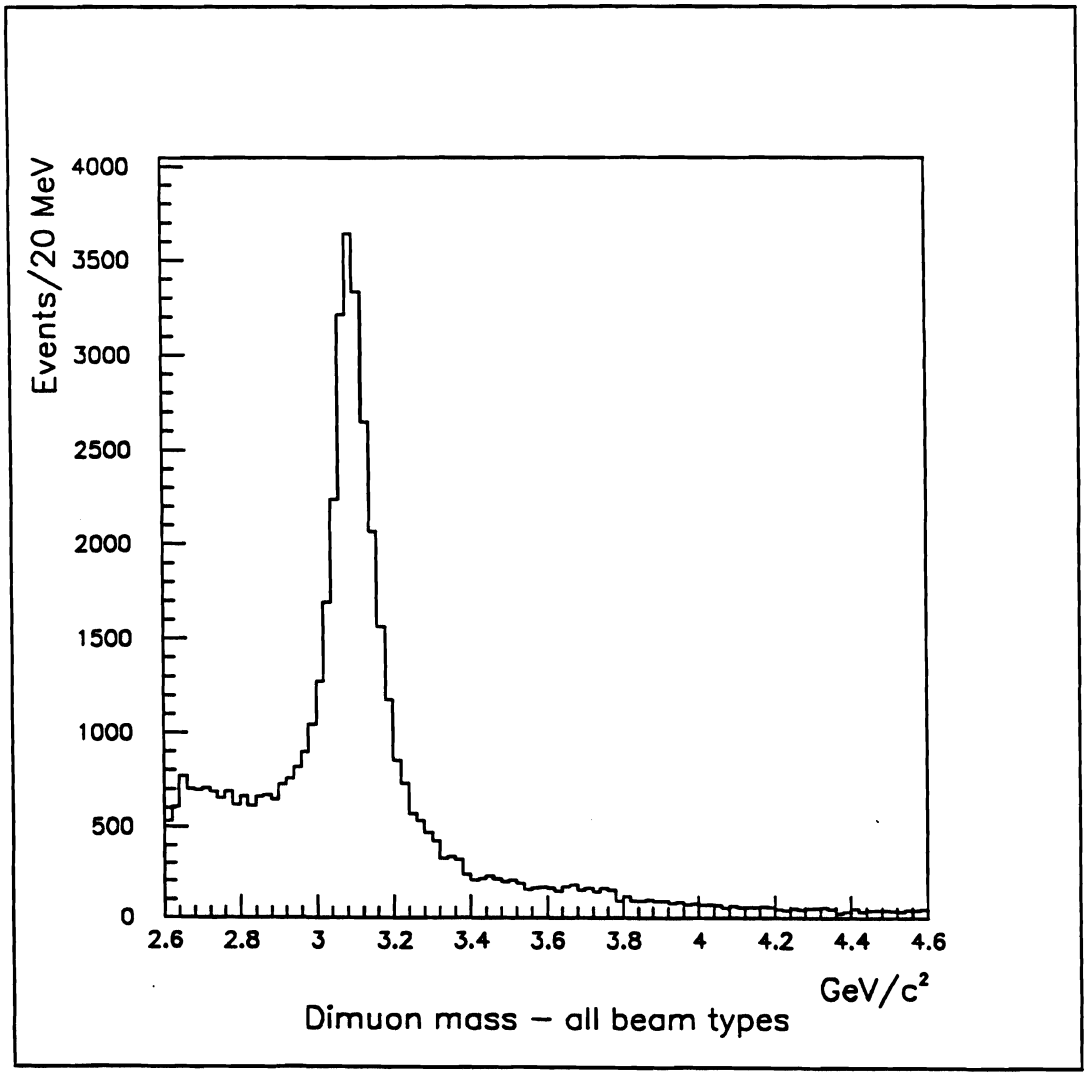

Figure 5.24 Dimuon mass: all beam types

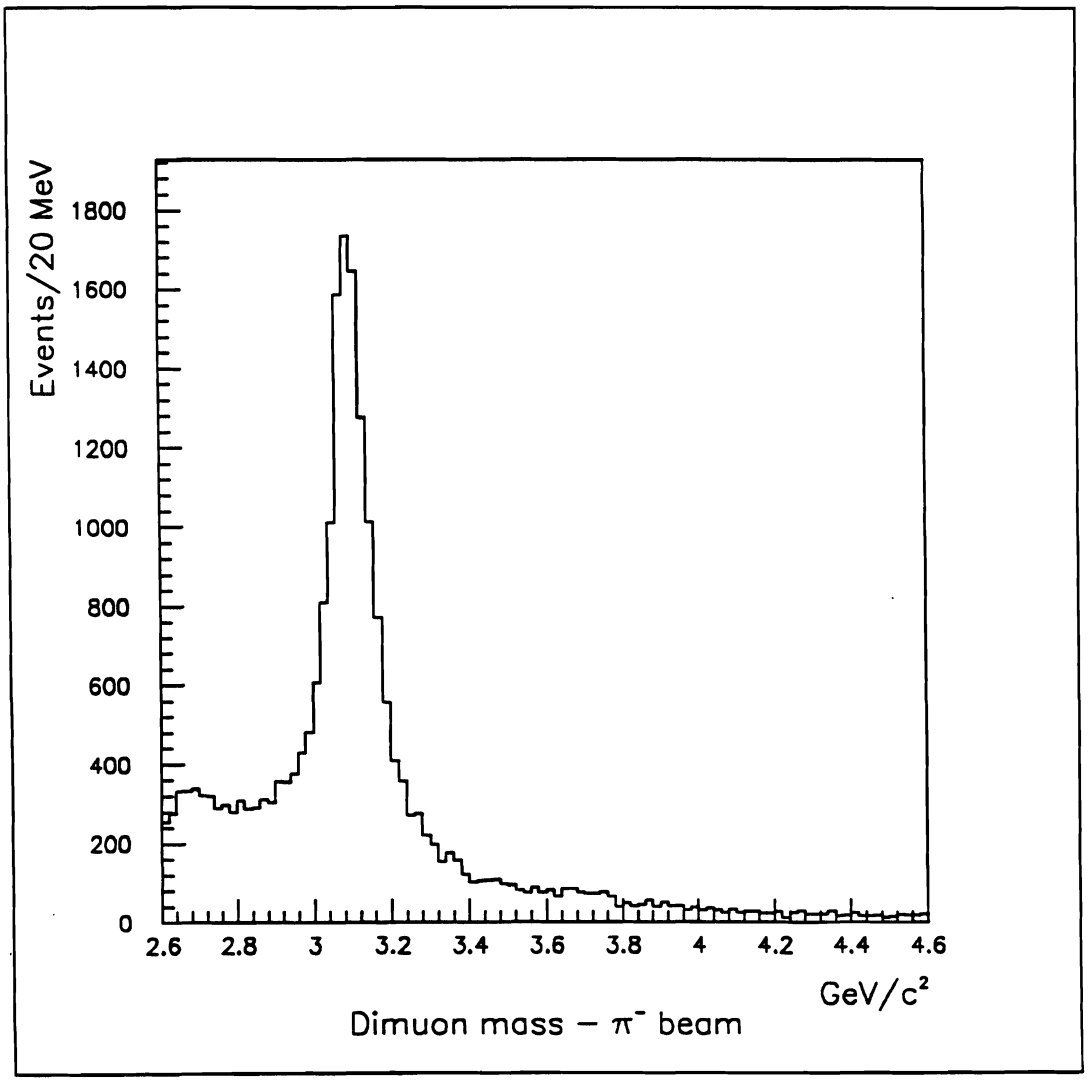

Figure 5.25 Dimuon mass: π- beam

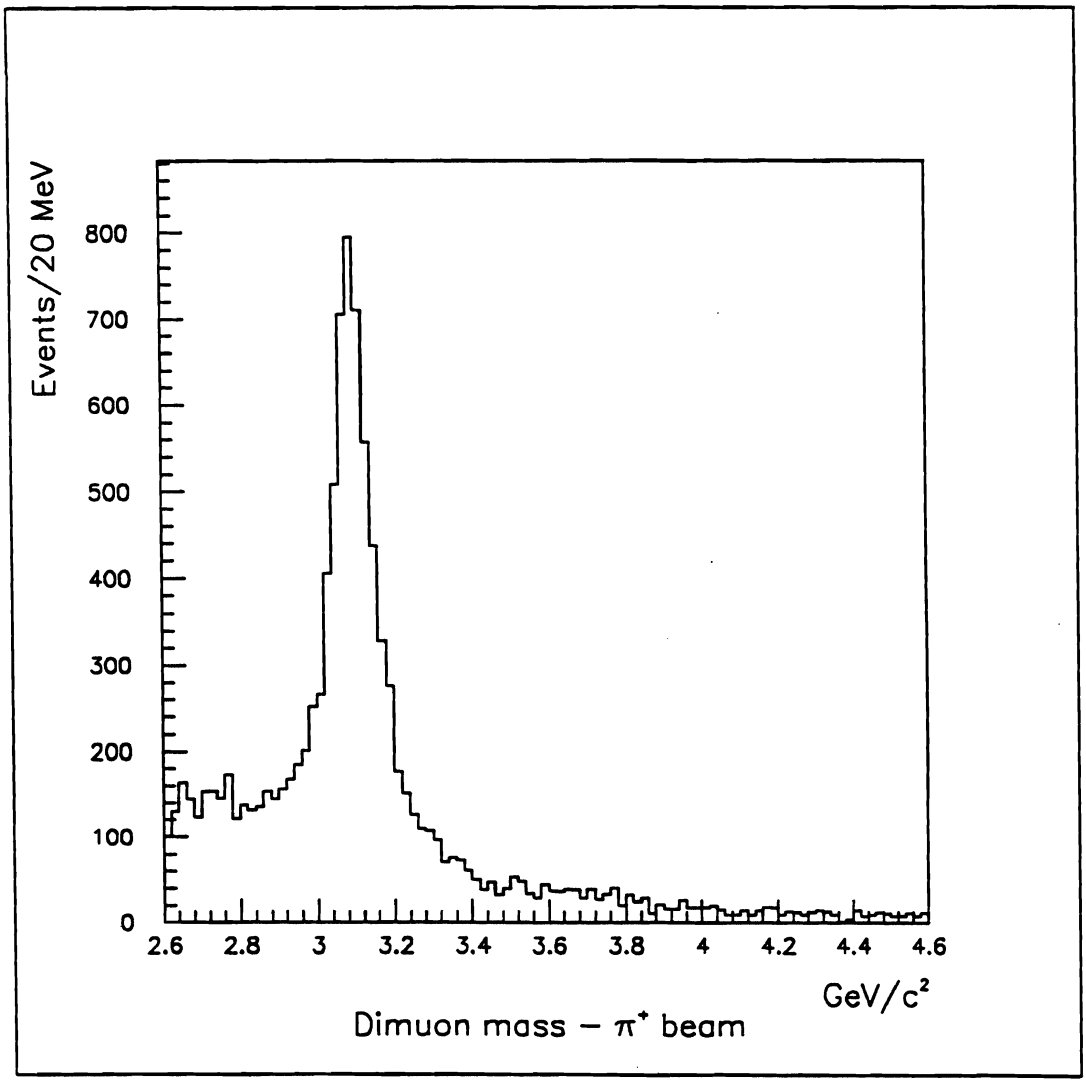

Figure 5.26 Dimuon mass: π+ beam

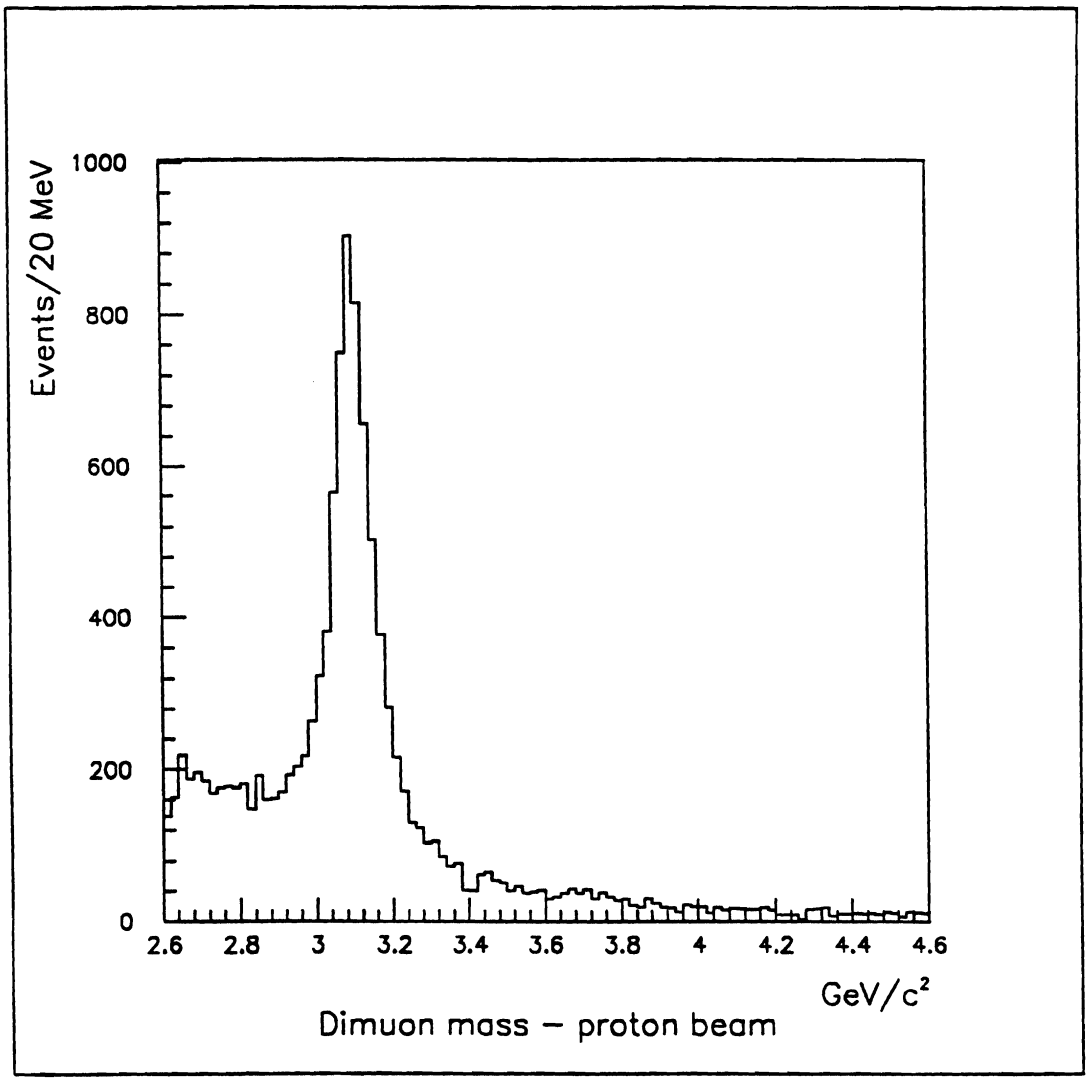

Figure 5.27 Dimuon mass: proton beam

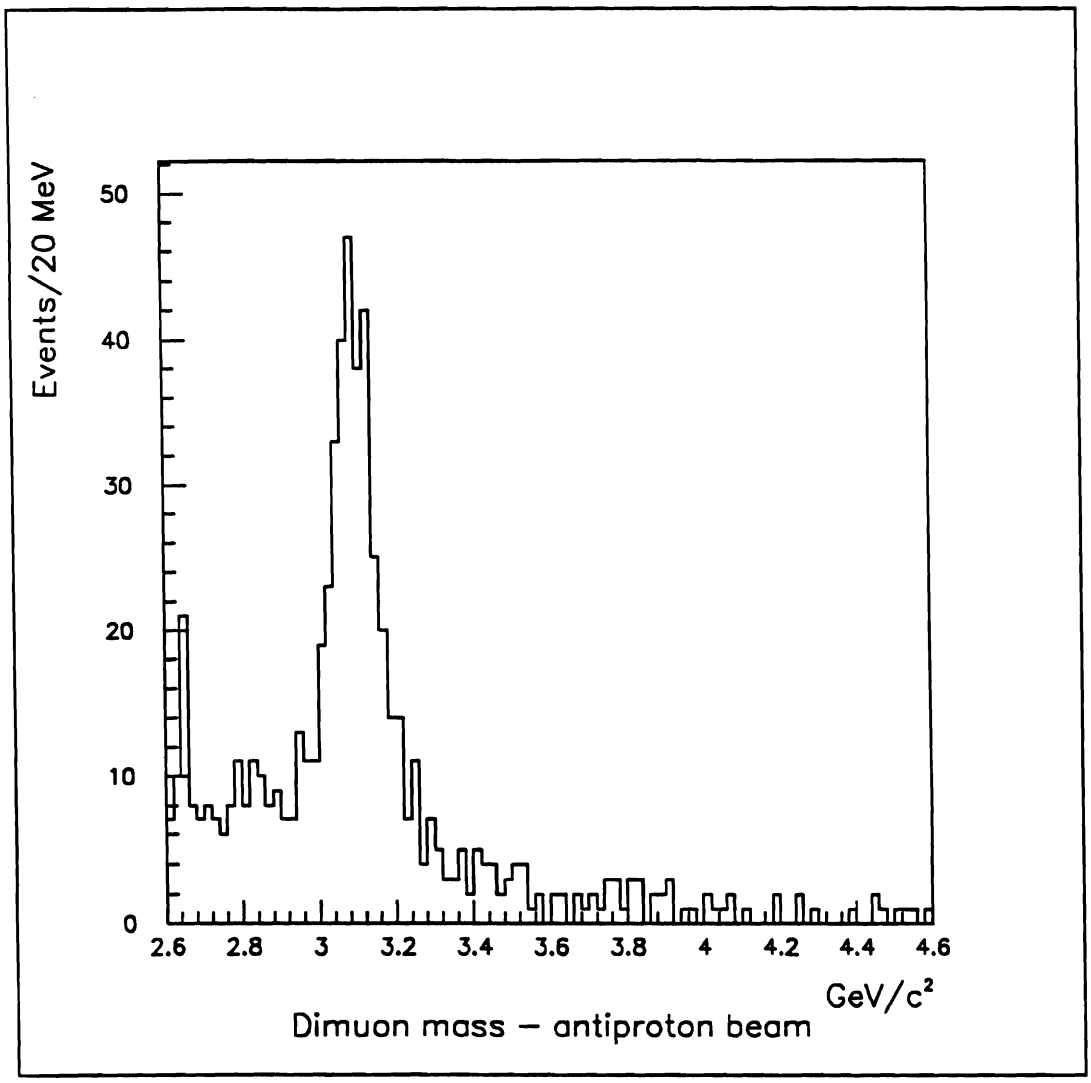

Figure 5.28 Dimuon mass: antiproton beam

Table 5.11

Reconstructed J/ψ's

Era	Beam Type	Number of J/ψ's
August Negative	π-	1500 ± 50
	antiproton	15 ± 7
September Negative	π-	6860 ± 120
	antiproton	48 ± 13
November Positive	π+	3190 ± 80
	proton	3260 ± 80
January Negative	π-	3000 ± 70
	antiproton	54 ± 12
January Positive	π+	2720 ± 80
	proton	2190 ± 70

The data from two periods were excluded from the inclusive cross-section analysis. The first was the August era data before tape YA0920. Tape YA0920 was the first alignment/efficiency tape; before that, we have no direct measurement of chamber efficiency. Extrapolating backwards in time seems risky, especially to a period where the spectrometer was still being tuned, and stable running conditions were being established. The second was the period between tape YA1290 and YA2077. This period had a number of intermittent hardware problems. For example, the X-plane in DC1 had an amplifier card that was exhibiting intermittent problems (many "hot channels") during this period. In addition, the residual distance between the track projection and the hit distribution showed a 40% increase over normal data, as well as over alignment data, and several chambers' efficiencies, as measured in data, varied by up to a factor of two. In these periods of widely fluctuating efficiencies, it is very difficult to extract a cross-section reliably, so this period was excluded.

Table 5.12

Reconstructed J/ψ's Included in Inclusive Cross-section Analysis

Era	Beam Type	Number of J/ψ's ($x_F > 0$)	Beam Particles (10^9)
August Negative	π-	830 ± 50	179 ± 18
	antiproton	15 ± 7	3.2 ± .3
September Negative	π-	3974 ± 120	749 ± 75
	antiproton	48 ± 13	11.7 ± 1.2
November Positive	π+	2603 ± 63	562 ± 34
	proton	2672 ± 67	725 ± 51
January Negative	π-	2514 ± 63	641 ± 71
	antiproton	54 ± 12	20.5 ± 2.3
January Positive	π+	1727 ± 51	485 ± 51
	proton	1829 ± 56	563 ± 45

Experimentally, a cross-section σ of a final state f is measured by

$$\frac{N_f}{N_{beam}\, N_n} \tag{5.14}$$

where N_f is the number of occurrences of final state f, N_{beam} is the number of incident beam particles, and N_n is the number of particles in the target per unit area. Expressing N_n in terms of the atomic number A, effective (corrected for absorption) target length L_{eff}, density ρ, and Avagadro's Number N_A we obtain:

$$\frac{N_f}{N_{beam}} \frac{A}{\rho\, L_{eff} N_A} \tag{5.15}$$

and where L_{eff} is given by:

$$L_{eff} = L_{abs}\,(\,1 - e^{-(L/L_{abs})}\,)\,. \tag{5.16}$$

Because our target is not a perfect right circular cylinder — the ends normal to the beam were not parallel — we used an indirect method to calculate its average length. The target's diameter was measured at for different positions along its length: 10.02, 9.98, 9.92 and 9.89 centimeters. The average radius is therefore 4.976 ± 0.003 centimeters. The target weighed 1347.5 ± 0.1 grams, and the density of lithium is 0.534 g/cm^3, so the volume is 2523 ± 5 cm^3, and since the area is given by πr^2, the average length is 32.43 ± 0.06 centimeters. This agrees with the target length measurement of 32.8 ± 1.0 centimeters, where the uncertainty arises from the non-parallel edges, but the uncertainty in the indirect measurement is substantially smaller. The indirect measurement has the additional advantage of automatically correcting for voids or gas bubbles inside the target. Using this method, the effective length is

$$L_{eff} = L_{abs} \left(1 - e^{-(m/\rho A L_{abs})} \right) . \tag{5.17}$$

Additionally, there must be a correction for efficiency and acceptance. This number, ε_A, was calculated in the above described Monte Carlo by dividing the number of reconstructed J/ψs passing all cuts by the total number generated. Since it is conventional to quote only forward hemisphere cross-sections, only those events with positive x_F were considered in this calculation. Tables 5.3 and 5.4 tabulate these efficiencies in each epoch. To go from the several dozen efficiency measurement points to the five eras, the efficiencies were averaged, weighted by the number of tapes nearest to the tape where the measurement was taken. The same procedure was followed to obtain a single efficiency measurement for all beam types.

Finally, the beam particle tagging efficiency, ε_{tag}, must also be incorporated. This is the probability that a particle identified as a proton (or pion) by the on-line

tagging will also be identified as a proton (or pion) by the off-line tagging. It is a correction for the "ambiguous" case.

With all corrections applied, the branching fraction times cross-section is give by:

$$\mathrm{BF}\,\sigma = \frac{N_f\,A}{N_{beam}\,\rho\,\varepsilon_{tag}\,\varepsilon_A\,N_A\,L_{abs}\,(1 - e^{-(m/\rho A L_{abs})})}. \tag{5.18}$$

In the antiproton case, an additional correction for Cerenkov counter efficiency is needed. If C1 has an efficiency $\varepsilon 1$ and C2 has an efficiency $\varepsilon 2$, a fraction $(1 - \varepsilon 1)(1 - \varepsilon 2)$ of the pions will be erroneously tagged as antiprotons. The correction to go from the observed cross-section to what it would be with no pion contamination is:

$$\sigma(\bar{p}) = \sigma(\bar{p})_{\mathrm{tag}} - \frac{N_\pi}{N_{\bar{p}}}\frac{\varepsilon_1\varepsilon_2\,(1-\varepsilon_1)(1-\varepsilon_2)}{\varepsilon_1 + \varepsilon_2 + \varepsilon_1\varepsilon_2}\,\sigma(\pi). \tag{5.19}$$

Since N_π/N_p is approximately 50 for negative beam and 0.7 for positive beam, and $\varepsilon_1 \approx 95\%$ and $\varepsilon_2 \approx 91\%$ the antiproton correction is 7% of the pion cross-section, but the proton correction is only 1/10 of 1%. This correction was therefore applied only to the antiprotons.

For comparison with other experiments, an additional correction is necessary; convention is to give cross-sections per nucleon. Our target was made of natural lithium with an admixture of some minor impurities, with an average $A = 6.94$.[47] Other experiments, such as E-537[48] and E-772[49] have shown that the cross-section for hadronically produced J/ψs does not grow linearly with the number of nucleons, but rather as A^α, with $\alpha = 0.92 \pm 0.008$. Accordingly, to convert between measured

cross-section per nucleus and cross-section per nucleus (for comparison with other experiments) we have to divide by $(6.94)^{0.92} = 5.94$. Table 5.13 shows our cross-section measurements (times branching fraction into two muons) for all eras and particle types per nucleus and per nucleon.

Table 5.13
J/ψ Branching Fraction times Cross-Section by Era ($x_F > 0$)

Era	Beam Type	B σ /nucleus (nb)	B σ /nucleon (nb)
August Negative	π-	57.7 ± 2.4 ± 6.0	9.7 ± 0.4 ± 1.0
	antiproton	49.6 ± 25.6 ± 5.1	8.4 ± 4.3 ± 0.9
September Negative	π-	60.3 ± 1.1 ± 6.1	10.2 ± 0.2 ± 1.0
	antiproton	42.4 ± 11.5 ± 4.3	7.1 ± 1.9 ± 0.7
November Positive	π+	66.0 ± 1.8 ± 4.3	11.1 ± 0.3 ± 0.7
	proton	54.9 ± 1.4 ± 5.7	9.2 ± 0.2 ± 1.0
January Negative	π-	77.0 ± 1.9 ± 8.8	13.0 ± 0.3 ± 1.5
	antiproton	42.7 ± 9.5 ± 5.0	7.2 ± 1.6 ± 0.8
January Positive	π+	57.5 ± 1.8 ± 6.3	9.7 ± 0.3 ± 1.1
	proton	48.3 ± 1.5 ± 4.1	8.1 ± 0.3 ± 0.7

There were four major sources of systematic errors: the uncertainty in the beam normalization, the uncertainty in the muon counter efficiencies, the statistical uncertainty in the Monte Carlo, and the uncertainty in the differential distributions. To obtain the final systematic error, the individual contributions were added in quadrature. This assumes that the various sources are independent. The Monte Carlo statistics were chosen so that this would not dominate the uncertainties — the typical contribution from the Monte Carlo per era was 1.5%. To obtain the differential distribution uncertainty, we compared the acceptance for protons with the acceptance for pions, and found that it is 21.3 ± 2.7% larger. Since the acceptance in transverse momentum is almost flat, this must be due to the uncertainty in Feynman-x. These

distributions differ in n_1 by 2.9 units, so there is an uncertainty in the inclusive cross-section in the forward hemisphere of 7.3 ± 0.9% per unit of uncertainty in n_1. For pions, this reduces to 1.1 ± 0.1%, and for protons we obtain 2.2 ± 0.3%. These are small in comparison to the uncertainties normalization and muon counter efficiencies. One way of interpreting this uncertainty is as the uncertainty in extrapolating the number of J/ψs from the region in x_F that we observe to the region where we cannot. Although we can measure just under half of the forward hemisphere ($0 < x_F < 0.475$), if the cross-section continues to decrease with increasing x_F, it is the half where the majority of ψs are produced, so the extrapolation error is small.

The following tables show the cross-section times branching fraction and cross-section for each beam type, averaged over all eras, weighted by the number of data tapes recorded in each era. Because of the recent Mark III result[50] that the J/ψ branching ratio to two leptons is 5.91 ± 0.11 ± 0.20 %, an improvement in precision of almost an order of magnitude, it is now reasonable to quote a cross-section for positive x_F without the branching fraction folded in; the uncertainty on the branching fraction is now small compared with experimental uncertainties.

Table 5.14
J/ψ Branching Fraction times Cross-Section ($x_F > 0$)

Beam Type	B σ /nucleus (nb)	B σ /nucleon (nb)
π-	63.7 ± 2.1 ± 6.9	10.5 ± 0.3 ± 1.1
π+	62.5 ± 2.1 ± 5.2	10.3 ± 0.3 ± 0.9
proton	50.4 ± 1.6 ± 5.3	8.4 ± 0.3 ± 0.8
antiproton	48.2 ± 6.7 ± 4.2	8.1 ± 1.1 ± 0.7

Table 5.15
J/ψ Cross-Section ($x_F > 0$)

Beam Type	σ /nucleus (nb)	σ /nucleon (nb)
π-	1080 ± 40 ± 120 ± 40	182 ± 7 ± 20 ± 7
π+	1060 ± 40 ± 90 ± 40	179 ± 7 ± 15 ± 7
proton	850 ± 30 ± 90 ± 30	143 ± 5 ± 15 ± 5
antiproton	820 ± 110 ± 70 ± 30	138 ± 19 ± 12 ± 5

It is also possible to calculate ratio of the π^+ cross-section relative to the proton cross-section:

$$\frac{\sigma(\pi^+)}{\sigma(p)} = \frac{N_\psi(\pi)\, N(p)\, L_{eff}(p)\, \varepsilon_A(p)}{N_\psi(p)\, N(\pi)\, L_{eff}(\pi)\, \varepsilon_A(\pi)} \tag{5.20}$$

This has the advantage of a lower systematic error, since the muon counter efficiencies divide out. The Cerenkov systematics are included in the ε_A's. For November data, $\sigma(\pi^+)/\sigma(p) = 1.254 \pm .046 \pm .033$, for January data, $\sigma(\pi^+)/\sigma(p) = 1.237 \pm .055 \pm .028$, and combining both eras yields a $\sigma(\pi^+)/\sigma(p)$ of $1.246 \pm .034 \pm .022$. No advantage accrues from doing this for the negative beam case, since the antiproton cross-section uncertainty is dominated by statistical rather than systematic uncertainties.

Chapter 6: States Heavier than 3.097 GeV/c^2

A. Monte Carlo

To study the geometric acceptance and reconstruction efficiency of heavier charmonium states, in particular the $\psi(2S)$ in its decays to $\mu^+\mu^-$ or $J/\psi\pi^+\pi^-$, modifications were made to the J/ψ Monte Carlo program. For the former, MCGEN (as described in Chapter 5) was modified to generate dimuons with a mass of 3686 MeV instead of 3097 MeV; for the latter the decay by two pion emission was included. Instead of generating two tracks, both muons, in the $J/\psi\pi^+\pi^-$ mode MCGEN creates four tracks — two muons and two pions. In both cases, the x_F and p_T distributions for the $\psi(2S)$ were taken to be the same as the J/ψ. The small sample and poor signal to noise of the ψ' precludes a direct measurement of the x_F and p_T distributions, but since both of these particles are vector charmonium states, with only a 20% difference in mass, it is reasonable to expect that the distributions in the kinematic variables will be similar. In the $\psi' \rightarrow J/\psi\pi\pi$ case, the dipion invariant mass distribution was chosen to agree with Mark III's observed distributions[51][52] (Mark III being a recent, high statistics measurement), and the decay angle distribution of the $\psi(2S)$ was taken to be isotropic, again because of absence of evidence to the contrary.

Approximately 600,000 accepted $\psi(2S)$'s in the dimuon channel and 200,000 in the $\psi 2\pi$ channel were generated.

Next, we attempt to measure the production of $\psi(2S)$'s, by fitting the data by two peaks on an exponential background, where the shapes of the peaks are determined from the Monte Carlo. The dimuon mass spectrum from the Monte Carlo (for pion beam data) is shown on the following page.

A fit to the form

$$\frac{1}{1 + z^2 - 0.05236z^3 + 0.01475z^4} \tag{6.1}$$

where $z = (m - m_{\psi(2S)})/\Gamma_{\psi(2S)}$, is superimposed. Note that the corrections induced by the z^3 and z^4 terms are small over the region of small z where the majority of $\psi(2S)$'s are reconstructed. The fit has a χ^2 per degree of freedom of 1.381 ($\nu = 95$). Because functions of the form $1/(1 + z^2 + \alpha z^3 + \beta z^4)$ are not guaranteed to have second moments, the standard deviation is not always defined. However, a full width at half maximum Γ always exists, and for a Gaussian distribution $\Gamma = 2.36\sigma$. Like the J/ψ case, we therefore define an extended standard deviation σ to be $\Gamma/2.36$. Under this convention, the Monte Carlo indicates $\sigma = 53.1$ MeV for π induced $\psi(2S)$'s.

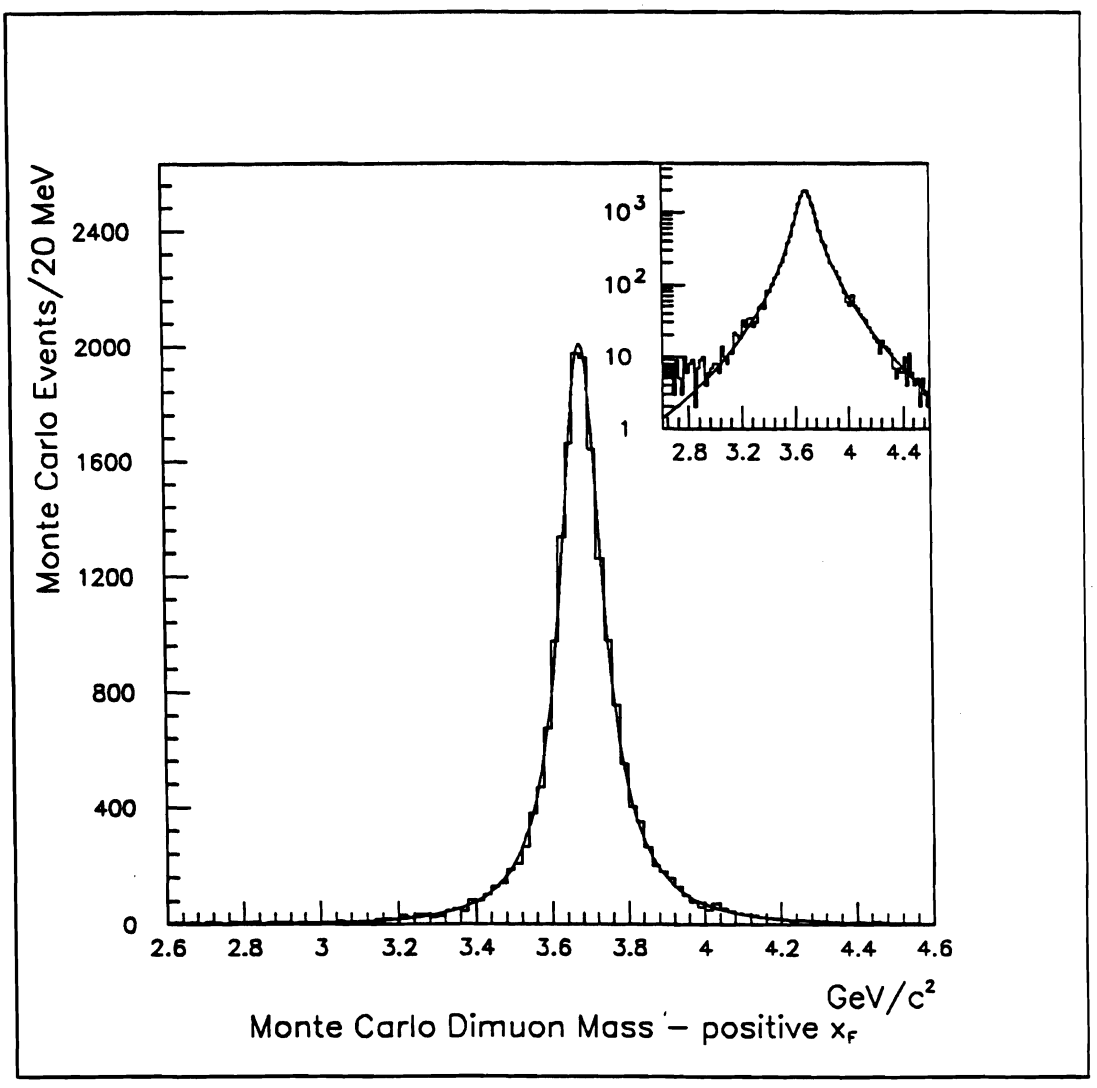

Figure 6.1 Monte Carlo ψ(2*S*) mass spectrum (pion beam)

For proton beam, the shape of the ψ(2*S*) is given by

$$\frac{1}{1 + z^2 - 0.20358z^3 + 0.12202z^4} \tag{6.2}$$

with $\sigma = 49.8$ MeV and a χ^2/ν of 1.201. Figure 6.2 shows the dimuon mass spectrum for $\psi(2S)$'s produced by protons.

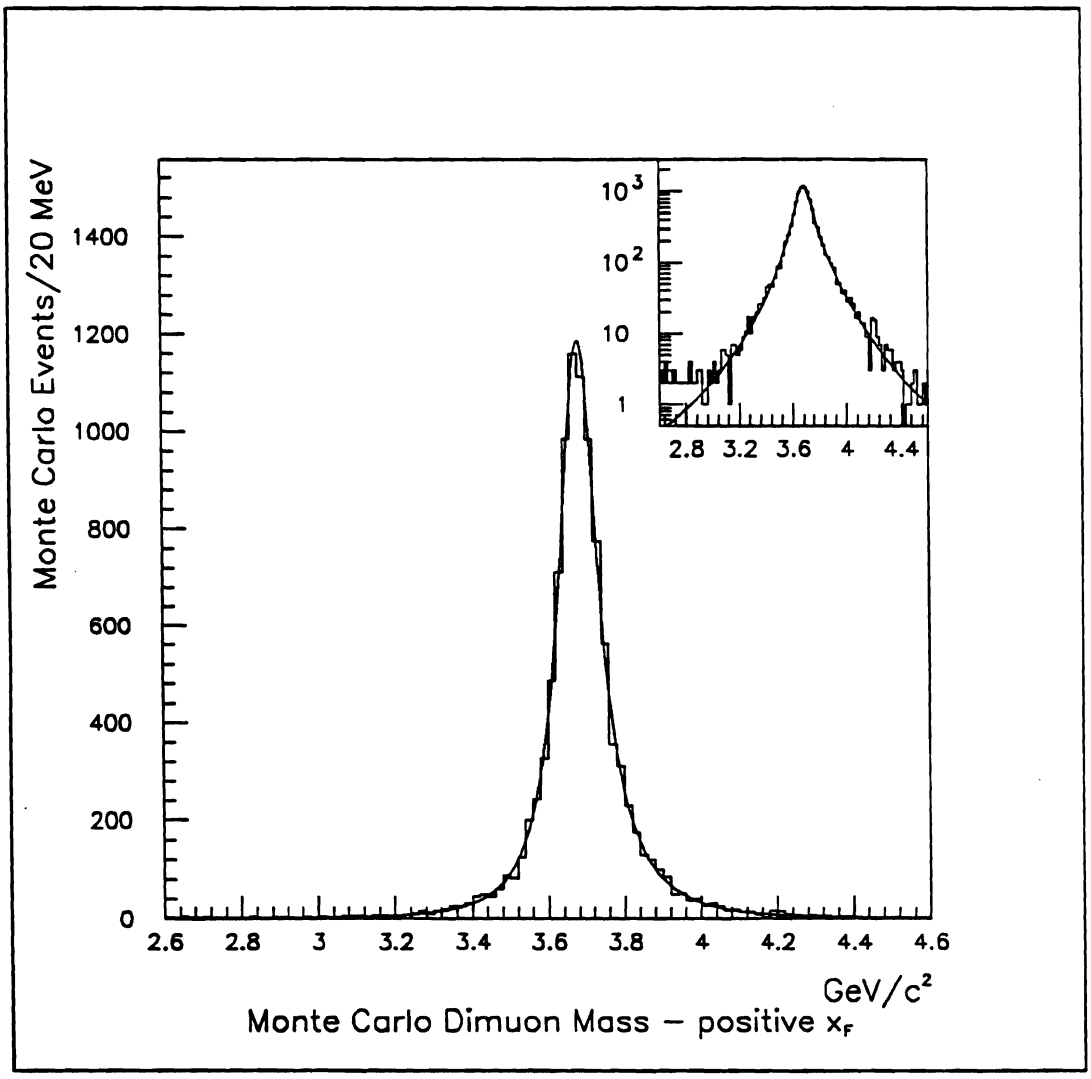

Figure 6.2 Monte Carlo $\psi(2S)$ mass spectrum (proton beam)

B. Dimuon spectrum & $\psi(2S)/\psi(1S)$ relative cross-section

The second pass cuts used in the ψ analysis do not sufficiently reduce background to show a clear $\psi(2S)$ signal. Tighter cuts were employed which kept 80% of the signal while cutting over half of the background (c.f. Table 6.1) Even so, the signal to noise ratio is only approximately 1:2.5. The dimuon mass spectrum is shown in figure 6.3.

Table 6.1
Cuts For $\psi(2S)$ Analysis

	Standard Pass 2 (Psi)	Psi Prime
Minimum Muon Momentum	no cut	6 GeV
Maximum Muon Momentum	320 GeV	100 GeV
Segment matching at magnet	4cm in x, 1cm in y	$\sqrt{12}\sigma$
Δ y-slope	15 mR	8 mR
μ momentum asymmetry	no cut	75%
Closest point of approach	no cut	12 mm

The σ in the segment matching cut refers to a defined by

$$\sqrt{\left(\frac{\Delta x}{0.218\text{cm}}\right)^2 + \left(\frac{\Delta y}{0.93\text{cm}}\right)^2} \qquad (6.3)$$

and is a measure of how well the muon tracks match at our matching plane of z = -4.8 centimeters. The numbers in the denominators are measured sigmas of the distribution of match deviations in the X and Y views. Independent Δx and Δy cuts have a shortcoming — a track that was barely within the limits in both x and y is of lower quality than a track with a marginal match in only a single view. If the resolution were the same in both x and y, a Δr cut (i.e. circular) would be reasonable. Since the resolution in the X view is four times better than that in the Y view, the area inside the

cut has an elliptical shape, with the axes determined by the widths of the match deviation distributions.

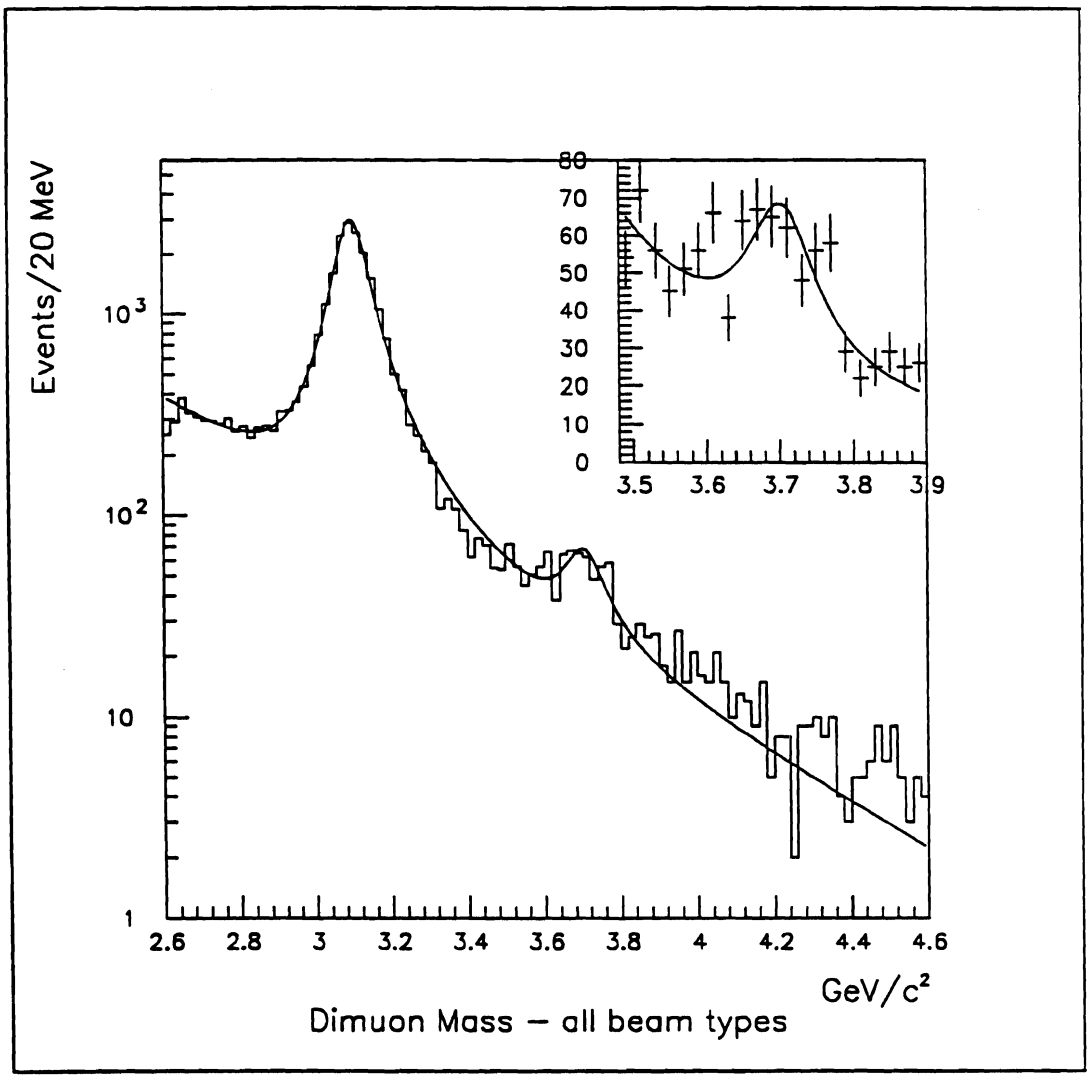

Figure 6.3 Dimuon mass spectrum with Table 6.1 cuts applied. All beam types.

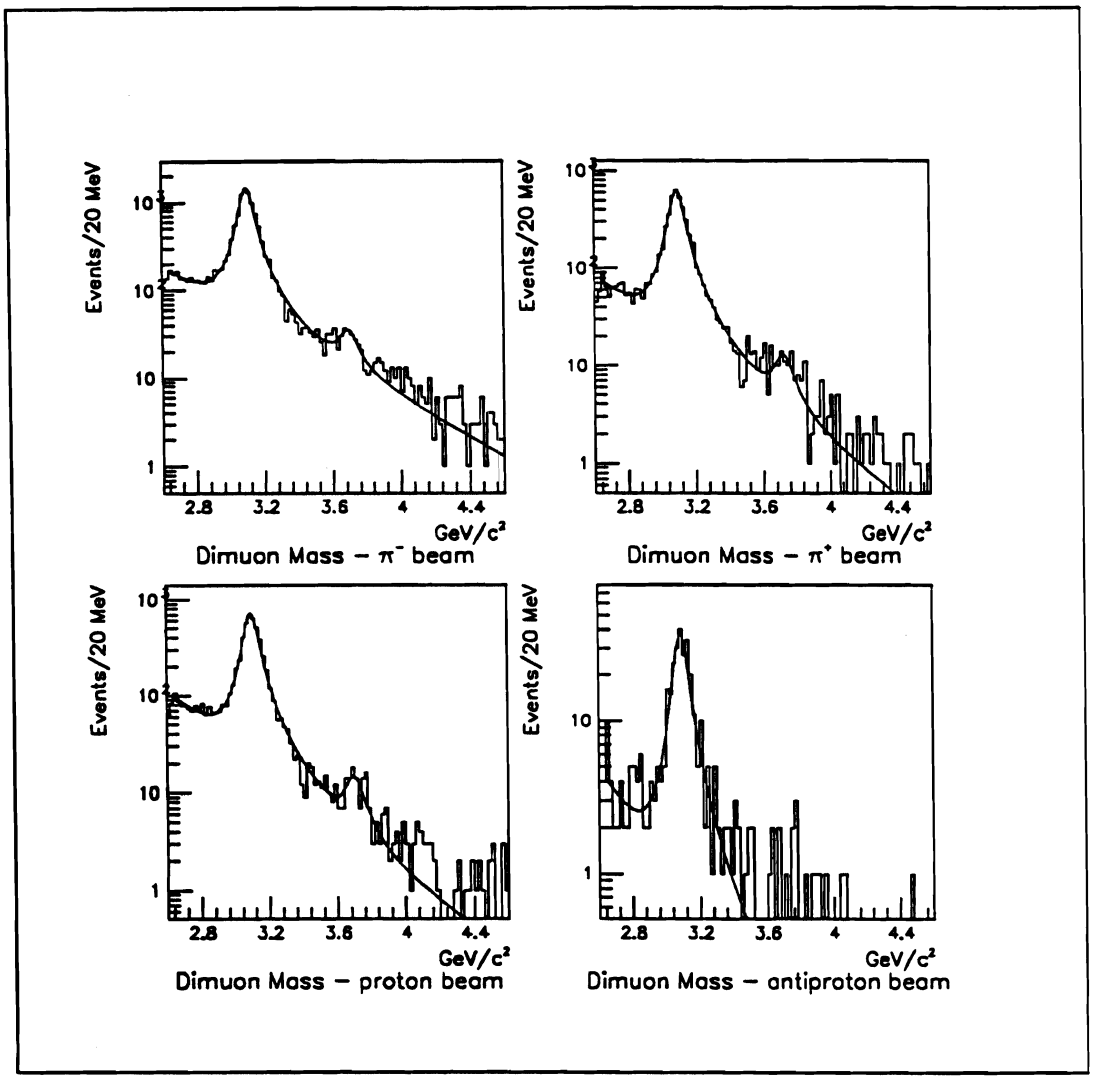

Figure 6.4 Dimuon mass spectrum with Table 6.1 cuts applied. Upper left, π^- beam. Upper right, π^+ beam. Lower left, proton beam. Lower right, antiproton beam.

The product of efficiency and acceptance for the $\psi(2S)$ was calculated using the same method as for the $\psi(1S)$ described in Chapter 5. Results are shown in tables 6.2 and 6.3.

Table 6.2

Monte Carlo Computed $\psi(1S)$ and $\psi(2S)$ Acceptance Times Efficiency Compared: π beam

Tape Number	ε_A for J/ψ (percent)	ε_A for ψ' (percent)
920	4.66 ± 0.13	5.22 ± 0.19
1209	4.41 ± 0.13	4.81 ± 0.19
1381	5.11 ± 0.14	6.00 ± 0.21
2150	5.00 ± 0.13	5.40 ± 0.21
2465	5.33 ± 0.13	6.14 ± 0.21
2770	4.10 ± 0.12	4.33 ± 0.19
3220	3.79 ± 0.12	4.80 ± 0.20
3669	4.03 ± 0.14	4.33 ± 0.18
3770	3.99 ± 0.13	4.56 ± 0.19
4200	4.21 ± 0.12	4.98 ± 0.20
4534	4.24 ± 0.12	4.74 ± 0.19
4871	3.92 ± 0.12	4.61 ± 0.19
5155	4.64 ± 0.13	5.50 ± 0.23
5420	4.29 ± 0.13	4.75 ± 0.19
5500	2.72 ± 0.11	3.38 ± 0.17
5751	2.92 ± 0.11	3.25 ± 0.15
6000	2.89 ± 0.11	3.41 ± 0.16
6130	1.92 ± 0.09	2.57 ± 0.15
6260	4.40 ± 0.12	5.10 ± 0.19
6500	3.78 ± 0.12	4.03 ± 0.18
6750	4.29 ± 0.13	4.44 ± 0.19
7000	4.41 ± 0.13	5.13 ± 0.20
7115	4.22 ± 0.13	5.02 ± 0.20

Table 6.3

Monte Carlo Computed $\psi(1S)$ and $\psi(2S)$ Acceptance Times Efficiency Compared: p beam

Tape Number	ε_A for J/ψ (percent)	ε_A for ψ' (percent)
3220	4.66 ± 0.13	5.38 ± 0.21
3669	4.74 ± 0.12	4.79 ± 0.19
3770	4.64 ± 0.13	5.47 ± 0.29
4200	4.81 ± 0.14	5.73 ± 0.22
4534	4.62 ± 0.13	5.20 ± 0.20
4871	4.61 ± 0.13	5.22 ± 0.20
6130	2.49 ± 0.09	2.80 ± 0.15
6260	5.41 ± 0.15	5.85 ± 0.27
6500	4.25 ± 0.12	4.92 ± 0.21
6750	4.72 ± 0.14	5.49 ± 0.22
7000	5.20 ± 0.14	5.47 ± 0.21
7115	4.91 ± 0.14	5.47 ± 0.22

To calculate the relative cross-section, the relative acceptance is a more useful measure than the era-by-era acceptance. Figures 6.5 and 6.6 show the acceptance times efficiency for the $\psi(2S)$ plotted against that for the $\psi(1S)$.

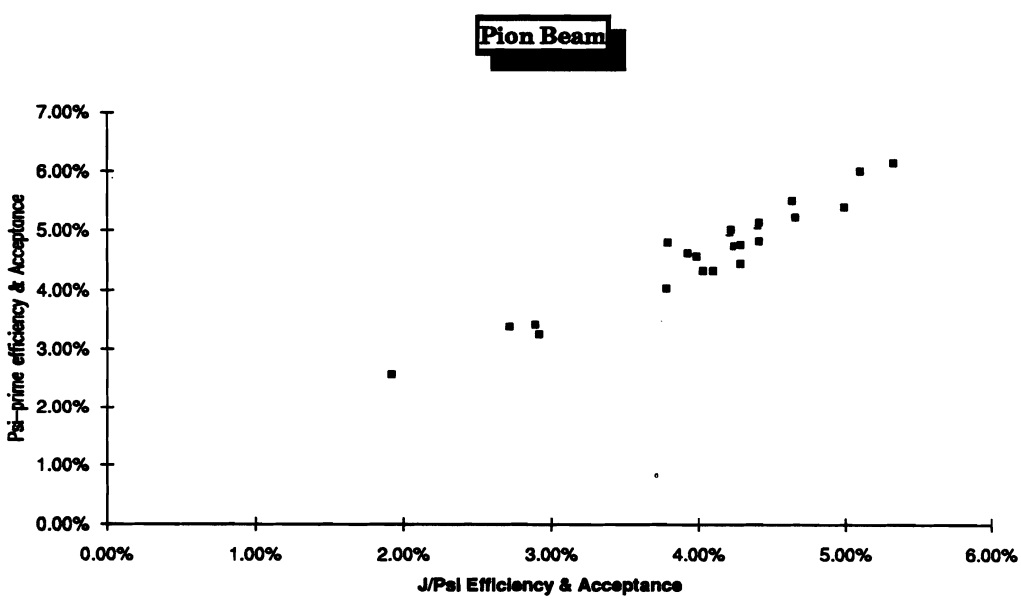

Figure 6.5 $\psi(2S)$ vs. $\psi(1S)$ acceptance times efficiency (pion beam)

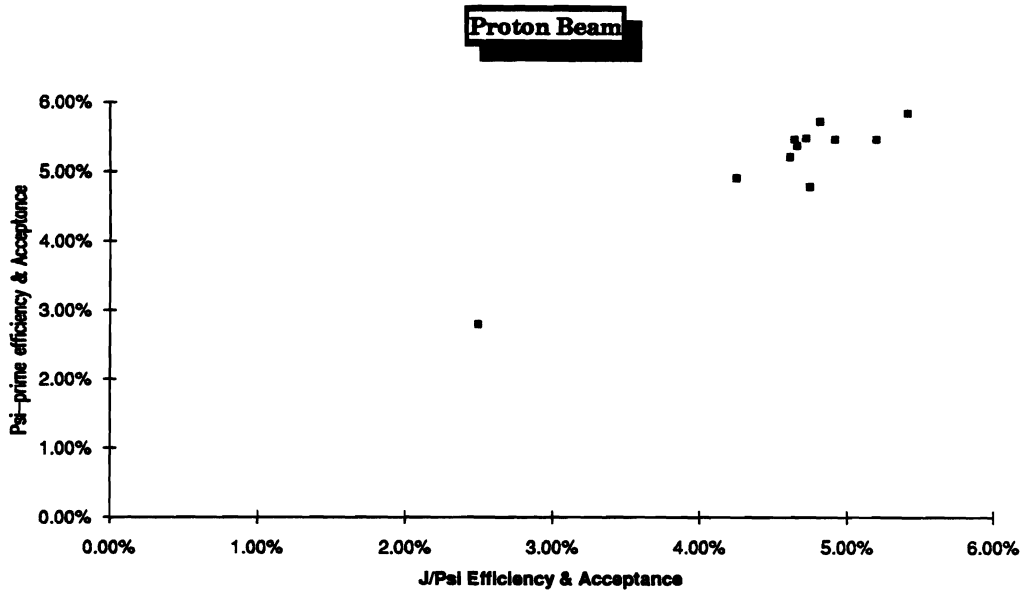

Figure 6.6 $\psi(2S)$ vs. $\psi(1S)$ acceptance times efficiency (proton beam)

Next, lines through the origin were fitted, and the slopes are the relative efficiencies for reconstructing $\psi(2S)$'s with respect to J/ψ's. For π beam, this is 1.142 ± .028 and for p beam it is 1.120 ± .031 %. Approximately a factor of 1.08 is due to the trigger processor; it is much less likely that a state of mass 3.686 GeV/c^2 will be reconstructed by the trigger processor as having a mass under 2.4 GeV/c^2 than a state of mass 3.097 GeV/c^2. The remaining 1.04-1.06 is due to the slightly larger average opening angle of $\psi(2S)$'s relative to J/ψ's.

The mass spectra were fit to the Monte Carlo shapes of the J/ψ and ψ' and an exponential background. The ratio of the number of observed ψ's to the number of observed J/ψs, R, was one of the parameters of the fit. This automatically removes the correlation between the uncertainty in the number of reconstructed ψ's and the number of reconstructed J/ψs. If the relative reconstruction efficiency and acceptance

is given by E, the relative branching fraction times cross-section is given by equation 6.4:

$$\frac{BF \cdot \sigma(\psi(2S))}{BF \cdot \sigma(\psi(1S))} = \frac{R}{E} \quad . \qquad (6.4)$$

The ψ' cross-section times branching fraction measured relative to the ψ is given below. The first errors are statistical, the second systematic.

Table 6.4
$\psi(2S)$ Production Cross-Section times Branching Fraction

Beam	Observed Ratio $\psi(2S)/\psi(1S)$	Relative Acceptance $\psi(2S)/\psi(1S)$	$BF \cdot \sigma$ $\psi(2S)/\psi(1S)$
π^+	1.9 ± 0.5 %	1.142 ± 0.028	1.66 ± 0.44 ± 0.04 %
π^-	2.2 ± 0.3 %	1.142 ± 0.028	1.93 ± 0.26 ± 0.05 %
$\pi^\pm$	2.2 ± 0.3 %	1.142 ± 0.028	1.93 ± 0.26 ± 0.05 %
proton	2.1 ± 0.3 %	1.120 ± 0.031	1.88 ± 0.27 ± 0.05 %
antiproton	3.9 ± 3.4 %	1.120 ± 0.031	3.48 ± 3.04 ± 0.10 %
all	2.2 ± 0.2 %	1.136 ± 0.019	1.94 ± 0.26 ± 0.03 %

Taking the $\psi(2S) \rightarrow \mu^+\mu^-$ branching fraction to be the weighted average of the observed $\psi(2S) \rightarrow \mu^+\mu^-$ and $\psi(2S) \rightarrow e^+e^-$ branching ratios (i.e. assuming lepton universality) or .82 ± .11% and the $\psi(1S) \rightarrow \mu^+\mu^-$ branching fraction as the Mark III measurement[53] of 5.91 ± 0.11 ± 0.20 %, the relative probability of a dilepton decay is 7.2 ± 1.0 times greater for the J/ψ than the ψ'. This can be used to express the data in terms of relative cross-sections, shown in the table on the following page. The first errors are statistical, the second systematic, and the third reflect the uncertainty in the relative dilepton branching fractions.

Table 6.5

$\psi(2S)$ Production Cross-Section

Beam	BF · σ $\psi(2S)/\psi(1S)$	Relative Cross-Section (σ) $\psi(2S)/\psi(1S)$
π^+	1.66 ± 0.44 ± 0.04 %	12 ± 3 ± 0.3 ± 2 %
π^-	1.93 ± 0.26 ± 0.05 %	14 ± 2 ± 0.4 ± 2 %
$\pi^\pm$	1.93 ± 0.26 ± 0.05 %	14 ± 2 ± 0.4 ± 2 %
proton	1.88 ± 0.27 ± 0.05 %	14 ± 2 ± 0.4 ± 2 %
antiproton	3.48 ± 3.04 ± 0.10 %	25 ± 22 ± 0.7 ± 4 %
all	1.94 ± 0.26 ± 0.03 %	14 ± 2 ± 0.2 ± 2 %

C. $\psi 2\pi$ spectrum and $\psi(2S) \rightarrow \mu\mu$ branching fraction

In addition to the decay $\psi' \rightarrow \mu^+\mu^-$ there is also a decay $\psi' \rightarrow \psi\pi^+\pi^-$; if the J/ψ subsequently decays to a pair of muons, we can trigger on these events. This requires reconstructing non-muon tracks in addition to muons.

E-705 had no RICH or similar detector for explicit particle identification: pions were identified as follows: a track that could be identified as neither a muon nor an electron was declared to be a pion. Since most hadrons produced in these interactions are pions, it is reasonable to assume a track to be a pion unless there is evidence to the contrary. As described in Chapter 4, a track that points to a muon triple coincidence (within distances given in Table 4.2) is identified as a muon. In the 170,000 event sample of dimuon candidates, fewer than 100 events contain a third muon passing all of the cuts.

Electrons are useful for shower calibration purposes, important for the $\chi \rightarrow \psi\gamma$ aspect of this experiment. Once a sample of electrons has been identified, there is no reason not to remove them from the pion data sample. Furthermore, they can also be used as a diagnostic for our ability to reconstruct low momentum tracks.

These electrons are identified primarily via calorimeter information; electrons will deposit all of their energy E (equal to their momentum p) in the calorimeter. To

start, there is a requirement that at least 2 GeV be deposited in a cluster of blocks. Tracks with less than 2 GeV are not accepted by the spectrometer, so a cluster under 2 GeV will not be identified as an electron anyway. Below 2 GeV, the energy measurement of a shower becomes difficult. First, the fractional resolution of our calorimeter is proportional to $1/\sqrt{E}$, so as E decreases the uncertainty on E increases. Secondly, the Molière radius is proportional to $1/E$, so low energy showers are distributed over more calorimeter blocks than high energy showers; the energy per unit block falls even more rapidly. Our electromagnetic reconstruction algorithm has a requirement of 1 GeV in the peak calorimeter block, a requirement that few showers under 2 GeV meet.

Next, we required that a track point to the shower: within 3 centimeters in both the X and Y views. This also requires some energy (200 MeV) deposited in the active plane, which had position resolution superior to the main array.

In addition, there was a shower shape requirement. Electromagnetic showers have a well-defined shape; hadronic showers on the other hand have a less well-defined shape, and one that is in general broader than the electromagnetic shape. The amount of energy that should have been deposited in each calorimeter block for an electromagnetic shower of energy E was calculated from tables derived from an EGS Monte Carlo simulation, and a χ^2 per degree of freedom was calculated. If this was low (below 10) the shower was identified as electromagnetic.

Unlike hadrons, electrons shower early — begin depositing energy in the active plane. Figure 6.7 shows E/p as a function of the active plane energy divided by $\sqrt{E}$, the square root of the total energy in the shower for showers with at least 200 MeV in the active plane. This particular figure of merit was chosen because the active plane is a sampling device; the energy deposited in a thin layer is proportional to the

square root of the total energy. The band at *E/p* near 1 is due to electrons, and the band at active plane energy divided by $\sqrt{E}$ near zero is due to hadrons.

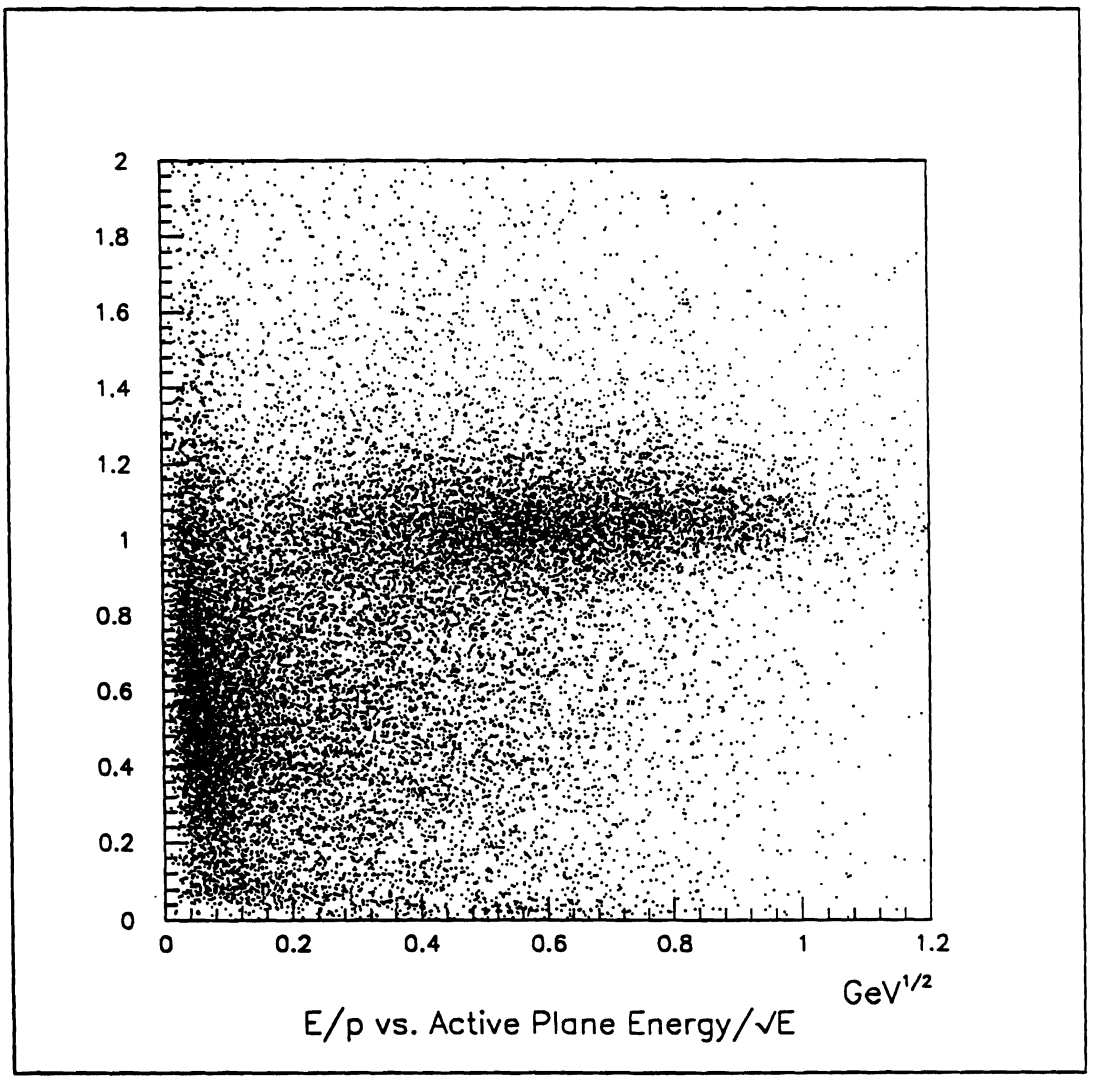

Figure 6.7 *E/p* vs. Active Plane Energy/$\sqrt{E}$

A summary of the requirements to identify a track as an electron are listed in table 6.6, and an *E/p* distribution for these candidates is shown in Figure 6.8. The low *E/p* tail is due to hadrons.

Table 6.6
Electron Identification Cuts

Item	Cut
E/p	between 0.8 and 1.2
Shower Shape	$\chi^2 < 10$
Active Plane Energy	> 200 MeV
	$> .15\ (\mathrm{GeV})^{1/2}/\sqrt{E}$
Cluster Proximity to Track Position	> 3 cm in x and y
Cluster Energy	> 2 GeV

Approximately 9000 electrons were identified in the J/ψ candidate data sample. This corresponds to 5.3% of the tracks being identified as electrons.

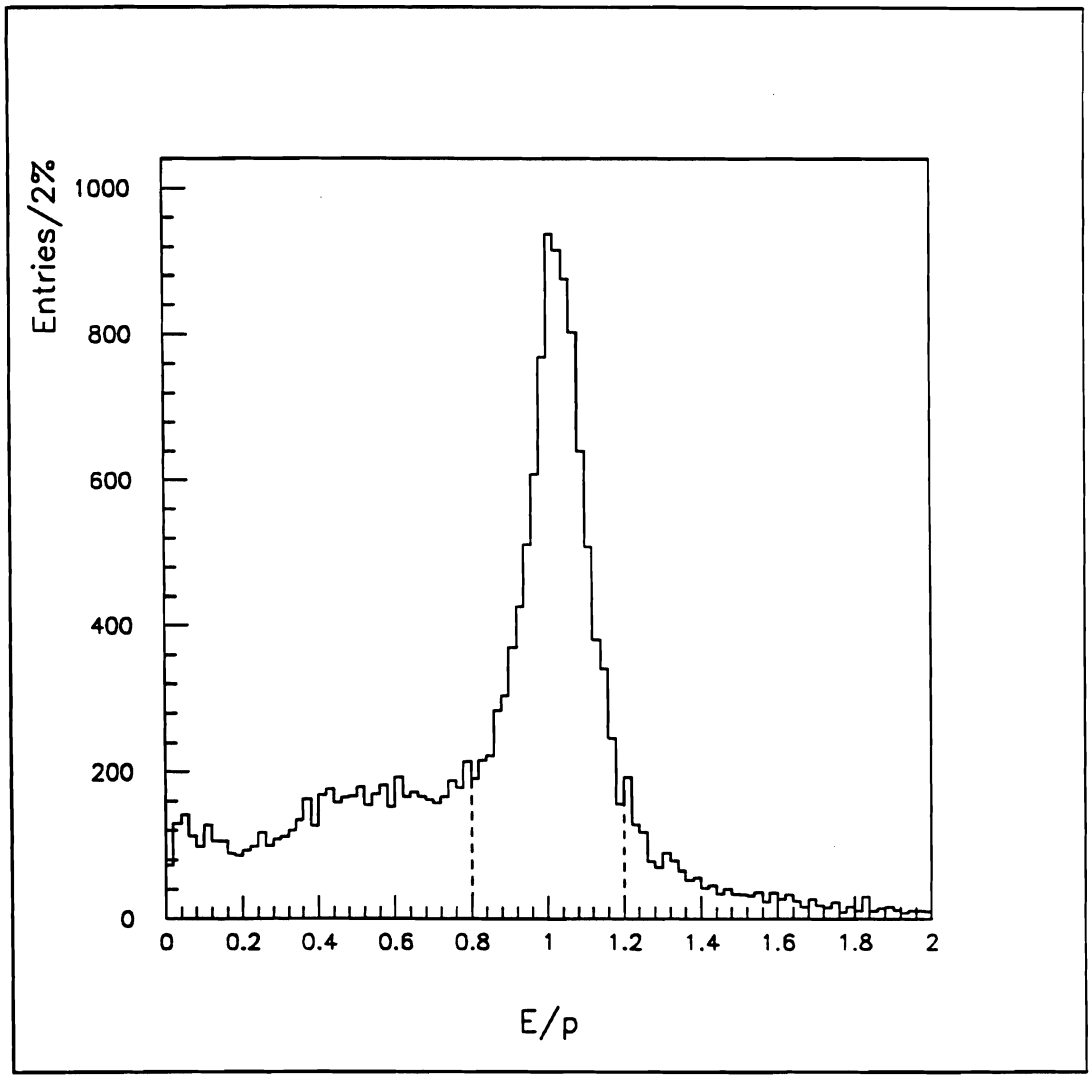

Figure 6.8 *E/p* for electron candidates

Pions of all charges are produced in equal numbers. Neutral pions decay into two photons, and since the majority of charged tracks are pions, the number of photons is therefore approximately the same as the number of charged tracks. Our target is 20% of a radiation length, and on average the interaction occurs in the middle of the target, allowing 10% of the produced photons to convert to electron-positron pairs. On the following page is the dielectron mass distribution for these electron

candidates.The pairs with opposite charge show a peak at low invariant mass consistent with this production mechanism; the pairs with the same charge do not. The 5.3% of tracks being identified as electrons is consistent with an electron component of tracks being 10% of the pion component. Acceptance for electrons is lower than that of pions because their mean momentum is smaller, causing more of them to be swept outside the spectrometer by the magnet. Also, these cuts are not perfectly efficient: some real electrons are not identified as such. This inefficiency is not critical for this analysis: the intention is to remove particles which are obviously not pions from the pion data sample, even though the potential contamination was small to begin with.

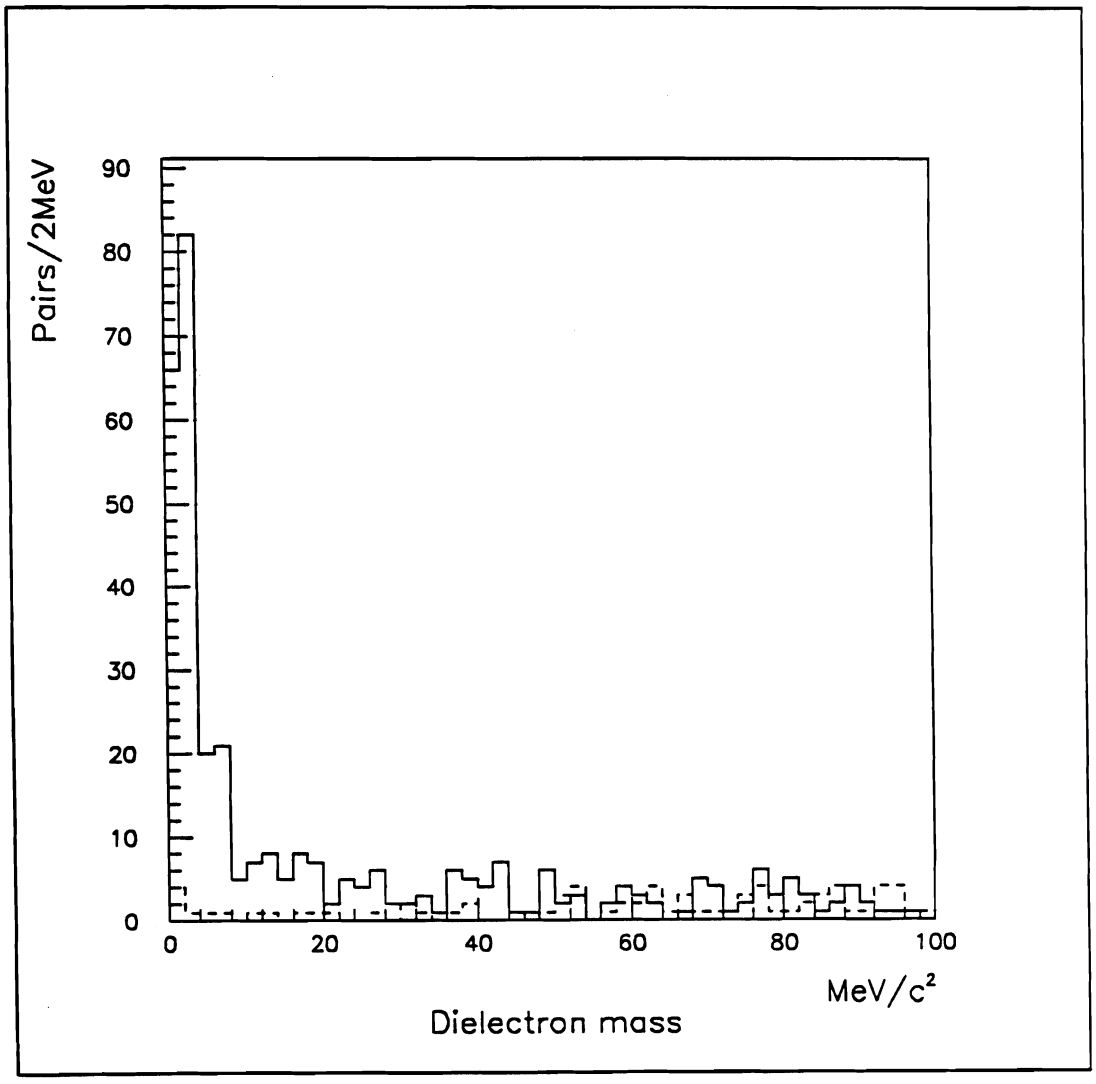

Figure 6.9 Dielectron mass for electron candidates. The solid line is the mass distribution for opposite signed pairs, the broken line for like signed pairs. The peak at low mass in the opposite signed spectrum is from photon conversions.

Besides the particle identification requirements, other cuts were imposed for the $\psi\pi\pi$ channel analysis. These cuts are listed in the following table:

Table 6.7

Cuts for $\psi\pi\pi$ Analysis

Item	Cut
Dimuon Mass (Psi selection)	within 2σ of J/ψ
Δy slope (pions)	< 10 mR
Rear segment χ^2 (pions)	< 6
Pion multiplicity	< 6 /event
Dipion mass	> 80% of maximum
Pion particle i.d.	No muon triple coincidence
	Not an identified electron
Number of distinct upstream segments	4

The dimuon mass cut is intended for J/ψ selection, and is based on the width of the J/ψ, as measured by a single Gaussian fit, is, as a function of the J/ψ momentum p:

$$\sigma(p) = \frac{.92\ \text{MeV}}{p}, \tag{6.5}$$

The y-slope cut and rear segment χ^2 cut are track quality cuts. The χ^2 cut is set at the same value as for the dimuon analysis, while the y-slope cut is tighter. Very few J/ψ's fail this tighter cut, but for the cross-section analysis, statistics were more important than signal to noise. In this analysis, because of the large backgrounds, signal to noise is at more of a premium, so the somewhat tighter cut is employed.

One of the best cuts for reducing signal to noise is the multiplicity cut. At most, there is one real $\psi\pi\pi$ decay in an event. However, with P positive pions and N negative pions, there are PN entries in the mass plot; those rare events that have high multiplicities dominate the histogram. (For example, an event with 7 positive and 5

negative pions can have at most one real $\psi\pi\pi$ combination, but will contribute 35 entries in the plot. Removing high multiplicity events reduces the combinatoric background.) The average number of identified pions in an event is 3.3 in negative beam data and 3.6 in positive beam data. Requiring at most five (matched) pions in an event reduces the number of entries by almost a factor of three, but reduces the signal by under 10%. This was calculated by observing that there were 1916 ± 66 J/ψs failing the multiplicity cut out of a total of 20731 ± 180. Dividing, one sees that 8.7 ± .4 % of the ψs fail the cut, or 91.3 ± 0.4 % pass it.

The requirement for a high dipion mass seems rather mysterious; however, it is justified. Phase space considerations in the decay $\psi' \rightarrow \psi\pi\pi$ yield the dipion mass distribution below:

$$\frac{d\Gamma}{dm_{\pi\pi}} \sim \sqrt{(m_{\psi'}^2 - m_\psi^2)^2 - 2(m_{\psi'}^2 + m_\psi^2)^2 m_{\pi\pi}^2 + m_{\pi\pi}^4}\sqrt{(m_{\pi\pi}^2 - 4m_\pi^2)} \qquad (6.6)$$

Brown and Cahn[54], and others, point out that chiral symmetry considerations modify this by a factor of

$$(m_{\pi\pi}^2 - 2m_\pi^2)^2. \qquad (6.7)$$

This has the effect of skewing the dipion mass distribution towards the high end. This model is admittedly simple; it does not include chiral symmetry breaking terms nor final state pion scattering. Nevertheless, Mark III data[55] shows this predicted high mass excess. Requiring the dipion mass to be at least 80% of its maximum value in this model passes 69% of the ψ's. If the background dipion mass

distribution is given by only phase space considerations, only 37.7% background events pass this cut, resulting in an improvement in the signal-to-noise ratio of nearly 2.

There are several reasons to require four distinct upstream segments. First, this cut also imposes a requirement that all four tracks be matched at the magnet. Second, it eliminates electron-positron pairs from conversions, because these conversion pairs share a single upstream segment. Finally, it eliminates the case where a single upstream track is matched to two downstream tracks, one pointing to a muon triple coincidence. In this case, one of the upstream segments may have not been found by the tracking, and the other segment matched to the incorrect one. For example, the upstream and downstream segments to the pion may be found, and the downstream segment of the muon erroneously linked with the upstream segment of the pion. This induces a systematic error of unknown magnitude in the momentum determination of the muon. By removing these events, we avoid this problem.

Backgrounds were generated in two ways: mispairing dimuons from one event with dipions from another, which preserves dipion correlations (such as caused by $\rho \rightarrow \pi\pi$ decays) and allows arbitrarily high statistics, and looking at the same sign pion ($\psi\pi^{\pm}\pi^{\pm}$) events. Mispairing does have some limitations: although the dipion correlations are preserved, the true background also has ψ-dipion correlations which are removed by this technique. For example, transverse momentum must balance; there is a correlation caused by spectator quark hadronization; in a color evaporation model, there will be also correlations due to the hadronization (into pions) of the bleaching gluon. Also, the requirement that the ψ and both pions be accepted forces the ψ into a restricted range of momentum, so the mass of a mispaired combination is not greatly displaced from that of a correctly paired one.

For the mispairing technique, each event was paired with the 100 previous events. A check on the ability of the mispairing to generate the correct background is to see how well the same-sign mispaired agrees with the same-sign correctly paired spectrum. The backgrounds are shown below, separately and together, normalized to the same number of entries.

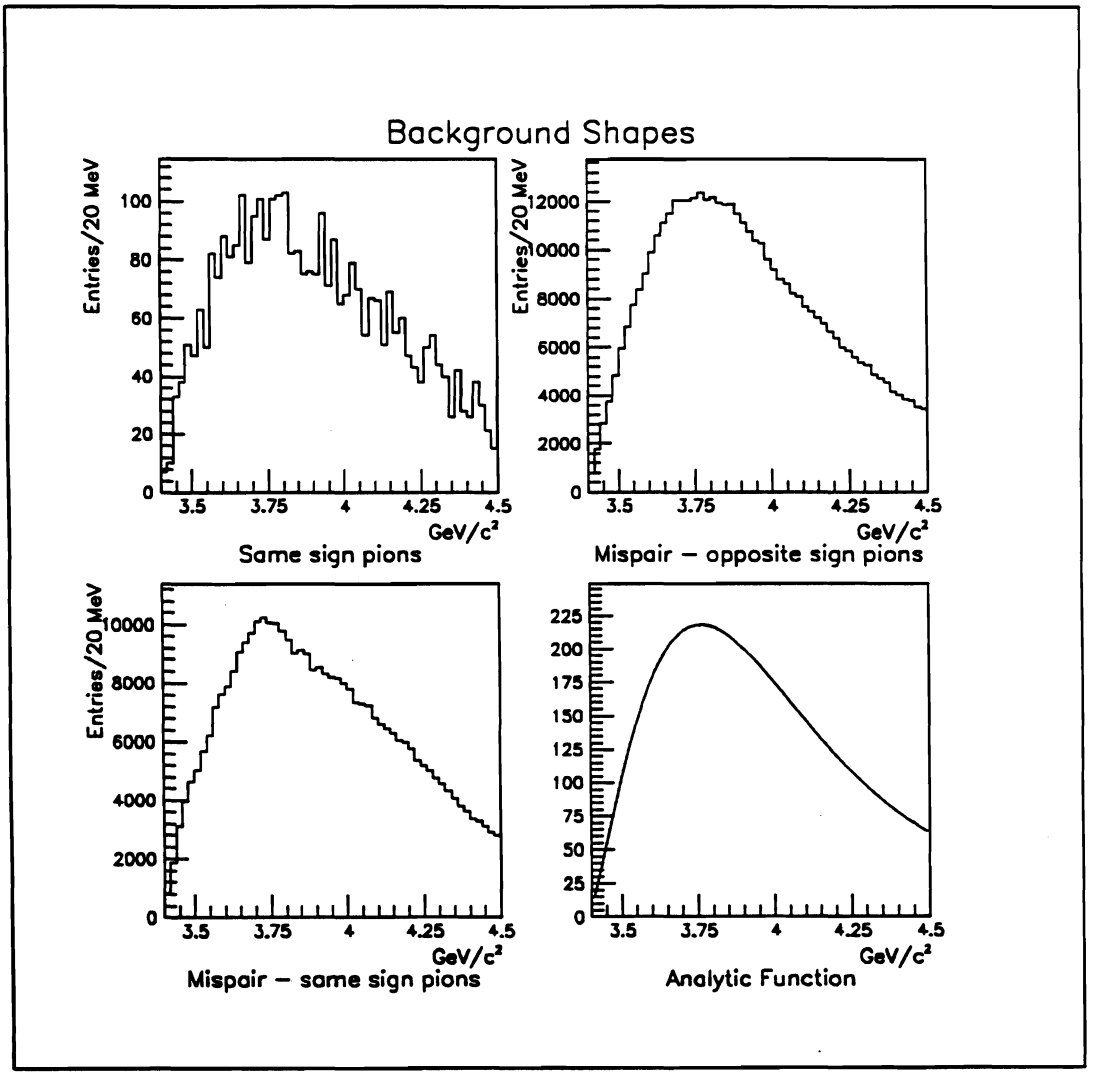

Figure 6.10 Backgrounds for $\psi\pi\pi$, standard cuts. Upper left: Same-sign pions. Upper right: Mispaired events, opposite signed pions. Lower left: Mispaired events, same-sign pions. Lower right: Analytic background curve fit to mispair data.

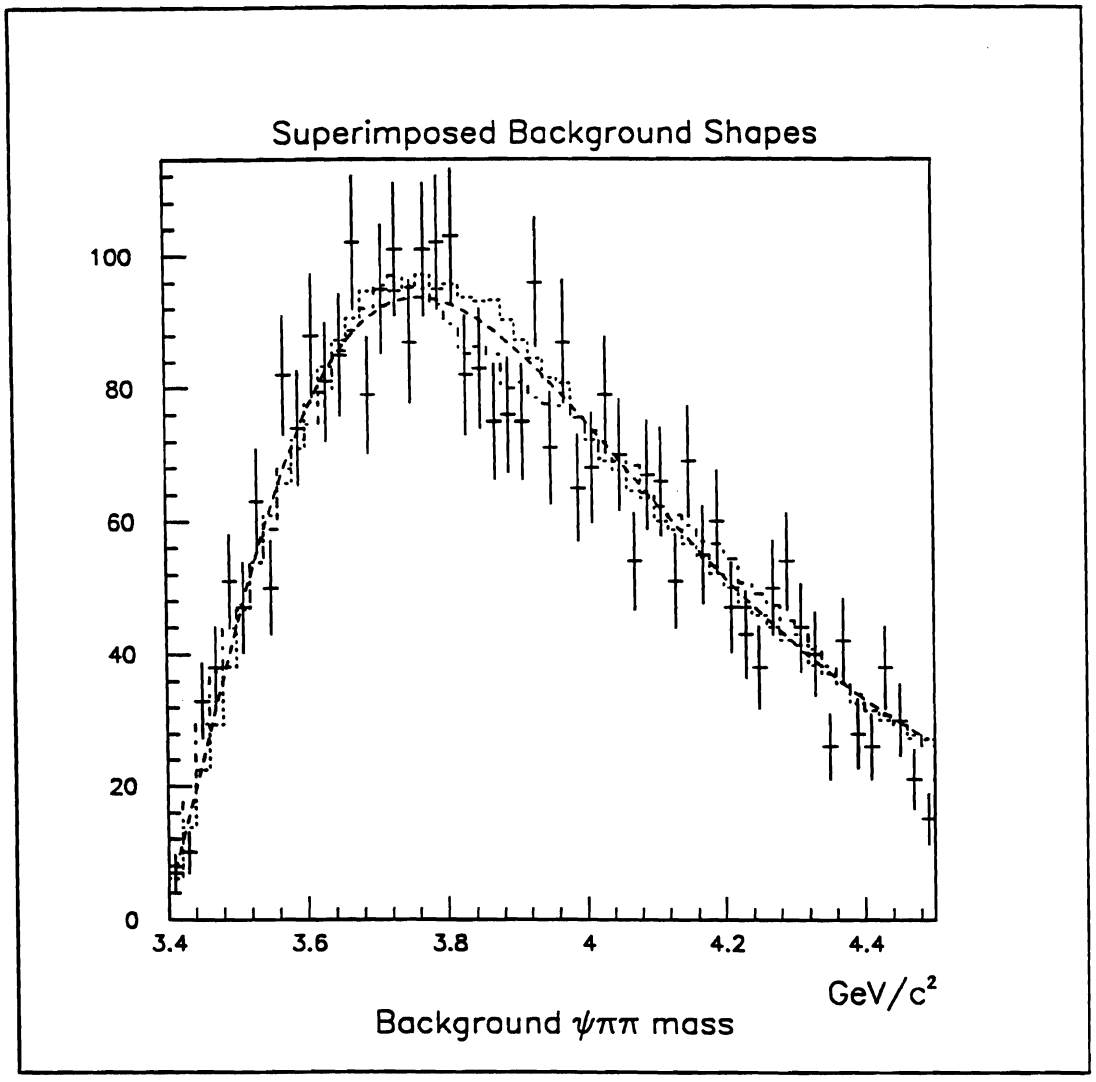

Figure 6.11 Backgrounds for ψππ, standard cuts, overlaid.

The expression for the background shape for the various sets of cuts is:

$$\frac{d\sigma}{dm} = \alpha e^{[-(\gamma z)^2 - \delta z^3]} \, [z + \eta z^2] \qquad (6.8)$$

where $z = (m - \beta)$, and α, β, γ, δ and η are all parameters of the fit. The parameter α is a measure of the height of the background, and the other four determine the shape. This shape depends on the cuts used. In particular, when looking at the $\psi\pi\pi$ spectrum in bins of dipion mass, β in particular is dependent on the dipion mass, as given by $\beta \approx m(\psi) + m(2\pi)$.

The dipion mass spectrum for the negative beam (predominantly pion) is shown on the following page. The September data excluded from the J/ψ analysis is also excluded here. Whatever is reducing the efficiency of reconstructing the ψ is also going to make it difficult to reconstruct the ψ'. It will probably affect the ψ' to a greater degree, since four tracks, rather than two, have to be reconstructed.

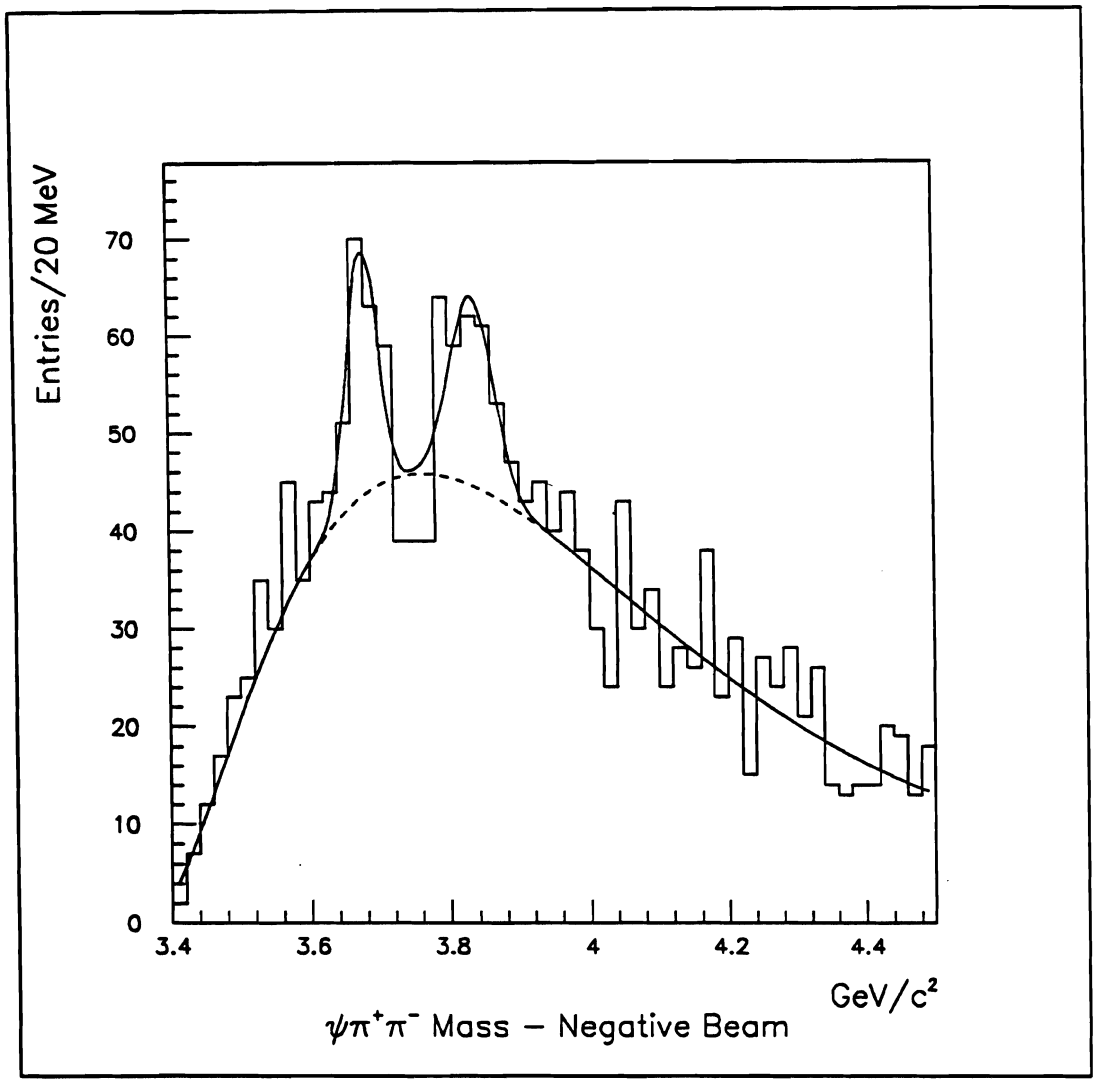

Figure 6.12 $\psi\pi\pi$ mass spectrum, standard cuts, negative beam.

A single peak above background does not fit the observed signal well. A second peak above the ψ' was added to the fit to improve this. The fit parameters are shown on the following page:

Table 6.8

$\psi' \rightarrow \psi\pi\pi$ Decays, Negative Beam

	Peak One	Peak Two
Number of Entries	68 ± 16	74 ± 22
Mass	3678 ± 6 MeV	3842 ± 10 MeV
Width (σ)	21 ± 6 MeV	31 ± 6 MeV

For the positive beam, no obvious peaks appear, as shown in the following figure. The fitted curve is the best fit to the background shape, allowing only the height to vary.

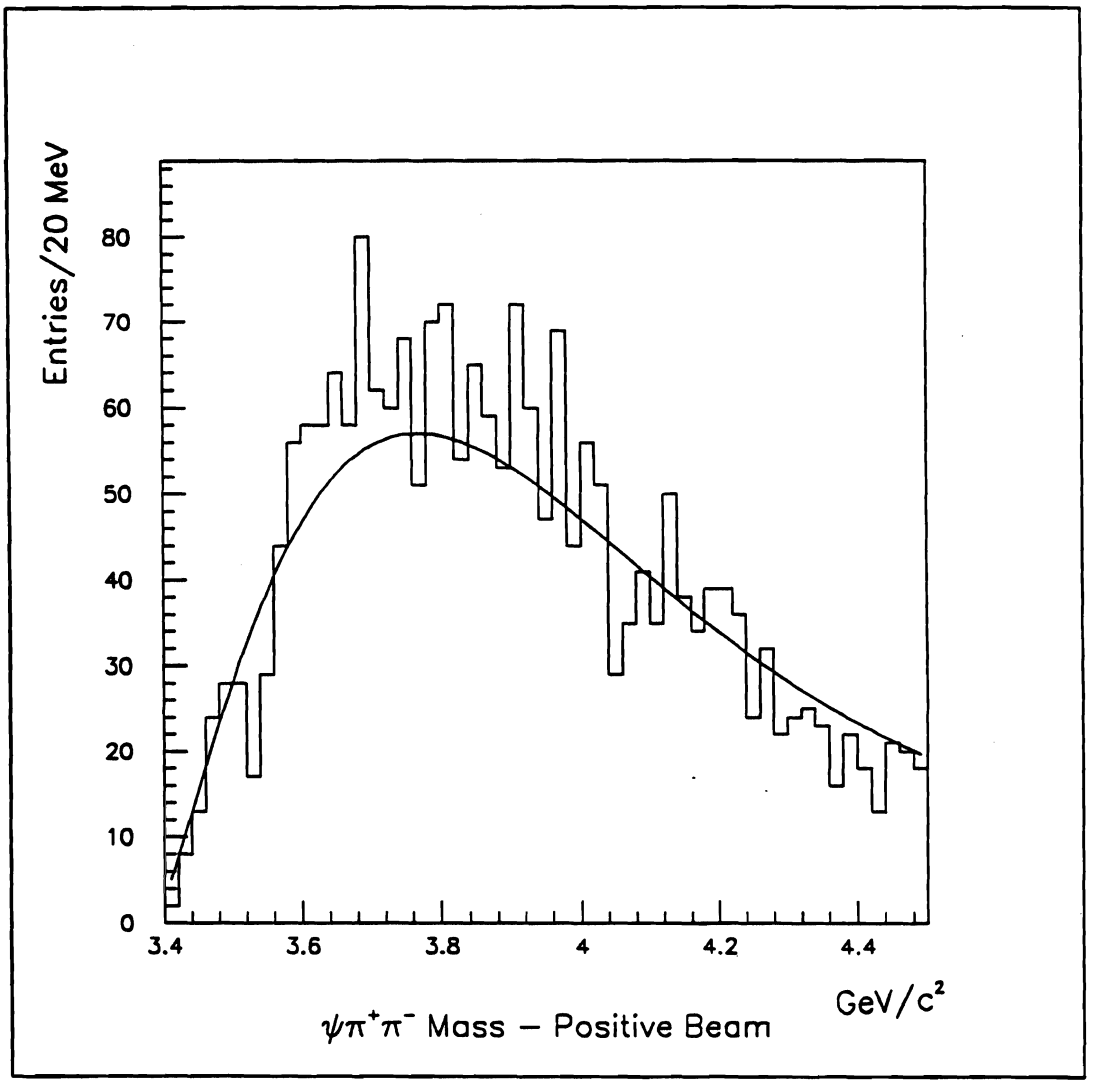

Figure 6.13 $\psi\pi\pi$ mass spectrum, standard cuts, positive beam.

A better fit cam be obtained, however, by adding two peaks at the same position and width as observed in the negative beam data. Fitting, allowing only the background height and the number of entries in each of the two peaks to vary, we get the results in table 6.9 and figure 6.14.

Table 6.9

$\psi' \rightarrow \psi\pi\pi$ Decays, Positive Beam

	Peak One	Peak Two
Number of Entries	36 ± 17	25 ± 20
Mass	3678 ± 6 MeV	3842 ± 10 MeV
Width (σ)	21 ± 6 MeV	31 ± 6 MeV

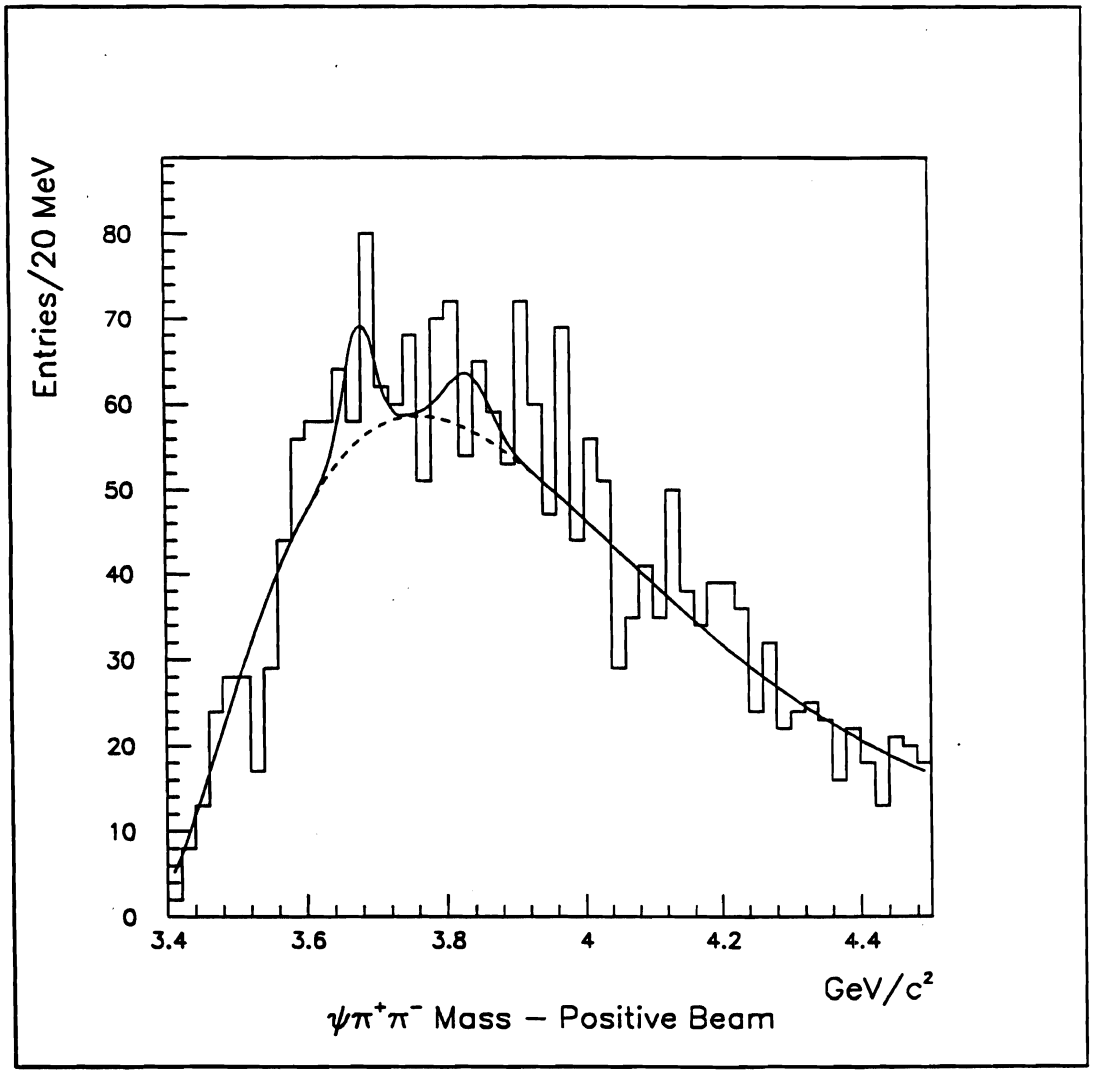

Figure 6.14 $\psi\pi\pi$ mass spectrum, standard cuts, positive beam.

To check consistency between the negative and positive beam data, we can measure the cross-section of the ψ' relative to the J/ψ again in the $\psi' \rightarrow \psi\pi^+\pi$ mode, and compare with the measurement from the $\psi' \rightarrow \mu^+\mu$ channel. This is given below:

$$\frac{\sigma(\psi')}{\sigma(J/\psi)} = \frac{\left[\dfrac{N(\psi' \rightarrow \psi\pi^+\pi^-)}{\varepsilon_A \, BF(\psi' \rightarrow \psi\pi^+\pi^-)}\right]}{N(J/\psi \rightarrow \mu\mu)} \qquad (6.9)$$

where the symbol BF(particle $\rightarrow$ channel) denotes the branching fraction of a particle into a particular channel, N(particle $\rightarrow$ channel) is the number of particles observed in a given channel, and ε_A is the product of the efficiency and acceptance of the $\psi 2\pi$ decay, given that the subsequent $J/\psi \rightarrow 2\mu$ decay was accepted and reconstructed. This is calculated via Monte Carlo and is tabulated below:

Table 6.10
Efficiency and Acceptance of $\psi\pi\pi$ Given $J/\psi \rightarrow \mu\mu$ is Accepted

Beam	Era	Dipion Relative Acceptance
Negative (98% π^-)	AUGN	10.1 ± 1.6 %
	SEPN	10.8 ± 1.6 %
	JANN	8.2 ± 2.1 %
	Negative Total	9.9 ± 1.9 %
Proton	NOVP	8.9 ± 1.7 %
	JANP	9.3 ± 2.3 %
	Proton Total	9.1 ± 2.0 %
π^+	NOVP	8.2 ± 1.9 %
	JANP	8.6 ± 1.6 %
	π^+ Total	8.3 ± 1.7 %
Positive	Positive Total	8.7 ± 1.9 %

Applying this method, we calculate the cross-section of the ψ' relative to the J/ψ to be $20 \pm 5 \pm 4$ % for the negative beam, and $12 \pm 6 \pm 3$ % for the positive beam, where the first error is statistical uncertainty and the second is systematic. These agree within errors with the measurement from the dimuon channel.

A second (not independent) way of performing this consistency check is to calculate the branching fraction for $\psi' \rightarrow \mu^+\mu$ assuming the published value for the branching fraction for $\psi' \rightarrow \psi\pi^+\pi$ is correct, and to compare the branching fraction obtained with the other beam sign as well as the accepted value.

The branching fraction for the $\psi(2S)$ into two muons is

$$BF(\psi' \rightarrow \mu\mu) = \frac{BF(\psi' \rightarrow \psi\pi^+\pi^-)\, N(J/\psi \rightarrow \mu\mu)\, BF\sigma(\psi':\psi)}{\left[\dfrac{N(\psi' \rightarrow \psi\pi^+\pi^-)}{\varepsilon_A\, BF(J/\psi \rightarrow \mu\mu)}\right]} \tag{6.10}$$

where the symbol BF(particle $\rightarrow$ channel) denotes the branching fraction of a particle into a particular channel, N(particle $\rightarrow$ channel) is the number of particles observed in a given channel, $BF\sigma(\psi':\psi)$ is the measured (in Section 6.B) branching fraction into two muons times cross-section for the ψ' relative to the J/ψ and ε_A is the product of the efficiency and acceptance of the $\psi 2\pi$ decay, given that the subsequent $J/\psi \rightarrow 2\mu$ decay was accepted and reconstructed. For the negative beam, the ψ' branching fraction into two muons is $.65 \pm .23 \pm .14$ %, and for positive beam it is $.82 \pm .47 \pm .19$ %. Combining the two gives $.70 \pm .22 \pm .15$ %, compared with the accepted value of $.77 \pm .17$ %.[56] Lepton universality tells us that the branching fraction into two muons is the same as into two electrons, but there is a slight discrepancy between muon and

electron values: the best electron value is .88 ± .14 %. Our data better supports the smaller number, but are consistent with both.

It is reassuring that the positive and negative beam data agree on this branching fraction. The nearly invisible ψ' peak is exactly what is to be expected from the cross-section, efficiency and acceptance.

The negative beam $\psi\pi\pi$ data's signal to noise ratio is large enough to measure a dipion mass distribution. The data were divided into 100 MeV bins of dipion mass. Individual background shapes from the mispairing data were fit for each bin, and the data were fit to a Gaussian peak on top of this background distribution. The total number of events in the peaks for each bin are shown below:

Table 6.11
Dipion Mass Distribution: $\psi' \rightarrow \psi\pi\pi$

Dipion Mass Range	$\psi(2S)$s observed
300 — 400 MeV	9 ± 14
400 — 500 MeV	5 ± 16
500 — 600 MeV	39 ± 14
600 — 700 MeV	17 ± 10

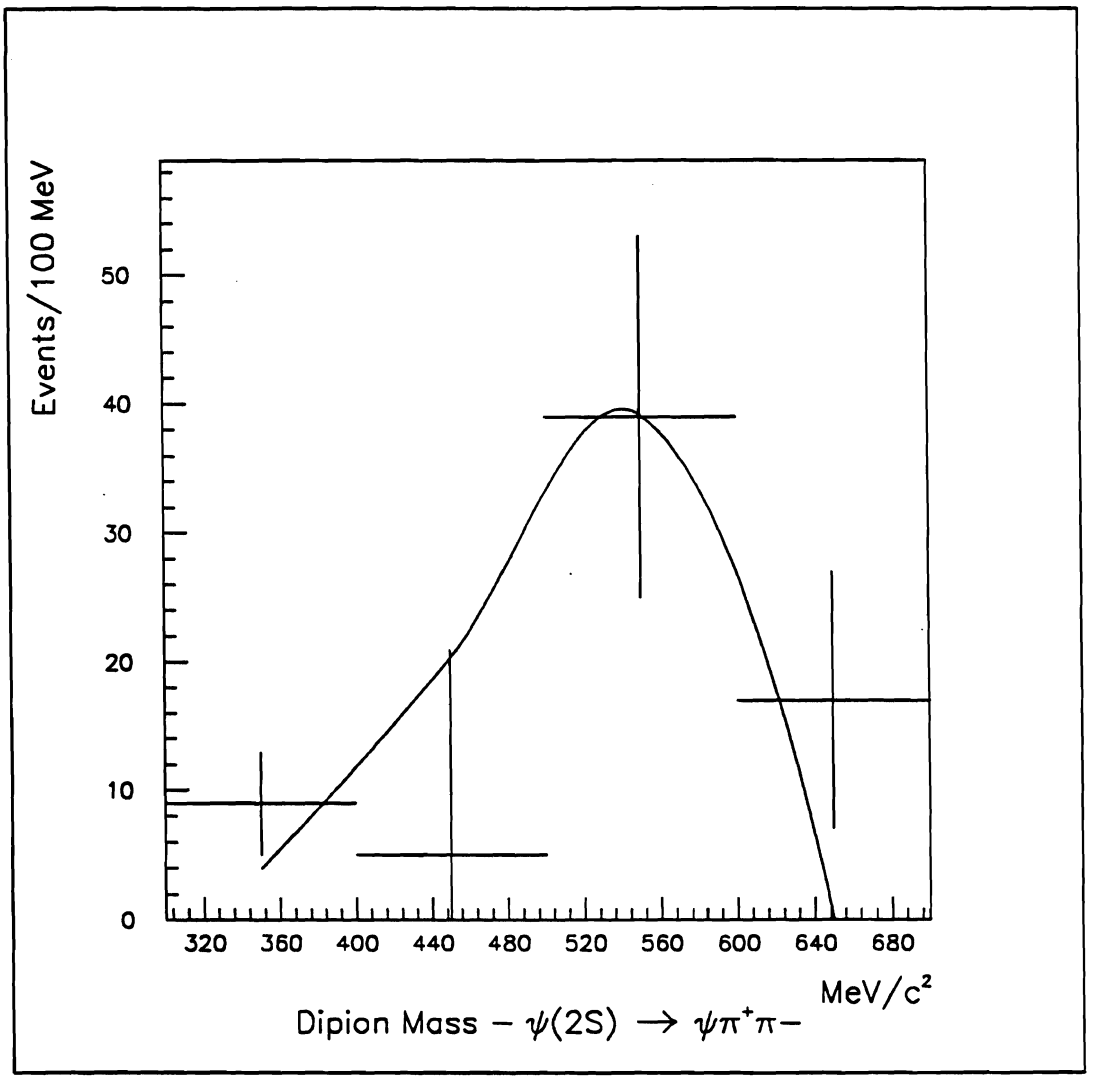

Figure 6.15 $\psi' \rightarrow \psi\pi\pi$ dipion mass distribution. Curve is fit to Brown and Cahn shape.

D. ψ_x(3837) signal and cross-section times Branching Fraction

It is both disturbing and interesting to have to have a second peak in the $\psi\pi\pi$ data. This peak will be referred to as the ψ_x in this and the following chapter. One fairly remote possibility is that it is some sort of "reflection" of the $\psi(2S)$. That is,

there might be some sort of systematic reconstruction error (due to, for example, the drift chambers' left-right ambiguity) that causes some $\psi(2S)$'s to be reconstructed at the correct mass and others to be reconstructed at a higher mass. The Monte Carlo reconstructed mass distribution (shown below) shows no such effect, however. Furthermore, since the number of $\psi(2S)$'s seen in this channel agrees with the number seen in the dimuon channel, corrected for all efficiencies and acceptances, having a factor of two more $\psi(2S)$'s in the $\psi 2\pi$ channel (from including the second peak) is not consistent with the dimuon channel.

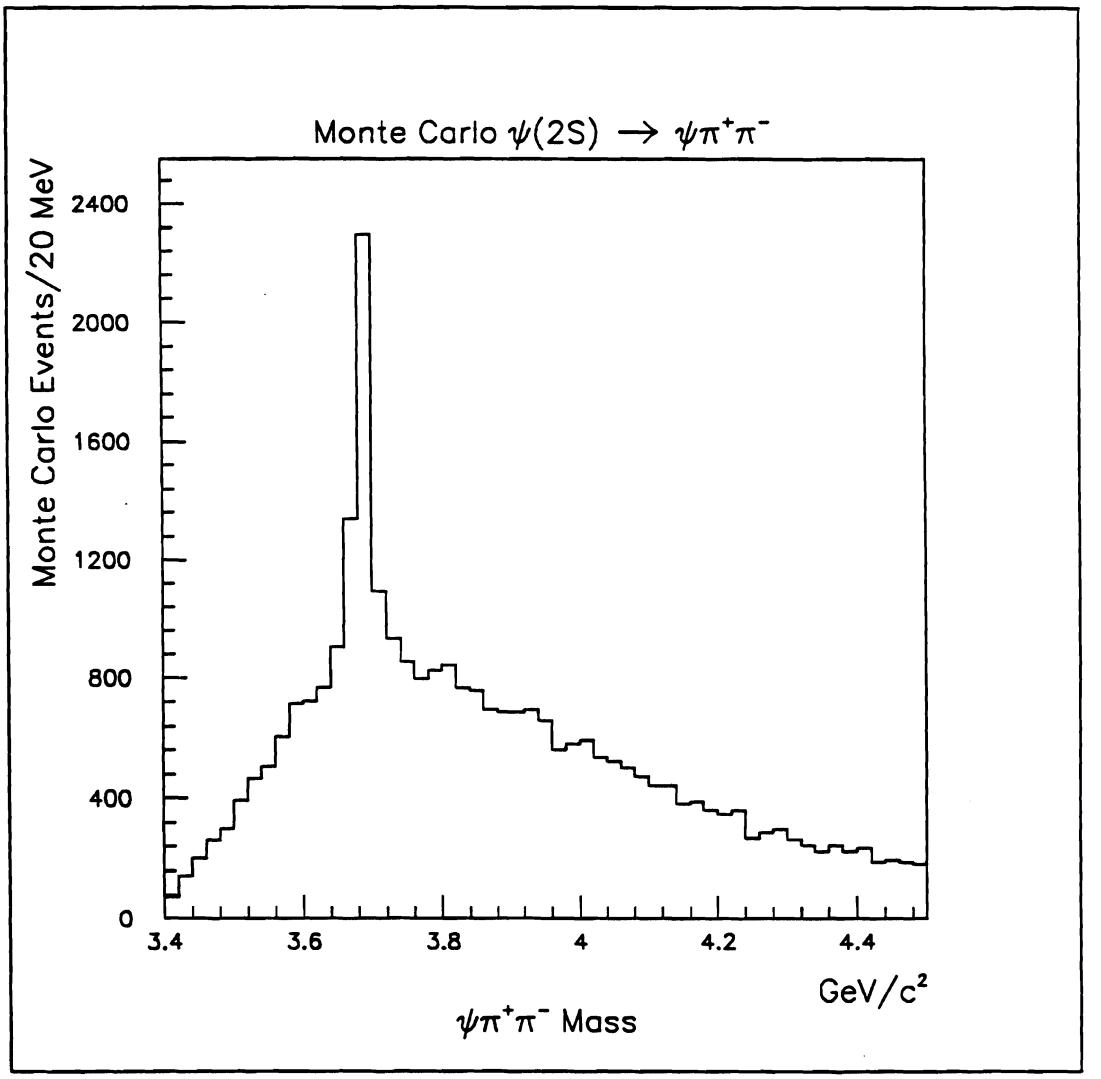

Figure 6.16 Monte Carlo $\psi' \rightarrow \psi\pi\pi$ mass distribution. $\sigma \approx 15$ MeV.

A second unlikely possibility is that the peak is the result of the decays $\chi \rightarrow J/\psi e^+e^-$, where the dielectron pair is either from Dalitz decays or photon conversions, and the electrons are somehow misidentified as pions. The requirement of four distinct upstream segments excludes the conversion possibility — the characteristic geometry of a pair conversion is a single upstream segment linked to two downstream segments. Dalitz decays are typically two orders of magnitude smaller than radiative

decays, and so are too rare to produce this peak: If the Dalitz peak is comparable to the ψ' in size, the radiative decays to $\psi\gamma$ must be hundreds of times larger. This would produce a very small ratio of the ψ' to J/ψ cross-section: under one percent. The observed value is too large to permit this possibility.

Having a second peak near the maximum of phase space makes it particularly difficult to determine if it is real or not. To partially overcome this, a cut on total di-pion energy in the lab frame was imposed, and this cut was set at 18 GeV, 15 GeV and 12 GeV. This cut has the effect of moving the peak of background towards lower mass, so the ψ_X signal then is on the high mass tail of the background distribution.

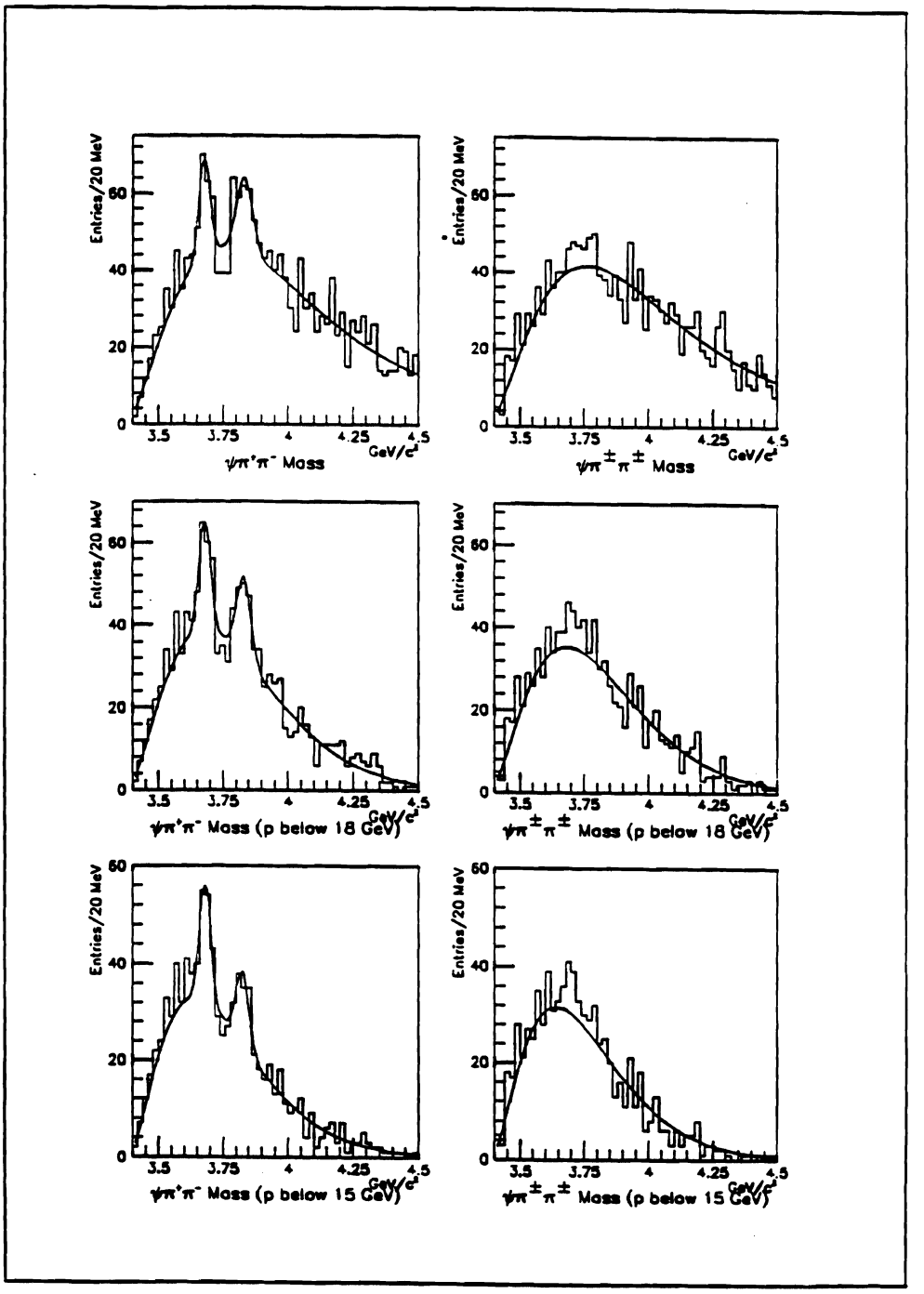

Figure 6.17 $\psi\pi\pi$ **mass spectrum for negative beam, Left: opposite sign pions. Right: same signed pions. Top: No dipion momentum cut. Middle: 18 GeV dipion momentum cut. Bottom: 15 GeV dipion momentum cut.**

The results of fitting the second peak using the same procedure are shown in table 6.12. Here the ratio of observed ψ_xs to ψ's was fitted holding the other fit parameters constant, and the mass was calculated by fitting the mass difference between the two peaks and adding the accepted value of the ψ' mass to that difference. (The measured ψ' mass was 3680 ± 4 MeV.)

Table 6.12
ψ_x Characteristics: Negative beam

Momentum Cut	Number ψ_xs	ψ_x/ψ' Ratio	ψ_x Mass (MeV)	ψ_x Width (MeV)
none	74 ± 22	109 ± 27 %	3842 ± 8	31 ± 8
< 18 GeV	65 ± 18	86 ± 20 %	3837 ± 6	27 ± 7
< 15 GeV	48 ± 13	71 ± 18 %	3832 ± 6	25 ± 5

By performing a weighted average of the masses in each of the three plots, one gets a best estimate for the mass of 3837 ± 4 MeV. The width of the ψ_x is 128 ± 26 % of the width of the ψ'; the Monte Carlo width ratio for two infinitely narrow states is 120 ± 11 %. Therefore, it appears that the observed width is due to resolution — the intrinsic width is smaller than our sensitivity. However, the observed width of the ψ' is 1.5 times the prediction of the Monte Carlo. This is attributed to systematic difficulties peculiar to low momentum tracks: multiple scattering in the target, and the increased sensitivity to the magnetic field. Our analysis magnet, Rosie, was only mapped in one quadrant and an assumed symmetry was used to reflect this field measurement to the other quadrants. It is possible that there were small, unnoticed asymmetries in the field.

It is also possible to measure the dipion mass distribution, using the same technique used for the $\psi(2S)$.

Table 6.13
Dipion Mass Distribution: $\psi_x \rightarrow \psi\pi\pi$

Dipion Mass Range	ψ_xs observed
300 — 400 MeV	0 ± 11
400 — 500 MeV	0 ± 13
500 — 600 MeV	13 ± 15
600 — 700 MeV	54 ± 15
700 – 800 MeV	22 ± 7
800 — 900 MeV	3 ± 3

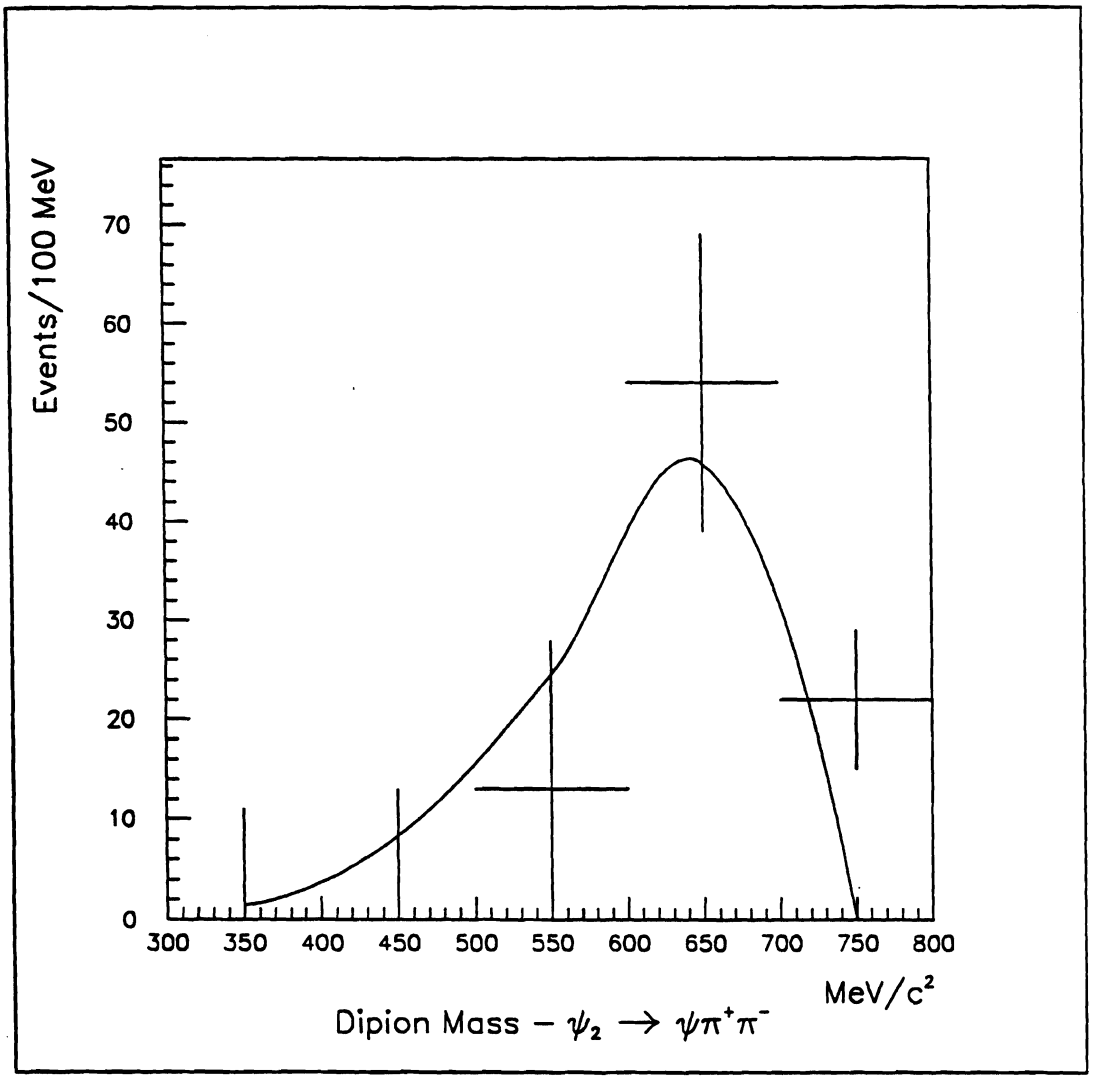

Figure 6.18 $\psi_x \rightarrow \psi\pi\pi$ dipion mass distribution. Curve is fit to Brown and Cahn shape.

The cross-section of this peak cannot be measured independently of the branching fraction, but it is possible to measure the cross-section times branching fraction. We first calculate the cross-section times branching fraction relative to the ψ', as seen in the $\psi' \rightarrow \psi 2\pi$ channel, in the following table:

Table 6.14
$\psi_x \rightarrow \psi\pi\pi$ Cross-section times Branching Fraction (Negative Beam)

Momentum Cut	Observed ψ_x/ψ' Ratio	$\varepsilon_A\ \psi_x/\psi'$	Corrected ψ_x/ψ' Ratio
none	109 ± 27 %	89 ± 6 %	122 ± 30 ± 8 %
< 18 GeV	86 ± 20 %	74 ± 6 %	116 ± 27 ± 9 %
< 15 GeV	71 ± 18 %	62 ± 6 %	115 ± 29 ± 11%

Next, we take the observed relative branching fraction times cross-section of 122 ± 30 ± 8% and multiply it by the measured branching fraction for $\psi' \rightarrow \psi\pi^+\pi^-$ of 32.4%. This yields a value for BF $\sigma(\psi_x \rightarrow \psi\pi^+\pi^-) / \sigma(\psi')$ of 39.5 ± 9.7 ± 2.6%. Next, multiplying by the ratio of $\sigma(\psi')/\sigma(\psi)$ of 14 ± 3%, we obtain the value for BF $\sigma(\psi_x \rightarrow \psi\pi^+\pi^-) / \sigma(J/\psi)$ of 5.5 ± 1.4 ± 1.2%. Finally, multiplying by the J/ψ cross-section of 182 ± 22 nb (for $x_F > 0$), we calculate a BF $\sigma(\psi_x \rightarrow \psi\pi^+\pi^-)$ of 10.0 ± 2.5 ± 2.5 nb per nucleon.

Next we consider possible quantum number assignments to the ψ_x. Unfortunately, the number of signal events and signal to noise ratio are inadequate for a spin-parity analysis. Nonetheless, it is possible to make some inferences about its quantum numbers. First, there is a J/ψ in the final state. This makes it extremely probable that there is a charmed quark-antiquark component in the particle; otherwise this decay would be strongly OZI-suppressed. Second, the observation of the decay in the $\psi\pi\pi$ mode implies that decay into open charm is forbidden, or at least strongly suppressed. Otherwise, we would have a situation like the ψ'', which has only a tiny probability to decay into anything other than open charm. This state is above $D\bar{D}$ threshold, so the quantum numbers 0^{++}, 1^{--}, 2^{++}, and 3^{--}, corresponding to S, P, D and F-wave decays to $D\bar{D}$ are disallowed. On the following page is a summary of possible quantum number assignments assuming a charmonium state:

Table 6.15

Possible Quantum Number Assignments for State at 3837 MeV

Spin-Parity (J^{PC})	G-parity	$^{(2S+1)}L_J$	Reason for Excluding
0^{++}	even	$^3P_0$	G-parity, Open Charm
0^{+-}	odd	exotic	possible
0^{-+}	even	$^1S_0$	G-parity
0^{--}	odd	exotic	possible
1^{++}	even	$^3P_1$	G-parity
1^{+-}	odd	$^1P_1$	possible
1^{-+}	even	exotic	G-parity
1^{--}	odd	$^3S_1$ $^3D_1$	Open Charm
2^{++}	even	$^3P_2$ $^3F_2$	G-parity,Open Charm
2^{+-}	odd	exotic	possible
2^{-+}	even	$^1D_2$	G-parity
2^{--}	odd	$^3D_2$	possible
3^{++}	even	$^3F_3$	G-parity
3^{+-}	odd	$^1F_3$	possible
3^{-+}	even	exotic	G-parity
3^{--}	odd	$^3D_3$	Open Charm

If one eliminates the states with exotic quantum numbers from consideration, the three remaining possibilities would be the $^1P_1$ (h_c), the $^3D_2$ (ψ_2) and the $^1F_3$ (h_{c3}). Discussion of this enhancement will be resumed in Chapter 7.

E. $\psi'\pi^{\pm}$ spectrum

E-705 is also sensitive to a decay of an isotriplet bound ($c\bar{c}q_1\bar{q}_2$) state, if such a state's decay into $\psi(2S)\pi$ is a significant source of $\psi(2S)$'s. Such an observation would be an unequivocal signature of a ($c\bar{c}q_1\bar{q}_2$) state: there is no way to reconcile charmonium and net electric charge (and thus isospin) using only a quark-antiquark pair. Such a state with mass near 3850 MeV (such as a bound D and D^*) could appear as a threshold enhancement in the $\psi(2S)\pi$ spectrum. This signature possesses a strong experimental advantage: the signal is in a region where the background is small. The

ψ' is chosen over the more abundantly produced ψ because the only $(c\bar{c}q_1\bar{q}_2)$ state that would be at threshold for the J/ψ is a bound state of a ψ and a π. As discussed in the first chapter, the pion is too light to be bound. Indeed, the $\psi - \pi$ system is examined in the following pages, and as expected, no strong threshold enhancement is observed. (There is the possibility of a final state interaction between the J/ψ and the π producing a small enhancment at low relative mass due to the relative attraction between the two particles.)

To calculate the acceptance of such a state and decay mode, we modified the standard Monte Carlo to generate a state at 3850 MeV, with the J/ψ kinematic distributions, and decay it to a $\psi(2S)$ and a single charged pion. The $\psi(2S)$ then decayed to a muon pair, and all three tracks were propagated through the spectrometer. All decays were isotropic.

Like the standard J/ψ Monte Carlo, these tracks are overlapped on a dimuon trigger without a J/ψ in it, and the muon counter hits removed. This causes the triggering dimuon to appear as two pions to the analysis program. The overlaid tracks are subject to the measured chamber and counter efficiencies, and the final composite event is analyzed by the software simulation of the trigger processor and the tracking program.

Acceptance is remarkably low for these events, primarily because of geometry — the pion tends to be in the dead region upstream, and/or swept outside the spectrometer by Rosie. A detector optimized for reconstruction of the decay $\chi \rightarrow$ J/ψ + γ is not optimized for $(c\bar{c}q_1\bar{q}_2) \rightarrow \psi' + \pi$. Approximately 600,000 Monte Carlo events were generated, and overlapped on raw data events from all five eras and the product of efficiency and acceptance for the charged pion, provided that the ψ' itself

was accepted and reconstructed is 9.9 ± 1.0 %. Had the PCB chambers been more reliable, the acceptance would be greater.

Several methods of generating backgrounds were used. One was mispairing events: taking a dimuon from one event, and combining it with a pion from a different event. Three different mispairings were used:

- Dimuons from $\psi(2S)$ paired with pions from other $\psi(2S)$'s,
- Dimuons from $\psi(2S)$ paired with pions from events with a J/ψ,
- Pions from events with a $\psi(2S)$ paired with dimuons from J/ψ decay.

The events were broken down into 5 categories: J/ψs (within 50 MeV of 3097 MeV), ψ's (within 50 MeV of 3686 MeV), the low sideband (below 3047 MeV), the high sideband (above 3736 MeV) and the middle sideband, between the J/ψ and the ψ'. Each event was paired with the previous thousand events in the same category.

The other method was to compare the $\psi(2S)\pi$ mass difference spectrum with the $J/\psi\pi$ spectrum, which has no threshold enhancement. Figures 6.19 and 6. 20 show these background distributions.

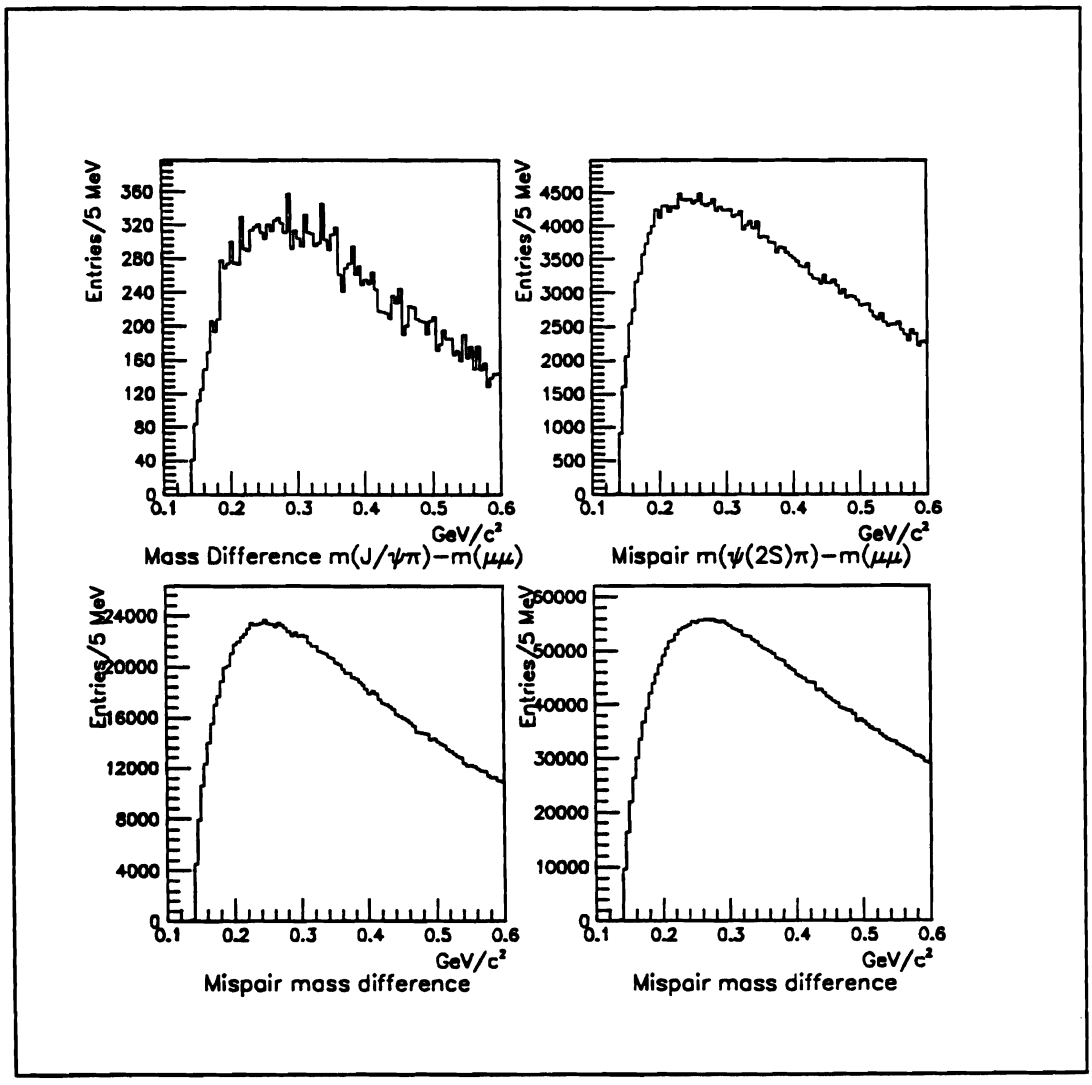

Figure 6.19 Background μμπ mass spectra. Top left: J/ψπ mass difference spectrum. Top right: Mispaired ψ'π spectrum. Bottom left: Spectrum from mispairing dimuons from J/ψs with pions from ψ' events. Bottom right: Spectrum from mispairing dimuons from ψ's with pions from J/ψ events.

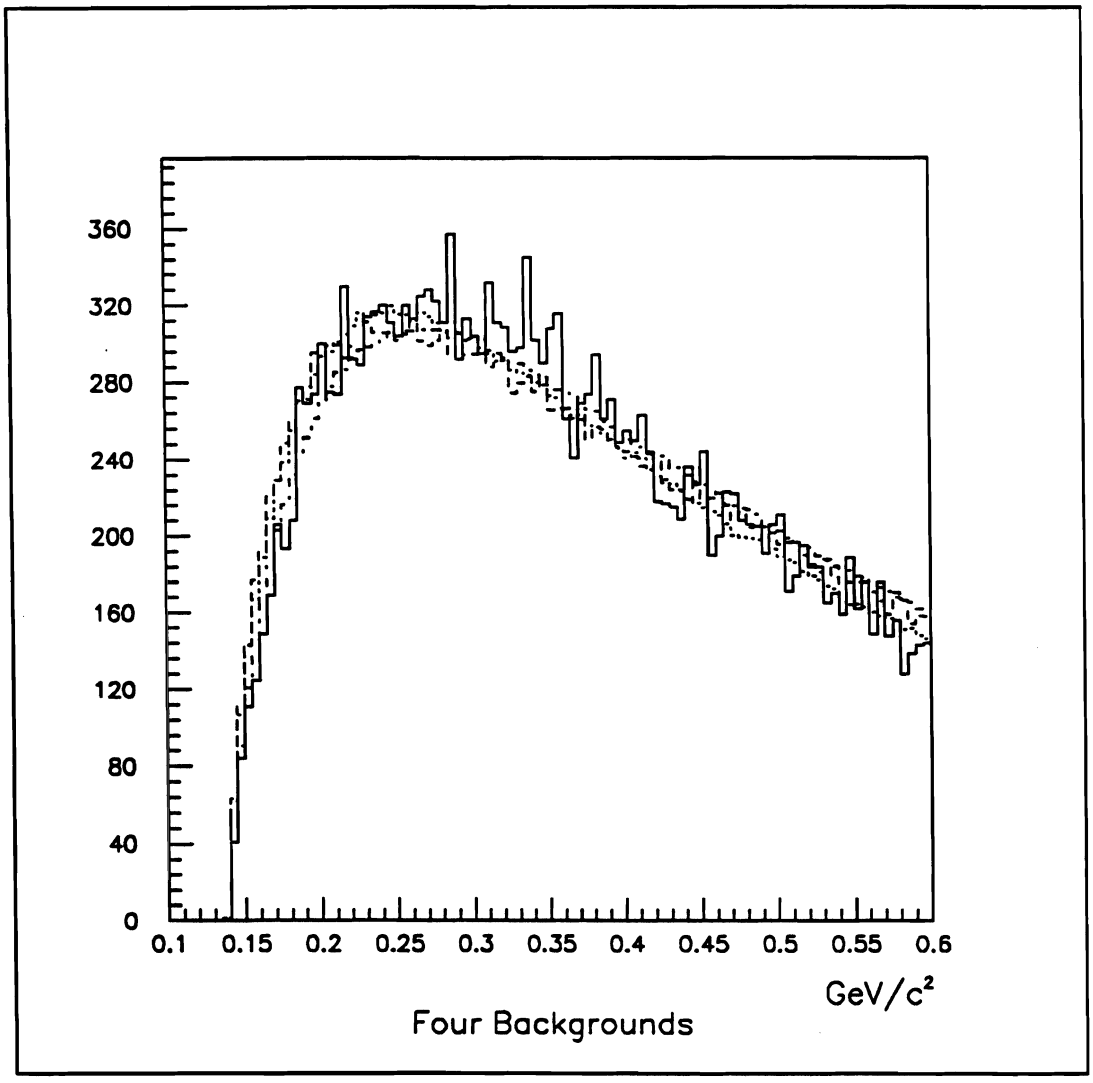

Figure 6.20 Background $\mu\mu\pi$ mass spectra, normalized to the same total number of entries.

Figure 6.20 has all four backgrounds normalized to the same number of entries, and they fit to within 5% of each other. However, the largest uncertainty in background estimation is in normalization: normalizing between 0 and 600 MeV mass difference vs. 0 to infinity changes the normalization from method to method by 10%. Therefore, to be conservative, the error on the background is estimated to be 10%.

Figure 6.21 is the J/ψπ mass difference spectrum with a background of J/ψs mispaired with pions from other J/ψ events. In this case, the background and signal agree well: there is no evidence for any new particle decaying into J/ψπ at or near threshold as expected. Figure 6.22 shows the first 30 MeV of figure 6.21.

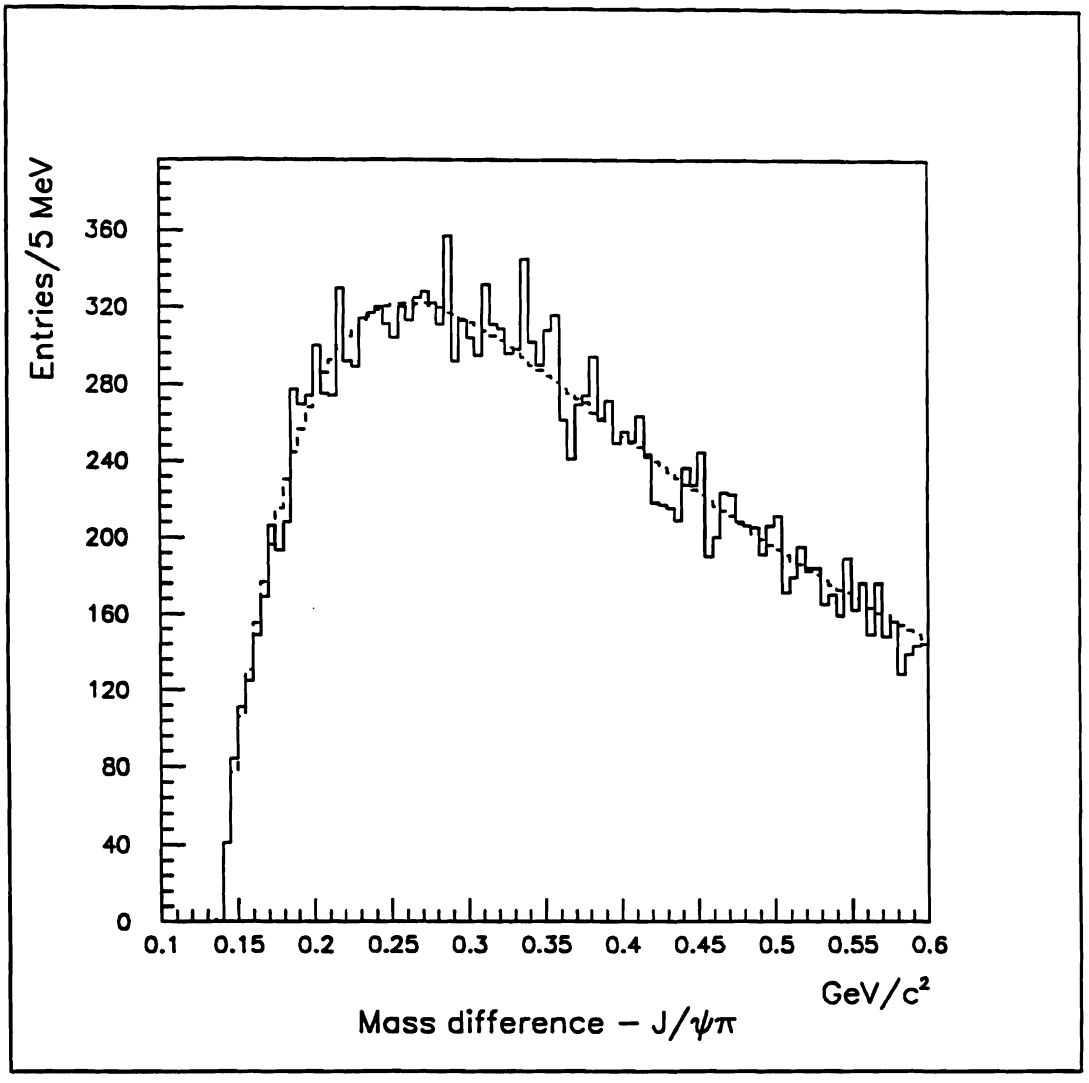

Figure 6.21 Mass difference m(J/ψπ) — m(μμ).

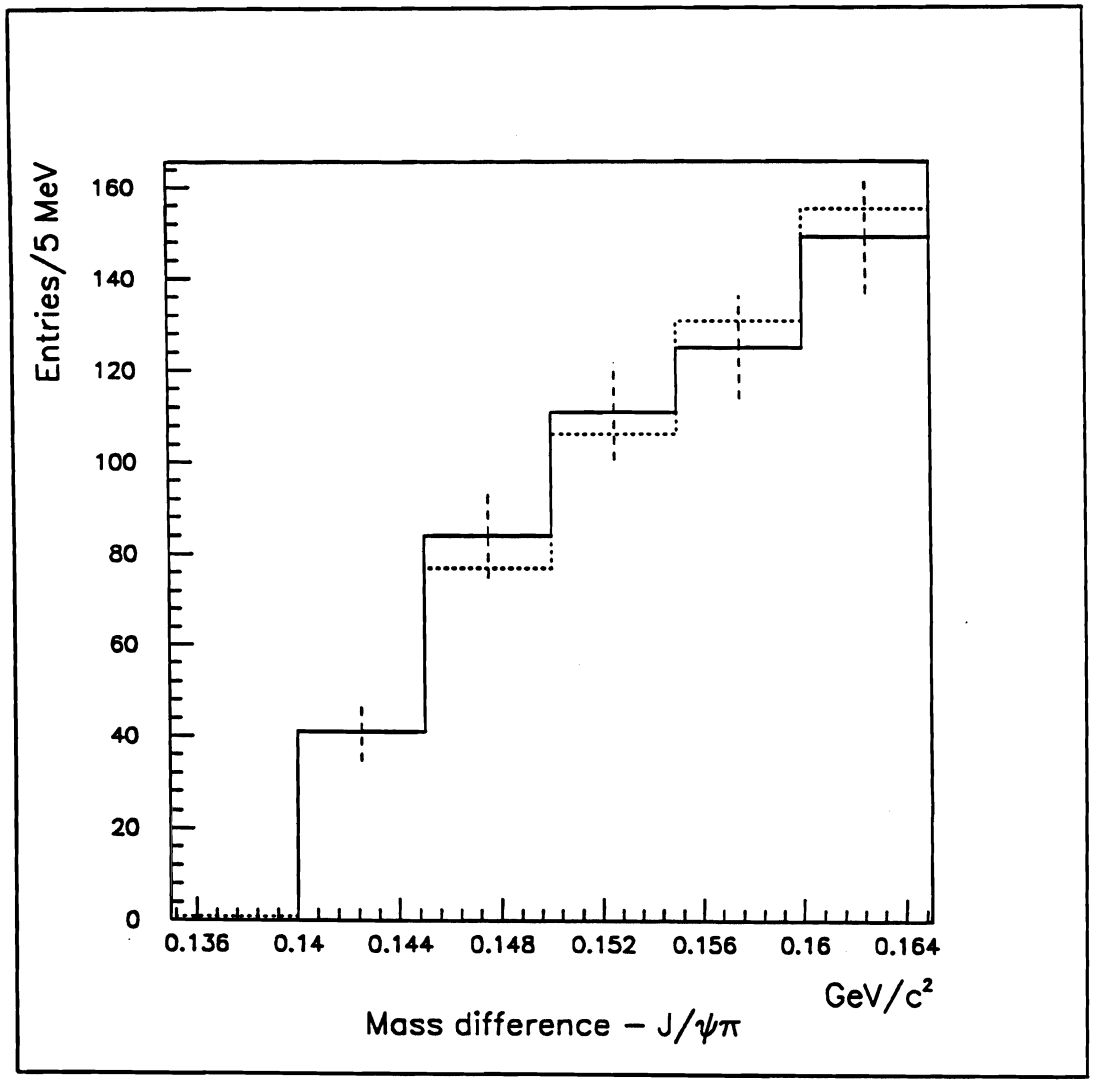

Figure 6.22 Mass difference m(J/ψπ) — m(μμ).

Returning to ψ'π, the following cuts were applied to the data:

Table 6.16

ψ(2S)π Cuts

Item	Cut
ψ' mass window	3686 ± 50 MeV
π track	matched
π rear segment χ^2	< 6
π Δy slope	< 12 mR
π momentum	< 100 GeV

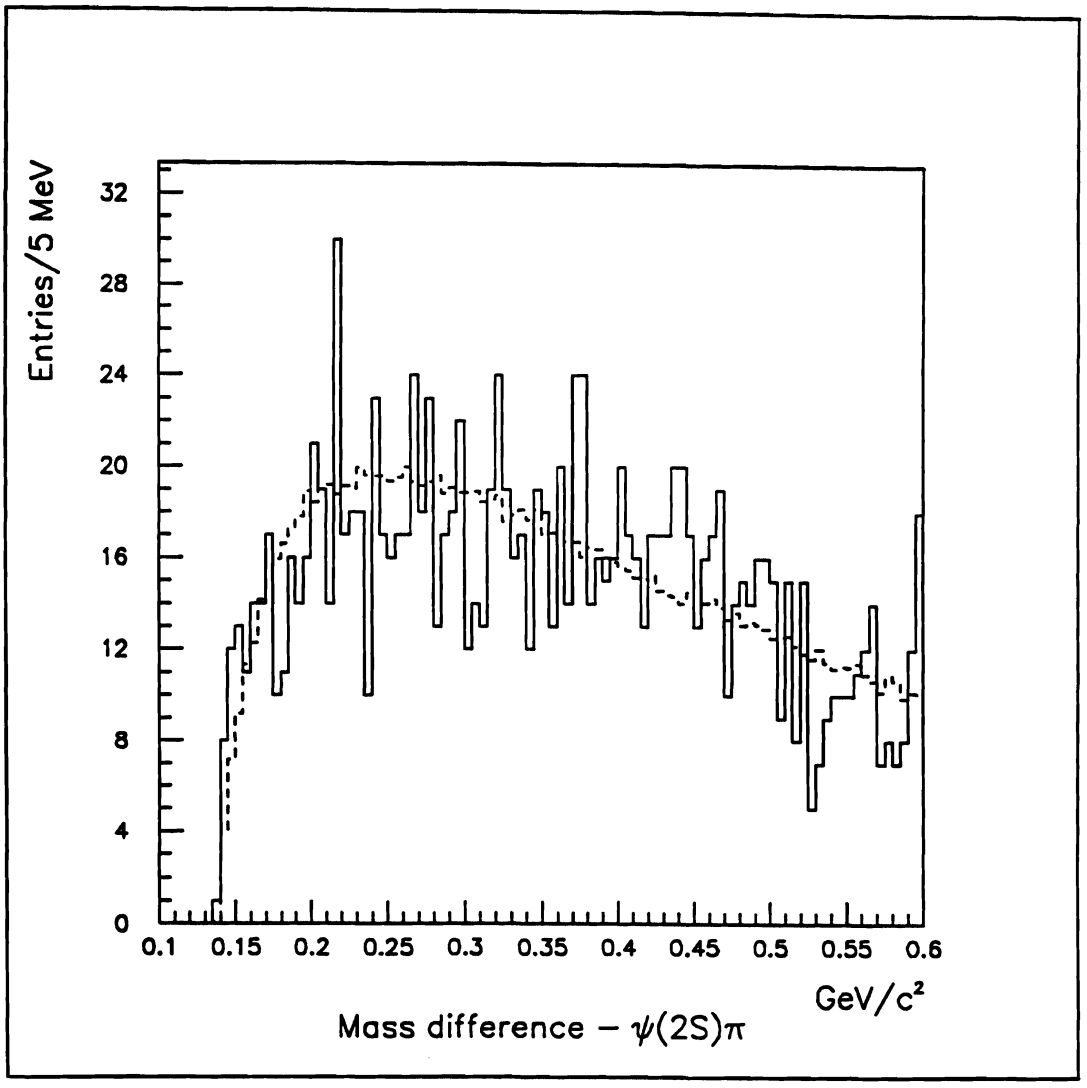

Figure 6.23 Mass difference m(ψ'π) — m(μμ).

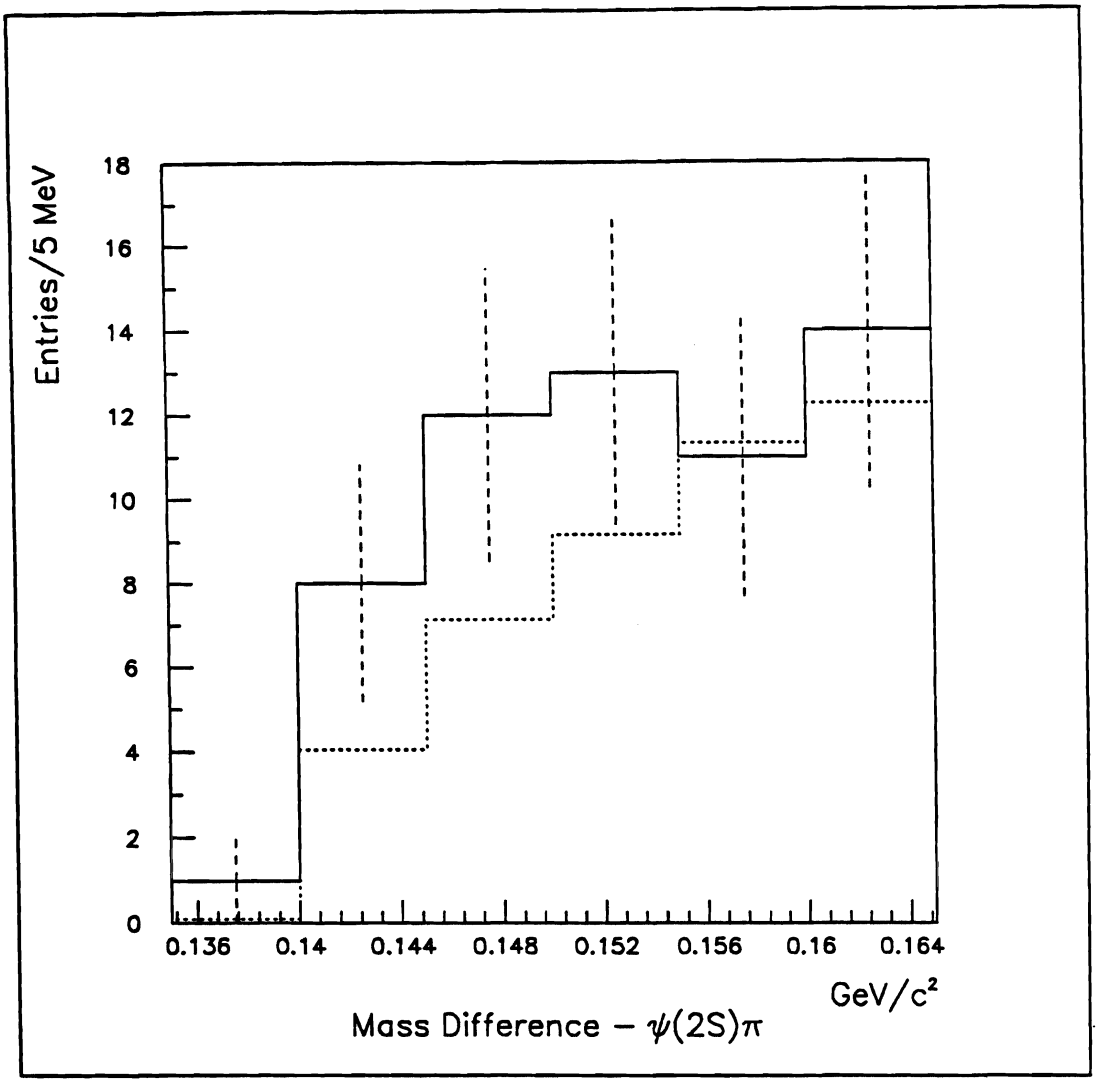

Figure 6.24 Mass difference m(ψ'π) — m(μμ).

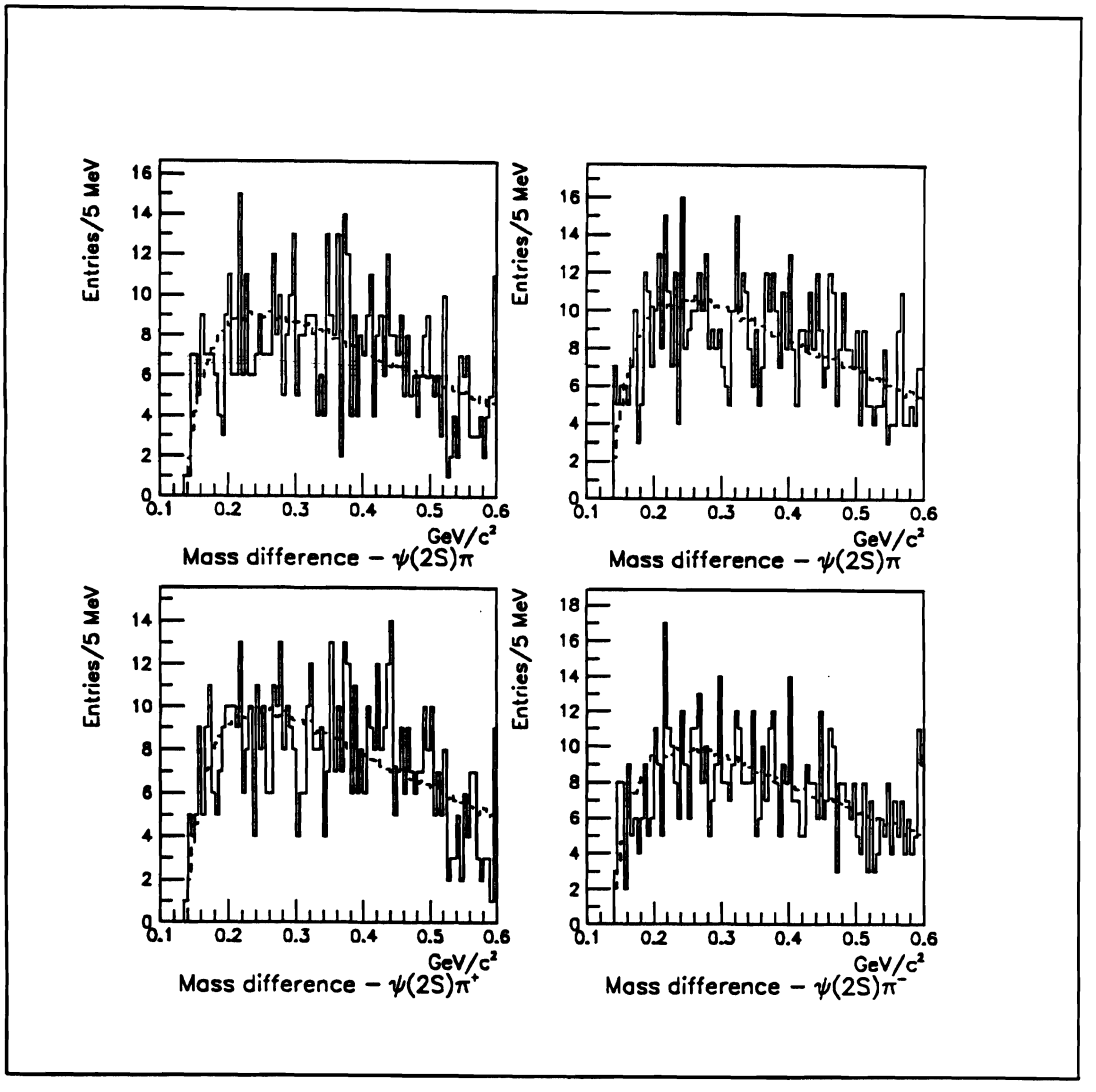

Figure 6.25 Mass difference m(ψ'π) — m(μμ) Upper left: Negative beam data. Upper right: Positive beam data. Lower left: ψ'π⁺ data. Lower right: ψ'π⁻ data.

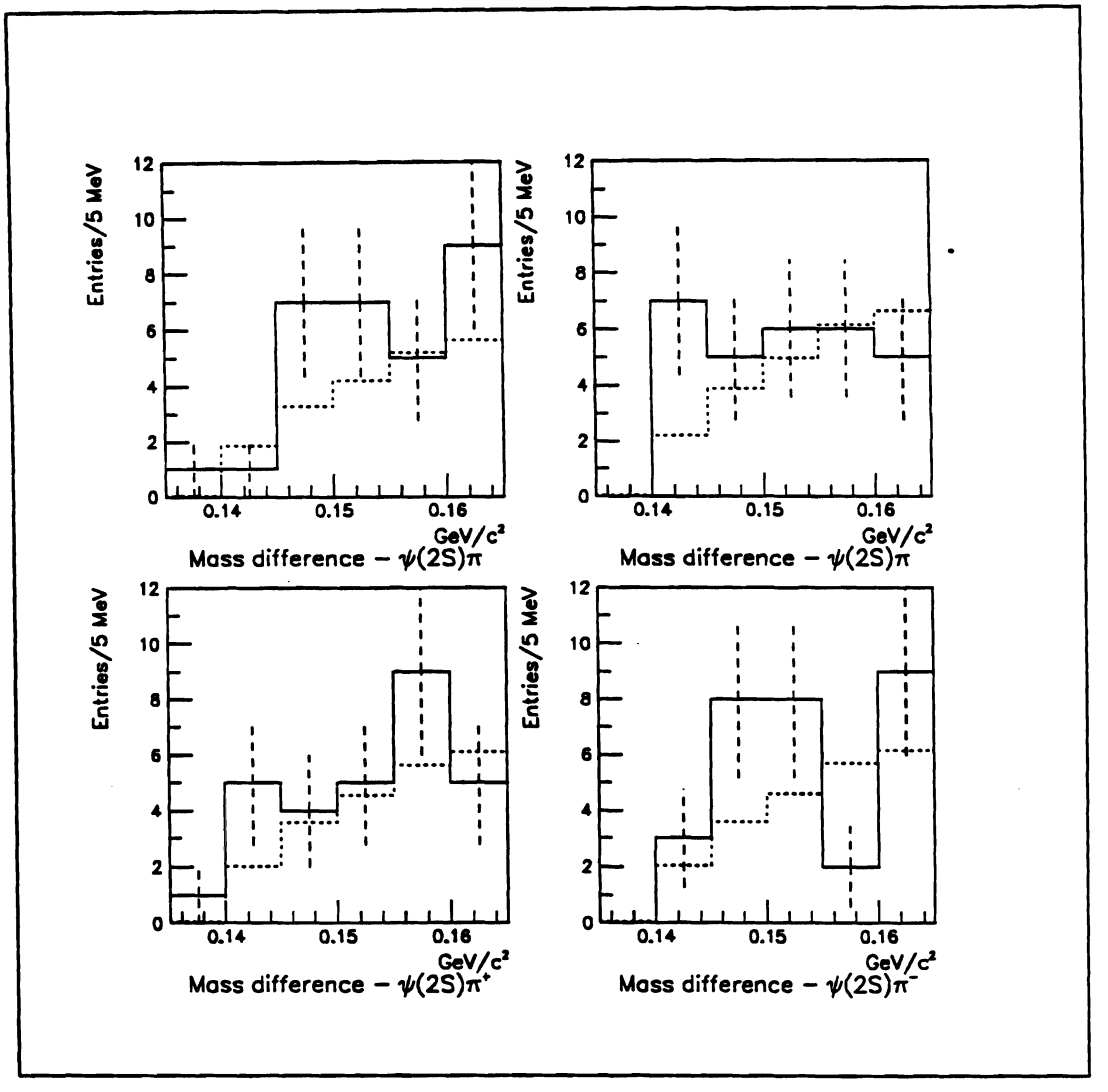

Figure 6.26 Mass difference m(ψ'π) — m(μμ) Upper left: Negative beam data. Upper right: Positive beam data. Lower left: ψ'π⁺ data. Lower right: ψ'π⁻ data.

Figure 6.24 shows the total data sample with the Table 6.15 cuts applied. Figure 6.25 shows the data divided by beam type and by charge of the pion. Figure 6.26 shows the first 30 MeV of figure 6.25. In all of these plots, the background (smooth

curve) is from mispairing dimuons from $\psi(2S)$ paired with pions from other $\psi(2S)$'s. The difference obtained by using one of the other methods of background generation is treated as a systematic error in the analysis, but as mentioned earlier, *where* to normalize is a much more significant uncertainty than *how* to normalize.

Assuming that 100% of the $\psi(2S)$'s came from decay of a hadronic molecule decaying into $\psi'\pi$. There are 20,300 J/ψ's, and we measure $N(\psi')/N(J/\psi)$ to be 2.2 ± 0.2%. This gives us 450 ± 40 observed $\psi(2S)$'s. Assuming charge independence, two-thirds of these should be associated with a charged pion — in the other one-third, we have an associated π^0, which decays immediately to two photons. That leaves us with 300 ± 30 $\psi(2S)$'s of interest. Multiplying by the acceptance of 10.0 ± 0.7 % and that leaves at most 30 ± 4 candidate events.

In the entire data sample, we observe an excess of 20 ± 12 events in the first 8 bins. (and 14 ± 6 in the first four) Dividing, this implies that

$$\frac{20 \pm 12}{30 \pm 4} = 67 \pm 40 \pm 8\ \% = 67 \pm 41\ \% \qquad (6.11)$$

of the ψ's come from a higher state, at around mass 3850 MeV.

The effect is significant at about the 1.6σ level, which corresponds to about a 1 in 17 probability of being due solely to chance.

To improve signal to noise an additional energy cut was imposed on the ψ'. Since the J/ψ signal to noise is a decreasing function of lab frame energy, we imposed an 80 GeV upper limit on the dimuon momentum and repeated the entire analysis. Figures 6.27 — 6.29 are equivalent to figures 6.24 — 6.26 with this additional cut.

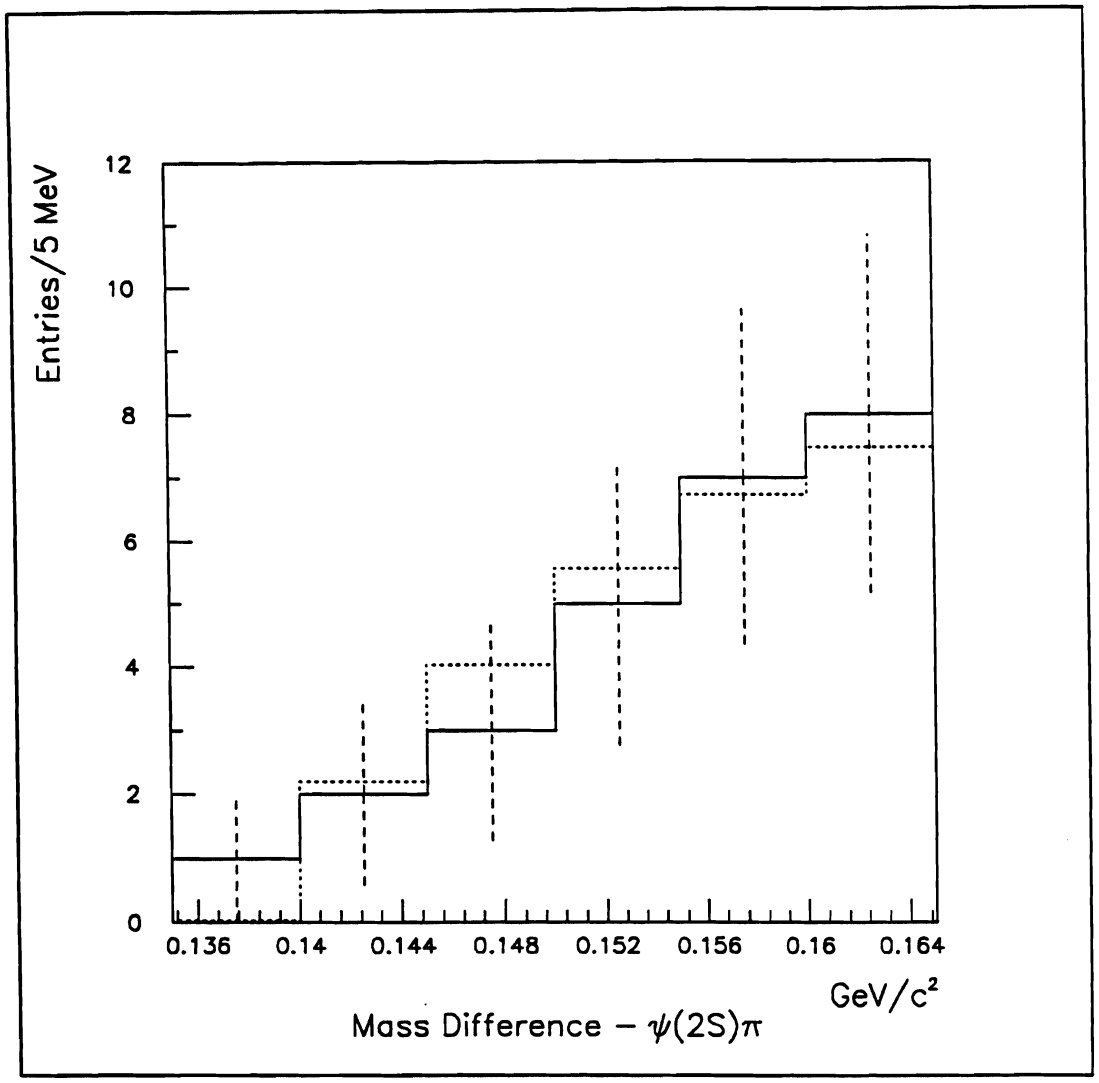

Figure 6.27 Mass difference m(ψ'π) — m(μμ) with high momentum ψ's excluded.

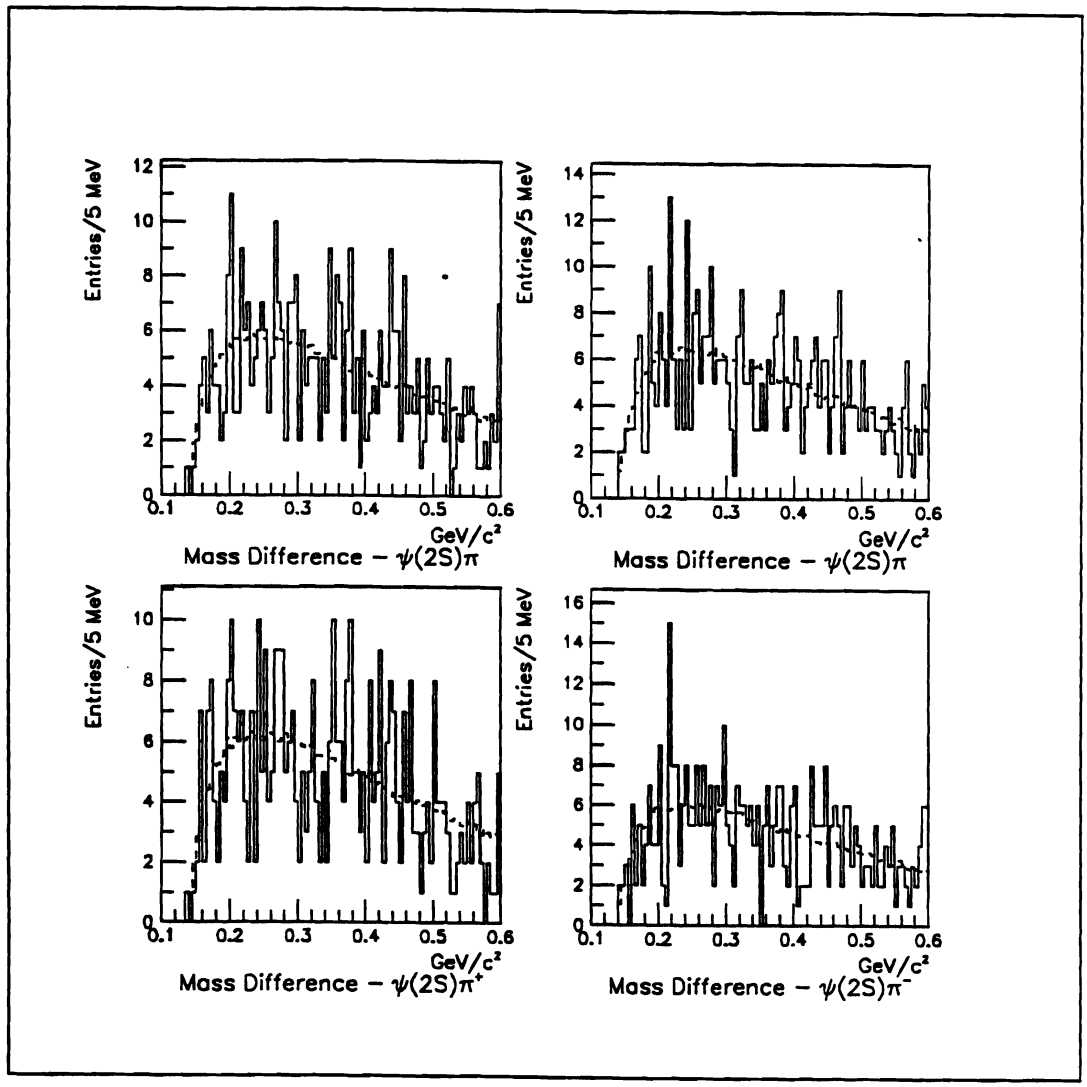

Figure 6.28 Mass difference m(ψ'π) — m(μμ) with high momentum ψ's excluded. Upper left: Negative beam data. Upper right: Positive beam data. Lower left: ψ'π⁺ data. Lower right: ψ'π⁻ data.

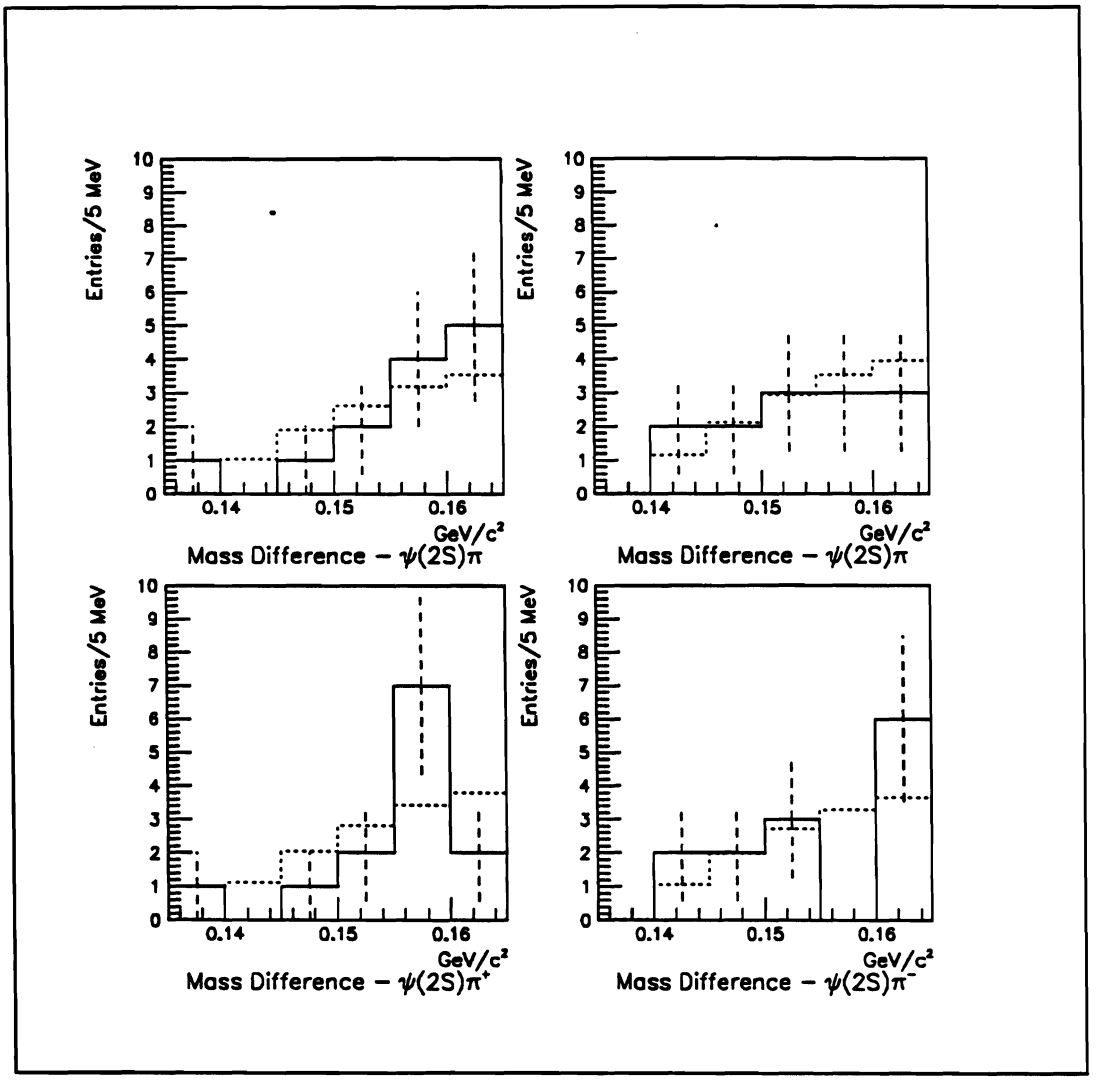

Figure 6.29 Mass difference m(ψ'π) — m(μμ) with high momentum ψ's excluded. Upper left: Negative beam data. Upper right: Positive beam data. Lower left: ψ'π⁺ data. Lower right: ψ'π⁻ data.

With this more restrictive set of cuts, the combined efficiency and acceptance of the pion given that the ψ' was accepted drops to 9.0 ± 0.7 %. For 100% of ψ's coming from the decay of this supposed state, we should observe 27 ± 3 events. The

number of excess low-mass $\psi'\pi$ events passing these cuts is 0 ± 5, however. Dividing, this implies that

$$\frac{0 \pm 5}{27 \pm 3} = 0 \pm 19 \pm 11\ \% = 0 \pm 22\ \% \tag{6.12}$$

of the ψ's are associated with a pion with an invariant mass of the $\psi'\pi$ system near threshold.

One could consider the possibility that the production kinematics for the parent particle are different from the J/ψ's, and that the 20 events cut by the dimuon momentum cut are in fact real. However, this would mean that in the region cut that over 600% of the ψ's come from resonant $\psi'\pi$ decay, which is obviously impossible. Using the analysis from the data sample with the tighter cuts, we set an upper limit (90% confidence level) that no more than 30% of the ψ's are associated with a $\psi'\pi$ threshold enhancement.

Chapter 7: Discussion of Results & Summary

A. J/ψ inclusive cross-sections

The antiproton beam cross-section is not substantially larger than that for proton beam. This suggests that gluon fusion is the dominant mechanism for J/ψ production at 300 GeV. Had quark-antiquark annihilation been a major contributor to the number of J/ψ's produced, there would have been a substantial increase in cross-section in going to antiproton beam.

A natural interpretation of the 25% higher cross-section in the pion data would be that 25% of the J/ψ's from the pion beam are produced via annihilation of valence quarks. However, this is not the only possible interpretation. If a larger total fraction of the pion's momentum is carried by the gluons, the cross-section from gluon fusion will also increase. This is to be expected; as discussed in chapter 1, there is a factor of two difference in the depth of the one gluon exchange potential between mesons and baryons. Alternatively, if the momentum distribution for individual gluons in pions is stiffer, there will also be an enhancement in J/ψ production due to the larger overlap integral of the beam and target structure functions subject to the constraint that $x_1 x_2 = \tau$ becomes larger.

That the inclusive cross-section is the same for pion beams of either sign agrees with predictions based on charge independence.

Comparison of the results from E-705 with other experiments is shown in the following table and four figures:

Table 7.1

J/ψ Branching Fractions times Cross-Sections ($x_F > 0$) for Selected Experiments

Experiment	p(beam)	Target	Beam	B·σ (nb/nucleus)	B·σ (nb/nucleon)
E-537 [57]	125 GeV	Be	π-	41 ± 4	5.3 ± 0.5
		A = 9	antiproton	34.2 ± 3.4	4.4 ± 0.4
		Cu	π-	267 ± 24	5.6 ± 0.5
		A = 63.5	antiproton	209 ± 21	4.4 ± 0.4
		W	π-	585 ± 40	4.6 ± 0.3
		A = 184	antiproton	510 ± 27	4.0 ± 0.2
NA3 [58]	150 GeV	H	π+	6.2 ± 1.0	6.2 ± 1.0
		A = 1	π-	6.5 ± 0.9	6.5 ± 0.9
			antiproton	6.6 ± 1.0	6.6 ± 1.0
		Pt	π+	969 ± 160	7.2 ± 1.2
		A = 195	π-	884 ± 130	6.6 ± 1.0
			proton	371 ± 90	2.8 ± 0.7
			antiproton	800 ± 130	5.9 ± 1.0
	200 GeV	H	π+	5.8 ± 0.8	5.8 ± 0.8
		A = 1	π-	6.3 ± 0.8	6.3 ± 0.8
			proton	3.6 ± 0.9	3.6 ± 0.9
		Pt	π+	976 ± 150	7.2 ± 1.1
		A = 195	π-	960 ± 150	7.1 ± 1.1
			proton	509 ± 130	3.8 ± 1.0
			antiproton	730 ± 150	5.4 ± 1.1
	280 GeV	H (A=1)	π-	8.7 ± 0.8	8.7 ± 0.8
		Pt (A=195)	π-	1270 ± 120	9.4 ± 0.9
E-444 [59]	225 GeV	C	π+	82 ± 12	8.1 ± 1.2
		A = 12	π-	88 ± 12	8.7 ± 1.2
			proton	53 ± 7	5.3 ± 0.7
			antiproton	85 ± 40	8.4 ± 4.0
E-331 [60]	225 GeV	C	π+	122 ± 40	12.1 ± 4.0
		A = 12	π-	141 ± 26	14.0 ± 2.6
			proton	82 ± 24	8.1 ± 2.4
UA 6[61]	300 GeV	H	proton	4.5 ± 0.5 ± 0.3	4.5 ± 0.5 ± 0.3
		A = 1	antiproton	5.9 ± 0.8 ± 0.4	5.9 ± 0.8 ± 0.4
CS [62]	400 GeV	Fe (A =56)	proton	20 ± 4 (all x_F)	20 ± 4 (all x_F)
E-672 [63]	530 GeV	Be	π-	69 ± 15	9.0 ± 2.0
		A = 9	proton	59 ± 13	7.7 ± 1.7

If the experiment used its own value of α to convert from a per nucleus cross-section to a per nucleon cross-section it is used. Otherwise, an $A^{0.92}$ dependence[64] is used.

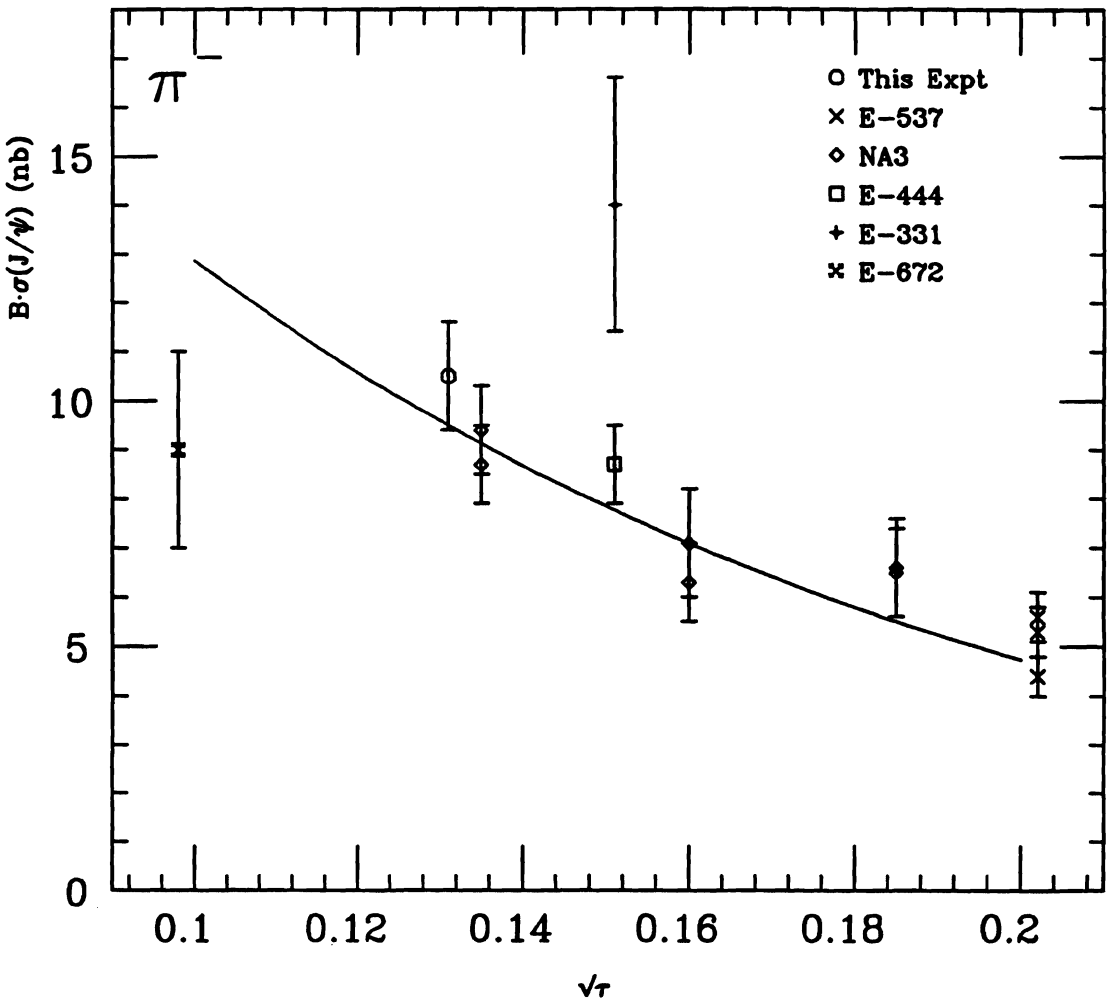

Figure 7.1: J/ψ cross-section times branching fraction for selected π- beam experiments. Solid curve is the Lyons prediction.

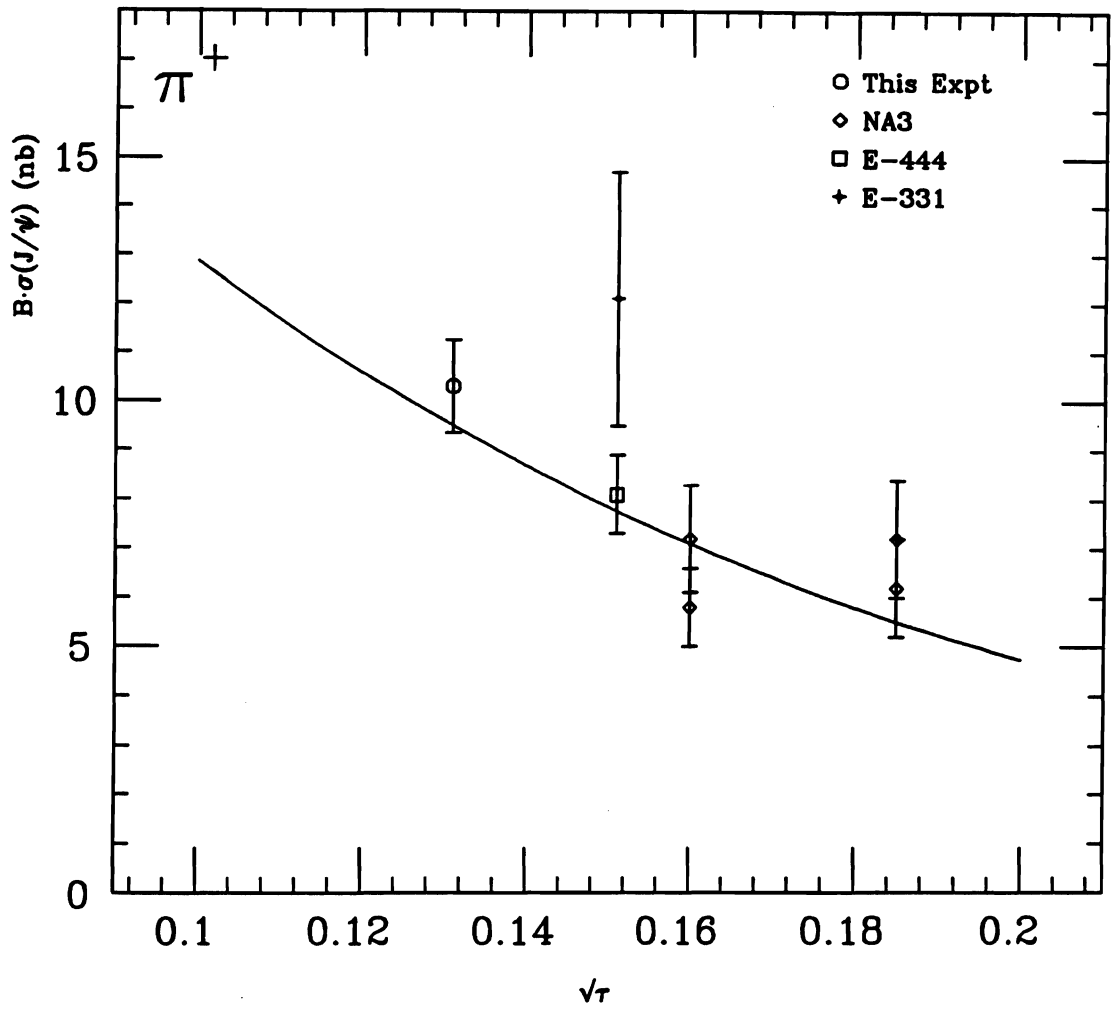

Figure 7.2: J/ψ cross-section times branching fraction for selected π+ beam experiments. Solid curve is the Lyons prediction.

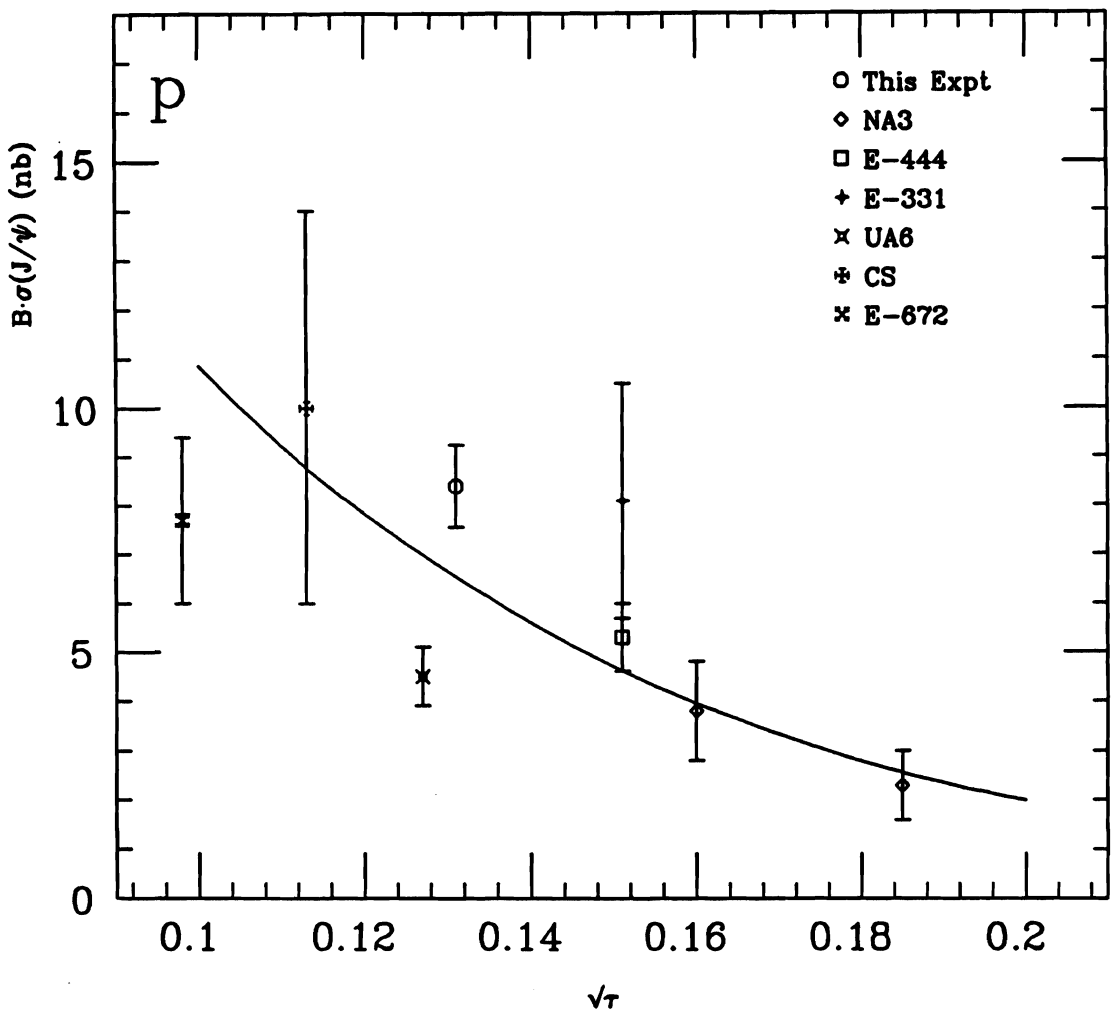

Figure 7.3: J/ψ cross-section times branching fraction for selected proton beam experiments. Solid curve is the Lyons prediction.

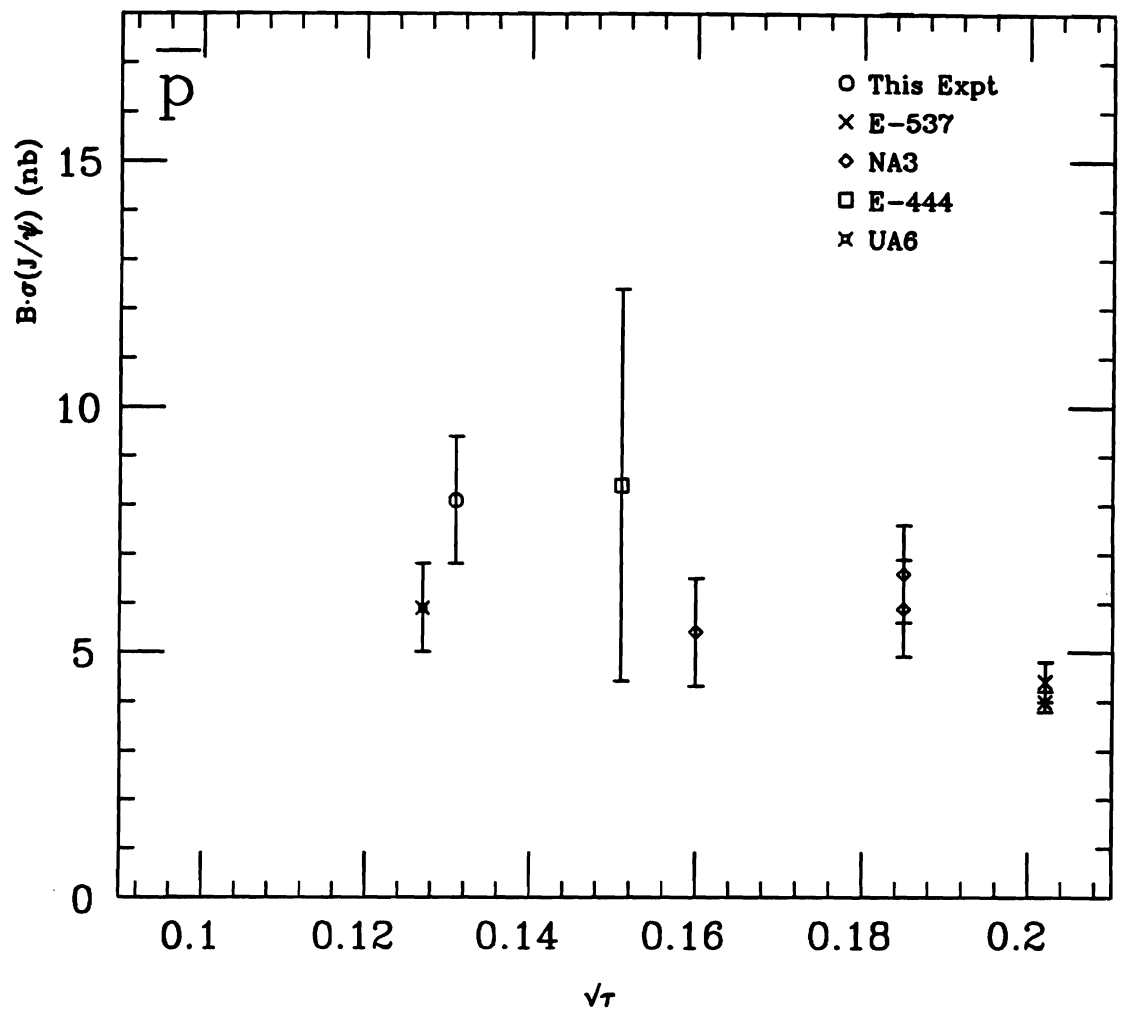

Figure 7.4: J/ψ cross-section times branching fraction for selected antiproton beam experiments.

B. J/ψ differential cross-sections

As pointed out in Chapter 1, from a set of structure functions and a production model the shape of the distribution $d\sigma/dx_F$ can be calculated. Using a model where J/ψ's are produced via the process $g + g \rightarrow$ J/ψ, and the structure functions of Duke

and Owens[65], the Feynman-x distributions were calculated via a Monte Carlo, and the results are shown in figures 7.5 and 7.6.

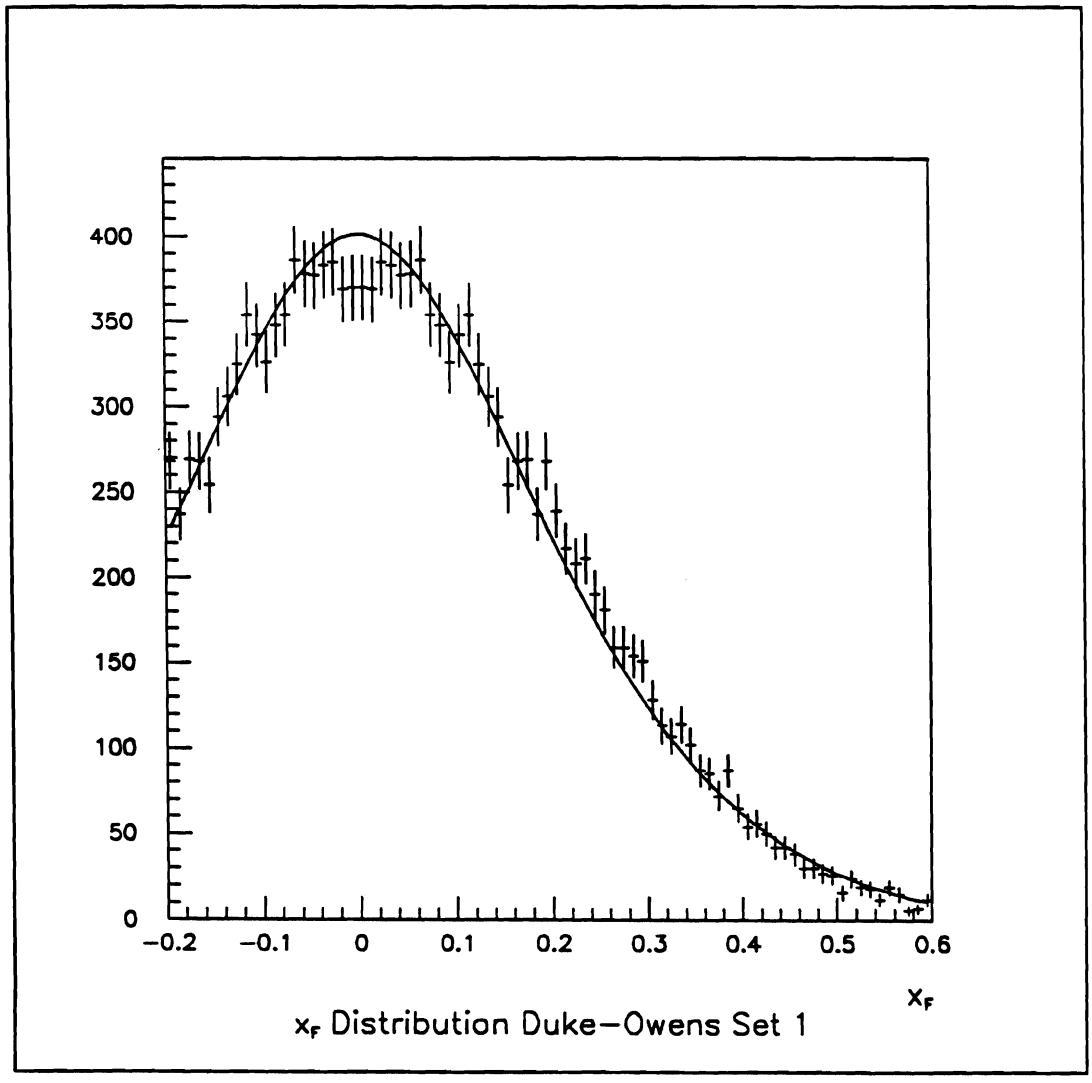

Figure 7.5 Monte Carlo Feynman-x distribution for Duke-Owens Set 1. No corrections for bleaching gluons or indirect J/ψ production applied.

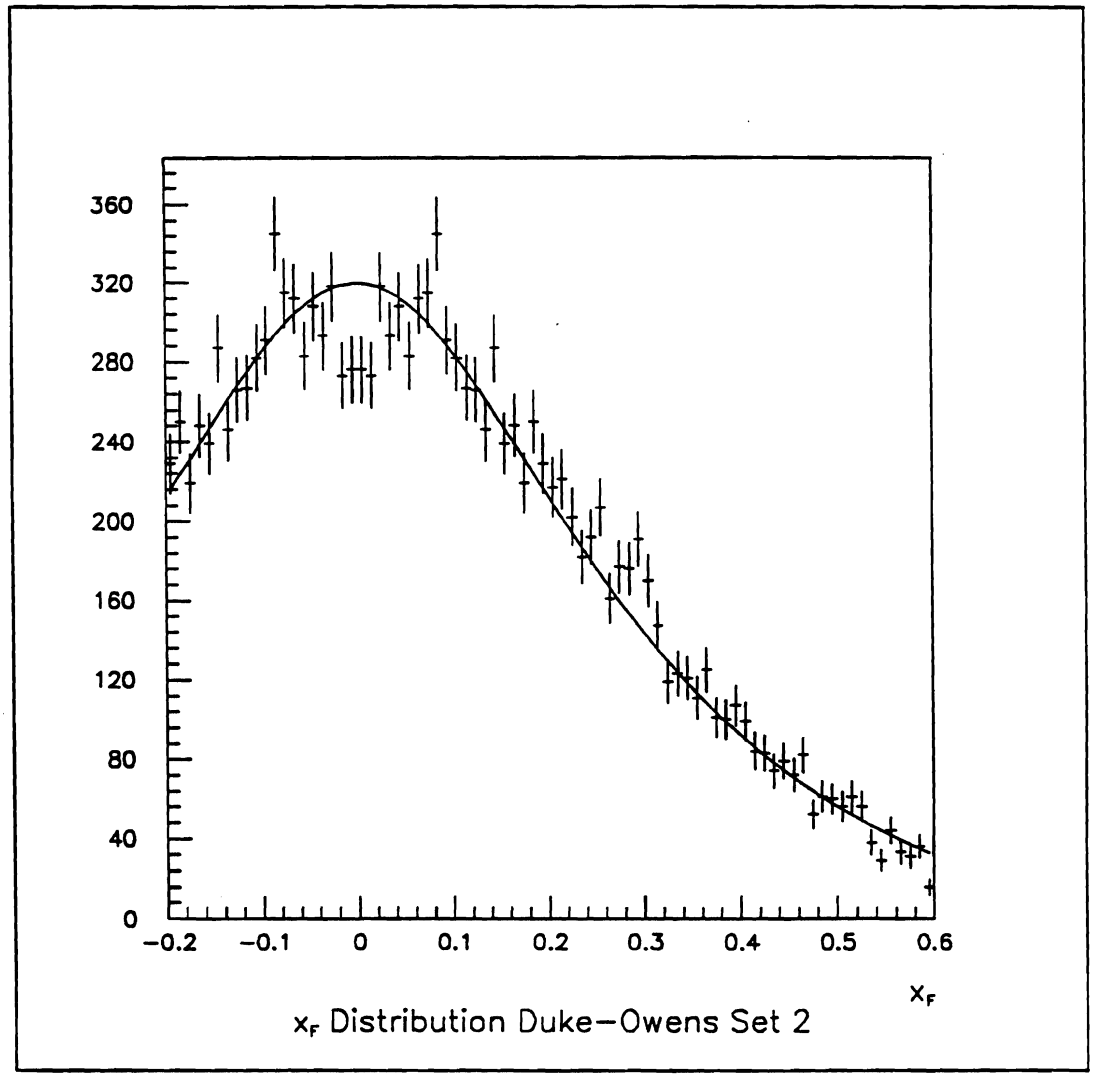

Figure 7.6 Monte Carlo Feynman-*x* distribution for Duke-Owens Set 2. No corrections for bleaching gluons or indirect J/ψ production applied.

This distributions were fit to the form

$$\frac{d\sigma}{dx_F} \sim \frac{(1-x_1)^n \quad (1-x_2)^n}{x_1 + x_2} \tag{7.1}$$

where again $x_1 = ½ \ (x^* + x_F)$, $x_2 = ½ \ (x^* - x_F)$, and $x^* = \sqrt{x_F^2 + 4m^2/s}$. Because of the symmetry of having a proton beam on a nucleon target, both terms have the same exponent, n. The actual production mechanism, however, is more complicated than two-gluon fusion. Two gluon fusion to form a J/ψ is forbidden by C-parity; either a gluon must be subsequently radiated, or the gluons fused to form a χ, which then decayed by radiation to a J/ψ. In either case, following the prescription of Kartvielishvili and Likoded[66] we raise the exponent by one. The predictions of both the simple gluon fusion model and gluon fusion with subsequent radiation (either photon or gluon) for both sets of Duke and Owens structure functions are shown in table 7.2.

Table 7.2
Feynman-x Distributions for Duke-Owens Structure Functions

	Duke-Owens Set 1	Duke-Owens Set 2
n (direct production only)	3.78 ± .04	1.90 ± .04
n (including bleaching gluons and indirect production via χ decay)	4.78 ± .04	2.90 ± .04

The measured value of n for the proton data, $n = 4.8 \pm 0.3$, which is in better agreement with the soft gluon distribution of Duke and Owens set 1 than the stiffer gluon distribution of Duke and Owens set 2.

For the pion data, the theoretical uncertainties are greater. The relative contributions of quarks and gluons to J/ψ production is not well known, although the inclusive cross-section suggests that the gluon component is larger. If one assumes that all of the J/ψs are produced via gluon fusion, and a gluon structure function for the pion of the form:

$$x\, G_\pi(x) \sim (1-x)^b \tag{7.2}$$

the observed measurement of n of 1.81 ± 0.14 corresponds to a b of 0.81 ± 0.14. This is substantially stiffer than the gluon structure function for the proton. It is possible that b is anomalously low because of quark-antiquark annihilation. In this production mechanism, there is not a gluon radiated in the final state at tree level, and the quark structure functions are stiffer. Both effects will tend to reduce the exponent b.

The antiproton $d\sigma/dx_F$ distribution falls midway between that of the pion and the proton. Unfortunately the statistics are so low that the error bars are consistent with either distribution; little information about parton distributions can be extracted.

The parameterization

$$\frac{d\sigma}{dx_F} \sim \left(1-\left|x_F - x_0\right|\right)^c \,, \tag{7.3}$$

shows a measurable asymmetry in the proton data; our measurement of x_0 = 0.026 ± 0.007 is not consistent with zero. This can be understood quantitatively as a softening of the gluon structure function for gluons in nuclei. Experiments that measure the A-dependence of J/ψ production report a depletion of large Feynman-x events in heavy nuclear targets relative to hydrogen or deuterium. The converse of this is that there is

an excess at large Feynman-x for protons over nuclear targets — this asymmetry would manifest itself as a slightly forward peaking of the x_F distributions for protons on lithium.

Also, in pion data, our measurement of $x_0 = .034 \pm .012$ is not consistent with $x_0 = .18$ as reported by E-672.[67] The peak of the distribution is in a region where our acceptance is large and *uniform*, so the corrections that we apply are small. Experiments that operate in a more forward region must try to extract the peak position in a region where the acceptance is steeply falling. The price we pay for this enhanced sensitivity in x_0 is poorer sensitivity to c. This parameter measures how quickly the cross-section falls with increasing x_F. We do not have the coverage at large x_F because our PCB chambers did not operate as expected, and the greater reach in x_F an experiment has, the more sensitive it is to the parameter c.

The transverse momentum distributions for pions show an enhancement at large p_T when compared to protons. This could be evidence for quark-antiquark annihilation. The stiffer quark structure functions should favor large transverse momentum.

That the differential cross-section in both Feynman x and transverse momentum is the same for pion beam of either sign agrees with predictions based on charge independence.

On the following pages are shown comparisons of our measured mean transverse momentum for J/ψs with other experiments. The data is linear in $\sqrt{\tau}$, as empirically observed by E-672[68], motivated by a QCD-inspired model.

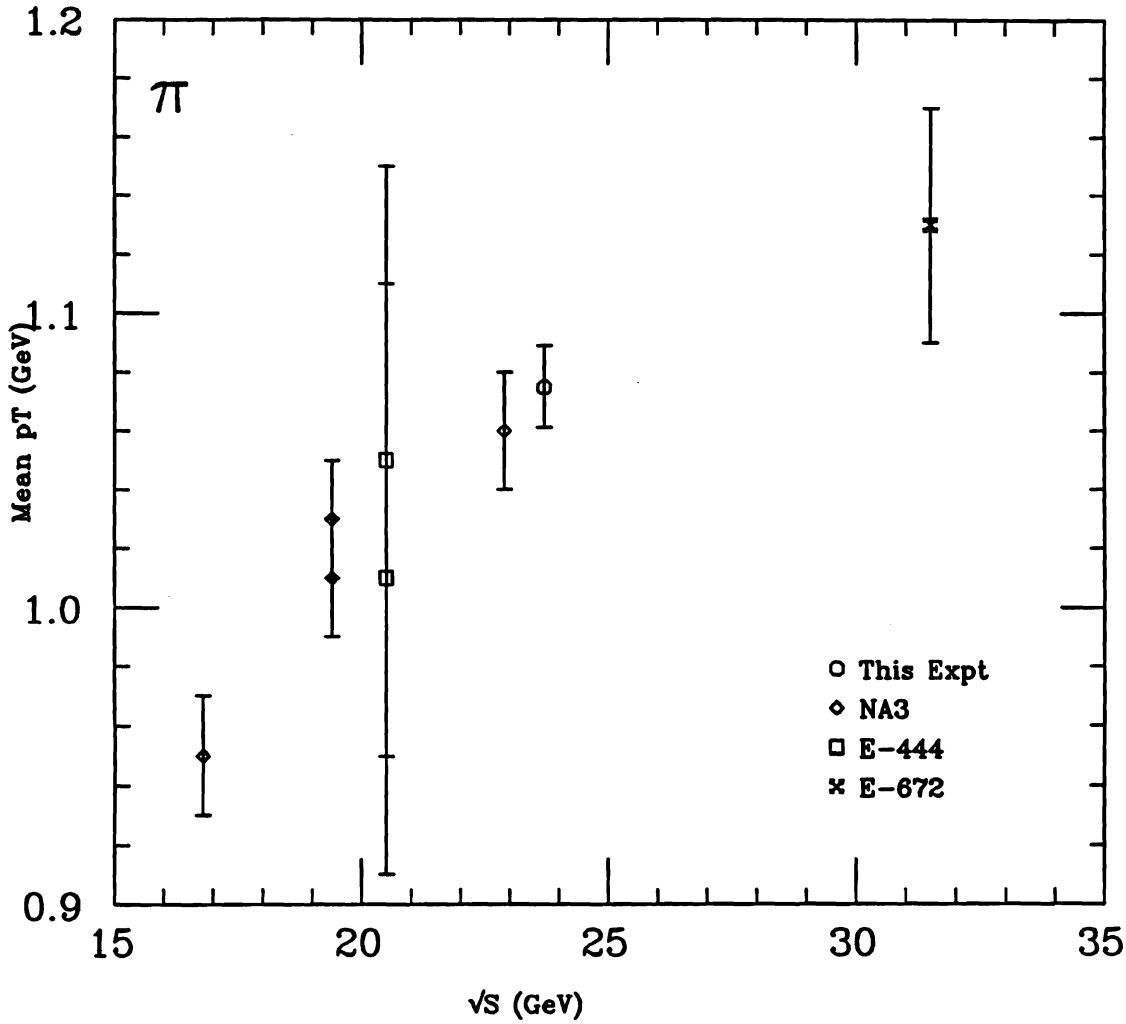

Figure 7.7: Mean J/ψ transverse momentum for selected experiments (pion beam).

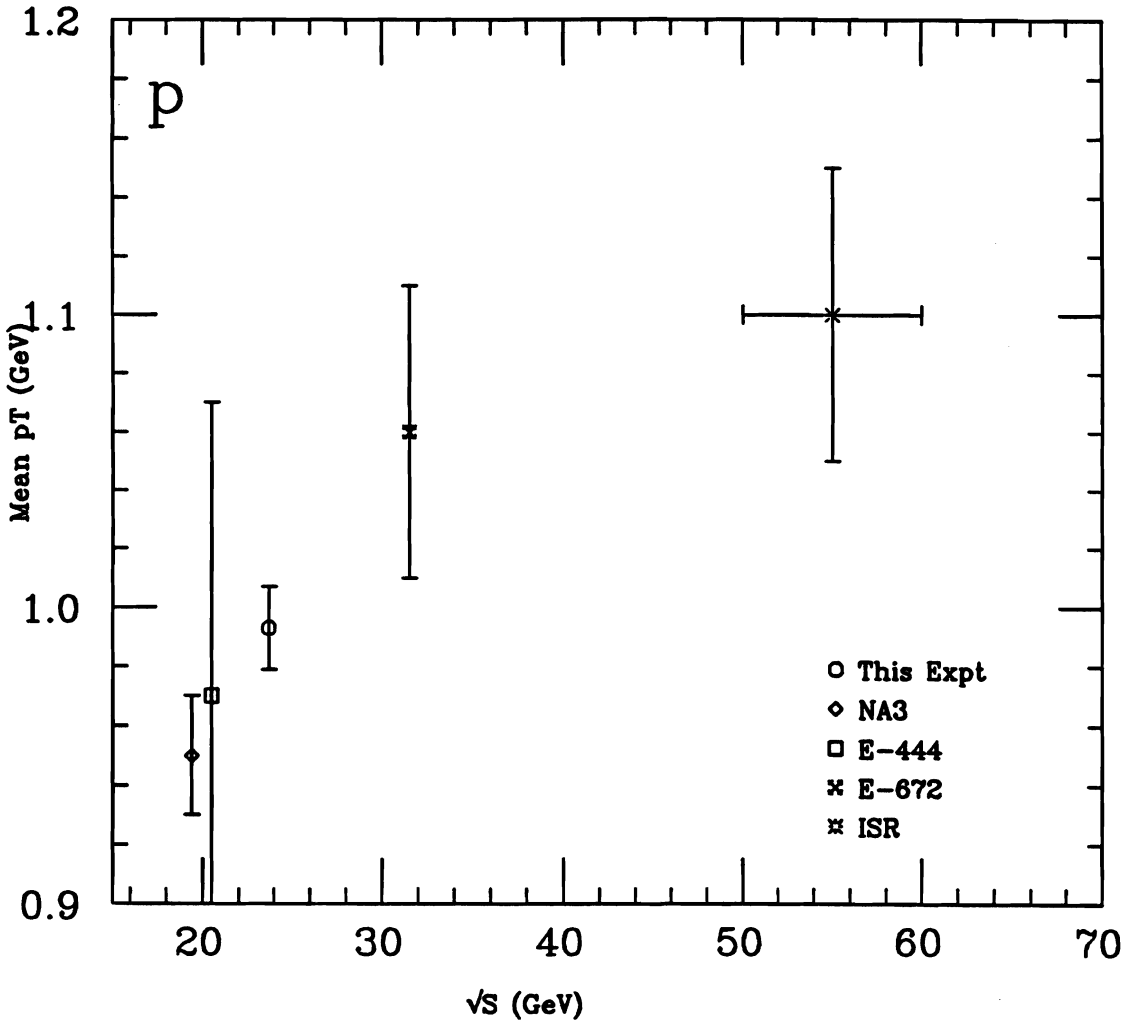

Figure 7.8: Mean J/ψ transverse momentum for selected experiments (proton beam).

C. ψ(2S) inclusive cross-sections

The following table shows measurements of the branching fraction times cross section for the $\psi(2S)$ relative to the $\psi(1S)$ for other experiments, and the following four figures show our data in comparison. In these plots, $\sqrt{\tau}$ is defined as the mass of the $\psi(2S)$ divided by $\sqrt{s}$.

Table 7.3

Bσ ψ(2S) / Bσ ψ(1S) for Selected Experiments

Experiment	$\sqrt{s}$ (GeV)	Target	π+	π-	p	$\bar{p}$
Omega [69]	8.6	W	3.7 ± 1.3 %	3.1 ± 0.6 %		
E-537 [70]	15.3	W		2.6 ± 0.6%		2.0 ± 0.6 %
WA-11 [71]	16.8	Be		2.0 ± 0.4 %		
E-331 [72]	20.6	C	1.8 ± 0.7%		0.7 ± 0.4 %	
E-444 [73]	20.6	C	1.7 ± 0.9 %	2.1 ± 0.6%	1.6 ± 0.9 %	
E-288 [74]	27.4	Be			1.7 ± 0.5%	
ISR [75]	52 & 63	H			1.9 ± 0.6%	
UA1 [76]	630	H				2.9 ± 1.0 %

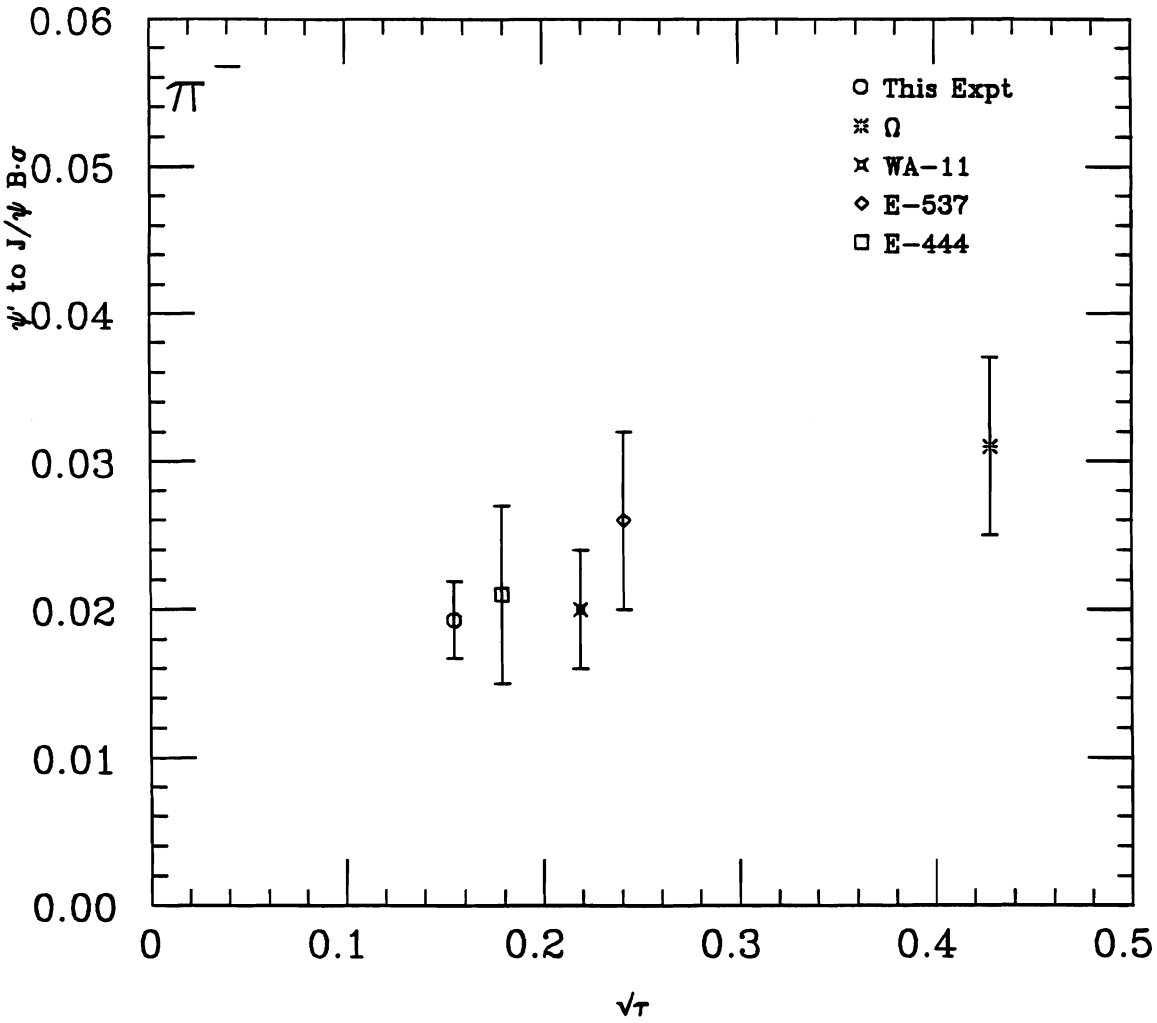

Figure 7.9: ψ':J/ψ cross-section times branching fraction ratio for selected π- beam experiments.

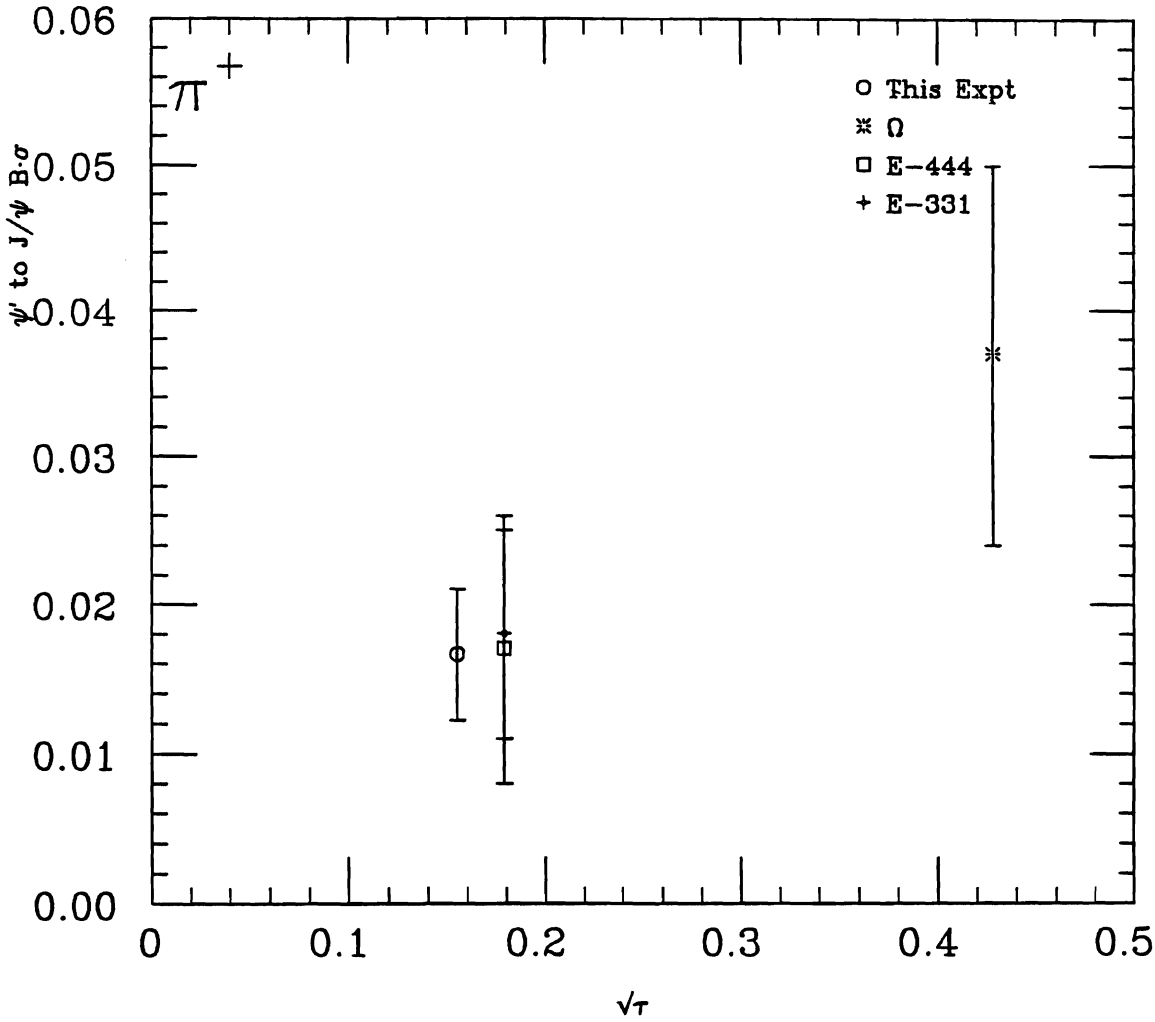

Figure 7.10: ψ':J/ψ cross-section times branching fraction ratio for selected π+ beam experiments.

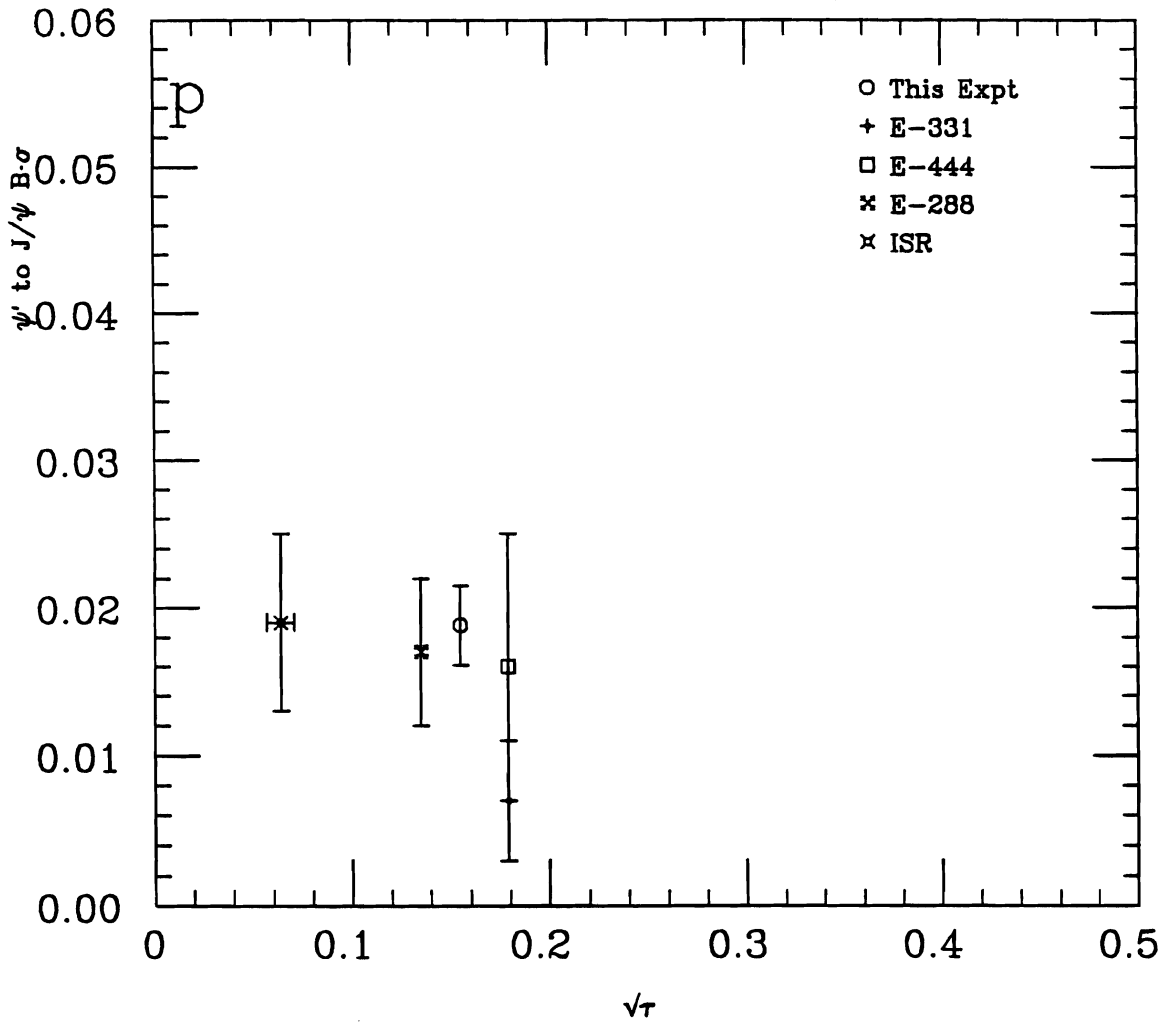

Figure 7.11: ψ':J/ψ cross-section times branching fraction ratio for selected proton beam experiments.

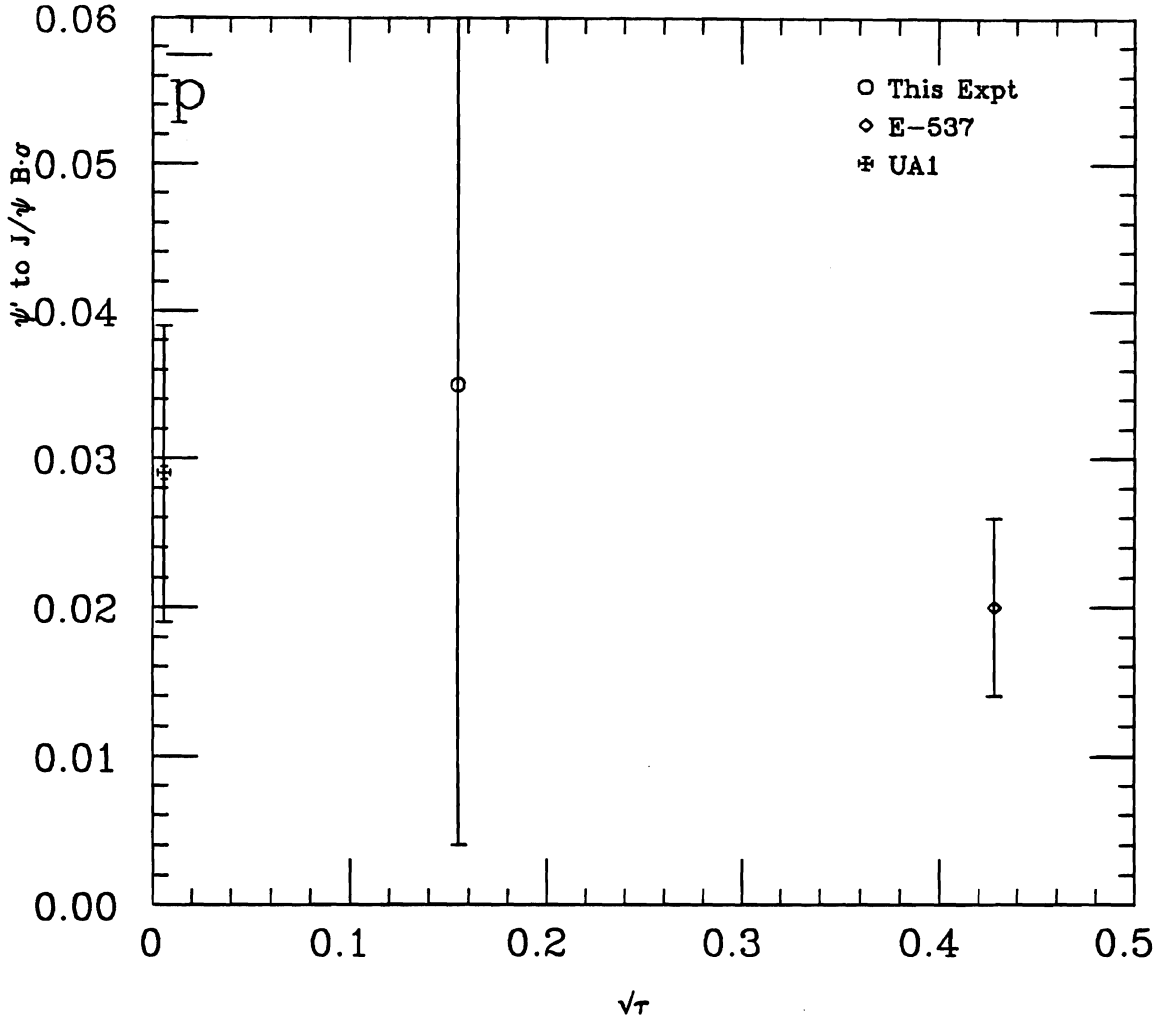

Figure 7.12: ψ':J/ψ cross-section times branching fraction ratio for selected antiproton beam experiments.

That the number of ψ's produced per J/ψ is roughly independent of beam type at 300 GeV suggests that the same production mechanism is responsible for both particles. This is not true at lower energies.

The branching fraction for the decay $\psi' \rightarrow \mu^+\mu^-$ was measured to be .70 ± .22 ± .15 %.

D. Search for hadronic molecules

No compelling evidence for an isotriplet bound state of a $(c\bar{c}q_1\bar{q}_2)$ state decaying into $\psi' + \pi$ has been seen. A 90% confidence level limit of fewer than 30% of the ψ's coming from this state has been established. This should not be construed as evidence against the production of hadronic molecules, merely that they do not feed the ψ' in any significant amount. Background generation is the largest source of uncertainty in this measurement.

E. State at 3837 MeV

An enhancement at 3837 ± 4 MeV is seen in the $\psi\pi^+\pi^-$ spectrum in the negative beam data, and positive beam data do not directly conflict with this observation. (The poor signal to noise is in agreement with Monte Carlo calculations, as evidenced by the consistent measurements of the branching fraction $\psi' \rightarrow \mu^+\mu^-$ in both positive and negative beam.) The measurement of the cross section times branching fraction of 10.0 ± 2.5 ± 2.5 nb indicates that this is a 4σ enhancement. The χ^2 for the best fit background is 78.894 for 54 degrees of freedom; adding only the ψ' peak reduces the χ^2 to 64.209 for 51 degrees of freedom; adding the second peak reduces the χ^2 still further to 49.536 for 48 degrees of freedom. The three additional degrees of freedom provided by the second peak improve the χ^2 by 14.673 units.

Two interpretations suggest themselves: one is a hadronic molecule with J^{PC} of 1^{++} and isospin 1, which would have the name $a_1(3837)$; the other is a previously unobserved level of charmonium.

The possible candidates in the charmonium interpretation are $^1P_1$, $^1F_3$ and $^3D_2$. The triplet state is more promising: the $^1P_1$ is predicted to lie at or near the

center of mass of the χ states, at 3525 MeV. Indeed, E-760 sees approximately 40 candidate events at mass 3526.15 ± .15 MeV.[77] This is 300 MeV lower than the enhancement we see. It is possible that this is the first radial excitation of this state, the 2 $^1P_1$, but then one is faced with the absence of the 1 $^1P_1$ signal in the same plot. (E-760 claims to see the h_c or $^1P_1$ in the $\psi\pi^0$ mode, but not in $\psi\pi^+\pi^-$.[78]) Whereas the $^1P_1$ was too light, the $^1F_3$ state is too heavy. In an inverse square force potential, the lowest energy F-wave states have the same energy as the 4*S* state. For the J/y, this is associated with the $\psi(4160)$ — 300 MeV too high. The $^3D_2$ interpretation is much closer: the prediction of Kwong, Quigg and Rosner[79] (which ignores coupled channel effects) is 3810 MeV. The Particle Data Group naming convention for hadrons suggests the symbol $\psi_2(3837)$ for the $^3D_2$ level of charmonium.

In the hadronic molecule case, the decay of the 3837 state would be via $\psi\rho$, and in the latter, the decay would be via $\psi 2\pi$, with a high dipion mass characteristic of quarkonium decays via double pion emission. Because the ρ mass is so close to the mass difference between the enhancement and the J/ψ it is difficult to distinguish between the two possible interpretations in this manner. Distinguishing via the width of the dipion spectrum is possible, but there are theoretical uncertainties as well — a bound ρ should have a smaller width than a free ρ, just as a neutron in a nucleus has a longer lifetime than a free neutron. A spin-parity analysis would distinguish between the states, if we had the statistics. In addition, observation of the charged mode isopartner via $\psi\pi^\pm\pi^0$ would confirm a hadronic molecule: net charge and hidden charm in the same particle requires four quarks.

F. Summary

While gluon fusion followed by color evaporation seems to agree well with proton beam data, there are still aspects of J/ψ production that are unexplained. The unusually stiff gluon structure function of the pion, as well as the excess of high p_T events suggests that a QCD quark-antiquark annihilation process contributes. Unfolding the two production mechanisms, particularly without *a priori* knowledge of the gluon structure function of the pion, will be difficult. There is not enough antiproton beam data to measure any difference between charmonium production by protons and antiprotons. This is particularly a shame, because the valence antiquark structure functions of the antiproton are well-known, and this would provide a check that the procedure for handling indirect production and color evaporation is correct.

In addition to the lack of antiproton beam data, several other aspects of the experiment proved disappointing. Having our beam normalization limited by the scalers' inability to count to better than 3% accuracy at high rates is unfortunate. Had this not been the case, our cross-sections would have been limited by our ability to measure the muon counter efficiencies. Regular muon scans would have helped here. Perhaps the biggest disappointment was the failure of the small PCB chambers to operate reliably. This reduced or removed our J/ψ acceptance at high x_F, which is a very interesting region for studying the production mechanisms: a large reach in x_F improves the ability to measure the parameters n and c, and is a region where quark-antiquark annihilation is enhanced in pion beam data. For the particle searches, however, good central coverage is even more vital: the pion tracks that are associated with the ψ or ψ' tend to be produced at small angles, and lost in the dead region of the spectrometer.

Since these tracks tend to be low momentum, they also tend to be swept away by the magnet. Tracking through the magnet would be helpful in salvaging these tracks, and would also improve the momentum resolution and track matching of tracks that are accepted into the downstream portion of the spectrometer.

Other experiments should look for the $\psi_x(3837)$. Both E-771 and CDF hope to obtain a very large sample of ψs in the upcoming run; it should be a simple manner to confirm or negate our hint of a new particle. Experiment E-760, which uses an antiproton beam to resonantly produce charmonium, should also look in that region; it should be rich in interesting physics. Besides the $\psi_x(3837)$, there will be one or two more accessible *D*-wave states, and perhaps several molecular states as well.

[1] Donald H. Perkins, *Introduction To High Energy Physics*, 3ed. (Menlo Park: Addison-Wesley, 1987) p.202

[2] J.J. Aubert et al.,*Phys.Rev.Lett.* **33**, 1404 (1974)

[3] J.E. Augustin et al., *Phys.Rev.Lett.* **33**, 1406 (1974)

[4] J.J. Hernandez et al.,*Phys.Lett.* **B239** (1990)

[5] J.J. Hernandez et al.,*Phys.Lett.* **B239** (1990)

[6] G. Zweig, CERN Report 8182/Th.401, CERN, Geneva Switzerland (1964)

[7] D. Griffiths, *Introduction To Elementary Particles*, (New York: Harper and Row,1987) p.75

[8] S.L Glashow, J. Illiopoulos, and L. Maiani, *Phys. Rev.* **D2,** 1285 (1970)

[9] J. Steinberger, *Phys. Rev.* **76**, 1180 (1949)

[10] E. Eichten. private communication

[11] W.M. Tanenbaum, J.S. Whitaker *et al., Phys.Rev.Lett.* **35**, 1323 (1975)

[12] S. Drell and T.M. Yan, *Phys.Rev.Lett.* **25**, 316, (1970) erratum, *ibid* **25**, 902, (1970).

[13] L. Lyons, *Prog. Nucl. Part. Phys.* **7**, 169 (1981)

[14] K.J. Anderson *et al., Phys. Rev.* **D21**, 3075 (1980); *Phys. Rev. Lett.* **42**, 944, 948 and 951 (1979).

[15] V. Barger and R. Phillips, *Collider.Physics* (Redwood City: Addison-Wesley, 1987) p.370

[16] W. Kwong, J. Rosner, C. Quigg, *Ann. Rev. Nucl. Part. Sci.* **37**:343 (1987)

[17] C.N. Yang, *Phys. Rev.* **77**, 242 (1950).

[18]V. Barger and R. Phillips, *Collider Physics* (Redwood City: Addison-Wesley, 1987) p.370

[19] Donald H. Perkins, *Introduction To High Energy Physics*, 3ed. (Menlo Park: Addison-Wesley, 1987) p.310

[20] J. G. Morfin, *A Global Analysis of Recent Experimental Results: How Well Determined Are The Parton Distribution Functions?* Proceedings of the Workshop on Hadron Structure Functions and Parton Distributions. (Singapore: World Scientific, 1990)

[21] P.N. Harriman et al., *Parton Distributions From a Global Analysis of Data*, Proceedings of the Workshop on Hadron Structure Functions and Parton Distributions. (Singapore: World Scientific, 1990)

[22] M.V. Purohit, *The Gluon Strucure Function From the Tagged Photon Lab*, Proceedings of the Workshop on Hadron Structure Functions and Parton Distributions. (Singapore: World Scientific, 1990)

[23] M. Rosati, PhD thesis

[24] V. Kartvielishvili and A. K. Likoded, *Sov. J. Nucl. Phys.* **39**, 298 (1984)

[25] E-672/706 Collaboration "Properties of J/ψ Production in π^-–Be and *p*–Be Collisions at 530 GeV/*c*" FERMILAB-Pub-90/62-E. (1991)

[26] R.J. Jaffe, *Phys. Rev.* **D15**, 267 (1977)

[27] D.O. Caldwell, *Two Photon Production of Spin-One Mesons*, Hadron 89: The Third International Conference on Hadron Spectroscopy (Cedex: Editions Frontieres, 1989)

[28] S. Ishida, M. Oda, H. Sawazaki, K.Yamada,*Prog. Theor. Physics* **82**,119 (1989)

[29] J.L. Rosen, *Heavy Hadronic Molecules*, Particles and Fields Series 36: Glueballs, Hybrids and Exotic Hadrons (New York: American Institute of Physics, 1988)

[30] J.L. Rosen, *Heavy Hadronic Molecules*, Particles and Fields Series 36: Glueballs, Hybrids and Exotic Hadrons (New York: American Institute of Physics, 1988)

[31] Lithium isotopic abundance is from H. Frauenfelder and E. M. Henley, *Subatomic Physics* (Englewood Cliffs: Prentice-Hall, 1974) p.528.

[32] A. Marchioni, private communication

[33] Marzia Rosati, PhD Thesis

[34] S. Conetti, J. Kuzminski, A. Marchioni, D. Stairs, et al., "Performance of 0.755 mm Pitch MWPC's Operating at High Rate," presented ar the 1988 IEEE Nuclear Science Symposium, Orlando FL, November 8-13, 1988.

[35] J. Appel et. al.,*Nuclear Instruments and Methods*, **127**, pp495-505 (1975)

[36] B. Cox et. al., *Nuclear Instruments and Methods*, **219**, pp 487-490 (1984)

[37] L. Spiegel et al., "Performance of a Lead Radiator, Gas-Tube Calorimeter", presented ar the 1988 IEEE Nuclear Science Symposium, Orlando FL, November 8-13, 1988 and FERMILAB TM-1573.

[38] J.J. Hernandez et al.,*Phys.Lett.* **B239** p. III.13. (1990)

[39] J.J. Hernandez et al.,*Phys.Lett.* **B239** p.III.5 (1990)

[40] H. Areti et. al, *Nucl. Inst. and Meth.* **212**, 135 (1983)

[41] J.J. Hernandez et al.,*Phys.Lett.* **B239** (1990)

[42] A. Simard, M.S. Thesis

[43] T. Nash, et al. Fermilab-Conf-88/97 (1988)
T. Nash et al., Fermilab-Conf-89/58 (1989)

[44] J.J. Hernandez et al.,*Phys.Lett.* **B239** (1990)

[45] J. Baider et al., *Z. Phys.* **C20**,101-116

[46] S. Tzamarias et al. "Psi Production in $\bar{p}N$ and $\pi^- N$ Interactions at 125 GeV and a Determination of the Gluon Structure Functions of the Antiproton and the π^-" Fermilab-Pub-90/63-E (1990)

[47] J.J. Hernandez et al.,*Phys.Lett.* **B239** (1990)

[48] S. Katsenavas et al., *Phys. Rev. Lett.* **60**, 2121 (1988)

[49] D.M. Alde et al.,*Phys.Rev.Lett.* **66**, 133 (1991)

[50] D. Coffman et al., "A Direct Measurement of the J/ψ Leptonic Branching Fraction" SLAC-PUB-5592 (1991) (Also U. of Iowa 91-17)

[51] D. Coffman et al., "A Direct Measurement of the J/ψ Leptonic Branching Fraction" SLAC-PUB-5592 (1991) (Also U. of Iowa 91-17)

[52] L.S. Brown and R.S. Cahn,*Phys. Rev. Lett.* **35** 1

[53] D. Coffman et al., "A Direct Measurement of the J/ψ Leptonic Branching Fraction" SLAC-PUB-5592 (1991) (Also U. of Iowa 91-17)

[54] L.S. Brown and R.S. Cahn,*Phys. Rev. Lett.* **35** 1

[55] D. Coffman et al., "A Direct Measurement of the J/ψ Leptonic Branching Fraction" SLAC-PUB-5592 (1991) (Also U. of Iowa 91-17)

[56] J.J. Hernandez et al.,*Phys.Lett.* **B239** (1990)
[57] S. Katsanevas et al. *Phys. Rev. Lett.* **60**,2121 (1988)

[58] J. Baider et. al. *Z. Phys.* **C20**, 101(1983)

[59] K. Anderson et al., *Phys. Rev. Lett.* **42**, 944 (1979)

[60] J. G. Branson et al., *Phys. Rev. Lett.* **38**, 1331 (1977)

[61] C. Morel et al. "Measurement of the Inclusive J/ψ Production Cross-Sections in $p\bar{p}$ and pp Collisions at $\sqrt{s} = 24.3$ GeV" CERN-PPE/90-127 (1990).

[62] E. J. Siskind et al., *Phys. Rev.* **D21**, 628 (1980)

[63] E-672/706 Collaboration "Properties of J/ψ Production in π^-–Be and p–Be Collisions at 530 GeV/c" FERMILAB-Pub-90/62-E. (1991)

[64] D.M. Alde et al.,*Phys.Rev.Lett.* **66**, 133 (1991)

[65] D.W. Duke and J.F. Owens, *Phys. Rev.* **D30,** 49 (1984)

[66] V. Kartvielishvili and A. K. Likoded, *Sov. J. Nucl. Phys.* **39**, 298 (1984)

[67] E-672/706 Collaboration "Properties of J/ψ Production in π^-–Be and *p*–Be Collisions at 530 GeV/*c*" FERMILAB-Pub-90/62-E. (1991)

[68] E-672/706 Collaboration "Properties of J/ψ Production in π^-–Be and *p*–Be Collisions at 530 GeV/*c*" FERMILAB-Pub-90/62-E. (1991)

[69] M.J. Corden et al.,*Phys.Lett.* **B96**,411

[70] S. Katsanevas et al.,*Phys. Rev. Lett.* **60**,2121 (1988)

[71] M. Abolins et al., *Phys.Lett.* **82B**, 145 (1979)

[72] J.G. Branson, et al. *Phys.Rev.Lett.* **38,** 1331 (1977)

[73] K. Anderson, et al. *Phys.Rev.Lett.* **42,** 944 (1979)

[74] H.D. Snyder, et al. *Phys.Rev.Lett.* **36**, 1415 (1979)

[75] A.G. Clark et al. *Nucl.Phys.* **B142**, 29 (1978)

[76] UA1 Collaboration "J/ψ and ψ' Production at the CERN $p\bar{p}$ Colider" CERN-PPE/90-154 (1990)

[77] J.L. Rosen, private communication.

[78] J.L. Rosen, private communication.

[79] W. Kwong, J. Rosner, C. Quigg, *Ann. Rev. Nucl. Part. Sci.* **37**, 343 (1987)